Introduction

The decorative thin films

The preparation techniques

Today the development of clean technologies, in all fields of industrial manufacturing, is a fundamental task, not only for material and metal finishing, but also for plasma surface engineering. Among the most crucial group of technologies that require to be replaced by alternative technologies, are processes used to produce functional galvanic and decorative coatings. The electroplating of several decorative parts, such as those involving hard chromium, cadmium and nickel in metal finishing is today recognized as a major source of environmental pollution [1]. Therefore wet bath technologies have started to lose influence compared with high performance dry coating methods such as those of *P*hysical *V*apour *D*eposition (PVD).

Beyond the purely decorative purpose, the results obtained with PVD coatings in metal cutting and forming in the last 25 years showed to be one the most promising solutions for the complicated situation of galvanic coatings that seemed to be technologically and economically irreplaceable [1]. Golden yellow PVD coatings are being increasingly used as a substitute for galvanic plating of watch cases, bracelets and other similar decorative items [1]. In these applications, the main reasons for the success of PVD coatings is a reduction in selling price through a lowering of material costs and the elimination of waste problems that are typical for electroplating processes. Préci-Coat [1] was the first company, worldwide, to succeed and to industrialise the yellow PVD coating for “high-value” decorative applications, in order to replace the traditional gold plating used in watch industry and jewellery, whose minimum gold thickness was of the order of several micron (usually around 10 μm).

Although PVD coatings have to meet a variety of requirements to be able for decorative applications: attractive colours, good wear resistance and good corrosion resistance, these quality requirements are more and more restricted by the low prices imposed by the market. Among all the PVD coating techniques, magnetron sputtering is nowadays one of the reference techniques, not only because of the easy transpose of laboratorial work towards the industrial environment, but above all, because of the simplicity of the parameters that need to be manipulated for the coating of a decorative (or other) object. Among the most important characteristics of this technique, it is worth mention: its capability of deposition in three-dimensional geometry parts; the possibility of deposition at temperatures lower than 200 °C, which allows coating some polymeric objects, watch band with sensitive spring components, porous cast materials, etc.

The decorative thin films

Nitrides and oxynitrides represent a group of modern ceramic materials of increasing technological importance. They have been extensively investigated over the past few years because of their remarkable properties in the domains of protective applications, such as wear, diffusion and corrosion-resistant ones [3-6]. Furthermore, their relatively high hardness, chemical stability, durability and electronic properties lead to a wide variation of multiple applications that range between the tribological to electric ones [7]. Although employment of decorative lacquer coatings allows the generation of a virtually unlimited spectrum of colour tones, such coatings lack the metallic sheen frequently desired on high quality products. Vacuum coating techniques (in particular the PVD ones) of decorative layers has been industrially used for more than 20 years.

Decorative hard coatings were first introduced on small consumer products such as watches, writing instruments, eyeglass frames, wristwatches, pens, kitchen and bathroom equipment, as well as jewellery parts. While enhancing the appearance and lending attractive colorations to surfaces, the films are supposed to provide scratch resistance and protection against corrosion and durability. Such films were primarily deposited using magnetron sputtering, based on nitrides or carbonitrides of titanium or titanium alloys [8]. The colour tones attainable were largely restricted to golden yellows, various shades of grey and black [9-19]. Included among those hard materials, exhibiting prominent inherent colourations, are several borides, such as LaB_6 (reddish purple) [20-23], YB_6 (blue-grey) [21,22], in addition to the better known yellowish nitrides and carbides (TiN - golden yellow; ZrN - greenish yellow; HfN - pale greenish yellow and TaC - golden brown) [12]. *Ph. Roquiny et al*. when depositing titanium nitride claimed that could obtain coatings with intrinsic colours that ranged from silver to gold-like yellow and finally to brown, just by increasing the partial pressure of nitrogen [24]. Similar results were also claimed by others authors [25,26].

J.F. Pierson and co-authors studied the Ti-B-N system, deposited with DC magnetron sputtering, and verified that increasing the nitrogen flow rate in the reactive mixture ($Ar + N_2$), the colour of the film evolves from silver grey to dark and then black [27].

Decorative coloured coatings based on oxide materials have also been produced, either by interferential colouring [28] or by adding a dye [29]. Protective-decorative coatings with different colour tones can also be produced by the use of ion-induced and ion-plasma deposition

of materials [30]. *Radjabov et al.* [31] used a two-layer Ta–Ta_2O_5 and Zr–ZrO_2 coatings, deposited by magnetron sputtering, as protective and decorative coatings on glass substrates, ceramics or natural stones, where the colour of the coatings was controlled by a quenching interference in the oxide-metal structure. With this method the authors were able to deposit coatings with interferential colours such as gray, light beige, brown, brown-violet, violet, dark blue, light blue, blue, metal, light yellow, gold, crimson, emerald and light green. Nevertheless the high variety of colours achieved, the production of protective-decorative coatings on dielectric substrates, requires taking into account the composition, and state of the surface, and also the substrate colour. Since the apparent colourations of interference films are primarily influenced by the thicknesses of the films, which, for complexly shaped substrates, cannot be maintained sufficiently constant over the entire surfaces of substrates when typical PVD methods are employed [32], these types of films appear to be less suitable choices as decorative coatings, except where specific short-lived fashion trends (e.g. colour gradations or multicolour effects) are involved [33,34].

Halary-Wagner and co-authors [35] used light-induced chemical vapour to deposit titanium dioxide for decorative applications, achieving good colour contrast for small thickness differences, covering all the colours of the visible spectrum with film thicknesses lower than 150 nm. Nevertheless the colour slightly changed with incident light.

Wang et al. used a thin anodic aluminium oxide film, with a channel size of about 30 nm of diameter, on an Al substrate and coated with carbon by chemical vapour deposition, to achieve a high variety of interferential colours [36].

As a result of technological progress in very recent years, a new challenge was passed onto decorative hard coatings. Increasing demands for durability of brass hardware for door locksets and bathroom equipment drive the request for the application of modern PVD processes for these products. In any case, the growing demand for low-cost products and reduced material resources imply that the continuous change in target materials and basic PVD deposition procedures to obtain different coloured films is clearly unsuitable. Taking these restrictions into account, a new class of materials has been gaining importance for decorative applications, the so-called metal oxynitrides, MeO_xN_y (Me stands for na early transition metal) [37-46].

F Vaz et al. used a Ar/(N_2 + O_2) mixture to deposit titanium oxynitride coatings with colours varying form bright yellow-pink to dark golden yellow and dark blue [40].

Their relevance arises from the fact that the presence of oxygen allows the tailoring of film properties between those of metallic nitrides, MeN, and those of the correspondent insulating oxides, MeO_x. Tuning the oxide/nitride ratio allows one to tune the band-gap, bandwidth, and crystallographic order between oxide and nitride and hence the electronic and optical properties of materials, including colour.

Relationship of the present work with foregoing investigation in the Minho University group (*Functional Coatings Group* – GRF)

The present project relates with foregoing investigation in the functional coatings group in several ways:

i) it is built in the previous knowledge in multiphase materials, phase transitions and relaxation phenomena; as well as in existence experience with different experimental techniques.

ii) the project represents a greater interest for fundamental problems with direct technological applications (the development of coloured films for several kinds of technological decorative objects), and a broader and interdisciplinary approach (physics and mechanics).

iii) it broadens the experimental techniques used by the group in order to solve fundamental problems, especially through the mechanical experiments, such as those of real life conditions: wear and corrosion. The vast experience in colour theory and characterization of the physics department members was used to obtain an accurate characterization of this property.

The deposited films were intended, and beyond the different achievable colours, to reveal good adhesion, corrosion, wear resistance and biocompatibility. The main strategy consisted in the adoption of the benefits revealed by these systems, namely those that result from the transition from a typical metal nitride to its correspondent metal oxide. This transition opens a wide range of properties, which may vary from a typical metallic/covalent material to an ionic one. The electronic properties of the material were then changed, and electrical and optical behaviour was thus modulated. The vast work done in the MeO_xN_y "extremes" - the nitrides and correspondent oxides and the large variations in the properties of these materials, allowed the fulfilment of the thesis main goal - the preparation of different coloured films.

References

[1]- B. Navinsĕk, P. Panjan, I. Milosĕv, Surf Coat Technol. 116–119 (1999) 476.

[2]- Raymond Constantin, Baham Miremad, Surf Coat Technol. 120–121 (1999) 728.

[3]- K. H. Jack, *Non-Oxide Technical and Engineering Ceramics*, Elsevier, Amsterdam, 1986, p. 1.

[4]- S. Saito, *Fine Ceramics*, Elsevier, Tokyo, 1985, p. 197.

[5]- S. Komarrneni, J. Mater. Chem. 2 (1992) 1219.

[6]- A. Navrotsky, J. Alloys Compd. 321 (2001) 300.

[7]- S. Dreer, R. Krismer, P. Wilhartiz, G. Friedbacher, Thin Solid Films 354 (1999) 43.

[8]- B. Zega, Surf. Coat. Technol. 39/40 (1989) 507.

[9]- B. Zega, M. Kornmann J. Amiguet, Thin Solid Films 45 (1977) 577.

[10]- A. Mumtaz, W. H. Class, J Vac Sci Technol. 20 (1982) 345.

[11]- B. Karlsson, J-E Sundgren, B-O Johansson, Thin Solid Films 87 (1982) 181.

[12]- A J Perry, J Schoenes, Vacuum 36 (1986) 149.

[13]- A. J. Perry, Thin Solid Films 138 (1986) 73.

[14]- A. J. Perry, M. Georgson, W. D. Sproul, Thin Solid Films 157 (1988) 255.

[15]- H. Randhawa, Surf. Coat. Technol. 36 (1988) 829.

[16]- H. Randhawa, P. C. Johnson, R Cunningham, J. Vac. Sci. Technol. A 6 (1988) 2136.

[17]- R. Luthier, F Lévy, Vacuum 41 (1990) 2205.

[18]- P. K. Banerjee, J. Skim, S. S. Mitra, Thin Solid Films 200 (1991) 341.

[19]- U. Kopacz, R. Riedl, Z. Metallkde 83 (7) (1992) 492.

[20]- R. W. Johnson, A. H. Daane, J Phys. Chem. 65 (1961) 909.

[21]- F. Binder, Radex-Rundschau 1 (1977) 52.

[22]- K. A. Schwetz, K. Reinmuth, A. Lipp, Radex-Rundschau 3 (1981) 568.

[23]- M. J. McKelvy, L. Eyring, E. K. Storms, J. Phys. Chem. 88 (1984) 1785.

[24]- F. Binder, Radex-Rundschau 1 (1977) 52.

[24]- Ph. Roquiny, F. Bodart, G. Terwagne, Surf. Coat. Technol. 116–119 (1999) 278.

[25]- G. Reiners, H. Hantsche, H.A. Jehn, U. Kopacz, A. Rack, Surf. Coat. Technol. 54-55 (1992) 273.

[26]- H. A. Jehn, *Materials and Processes for Surface and Interface Engineering*, Kluwer Academic, Dordrecht, 1995, pp. 359-370.

[27]- J. F. Pierson, E.Tomasella, Ph. Bauer, Thin Solid Films 408 (2002) 26.

[28]- R. L. Van Renesse, *Optical Document Security*, second ed., Artech House, Boston, 1998.

[29]- S. Jäger, Thin Solid Films 286 (1996) 154.

[30]- V.T. Barchenko, Yu A. Bystrov, E.A. Kolgin. *Ion-plasma technologies in electron units production,* St. Petersburg: Energoatomizdat; 2001.

[31]- T. D. Radjabov, A.I. Kamardin, A.V. Sharudo, Vacuum 75 (2004) 143.

[32]- S. Swann, Vacuum 38 (1988) 791.

[33]- B. Cotton, P. C. S. Hayfield, Trans Inst Metal Finish, 45 (1967) 48.

[34]- B. Seeley, Metal Finishing 84 (1986) 11.

[35]- E. Halary-Wagner, T. Bret, P. Hoffmann, Appl. Surf. Scie. 208-209 (2003) 663.

[36]- X. H. Wang, T. Akahane, H. Orikasa, T. Kyotani, Y. Y. Fu, Appl. Phys. Lett. 91 (2007) 011908.

[37]- R. Franchy, Surface Science Reports 38 (2000) 195.

[38]- E. Ariza, L.A. Rocha, F. Vaz, L. Cunha, S.C. Ferreira, P. Carvalho, L. Rebouta, E. Alves, Ph. Goudeau, J.P. Rivière, Thin Solid Films 469-470 (2004) 274.

[39]- F. Vaz, P. Carvalho, L. Cunha, L. Rebouta, C. Moura, E. Alves, A.R. Ramos, A. Cavaleiro, Ph. Goudeau, J.P. Rivière, Thin Solid Films 469-470 (2004) 11.

[40]- F. Vaz, P. Cerqueira, L. Rebouta, S. M. C. Nascimento, E. Alves, Ph. Goudeau, J. P. Rivière, K. Pischow, J. de Rijk, Thin Solid Films 447-448 (2004) 449.

[41]- E. Alves, A. Ramos, N. Barradas, F. Vaz, P. Cerqueira, L. Rebouta, U. Kreissig, Surf. Coat. Technol. 180-181 (2004) 372.

[42]-F. Vaz, P. Cerqueira, L. Rebouta, S. M. C. Nascimento, E. Alves, Ph. Goudeau, J. P. Rivière, Surf. Coat. Technol. 174-175 (2003) 197.

[43]- Jean-Marie Chappé, Nicolas Martin, Guy Terwagne, Jan Lintymer, Joseph Gavoille, Jamal Takadoum, Thin Solid Films 440 (2003) 66.

[44]- N. Martin, J. Lintymer, J. Gavoille , J.M. Chappé, Surf. Coat. Technol.201 (2007) 7720.

[45]- N. Martin, J. Lintymer, J. Gavoille , J.M. Chappé, Surf. Coat. Technol.201 (2007) 7727.

[46]- N. Martin, J. Lintymer, J. Gavoille , J.M. Chappé, Surf. Coat. Technol.201 (2007) 7733.

Chapter 1

Samples preparation:

Magnetron Sputtering

1.1. The deposition technique: reactive magnetron sputtering

Basic concepts

The sputtering phenomenon was first observed by Groves in 1852, but it was *Plücker* [1] in 1858 to suggest that it could be used as a tool to produce metallic films. Today, sputtering is used in such varied fields such as the deposition of thin films, in chemical analysis, to etch and clean, for surface protection or activation for further procedures, etc. In the basic sputtering process, a target plate is bombarded by energetic ions, generated by a glow discharge plasma, located in front of the target. The bombardment process causes the removal of atoms of the target, which will condense on a substrate (part to be coated) as a thin film [2]. Secondary electrons are also emitted from the target surface as a result of the ion bombardment. These electrons play an important role in maintaining the plasma.

Sputtering is a physical vapour deposition process (PVD) and is driven by momentum transfer between the ions and atoms in the material (Fig. 1.1). Collisions are elastic or inelastic, depending on whether the internal energy of the colliding specie is preserved. In an elastic collision, only kinetic energy is interchanged and there is conservation of the momentum and kinetic energy of translational motion, and no atomic excitation occurs and potential energy is conserved.

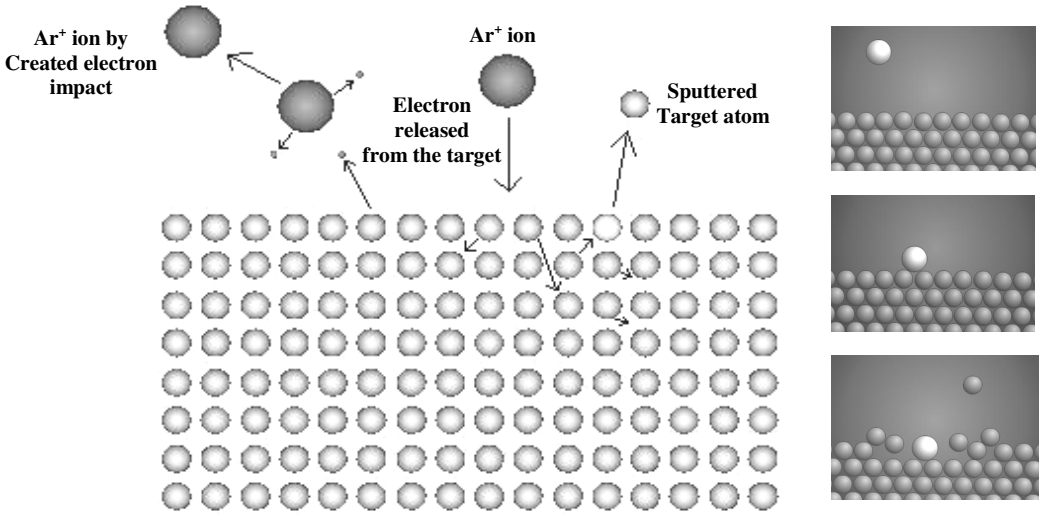


Fig. 1.1. Scheme of the sputtering of the target atoms.

As a result of both momentum and kinetic energy conservation laws, the ratio of the kinetic energies between the two species that collide is:

$$\frac{E_1}{E_2} = \frac{4M_1M_2}{(M_1+M_2)}\cos^2\theta \qquad \text{(Eq. 1.1)}$$

where (M_1, E_1) and (M_2, E_2) refer to the mass and energy of the impinging particles and the sputtered target atoms, respectively. The angle is defined by the initial trajectory of impinging particle and the line joining their centres at contact. Nevertheless, the first collision pushes atoms deeper into the material, the subsequent collisions between the atoms result in some of the atoms near the surface being ejected away from the surface of the target (Fig. 1.1).

The first and most well-known scientific work on the quantification of the sputtering process was carried out by *P. Sigmund* [3]. He proposed that the momentum transfer processes occurring at the surface are caused by a collision cascade, within the surface layers, Fig. 1.1. The amount of ejected atoms from the surface per incident particle is called the *sputter yield,* which is an important measure of the efficiency of the sputtering process. The sputter yield depends not only on the energy and masses of the incident ions, but also on the atoms of the target and their surface binding energy and/or on the possible compounds formed at the target surface [4-7].

The currently accepted theory for the sputtering yield from collision cascades, derived from *Sigmund's* theory [8], predicts that:

$$S = \frac{3\alpha}{4\pi^2}\frac{4M_1M_2}{(M_1+M_2)^2}\frac{E_1}{E_b}, \text{ for } (E_1 < 1 \text{ keV}) \qquad \text{(Eq. 1.2)}$$

and

$$S = 3.56\alpha\frac{Z_1Z_2}{Z_1^{2/3}+Z_2^{2/3}}\left(\frac{M_1}{M_1+M_2}\right)\frac{S_n(E)}{E_b}, \text{ for } (E_1 > 1 \text{ keV}) \qquad \text{(Eq. 1.3)}$$

where M_1 refers to the mass of the Ar ion and M_2 the mass of the target atom, E_b is the surface binding energy, α is a factor that is a measure of the efficiency of the momentum transfer in collisions and $S_n(E)$ is the reduced stopping power. This last term is a measure of the energy loss

per unit length due to atoms collisions, and is a function of the energy as well as masses and atomic numbers of the atoms involved.

Anyway, sputtering of a target atom is just one of the possible effects resulting from the surface ion bombardment. The other possibilities are summarised in the figure 1.2. Aside from sputtering, the second important process is the emission of secondary electrons from the target surface, which play a fundamental role in keeping the sputtering process itself.

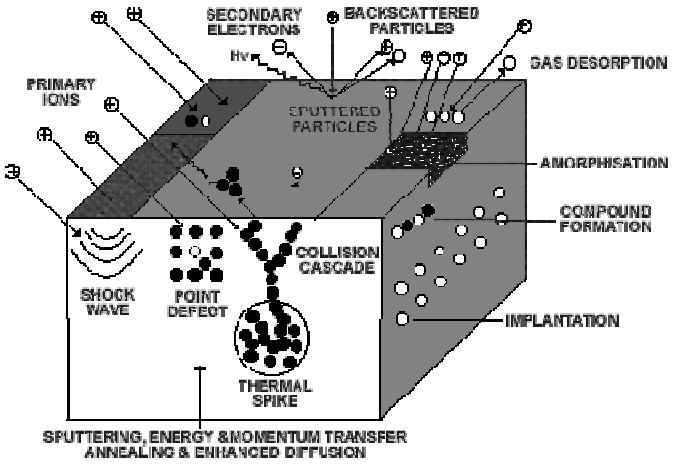


Fig. 1.2. Interactions due to ion bombardment [9].

During sputtering process there are two main processes that occur: plasma generation and ion bombardment. Plasmas are generated by supplying energy to a neutral gas causing the formation of charge carriers [10,11]. Any volume of a neutral gas contains always a few electrons and ions that are formed as the result of the interaction of cosmic rays or radioactive radiation with the gas [12]. These free charge carriers are accelerated by the electric field and new charged particles may be created when these charge carriers collide with atoms and molecules in the gas or with the surfaces of the electrodes. The ejected electron is subjected to the same field and will also be accelerated toward the anode (Fig. 1.3).

This leads to an avalanche of charged particles that is, eventually, balanced by charge carrier losses. Steady-state plasma is developed. Electrons and ions are produced in the gas phase when electrons or photons with sufficient energy collide with the neutral atoms and molecules in the feed gas (electron-impact ionization or photo-ionization) [12].

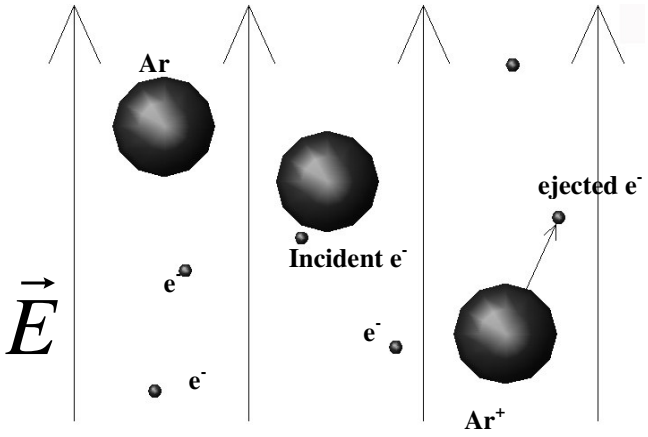


Fig. 1.3. Scheme of the collision of electrons with argon atoms, and the consequential plasma formation.

There are several ways to supply the necessary energy for plasma generation from a neutral gas. In magnetron sputtering the plasma is achieved by applying an electric field to a neutral gas (Fig. 1.4).

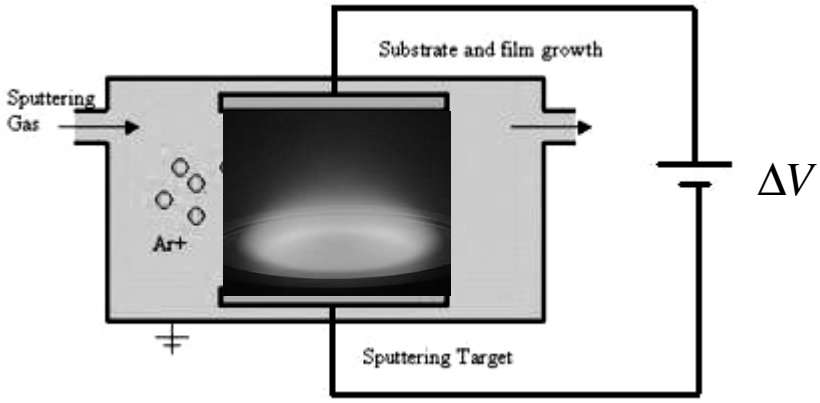


Fig. 1.4. Scheme of the system used to obtain the plasma.

A variety of power supplies are available for plasma generation, ranging from direct current, dc, to alternate current, ac (with frequencies into the mega-hertz range - radiofrequency, rf, are the most common ones). In dc sputtering, a potential difference of several hundred volts is

generated between the substrate holder and the magnetron, creating an intense electric field between them (Fig. 1.4).

The necessary voltage for the formation of plasma is known as the breakdown voltage (V_b).

$$V_b = a\frac{pd}{\log pd + b} \qquad \text{(eq. 1.4)}$$

where p is the gas pressure, d is the separation between the electrodes, and a and b are constants [13].

This voltage can be determined from plotting breakdown voltage versus pressure times electrode spacing (Fig. 1.5.) described by a *Paschen* law [14]:

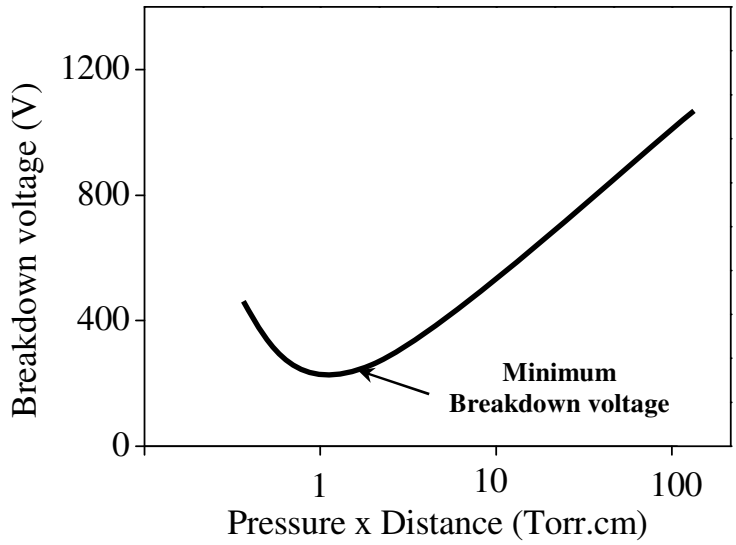


Fig. 1.5. Variation of breakdown voltage as a function of the pressure × electrode spacing.

Sputtering regimes

Several theories were proposed for the sputtering process. *Stark* [14] was the first to propose the momentum transfer theory, which claims that the ejected atoms from the sputtered surface were due to the moment transfer resulting from the collision of the accelerated ions to the target atoms. Actually the momentum transfer processes at the surface are believed to be caused by a collision cascade, proposed by *P. Sigmund* [3]. The same author developed the modern theory of sputtering, where he claims that several mechanisms may occur within the sputtering process, depending on the nature and kinetic energy of the bombarding ions [3].

At low kinetic energies (energies between 0 and bout 50 eV, Fig. 1.6.a), the ion does not have sufficient energy to dislodge the target atoms and thus the ejection of target particles occurs only for very special collision geometries. With moderate energies (between 50 and roughly 1 keV), the ions impact dislodge "knock-on" atoms into the target, which by their turn will dislodge other target atoms. Several studies showed that the ion energies must exceed four times the binding energy of the atoms of the target surface to induce sputtering [15,16]. This induces a collision cascade that eject atoms, ions, electrons and neutrals from the first 10 to 50 Å of the surface of a target [16]. Sputtering process resulting from momentum transfer from ion bombardment of target atoms requires a sequence of collisions, since the moment transferred from the ion impact will drive only the surface target atoms into the target. The collision cascade results on multiple interactions of bombarding gas ions with target atoms, as the ions impart their energy over a distance within the surface of the target. It is in this range of energies that most common PVD systems operate and can be illustrated schematically in figure 1.6.b).

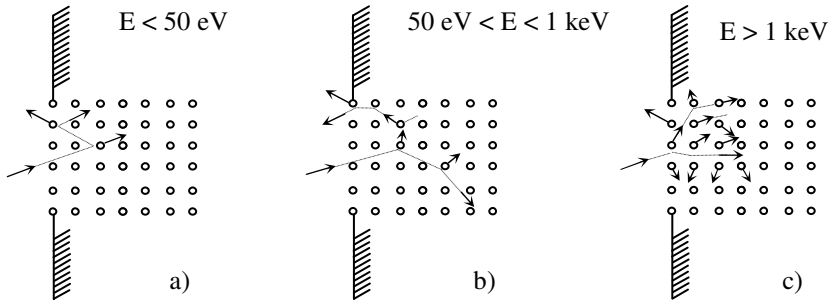


Fig. 1.6. Scheme of the three sputtering regimes [16]: **a)** single-knock-on; **b)** linear cascade; **c)** spike.

At energies above 1 keV (Fig 1.6c), the ions penetrate deeply, are implanted into the bulk and are specially used for material doping and/or implantation.

Magnetron sputtering

The basic sputtering process is known for many years and been successfully used to deposit several kinds of materials [17,18]. However, basic sputtering is limited by low deposition rates, low ionisation efficiencies in the plasma, and causes high substrate heating. These limitations

were overcome by the development of the *magnetrons*. Magnetrons make use of the fact that a magnetic field configured parallel to the target surface can constrain secondary electron motion to the vicinity of the target. Magnetron is, in basic terms, a system composed by magnets with a specific orientation, positioned behind the target. The magnets are positioned in order that one pole is situated at the central axis of the target and the second pole is formed by a ring of magnets around the outer edge of the target.

The introduction of a magnetic field allows the confinement of the plasma, "trapping" electrons, since they are forced to describe helicoidally trajectories near the target surface (Fig. 1.7).

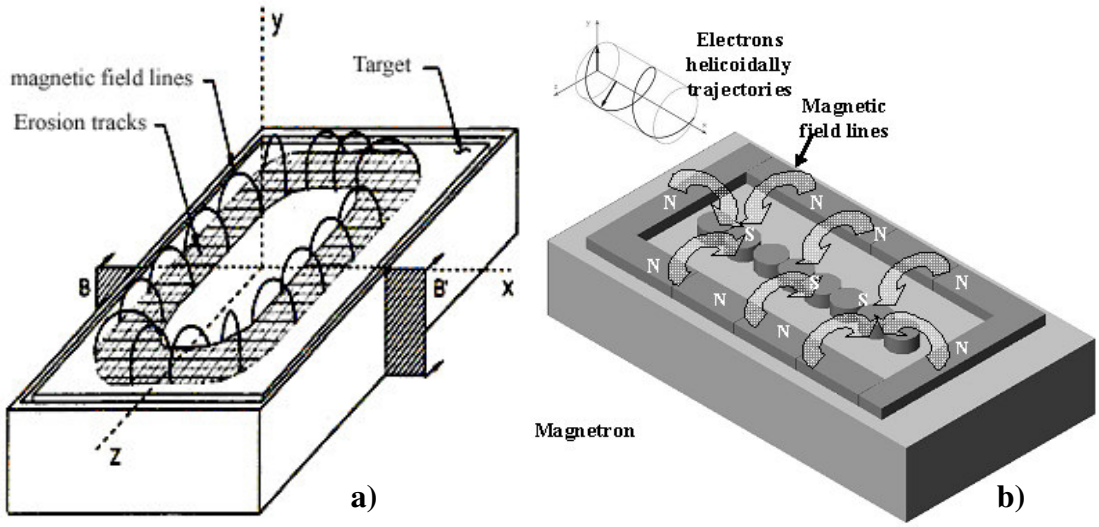


Fig. 1.7. Scheme of a magnetron and the correspondent magnetic field lines: **a)** general scheme and, **b)** the particular case of the magnetrons used to prepare the samples of this thesis.

This particular arrangement of magnets within the magnetrons increases the probability of electron-ion/atom collision occur, and thus increasing ionisation efficiency. This increased efficiency leads to an increased ion bombardment of the target, allowing to work with lowers target voltages and a reduction of the bombardment of the substrate with electrons. In addition, the increased ionisation efficiency allows working with lower working pressures, since the discharge could be maintained at lower operating pressures.

Nevertheless, these advantages (the localized high concentration of gas ions) induce a much localized sputtering phenomena, reducing the sputtered area of the target to lees than 30 % of the target material– the *erosion zone* [19] (Fig. 1.8).

It is important to refer that the characteristics of a target change as it erodes. This can lead to variations in sputtering rate of the metal atoms over the life-time of a target, and thus important variation in film properties during the life-time of the target.

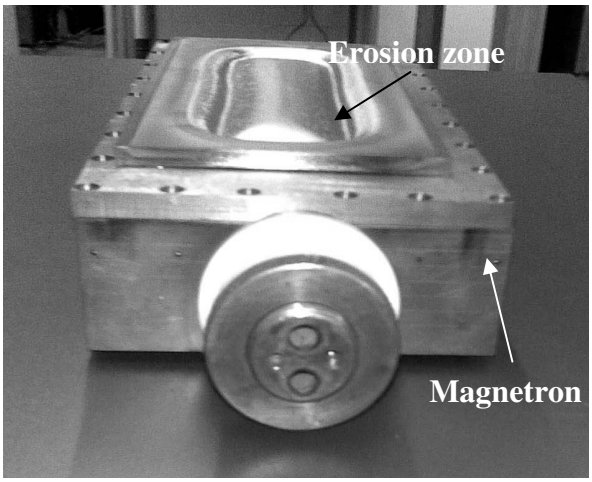


Fig. 1.8. Image of one of the magnetrons used in this work, where the target erosion area is particularly evident.

To overcome this limitation, new magnetrons have been designed in which the degree of *unbalancing* (see Fig. 1.9.b)) can be varied in situ - the *variable field strength magnetrons* [20].

There are two types of planar magnetrons, unbalanced and balanced with slight differences in design. In a balanced magnetron, the plasma is strongly confined to the target region, typically extending to few tens of millimetre (typically between 60 and 100 mm) from the target surface, (Fig. 1.9.a)) [21].

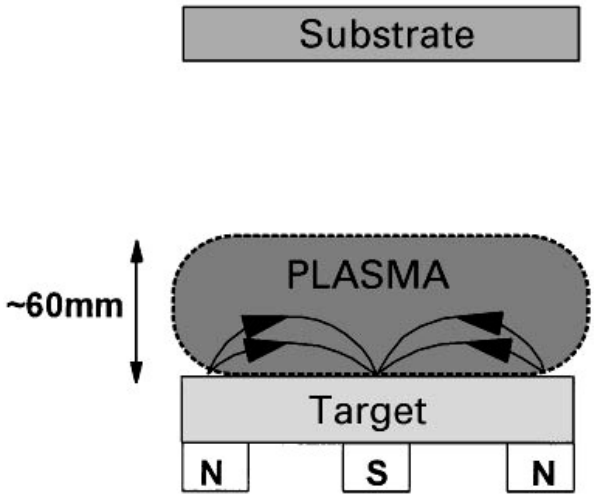


Fig 1.9.a) Schematic representation of the plasma confinement observed in balanced magnetron.

Films grown on substrates located within this region will be subjected to concurrent ion bombardment, which can strongly influence the structure and properties of the growing material [22,23]. Substrates positioned outside this region will be coated in an area with low plasma density, and the ion current drawn at the substrate will be insufficient to modify the structure of the film. In this case, the ion current drawn at the substrate is typically lower than 1 mA/cm^2, however, to deposit dense films without introducing excessive intrinsic stresses, a high flux (>2 mA/cm^2) of relatively low energy ions (typically about few hundreds of eV) is generally preferred [24].

In a different way, these conditions can be provided by an unbalanced-type magnetron (type 2), which was in fact the ones used to deposit the coatings that are studied in this thesis. In this type of magnetrons, not all the magnetic field lines are closed between the central and outer poles in the magnetron, but some are focussed in the direction of the substrate, Fig 1.9.b) [21], resulting that some secondary electrons are able to follow these field lines.

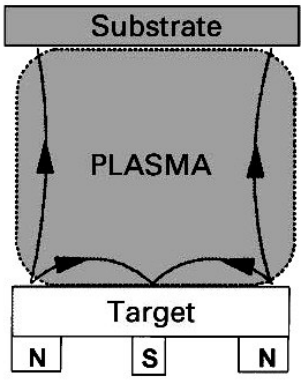


Fig 1.9.b) Schematic representation of the plasma confinement observed in unbalanced magnetron type 2.

This generates plasmas that are no longer strongly confined to the target region, but are also allowed to run out in the direction of the substrate, originating higher ionic currents from the plasma without the requirement of externally biasing the substrate. Thus, in addition to providing a high flux of adatoms, an unbalanced magnetron also acts as a very effective ion source.

Reactive sputtering

The deposition of ceramic materials, including oxides, nitrides and oxynitrides, by sputtering it is done in the presence of the appropriate reactive gas or gases. Reactive magnetron sputtering is a widely used technique to deposit coatings for a wide range of applications, due to

the capability of deposit metals and ceramic coatings with a high variety of composition variation. Nevertheless, and in spite of numerous cases of success, there are also documented some typical instability phenomena of experimental parameters, associated to the reactive process involving one metallic target with reactive gases [25-29].

In basic terms, reactive sputtering results from the sputtering of elemental targets in a reactive atmosphere. It is promoted the reaction between the sputtered atoms, but also between the reactive gas and the target surface. It is a widely used technique to deposit thin films and it is particularly suitable to modulate the chemical composition and so, the final properties of the coatings [30-37]. Oxides, nitrides, carbides, oxinitrides of single or multi-metallic elements can be synthesised by this method [38-45].

A typical feature of the reactive sputtering process is the nonlinear evolution of some experimental parameters versus the reactive gas injected in the deposition chamber. This behaviour is clearly identifiable in the hysteresis loop [46-51].

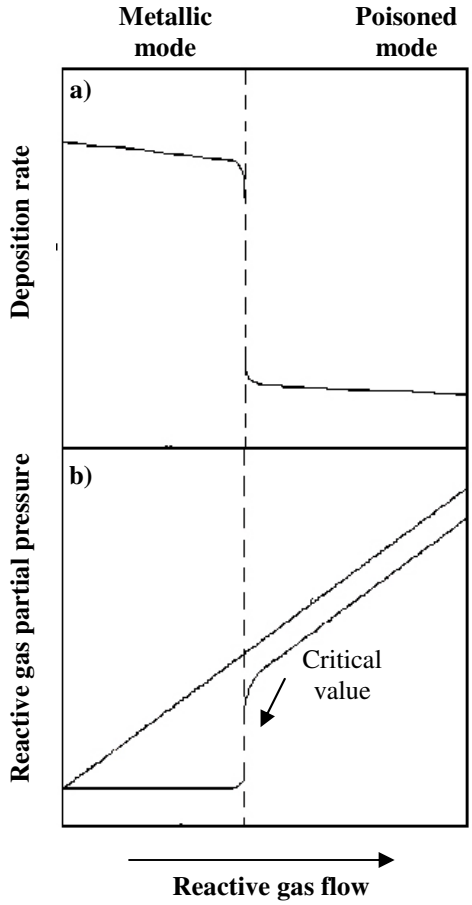


Fig. 1.10. Typical behaviour of the deposition rate, and partial pressure of the reactive gas, versus the reactive gas flow rate, during a reactive magnetron sputtering.

When the reactive gases are introduced into the sputtering chamber they react with the sputtered atoms, to produce the growing film, and with the target surface, as well. Increasing the reactive gas flow rate, the compound formation on the target surface raises until a total coverage of the target occurs – the target poisoning effect. This value of reactive gas flow is defined as the critical flow where transition between metallic and compound mode occur at the target. For reactive gas flows lower than the critical value, the target works in a "metallic mode", while for reactive gas flows higher than that critical value, it works in the "poisoned mode" (Fig. 1.10).

The transition from the "metallic mode" to "poisoned mode", most of the times, exhibits a hysteresis that can be reduced by increasing the pumping speed [52]. This was the selected solution for the deposition system used for this thesis, where the pumping speed was adjusted at a relatively high value - around 356 L s^{-1}.

Usually when the reactive gas flow is higher that the critical limit, the deposition rate decreases due to several phenomena among which the more relevant are:

i) the lower sputter yield of the compound formed in the surface of the target;
ii) in some cases, the increase of secondary electron emission coefficient, *y*, when the target surface is poisoned [53].

The increase of secondary electrons changes the plasma impedance, which is a decreasing function of *y*. Once the current is kept constant (which was the case of the films prepared for this work), when the target voltage decreases, and thus the sputter yield decreases [22]. This was not the case of this work since the compounds formed at the target surface present a lower secondary electron emission coefficient, than the sputtered metal, Zr.

Figure 1.10.b) shows the behaviour of the partial pressure of the reactive gas, as function of the reactive gas flow rate, when the plasma is on and off. When the plasma is off, the partial pressure varies linearly with the reactive gas flow rate injected into the deposition chamber, while when the plasma is on, the partial pressure of the reactive gas remains almost constant until the reactive gas flow reaches the critical value. This constancy of the partial pressure of the reactive gas is due to the trapping of the reactive gas, by compounds formation on the target surface, as well as by the metal deposited on the walls and the substrate (getter effect). When the reactive gas flow is higher than the critical value, the target becomes poisoned and the consumption of reactive gas drops, inducing linear behaviour of the partial pressure of the reactive gas with the reactive gas flow injection.

For a stable reactive magnetron deposition process, it is advantageous to work with the magnetron surface either fully or partially metallic, while keeping an adequately high partial pressure of the reactive gases at the substrate, to form the desired compound film. In order to minimize instabilities, several technical improvements have been developed. Two of these methods are presented below:

a) "overpump"

Several authors [26,54-58] proposed to "overpump" the deposition chamber to eliminate or decrease the hysteresis effect. If the pumping speed is high enough, the consumption of the reactive gas by the pumping system dominates that the consumption of the reactive gas by the growing film. In this case, a gradual transition between the metallic mode and the poisoned modes takes place.

b) gas pulsing

Recent studies referee the use of a non-conventional method to deposit nitride and oxide coatings, where the nitrogen (or oxygen) gas are introduced in the deposition chamber in a pulsed (on and off) way [59-65]. With this pulsing approach, various compounds were sputter deposited with a wide range of characteristics, allowing a higher number of freedom degrees to tune the films composition and thus the characteristics of the layers. The switching off allows the removal/decrease of the compound formed on the target surface before it accumulates and becomes irreversibly poisoned, and so the target works between metallic mode and the poisoned mode.

The reactive gas pulsing process (RGPP)

In a successful attempt to overcome some of major drawbacks of reactive sputtering (namely the target poisoning), *N. Martin* and co-workers [66] developed an innovative method to deposit titanium oxides and oxynitrides: the reactive gas pulsing process (RGPP). This author used a metallic target and both nitrogen and oxygen as reactive gases. Nitrogen mass flow rate was kept constant, whereas the oxygen mass flow rate was periodically modulated, flowing several different kinds of periodic functions (Fig. 1.11).

In a first approach, it was used the rectangular-type pulsing, using a constant pulse period, while the t_{on} and t_{off} times were systematically changed. In posterior studies the same author

studied in detail the same change routine to other functions and came up with a systematic model to explain the effects of this pulsing process [67-69].

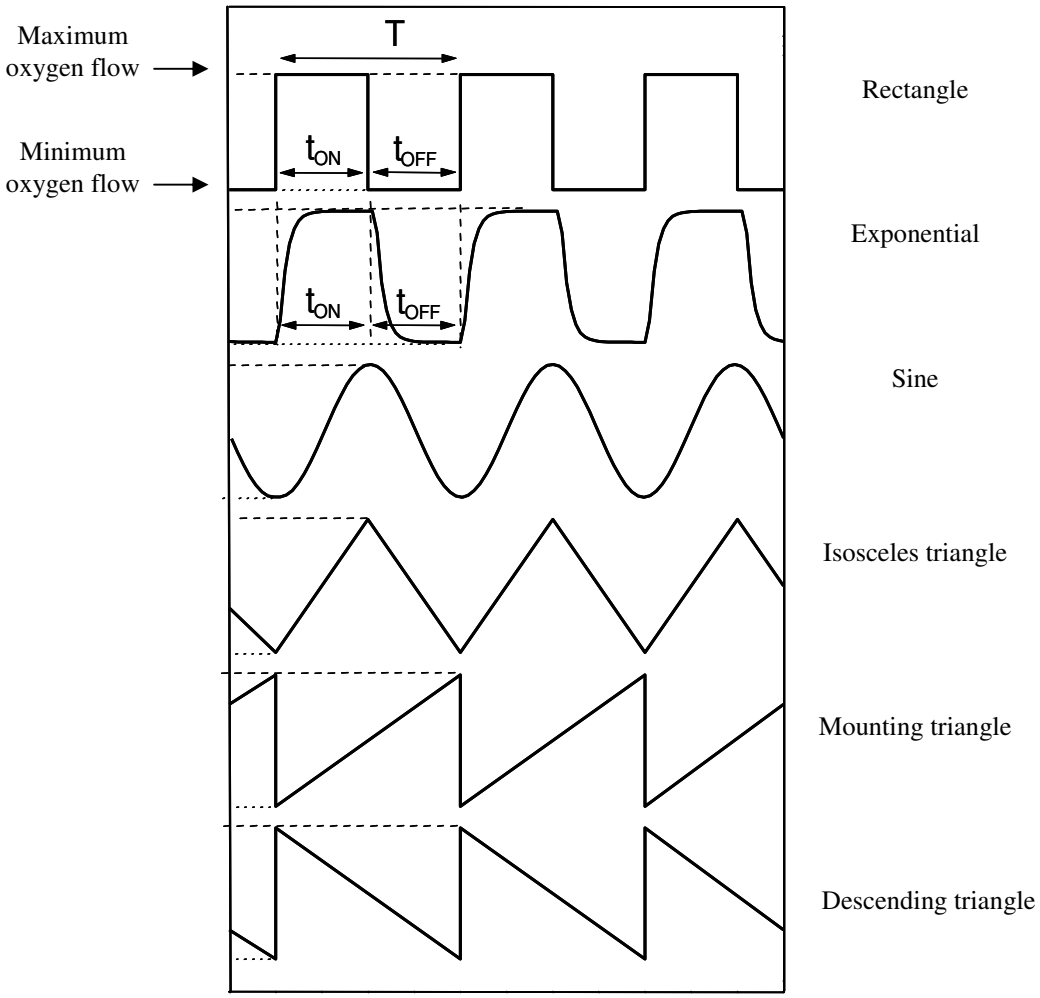


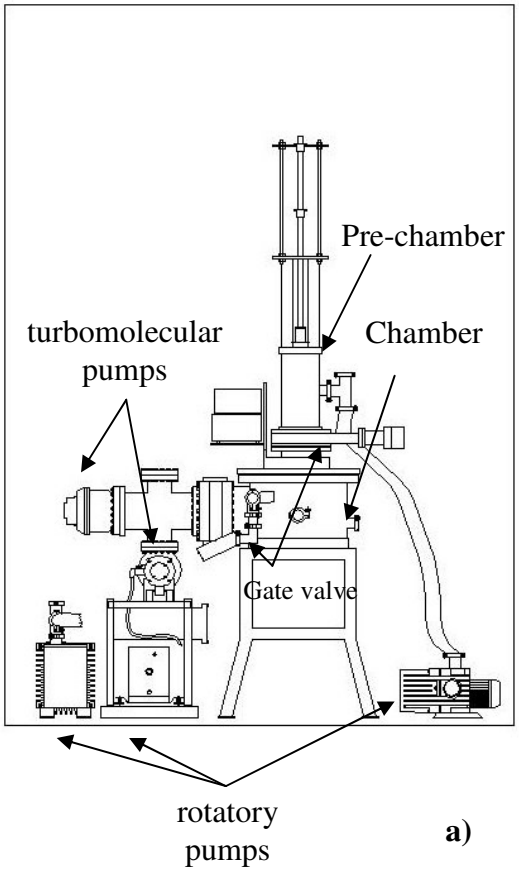
Fig. 1.11. Different types of pulsing patterns of the oxygen mass flow controller, generated by the RGPP system.

In these studies, the author also claims that the use of the reactive gas pulsing process is not solely an attractive way to deposit tuneable and homogeneous titanium oxynitride thin films, but also for other systems. Such a process can also be used to reach multilayered structures (e.g. periodic alternations of oxide/oxynitride, nitride/oxynitride or oxide/nitride) by adjusting the pulsing periods and the correspondent duty cycles. *N. Parreira et al* showed that this system allows depositing multilayer coatings, with very precise layers thicknesses [70].

1.2. Deposition System

For the present work, ZrO_x, ZrN_y and ZrO_xN_y thin films were prepared by dc reactive magnetron sputtering, in a laboratory-sized deposition system [71] (Fig. 1.12).

The system is mainly composed by a deposition chamber, a vacuum system, a gas flow control system, an electrical system, a pre-chamber and a control unit.



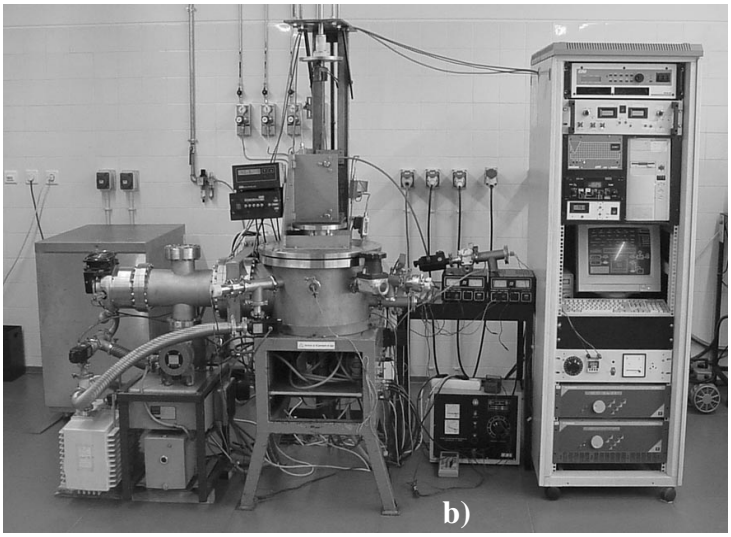


Fig. 1.12.

a) Schematic representation of the home-made deposition system;
b) image of the deposition system.

Deposition chamber

The deposition chamber has a cylindrical shape, with a diameter close to 0.4 m and with a volume of approximately 0.14 m^3. The system can accommodate four magnetrons in a closed or mirrored field configuration. In the case of the samples deposited in framework of this thesis, only one vertically rectangular magnetron (unbalanced of type 2), in a closed field configuration, [72] was used (Fig. 1.13).

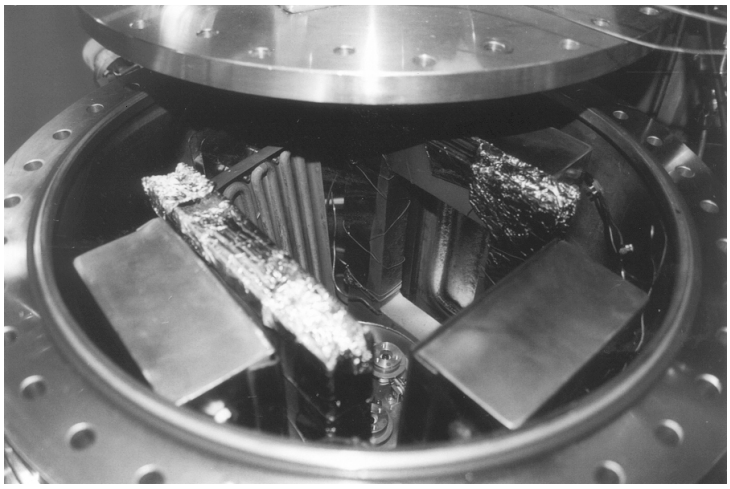


Fig. 1.13. Image of the inside of the deposition chamber.

The target rest in front of the water cooled magnetron with dimensions 200×100×6 mm (Fig. 1.14).

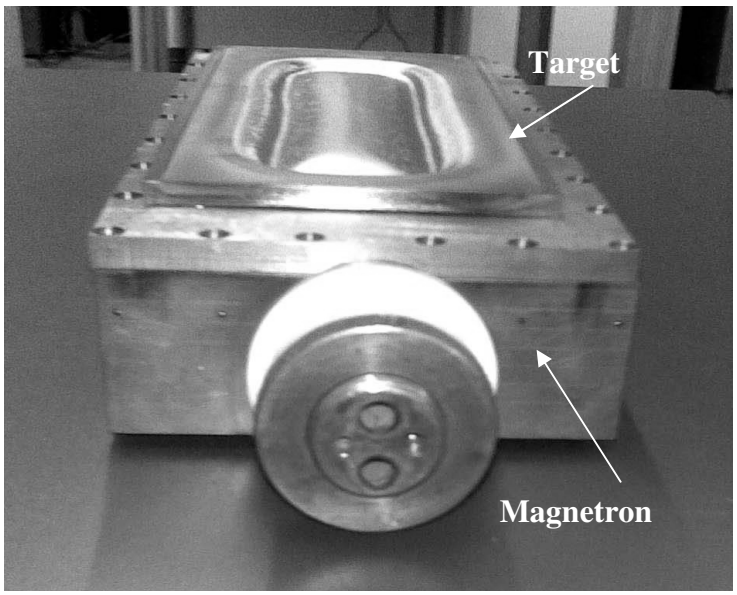


Fig. 1.14. Image of the used magnetron.

In the centre of the deposition chamber lays the substrate holder, capable of operating in rotation or static mode, see Fig. 1.15. The system allows also the biasing of the substrates.

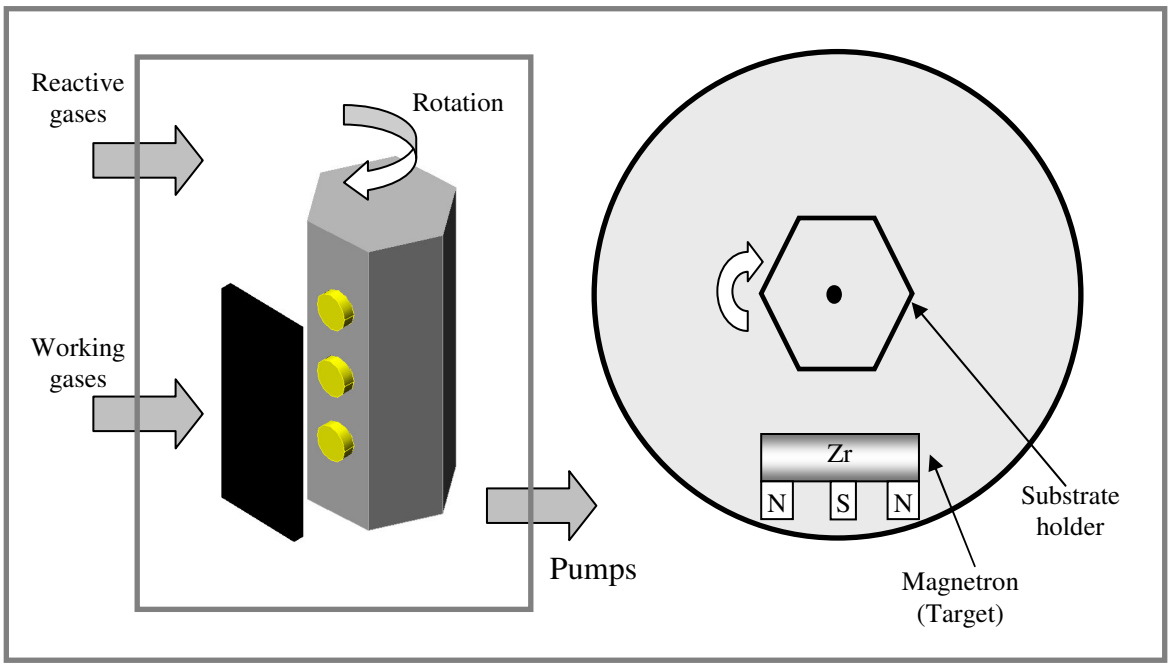


Fig. 1.15. Schematics representation of the disposition of the magnetron and substrate holder in the interior of the chamber.

Vacuum system

The vacuum system is composed by three rotatory pumps and two turbomolecular pumps, see Fig. 1.16.

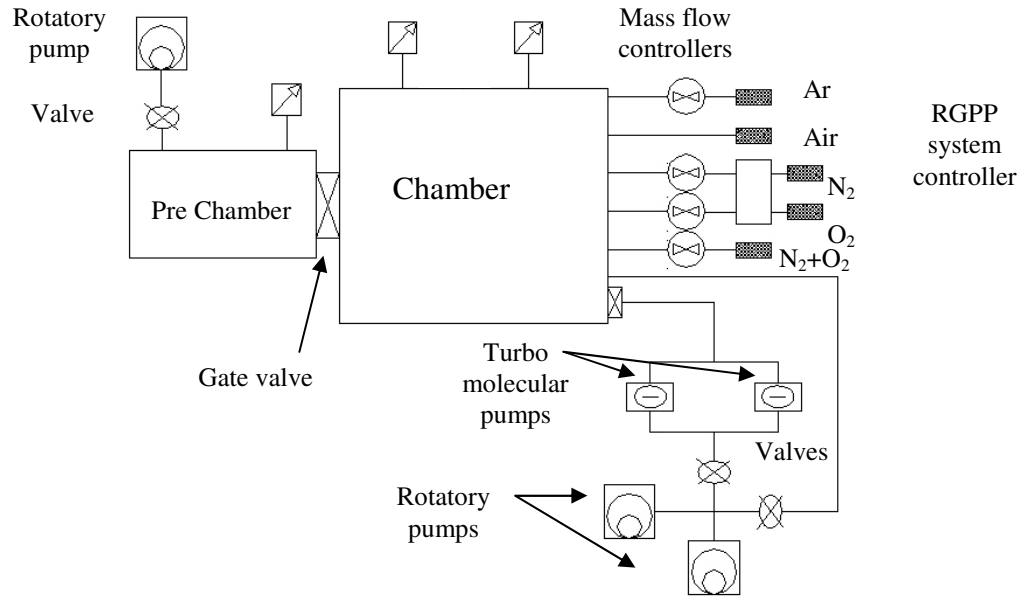


Fig. 1.16. Schematics of the vacuum system.

The primary vacuum (~0.5 Pa) in the deposition chamber is obtained by two parallel rotatory pumps: a Trivac D8B and a Balzers DUO 012A, with nominal pumping speeds of 2.36 L/s and 3.33 L/s, respectively. The base pressure was obtained by the two parallel turbomolecular pumps: a Balzers TPU200 and an Alcatel PTM 5400, with nominal pumping speeds of 190 L/s and 400 L/s, respectively. The overall pumping speed was measure to be approximately 356 L/s. The pressure inside the chamber was controlled by two pressure gauges: a pirany for primary vacuum (model PRL 10) and a penning (model CP25-K) for secondary vacuum, both models from Edwards.

Pre-chamber and electric system

A rotatory pump, Edwards E2M18, was connected to a pre-vacuum chamber, with a pumping speed of 5.7 L/s. This pump allowed reaching to a primary vacuum in the order of 2 Pa, before the substrates (placed at the substrate holder) were transferred, through a gate valve (placed between the main chamber and the pre-chamber) to the main chamber. This allowed reaching the base pressure much faster.

The electrical system is composed by two Hüttinger dc generators, a PFG 2500 DC and a PFG 7500 DC, with a maximum output power of 2.5 and 7.5 kW, respectively. A Pulsed power supply from ENI (model RPG 50) was used for the etching of the substrates (in-situ pre-cleaning). A current rectifier from Delta (Portugal) was used for the biasing of the substrates (maximum current of 2 A). The power supplies, as well as the different opening/closing of the valves and the gas feeds are computer controlled.

1.3. Samples preparation

In terms of the experimental work organization throughout the entire duration of the thesis, several steps were followed, which are described briefly in figure 1.17. In basic terms, the work consisted in the deposition of different series of samples, in which the main purpose was to study in detail the influence of deposition parameters in film's properties: firstly their colour (intrinsic or interference), and secondly their influence on the other scanned properties. Fours different sets of samples were prepared (see tables I through IV). For comparison purposes, a series of zirconium oxide films, ZrO_x and a series of zirconium nitride films, ZrN_y, were also prepared (see tables V and VI, respectively).

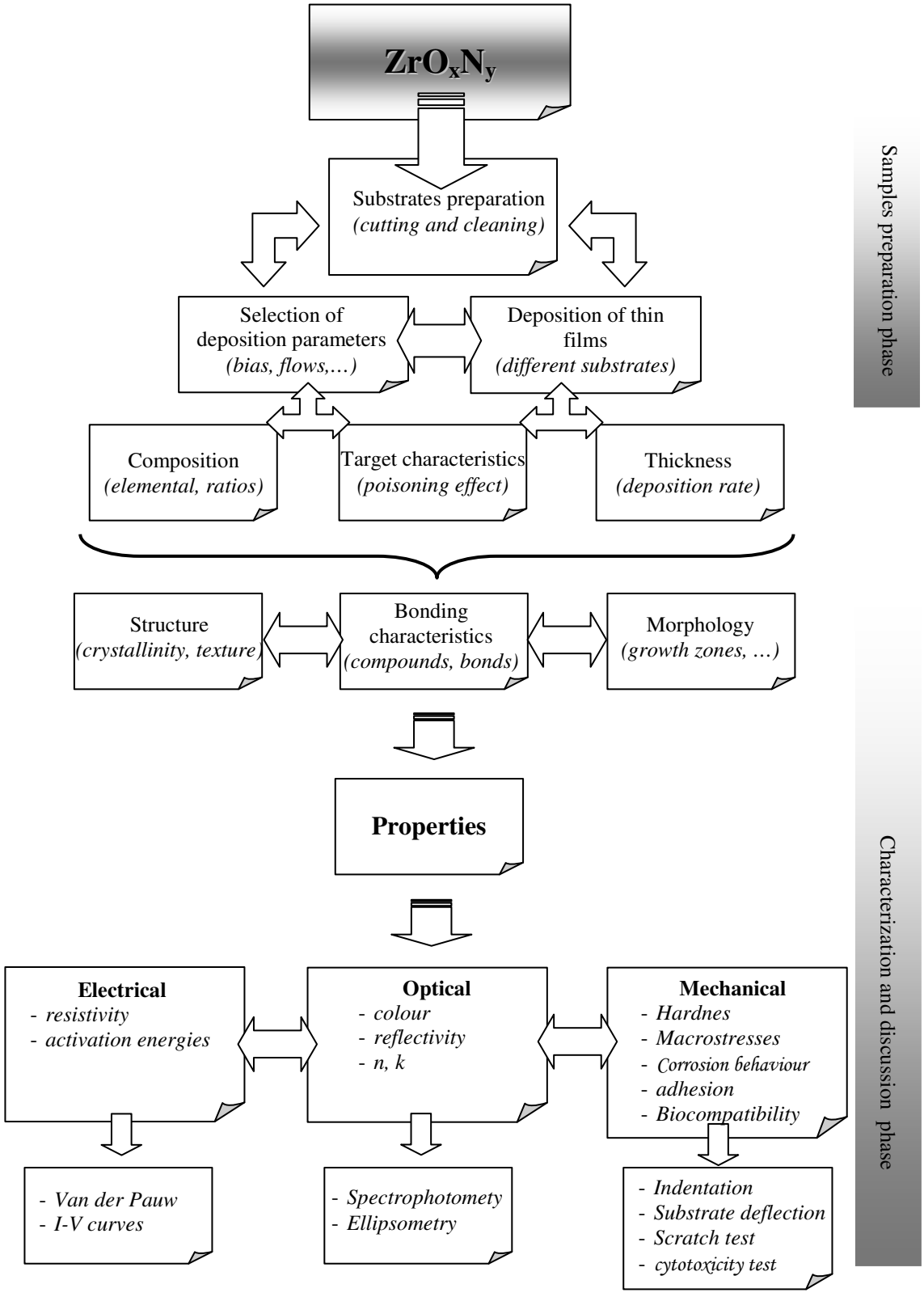


Fig. 1.17. Methodology used in the preparation and characterization of the thin films used in this thesis.
Prepared series

The first series, noted in the text as series 1, is a set of 15 samples that were prepared according to the *"Description of Work (DOW)"* of the European Project in which this thesis is inserted: *NMP3-CT-2003 505948 project "HARDECOAT"*. It is a series that was prepared using basic conditions: grounded substrates and no external heating.

The coated substrates were:

i) glass (used for optical and electrical characterization);

ii) stainless steel (AISI 316 – for residual stresses analysis);

iii) high speed steel (AISI M2 – for mechanical testing);

iv) silicon (100 – for structural, composition and morphological analysis)

To note that different substrates were always used for the same type of analysis in order to check differences that may have existed. In this first series, there were no significant differences when measurements were done in different substrates (namely composition, structure, etc.).

The films were prepared in static mode (substrates to be coated were fixed in front of the target), using a gas atmosphere composed of argon and a reactive gas mixture composed of 85 % N_2 + 15 % O_2 (17:3 ratio). The base pressure was always below 2×10^{-4} Pa. The temperature evolution of the coated substrates was monitored with a thermocouple placed close to the surface of the substrate holder. A delay time of five minutes was used before positioning the surface of the samples in front of the Zr target (99.6 at. % purity). This delay time was used to avoid the target poisoning resulting from previous depositions and also to assure a practically constant deposition temperature of the substrates during film growth.

Table I – Summary of deposition parameters selected for the deposition of films for *series 1*.

Parameter	Value
Target current density	100 $A.m^{-2}$
Argon flow	60 sccm
Gas mixture (N_2+O_2) flow	6 to 40 sccm
Gas mixture (N_2+O_2) partial pressure variation*	0.05 to 0.32 Pa
Total pressure during deposition	between ~0.4 and 0.5 Pa
Effective pumping speed	356 L s^{-1}

** measured from the gas flow*

The second series, noted in the text as series 2, is a set of 13 samples that were prepared using the same basic conditions as the first series (series I) but using a reactive $N_2 + O_2$ gas mixture composed of 95 % N_2 + 5 % O_2 (19:1 ratio).

The coated substrates were:

v) glass (used for optical and electrical characterization);

vi) stainless steel (AISI 316 – for residual stresses analysis);

vii) high speed steel (AISI M2 – for mechanical testing);

viii) silicon (100 – for structural, composition and morphological analysis)

Table II summarizes the deposition conditions used for this second series of samples.

Table II – Summary of deposition parameters selected for the deposition of films for *series 2*.

Parameter	Value
Target current density	100 $A.m^{-2}$
Argon flow	60 sccm
Gas mixture ($N_2 + O_2$) flow	4 to 17.5 sccm
Gas mixture (N_2+O_2) partial pressure variation*	0.03 to 0.15 Pa
Total pressure during deposition	between ~0.4 and 0.5 Pa
Effective pumping speed	356 L s^{-1}

** measured from the gas flow*

The third series, noted in the text as series III, is a set of 7 samples that were prepared using the same basic conditions as the first series (series I), but using a bias voltage of -70V. The depositions were made in rotation mode.

The coated substrates were:

ix) glass (used for optical and electrical characterization)

x) stainless steel (AISI 316 – for residual stresses analysis);

xi) high speed steel (AISI M2 – for mechanical testing);

xii) silicon (100 – for structural and composition analysis)

Table III summarizes the deposition conditions used for this third series of samples.

Table III – Summary of deposition parameters selected for the deposition of films for *series 3*.

Parameter	Value
Target current density	100 $A.m^{-2}$
Argon flow	60 sccm
Gas mixture (N_2 + O_2) flow	7.5 to 13.5 sccm
Gas mixture (N_2+O_2) partial pressure variation*	0.07 to 0.12 Pa
Total pressure during deposition	~0.4 Pa
Effective pumping speed	356 L s^{-1}

** measured from the gas flow*

The fourth series, noted in the text as series 4, is a set of 5 samples that were prepared using the same basic conditions as the first series: grounded substrates, no external heating and static mode, but using the RGPP system, were nitrogen mass flow rate was kept constant whereas the oxygen mass flow rate were periodically modulated as a sine wave function.

Table IV – Summary of deposition parameters selected for the deposition of films for *series 4*.

Parameter	Value
Target current density	100 $A.m^{-2}$
Argon flow	60 sccm
Nitrogen flow	10 sccm
Oxygen minimum flow	0 sccm
Oxygen maximum flow	3 sccm
Period of the pulse (T)	3 s
T_{on}	0.5 to 2.5 s
$\tau_{mounting}$	-10s
$\tau_{descending}$	0.1 s
Oxygen partial pressure *	~0.004 to ~0.025 Pa
Nitrogen partial pressure *	0.078 Pa
Total pressure during deposition	~0.4 Pa
Effective pumping speed	356 L s^{-1}

** measured from the gas flow*

The coated substrates were:

xiii) glass (used for optical and electrical characterization)

xiv) stainless steel (AISI 316 – for residual stresses analysis);

xv) high speed steel (AISI M2 – for mechanical testing);

xvi) silicon (100 – for structural and composition analysis)

1.4. References

[1]- J. Ito *et al.*, United States Patent #6,426,512, issued 2002.

[2]- S. M. Rossnagel in *Sputter Deposition*, Sproul WD, Legg KO, editors. Opportunities for Innovation: Advanced Surface Engineering. Switzerland: Technomic Publishing Co, 1995.

[3]- P. Sigmund, *Topics in Applied Physics*: Sputtering by Particle Bombardment I, ed. R. Behrisch, v. 47, Springer Verlag, Berlin, 1981.

[4]- J. L. Vossen, J. J. Cuomo, in *Thin Film Processes,* eds. J. L. Vossen and W. Kern, Academic Press, New York, 1978.

[5]- W. D. Westwood, in *Microelectronic Materials and Processes,* ed. R. A. Levy, Kluwer Academic, Dordrecht, 1989.

[6]- B. N. Chapman, *Glow Discharge Processes,* Wiley, New York, 1980.

[7]- J. A. Thornton, *Thin Solid Films* 54 (1978) 23.

[8]- P. Sigmund, Phys. *Rev.* 184 (1969) 383.

[9]- http://www.pvd-coatings.co.uk/theory-of-pvd-coatings-magnetron-sputtering.htm (Mai 08).

[10]- S. M. Rossnagel, J. J. Cuomo, W. D. Westwood in *Handbook of Plasma Processing Technology,* Park Ridge: Noyes, 1990.

[11]-A. Rutscher, H. Deutsch in *Wissensspeicher Plasmatechnik,* Leipzig: Fachbuchverlag, 1983.

[12]- H. Conrads, M. Schmidt, Plasma Sources Sci. Technol. 9 (2000) 441.

[13]- N. Kumar, K. Pourrezaei, B. Lee, E. C. Douglas, Thin Solid Films 164 (1988) 417.

[14]- K. Wasa, S. Hayakawa in *Handbook of Sputter Deposition Technology: Principles, Technology and Applications*, Noyes: New Jersey, 1992.

[15]- R. A. Powell, S. M. Rossnagel, Thin Films: PVD for Microelectronics: Sputter Deposition Applied to Semiconductor Manufacturing, Academic Press, San Diego, 1999.

[16]- G. K. Wehner, G. S. Anderson, Vacuum Technology, *Thin Films and Sputtering: an Introduction*, ed. R. V. Stuart, Academic Press, New York, 1983.

[17]- R. Behrisch, Sputtering by particle bombardment. *In: Applied Physics*, vol. 47, Berlin: Springer, 1981.

[18]- P. D. Townsend, J. C. Kelly, N. E. Hartley in Ion Implantation, *Sputtering and their Applications*. London: Academic Press, 1976.

[19]- L. I. Maissel, R. Gland (eds.) in *Handbook of Thin Film Technology*, McGraw – Hill, New York, USA, 1970.

[20]- Gencoa Product Information: V-Tech Magnetrons. Gencoa, 4 Wavertree Boulevard South, Liverpool L7 9PF, UK. Web address: www.Gencoa.com.

[21]- P. J. Kelly, R.D. Arnell, Vacuum 56 (2000) 159- 172.

[22]- S. M. Rossnagel, J. J. Cuomo, Vacuum 38 (2) (1988) 73.

[23]- J. S. Colligon, J. Vac. Sci. Technol. A, 13 (3) (1995) 1649.

[24]- F. Adibi, I. Petrov, J. E. Greene, L. Hultman, J. E. Sundgren, J. Appl. Phys, 73 (12) (1993) 8580-9.

[25]- W. D. Westwood, S. Maniv, P.J. Scanlon, J. Appl. Phys. 54 (1983) 6841.

[26]- S. Berg, H. O. Blom, T. Larsson, C. Nender, J. Vac. Sci. Technol. A 5 (2) (1987) 202.

[27]- J. Heller, Thin Solid Films 17 (1973) 163.

[28]- J. Affinito, R. R. Parsons, J. Vac. Sci. Technol. A 2 (1984) 1275.

[29]- F. Shinoki, A. Itoh, J. Appl. Phys. 46 (1975) 3381.

[30]- S. Hofmann, Thin Solid Films 191 (1990) 335.

[31]- G. Lemperière, J. M. Poitevin, Thin Solid Films 111 (1984) 301.

[32]- S. Berg, T. Larsson, C. Nender, H. O. Blom, J. Appl. Phys. 63 (1988) 887.

[33]- X. Chu, S. A. Barnett, M. S. Wong, W. D. Sproul, J. Vac. Sci. Technol. A 14 (1996) 3124.

[34]- L. J. Meng, M. P. Dos Santos, Thin Solid Films 250 (1994) 26.

[35]- A. Billard, C. Frantz, Surf. Coat. Technol. 59 (1993) 41.

[36]- P. Carvalho, F. Vaz, L. Rebouta, L. Cunha, C. J. Tavares, C. Moura, E. Alves, A. Cavaleiro, Ph. Goudeau, E. Le Bourhis, J. P. Rivière, J. F. Pierson, O. Banakh, J. Appl. Phys. 98 (2005) 023715.

[37]- Jean-Marie Chappé, Nicolas Martin, Guy Terwagne, Jan Lintymer, Joseph Gavoille, Jamal Takadoum, Thin Solid Films 440 (2003) 66.

[38]- J. Musil, S. Kaldec, J. Vyskocil, V. Poulek, Surf. Coat. Technol. 39-40 (1989)301.

[39]- W. D. Sproul, M. E. Graham, M. S. Wong, P. J. Rudnik, Surf. Coat. Technol. 61 (1993) 139.

[40]- H. Holleck, V. Schier, Surf. Coat. Technol. 76-77 (1995) 328.

[41]- S. Agouram, F. Bodart, G. Terwagne, Surf. Coat. Technol. 180-181 (2004) 164.

[42]- V. Teixeira, E. Sousa, M. F. Costa, C. Nunes, L. Rosa, M. J. Carvalho, M. Collares-Pereira, E. Roman, J. Gago, Thin Solid Films 392 (2001) 320.

[43]- H. M. Benia, M. Guemmaz, G. Schmerber, A. Mosser, J. C. Parlebas, Catalysis Today 89 (2004) 307.

[44]- A. P. Piedade , M. J. Gomes , J. F. Pierson , A. Cavaleiro, Surf. Coat. Technol. 200 (2006) 6303.

[45]- N. M. G. Parreira, N. J. M. Carvalho, F. Vaz , A. Cavaleiro, Surf. Coat. Technol. 200 (2006) 6511.

[46]- H. Schiller, U. Heisig, G. Beister, K. Steinfelder, J. Strumpfel, C. Korndorfer, W. Sieber, Thin Solid Films 118 (1984) 255.

[47]- A. Kinbara, E. Kusano, S. Baba, J. Vac. Sci. Technol. A 10 (1992) 1483.

[48]- D. K. Hohnke, D. J. Schmatz, M. D. Hurley, Thin Solid Films 118 (1984) 301.

[49]- A. H. Eltoukhy, B. R. Natarajan, J. E. Greene, T. L. Barr, Thin Solid Films 69 (1980) 229.

[50]- T. Abe, T. Yamashina, Thin Solid Films 30 (1975) 19.

[51]- C. Rousselot, Nicolas Martin, Surf. Coat. Technol. 142-144 (2001) 206.

[52]- T. Nyberg, S. Berg, U. Helmersson, K. Kartig, Appl. Phys. Lett. 86 (2005) 16410.

[53]- Brian Chapman in *Glow discharges processes*, Wiley, New York, 1980.

[54]- J. Musil, V. Valvoda, S. Kadlec, J. Vyskocil, IPAT 87, Proceeds of the 6th International Conference on Ion and Plasma Assisted Techniques, Brighton UK, 1987, pp. 184.

[55]- T. Larsson, H.O. Blom, C. Nender, S. Berg, J. Vac. Sci. Technol. A 6 (3) (1988) 1832.

[56]- A. Okamoto, T. Serikawa, Thin Solid Films 137 (1986)143.

[57]- C. D. Tsiogas, J. N. Avaritsiotis, J. Appl. Phys. 71 (10) (1992) 5173.

[58]- A. G. Spencer, R. P. Howson, R. W. Lewin, Thin Solid Films 158 (1988) 141.

[59]- A. J. Aronson, D. Chen, W. H. Class, Thin Solid Films 72 (1980) 535.

[60]- U. S. Patents 4,428,811 and 4,428,812.

[61]- R. P. Howson, N. Danson, I. Safi, Thin Solid Films 351 (1999) 32.

[62]- N. Martin, J. Lintymer, J. Gavoille, J. Takadoum, J. Mater. Sci. 37 (2002) 4327.

[63]- W. D. Sproul, Surf. Coat. Technol. 33 (1987) 73.

[64]- N. Martin, A. R. Bally, P. Hones, R. Sanjinès, F. Lévy, Thin Solid Films 377-378 (2000) 550.

[65]- N. Martin , R. Sanjinés, J. Takadoum, F. Lévy, Surf. Coat. Technol. 142-144 (2001) 615.

[66]- N. Martin, J. Lintymer, J. Gavoille, J.M. Chappé, F. Sthal, J. Takadoum, F. Vaz, L. Rebouta, Surf. Coat. Technol. 201 (2007) 7733.

[67]- N. Martin, J. Lintymer, J. Gavoille, J. M. Chappé, F. Sthal, J. Takadoum, F. Vaz, L. Rebouta, Surf. Coat. Technol. 201 (2007) 7720.

[68]- N. Martin, J. Lintymer, J. Gavoille, J.M. Chappé, F. Sthal, J. Takadoum, F. Vaz, L. Rebouta, Surf. Coat. Technol. 201 (2007) 7727.

[69]- N. M. G. Parreira, T. Polcar, A. Cavaleiro, Surf. Coat. Technol. 201 (2007) 5481.

[70]- E. Ribeiro, A. Malczyk, S. Carvalho, L. Rebouta, J. V. Fernandes, E. Alves, A. S. Miranda, Surf. Coat. Technol. 151-152 (2002) 515.

[71]- B. Window, N. Savvides, J. Vac. Sci. Technol. A 4 (1986) 196.

Chapter 2

Prepared samples

2.1. Introduction

Reactive sputtering is well-known to be a suitable technique to deposit several types of thin films, including the cases of metallic oxide and nitride thin films, and specially those of zirconium that are related to this work. Regarding its application, it is known that different films, using almost all periodic table elements, for the most varied purposes are being produced by Physical Vapour Deposition techniques, where reactive sputtering is one of the most used methods. Reactive sputtering has some important characteristics, among which, its high versatility should be one of most important ones, connected to an easy control of the deposition parameters and thus particularly suitable to modulate the final properties of the coatings [1-6]. Moreover, it is also recognized that reactive sputtering allows an appreciable quality of the produced films.

Although these positive particularities, the transposition of the laboratorial work for the industrial level, constitutes, for the majority of the cases, a fundamental problem, whose resolution is very much dependent on the existent knowledge (in the laboratory scale) and on the recognize of potential problems, mainly those related with targets and reactive atmospheres. For this, it is indispensable a careful characterization and control of the deposition process in the laboratory scale. One of the first controls that must be carried out in any deposition process is that of the initial parameters, such as pressure, species and respective flows, temperature of the substrate and power applied to target powers.

Within the different controls that are done in modern laboratories (and production lines), there are always special features that need to be taken into account if high quality films are expected to be prepared – the so-called *process instabilities*. If these process instabilities are always seen as undesirable and responsible for deviations in film's responses (electrical, optical, mechanical, among others), the case of decorative films is particularly serious since it will make consequence in the colour.

Among others, typical instability phenomena of experimental parameters are frequently met with the reactive process involving one metallic target with one (or more) reactive gas(es) [7-11]. Some improvements of the conventional reactive sputtering have been developed to avoid the main drawbacks of instability phenomena and to better control the process. A typical feature of the reactive sputtering process is the well-known hysteresis loop of some experimental parameters against the reactive gas supply in the system (Fig. 2.1.).

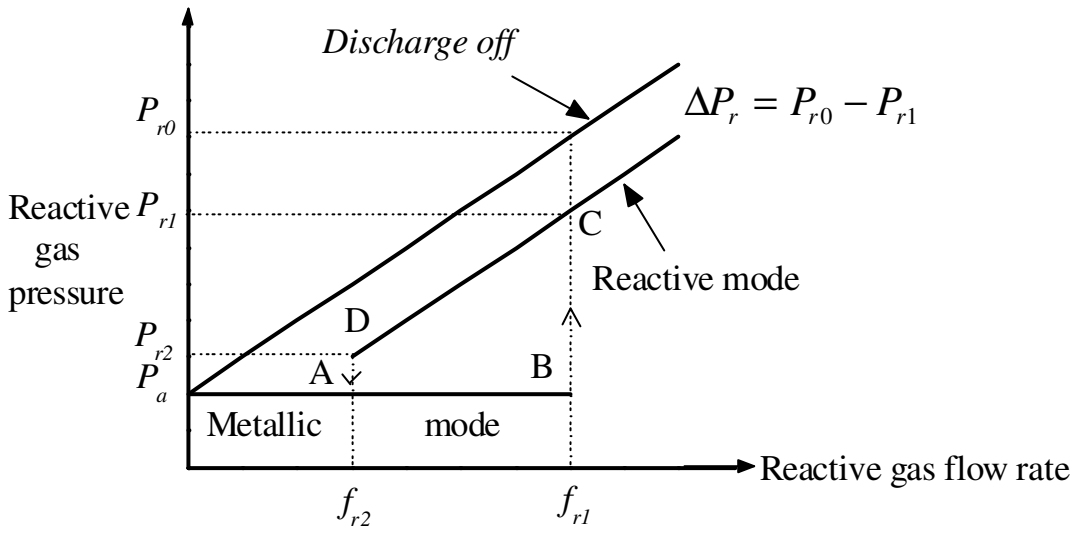


Fig. 2.1. The hysteresis behaviour of reactive magnetron sputtering [12].

Figure. 2.1. shows the hysteresis curve of the reactive gas partial pressure, P_r, as a function of the reactive gas flow rate, f_r, at a constant sputtering power, with constant partial pressure of non-reactive gas. At low values of reactive gas flows, almost all the available reactive gas is consumed by the growing film, and hence, no major changes in P_r are observed from the background level and the deposited film is metal-rich with high deposition rates. This remains until the flow rate of the reactive gas injected into the chamber becomes higher than the gettering rate of the sputtered metal (f_{r1} in Fig. 2.1) inducing a sharp rise in the reactive gas partial pressure to a new value, P_{r1} occurs at point C. Reducing fr following an increasing P_r to a high level, P_r not will not decrease with the same trajectory as it increased. A difference between reactive gas partial pressure (ΔPr) will remain until some value f_{r2} (point D) where the reactive gas pressure decreases to the background level.

This nonlinear evolution of the process has extensively been studied for many years [13-17]. Because of instability phenomena, some compositions are quite difficult to obtain without using particular devices to control the gas admittance in the reactor. A general focus of instability comes from the target surface contamination by species that are being formed or presence in the gas atmosphere. These target contaminations cause important modifications to the electron emission [18], and thus giving rise to target potential variations.

Taking into account that the materials that were prepared within the framework of this thesis were gowned combining two reactive gases, oxygen and nitrogen, these instability problems were always followed carefully and measurements during the deposition were carried out in order to characterize their influence. Moreover, and in order to establish correlations between depositions conditions and film properties such as the physical and chemical ones, this chapter starts with a brief discussion about the film's deposition rate, correlated with the target electrical features – the target potential variation during film deposition and its equilibrium value for the different prepared films.

2.2. Characterization techniques

Two main techniques were used in this chapter.

Calo Test

The Calo tester is a simple, quick, sheep but destructive equipment used to measure the thickness of thin films. The principle on how the Calo tester works are very simple. A rotating steel sphere of known diameter is pressed onto the surface of thin film, as show figure 2.2. A diamond solution is applied between the thin film and the steel sphere to increase abrasion and decrease friction. Depending on the sample/substrate system used, is selected the best rotation speed and time of abrasion parameters.

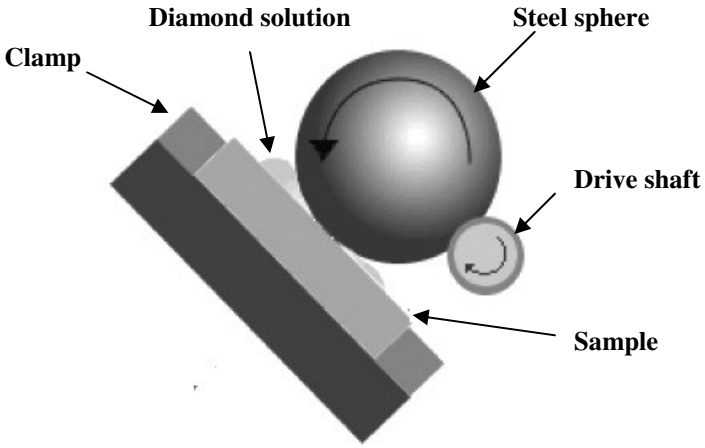


Fig. 2.2. Scheme of the calo test equipment.

The result from the abrasion is the formation of two concentric circles as show figure 2.3.

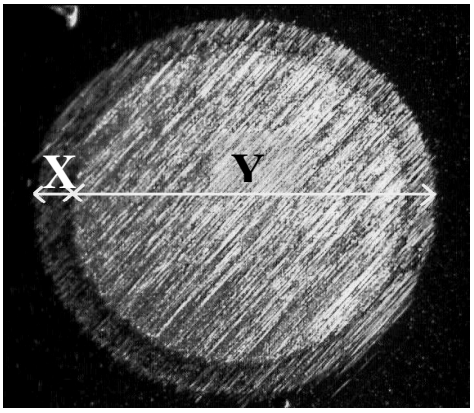


Fig. 2.3. Photo of a coating subjected to the Calo tester, the interior circle represents the substrate and the exterior circle the coating.

After measuring the distances *X* and *Y* (see Fig. 2.3.) using a optical microscope and considering that the diameter of the sphere is approximately tree orders of magnitude regarding the thickness of the coating, the last one is determinate by a simple equation:

$$t = \frac{X * Y}{D} \qquad \text{(Eq. 2.1)}$$

This technique allows determine the thickness of the coatings with an error inferior at 1% [19]. In the case of this work four craters were made and the error as determinate by maximum deviation to the average value.

Rutherford Backscattering (RBS)

Rutherford Backscattering (RBS) is a very common thin-film characterization technique [21] that relies on the change in trajectory and energy of very high energy (MeV) beams of low-mass ions when them interact with the atoms of a material. These ions can penetrate thousands of angstroms or even microns deep into films or film/substrate combinations with negligible sputtering of surface atoms, but loosing their energy through inelastic collisions with the electrons of the analysed sample, resulting in an electronic excitation and ionization of target atoms. These electronic collisions are so numerous that the energy loss can be considered to be continuous with depth. Some of the fast-moving light ions (usually He^+ or H^+) penetrate the atomic-electron-cloud shield and suffer close interaction with the nuclei of the much heavier

target atoms. The low-mass ions are scattered due to the Coulomb repulsion between ion and nucleus similar to the classical two-body elastic scattering.

Kinematic factor

Considering an ion of mass (atomic weight) *M* and energy $E_{0,}$ incident on a surface as shown in figure 2.4.

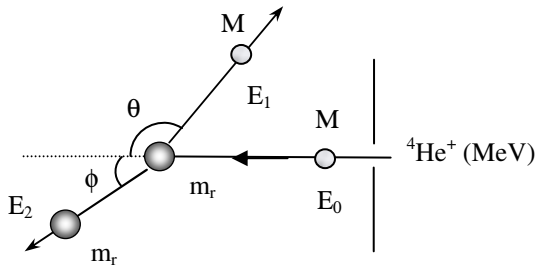


Fig. 2.4. Schematic representation of the classical two-body elastic scattering.

An elastic collision between this ion and a surface atom of mass m_r occurs, such that afterward the ion energy is E_1. The collision is insensitive to the electronic configuration or chemical bonding of target atoms, only depending on the masses and energies involved. Due to the energy and momentum conservation the relation of the initial ion energy and the energy after the impact with the sample atom, considering that $M < m_{r,}$ is given by the expression:

$$\frac{E_1}{E_0}=\left[\frac{M\cdot\cos\theta+\left(m_r{}^2-M^2\cdot\sin^2\theta\right)^{1/2}}{M+m_r}\right]^2 \quad \text{,where } \theta \text{ is the scattering angle} \qquad \text{(eq. 2.2)}$$

For a particular combination of M, $m_{r,}$ and θ the equation 2.2 allows to correlate the energy of the incident ion before and after to interaction with the target atom.

$$E_1 = K_i \cdot E_0 \qquad \text{(eq. 2.3)}$$

K_i is known as the kinematic factor and can be calculated from equation 2.3. Once the incident ion mass, energy and angular position of the ion detector are selected, K_i just depends on the atomic weight of the target atom. The majority of the incident ions penetrate below the film surface and are continuously losing energy at a linear rate with distance traversed, but the scattered ion energy is still given by equation 2.3 only the E_0 is now the ion incident energy at

that point in the matrix. The backscattered ions that collide with the detector generate an impulse that is proportional to the energy of the detected particles allowing the determination of their energy. Measuring the E_1 allows the determination of the mass of the target atmos. In the course of passage through the target material, the ion beam can be thought of as splitting into two separate chemical elements, each spanning a different range of energies. For each broad elemental peak detected, the highest and lowest energies correspond to atoms on the front and back film surfaces, respectively. Therefore, by measuring the number and energy of backscattered ions, information about the nature of the elements present, their concentration, and their depth distribution can all be simultaneously acquired.

In principle all elements and their isotopes including Li and those higher mass are detectable with He^+ ions. The critical test is how well neighbouring elements are resolved and this ultimately depends on the detector resolution. With 2 MeV He^+ions, isotopes with $\Delta M = 1$ can generally be separated for relative mass below approximately 40. At values of relative mass close to 200 only atoms for which $\Delta M > 20$ can be distinguish. This apparent benefit in separating low atomic mass elements is offset by their low cross sections for scattering. The cross sections is a measure of how efficiently target atoms scatter incoming ions and depend on the mass of the target atoms, on the mass of the incoming ions, on their energy and angle of scattering. Clearly, high atomic mass elements produce a stronger backscattered signal than low atomic mass elements. RBS analysis should ideally contain elements of widely different atomic weight stacked with the heavy atoms near the surface and the lighter atoms below them, otherwise there is the danger that elemental peaks will overlap. What that concerns to the samples analysed in this thesis, the close relative atomic mass between oxygen and nitrogen difficult a high accuracy in the separation of the oxygen and nitrogen signals. This increase the uncertainty in the determination at. % values of both elements.

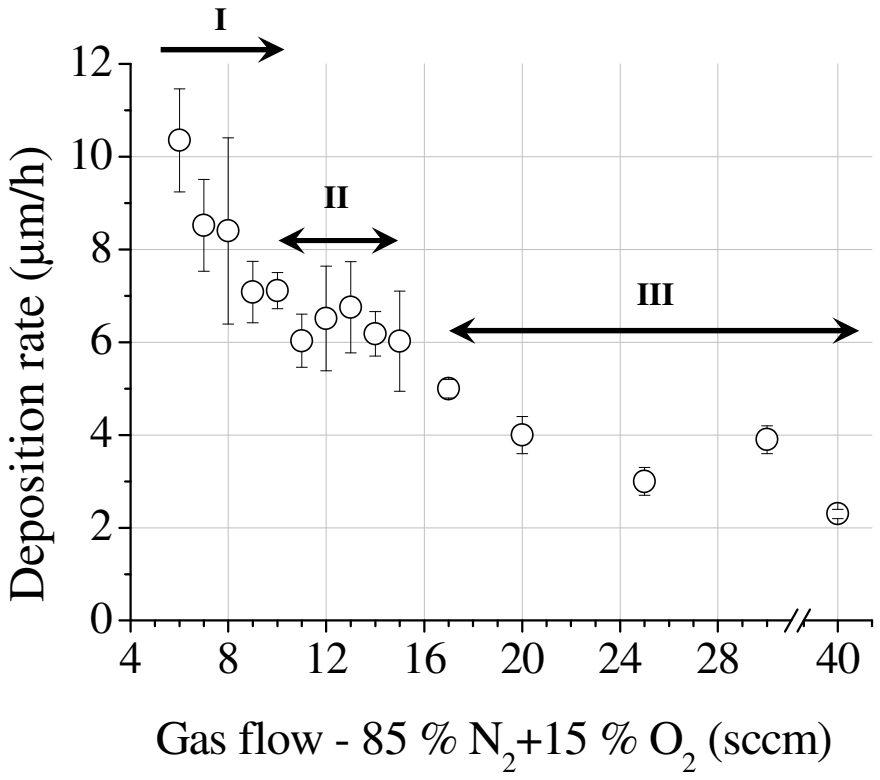
Regarding the coatings study in this thesis the atomic composition of the as-deposited samples was measured by Rutherford Backscattering Spectroscopy (RBS) using (1.4, 1.75) MeV and 2 MeV for the proton and ^4He beams, respectively. The scattering angles were 140º (standard detector, IBM geometry) and 180º (annular detector), tilt angles 0º and 30º. Composition profiles for the as-deposited samples were generated using software code IBA NDF v8.1i [57]. For the ^{14}N, ^{16}O and ^{28}Si data, the cross-sections are given in [20] were used. The analyzed area was about 0.5x0.5 mm^2.

Results and discussion

2.3. Deposition rate

The first characterization that was done to separate the prepared films within distinct groups was the evaluation of the deposition rate. Being a direct reflex of the material that constitutes the growing in the determination film, and thus related with the atmosphere present within the reactor, the characterization of the deposition rate enables to follow the first differences in the prepared films and, above all, to establish some rules of thumb regarding the types of films that have been grown: metallic-like, oxide-like, etc.

The variation of the deposition rate of a group of samples prepared with what we consider basic conditions (grown at grounded state and with no external heating - series 1, see details in chapter 1) is presented in figure 2.5, as a function of the gas mixture flow.



Gas flow (sccm)	Thickness (µm)
6	3.5 +/- 0.4
7	2.3 +/- 0.3
8	2.8 +/- 0.7
9	2.3 +/- 0.2
10	3.7 +/- 0.2
11	3.5 +/- 0.3
12	4.3 +/- 0.7
13	3.4 +/- 0.5
14	4.2 +/- 0.3
15	3.0 +/- 0.5
17	3.3 +/- 0.1
20	2.7 +/- 0.3
25	2.0 +/- 0.2
30	2.6 +/- 0.2
40	1.5 +/- 0.1

Fig 2.5. Deposition rate of the of Zr-O-N samples (series 1) as a function of reactive gas flow. The error bar was determinate by maximum deviation to the average value. For the sack of scientific accuracy and for further comparison purposes, the thickness values of the coatings are presented on the right-hand side of the figure.

The figure shows that the evolution of deposition rate with the reactive gas flow, can be divided into 3 different regimes. In the first regime, corresponding to the samples deposited with reactive gas flows below 10 sccm, there is a continuous decrease of the deposition rate with the increase of the reactive gas flow, from roughly 10 μm/h to about 7 μm/h. In the second regime (gas flows between 10 and 15 sccm) there is a stabilization of the values of this parameter, where the obtained values are roughly around 6.5 μm/h. In the last region, (gas flows above 15 sccm) there is another decrease of the deposition rate with the increase of the reactive gas flow, varying from ~6 μm/h to ~2 μm/h.

Regarding the available literature about this deposition rate variation issue, and based on Safi's hysteresis behaviour of reactive magnetron sputtering [12], *Spencer et al.* [22] proposed a conceptual model of the reactive sputtering process, in which the deposition rate variations were the motive of extensive analysis. This model describes the effects of raising the reactive gas partial pressure at the target and the substrate.

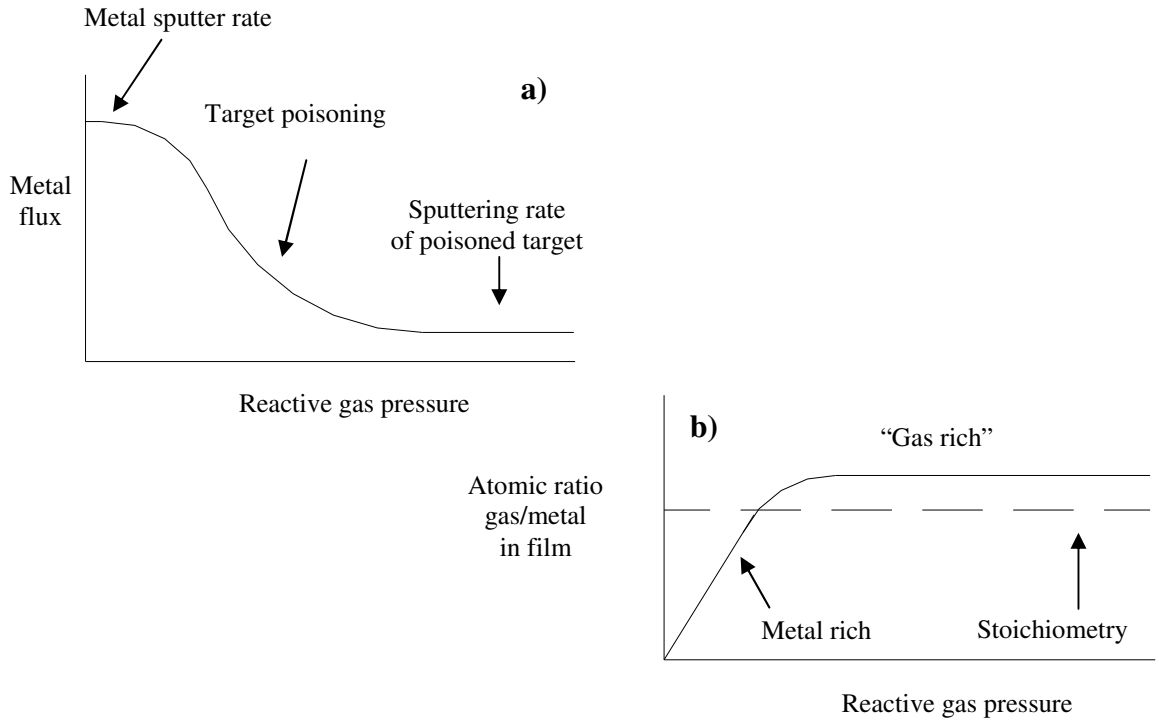


Fig 2.6. The origins of the reactive gas consumption reproduced from Spencer et al. [22]; **a)** Evolution of the metal flux as a function of reactive pressure; **b)** Evolution of the atomic ratio gas/metal as a function of reactive gas pressure.

At the target, the low reactive gas flow allows the cleaning sputtering rate overcomes the poisoning rate, and hence a metal flux arrives to the substrate, inducing higher deposition rates (Fig.2.6.a)). A partially poisoned surface of the target results when the poisoning rate is higher than the cleaning rate. Since the sputtering yield of metal atoms from a poisoned surface is less than that from a pure metallic target, the metal flux from the target decreases with increasing reactive gas partial pressure, decreasing the deposition rate until the entire target is poisoned (Fig. 2.6.a)). At the substrate, for low gas partial pressures, the formation rate of the film is limited by the impact rate and utilization of the reactive gas atoms and hence the films are metal-rich, or sub-stoichiometric (Fig.2.6.b)).

The increase of the partial pressure of the reactive gas induces an increase of the impact rate of the reactive gas atoms and hence, the reactive gas content of the film increases with the reactive gas partial pressure until a "gas-rich", or over-stoichiometric, film is deposited (Fig.2.6.b)).

Taking this into account, at the low values of the reactive gas flow, almost all the available reactive gas is gettered at the condensation sites and as a result, the deposition rate is relatively high, and the deposited films presented surface appearances typical of metal-rich type films (from grey to light yellow colours). The progressive decrease of deposition rate within the two last regimes is thus a consequence of the well-known poisoning effect of the target by both reactive gases of the mixture. Both zirconium nitride and oxide layers are formed at the surface of the Zr target. Since the sputtering yield of both compounds is lower than that of Zr, a decrease in the deposition rate is expected.

Anyway, and beyond these well-known variation types within both metallic and oxide-type regions, figure 2.5 shows that another type of behaviour seems to be developed for that group of samples prepared within the upper mentioned regime II. Although one might consider these samples (prepared with gas flows ranging from 10 to 15 sccm) as within a transition zone, where the target poisoning starts to prevail, the fact is that it is somewhat ambiguous, even if compared to the theoretical model from figure 2.6.a). The relatively high constancy of the deposition rate values within this zone induces that target poisoning is not the only factor to take into account, and thus other deposition parameters should be checked to correlate with this particular behaviour.

2.4. Target Potential

The characterization of target voltage is always seen as a simple, but also powerful technique, giving important indications on the process characteristics. In fact, and in terms of industrial production, this characterization is often used as the main measure for quality control.

In a general way, the behaviour of the target voltage during reactive magnetron sputtering can be mostly attributed to the formation of a compound layer on the target surface, which has a different ion-induced secondary electron emission (ISEE) coefficient than the target material. Since in this work a mixture of oxygen and nitrogen was used as a reactive gas, it is possible that the formation of oxide and nitride compounds takes place at the target surface, and thus ruling both potential and deposition rate behaviours.

In the case of the materials reported in this thesis, the detail analysis of the deposition rate variation has already shown some specific behaviour, whose accurate characterization will be a key tool to further understand the materials' behaviour. For this work, and taking into account the already mentioned different regimes, a detailed analysis of target electrical responses was carried out. figure 2.7.a) shows the measured variation of target potential during entire coating deposition of representative samples from series 1.

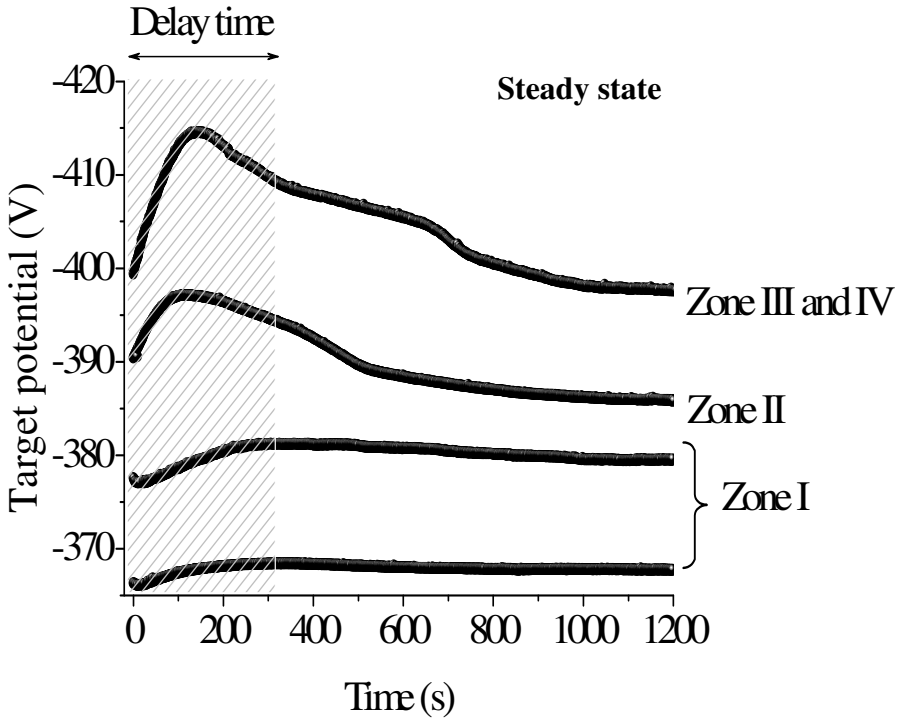


Fig. 2.7.a) Target potential variation during the deposition time.

The equilibrium (steady-stage) of the target potential are almost immediately achieved for the samples prepared with low gas mixture flows, and about 10 minutes for intermediate and high gas mixture flows. This delay in reaching the steady state occurs as consequence of impedance adjustments in the reactor due to the gas atmosphere inside the chamber (variation of gas flows) and the consequent target surface conditions (degree of poisoning). Moreover, due to this gas flow changes, the plasma conductance also varies and thus affecting the target potential stabilization. Finally, this initial increase of gas flow implies also some time to reach the pressure stabilization and thus contributing also to this initial target potential variation.

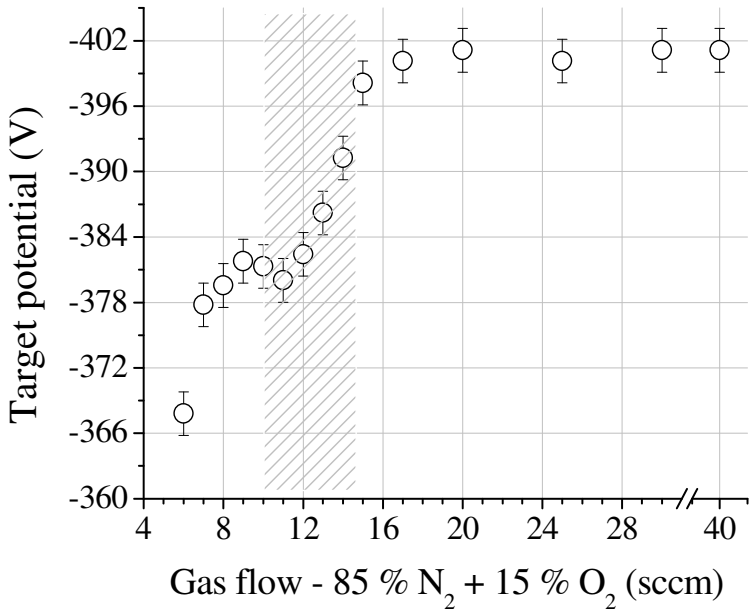


Fig. 2.7.b) Equilibrium values (steady state) of target potential as a function of reactive gas flow. The error was estimated in 2 V (the accuracy of the voltmeter).

Figure 2.7.b) shows the variation of the equilibrium target potential (steady-stage) values of samples from series 1 as a function of reactive gas flow. This plot shows that target potential presents a similar evolution as the deposition rate, where again three different zones (regimes) can be found, although the exact limits maybe slightly different. The coatings deposited with reactive gas flows up to 10 sccm show a non-linear increase of the target potential, with a significant increase of this parameter from a gas flow of 6 to 7 sccm, which varied from about -367 to -378 V, respectively. Since the gas mixture is composed of 85 % of nitrogen, the abrupt increase of the target potential for the sample deposited with 7 sccm (Fig. 2.7.b)) is probably due to the formation of zirconium nitride in the target surface. This hypothesis is well correlated with

variation of the coatings composition, where the abrupt increase of the target voltage is accomplished with an abrupt increase of nitrogen content of these coating regarding the sample deposited with 6 sccm, as we will discuss later on in this work. Reinforcing this hypothesis is the evolution of target potential and deposition rate of zirconium nitride and zirconium oxide coatings as a function of reactive gas flow, see Fig 2.8.a) and b) respectively.

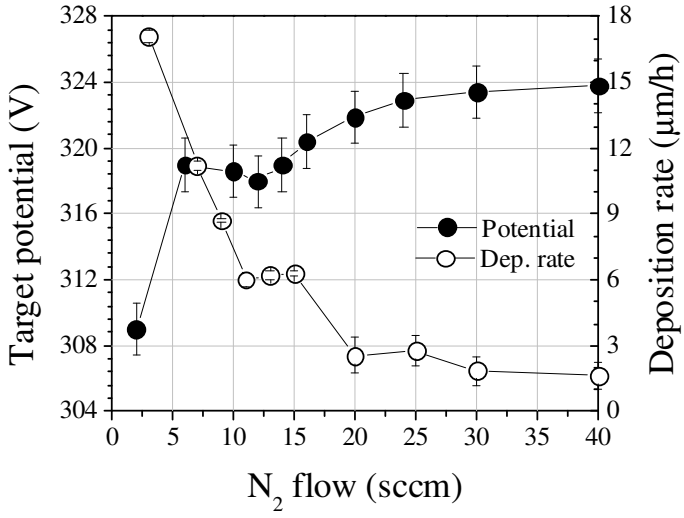
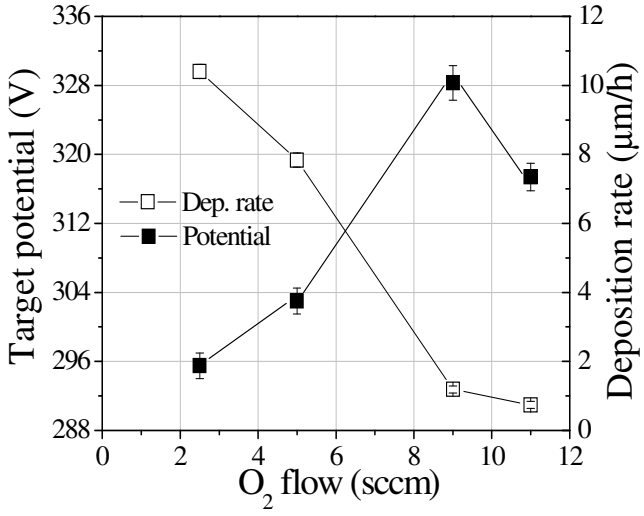


Fig 2.8.a) Target potential and deposition rate as a function of N_2 gas flow, for the binary system ZrN_y. The error bar for the deposition rate values was determinate by the maximum deviation to the average value. For the target potential, the error was estimated according to the maximum deviation observed during measurements (~2 V).

Fig 2.8.b) Target potential and deposition rate as a function of O_2 gas flow, for the binary system ZrO_x. The error bar was determinate by maximum deviation to the average value. The error bar for the deposition rate values was determinate by the maximum deviation to the average value. For the target potential, the error was estimated according to the maximum deviation observed during measurements (~2 V).



A close look into figure 2.8.a) shows that the binary Zr-N system presents a similar evolution of the target potential for low reactive gas flow, when compared to the ternary Zr-O-N system. The binary Zr-N system presents again a similar abrupt increase of ~10 V of the target potential for low reactive gas flows, again probably due to the formation of a thin nitride layer in

the target. On the other way around, the binary Zr-O system presents an almost linear evolution of the target potential, without any abrupt changes.

In figure 2.7.b) the samples deposited with gas flows from 8 to 11 sccm showed only slight variations in this parameter. With further increase of the gas mixture flows from 12 up to 15 sccm, there is a constant increase of the target voltage, which may be correlated with the previously mentioned zone II. This second zone is then followed by a stabilization of the target potential values, for the samples deposited with reactive gas flows higher than 15 sccm, which correspond to what was indexed previously with zone III.

Within the first regime, the increase of the gas mixture flow to values above that of the gettering rate of the sputtered metal induces a reaction of the gas with the target surface forming a layer of the gas metal compound, resulting in a decrease of the deposition rate and an increase of the target potential [12], which anyway seems to reach a steady state at gas flows between 8 and 11 sccm. This behaviour might be the direct result of a sputtering regime in an almost steady state (resulting from complete target coverage and a continuous consumption of the reactive gases).

Regarding zone II, it is important to note that although the deposition rate didn't change significantly, the target potential showed an important variation. This behaviour can be explained with the progressive increase of the target poisoning, due to the formation or increasing thickness of oxide and/or nitride compounds in its surface. This progressive but not abrupt increase of the target poisoning should be due to the relatively high pumping speed of the vacuum system (356 L s^{-1}). As a result of this relatively high pumping speed, a gradual transition between the reactive and complete oxidized state of the target is obtained. Nevertheless, the gas mixture contains 85 % of nitrogen, but oxygen is known to be extremely reactive (~100 times more reactive than nitrogen [23,24]) and thus the surface target potential is most likely to be the result of a progressive oxide layer formation rather than that of nitride.

For reactive gas flows above 14 sccm, there is a significant decrease of the deposition rate (Fig. 2.5.), with no significant changes in the target potential. The constancy of the target potential is probably due to the complete or almost complete oxidation of the target surface, due to the superior poisoning rate regarding the cleaning rate. The continuous decrease of the deposition rate should result from the increase of thickness of the nitride and oxide layers in the target surface [12].

2.5. Substrate temperature evolution

So, far its has been shown that there are some contact points between the deposited films (presented by their particular deposition rates) and the characteristics of the sputtering process, which were revealed by the evolution of the target potentials during he films preparation. The target poisoning effect resulting from the increase of the gas flow was one of the main factors that could explain the behaviour. In order to further disclose the deposition characteristics that were changing with the change of the deposition parameters (the reactive gas flows increase in particular), the evolution of the deposition temperature was another characteristic that was followed during the film's preparation. Because the films from series 1 were prepared in static mode, a thermocouple was placed close to the surface of the "substrate holder" and the temperature was monitored during the entire duration of the depositions.

This characterization allowed us to follow the differences in film's growing temperatures and thus to correlate them with the differences observed both in film's characteristics (the deposition rates for the particular case of this chapter) and the deposition process itself (the target potential variations for the case). Moreover, the characterization of film's growing temperatures allowed us to have some ideas about the level of adatom mobility during the deposition, and thus to explore some possible correlations with the kind of morphologies that were being formed as well as the kind of crystalline structures that were developed, namely in terms of phase mixtures, structure doping or even the degree of crystallinity. Two kinds of measurements were done: i) the temperature evolution during deposition (Fig.2.9.a)) and ii) the equilibrium temperature (which was calculated again after the growing temperature reached a steady state, Fig.2.9.b).

Figure. 2.9.a) shows the evolution of the deposition temperature as a function of the deposition time, for representative samples. The first observation that can be drawn is related to the equilibrium temperature time. With a closer look to the plot it is possible to observe that associated with the increase of equilibrium temperature, is an increase of the time needed to stabilize the deposition temperature with the increase of the reactive gas flow. The different compounds formed with deferent's thermal conductivities, as we will see later on in this thesis, should play an important role for this evolution. Zirconium nitride, in ZrN form is known for having high thermal conductivity [25], in contrast with zirconium oxide that is used as thermal barrier coating, due to the low thermal conductivity [26]. This opposite thermal behaviour should be responsible for the higher equilibrium temperature time for the higher gas flows, where due to

high oxygen contents (and its much higher reactivity), the formation of more oxide-based films is expected.

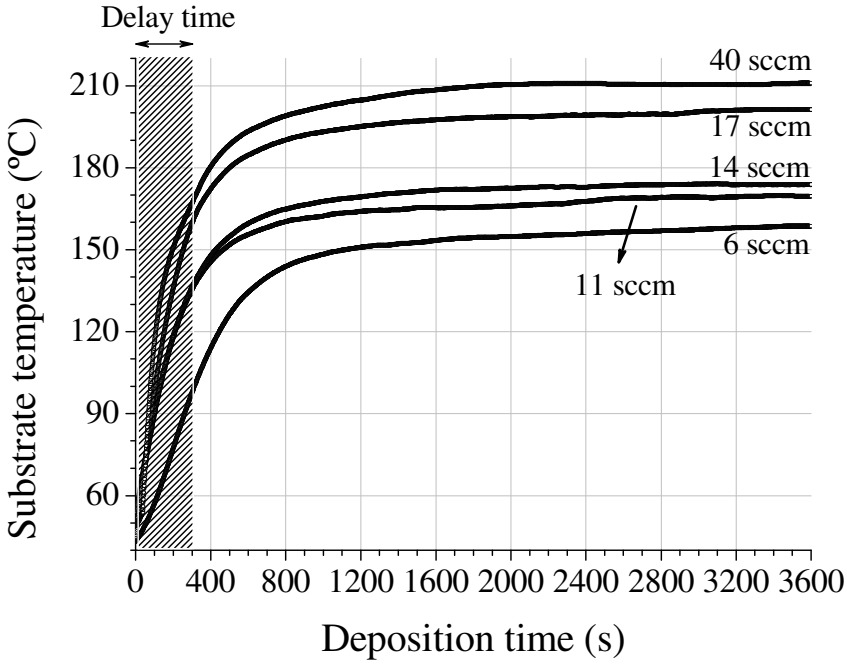


Fig. 2.9.a) Variation of the substrate temperature of the films as a function of deposition time.

The different formation enthalpies associated with different deposition rates, are expected to play a decide role for this variation. In fact, it seems rather interesting to see that the same almost constancy in the deposition rate is now obtained in the deposition temperatures in that region of gas flows between 8 to 14 sccm, inducing some (expected) correlation between the deposition temperature and the deposition rate.

Figure 2.9.b) presents the evolution of the equilibrium temperature of the films as a function of the reactive gas flow.

The first observation that can be drawn is that the deposition temperature varies roughly from 150 to 210 ºC, showing a first increase with the increase of gas mixture flow, until a stabilization that seems to occur for the highest gas flows. These low values of substrate temperature, less than 14 % (in K) of the ZrN melting point [27,28], and less than 18 % of ZrO_2 (in K) melting point [29,30], indicate that during deposition the adatom mobility may not be high enough to assure phase segregations (nitride/oxides). This may induce the possibility to have some “phase intermixing”, and thus the formation of metastable structures, with some atomic doping.

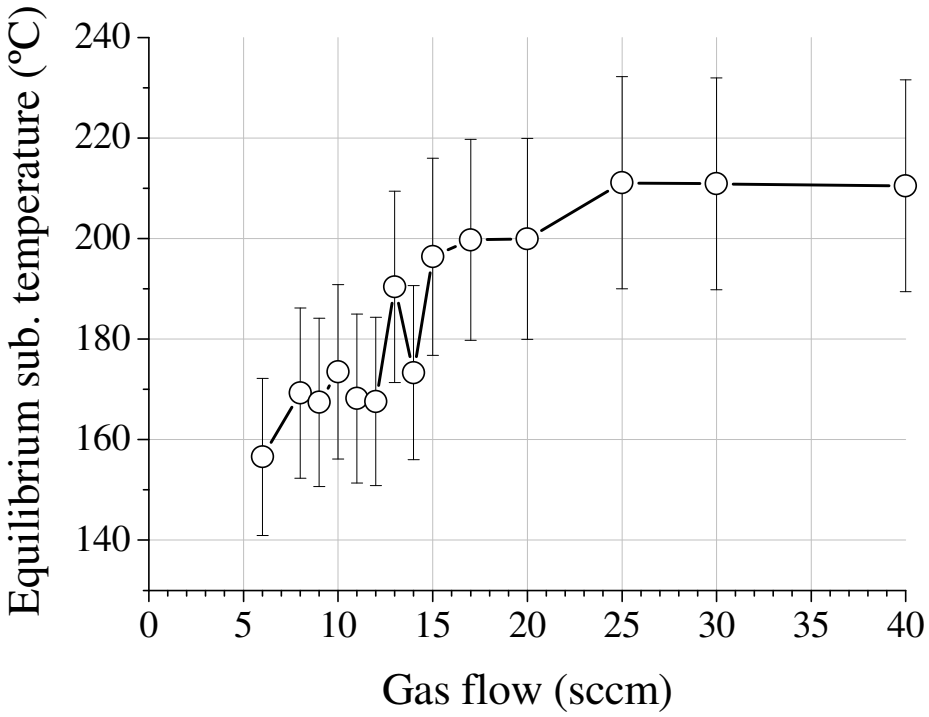


Fig. 2.9.b) Variation of the substrate temperature of the films as a function of the reactive gas flow. The error was estimated in 10 %.

This figure shows also some similarities with both the deposition rate and target potential evolutions. Some trends may be closely related with the different growth zones that are being analysed throughout this chapter. For example, and what concerns to both regions I and II (Fig. 2.5.). Figure 2.9.b) shows that the samples within these two zones grow with substrate temperatures that are roughly lower than those of zone III. The different bond characteristics that are being formed, promoted by the different compositional arrangements (nitride-based compounds vs. oxide-like ones) are certainly playing an important role for this difference.

Figure 2.10. shows the plot of the deposition temperatures versus the deposition rate. It is clear from this graphic that there is a tendency for decreasing the equilibrium deposition temperature with the increase of the deposition rate. Zirconium oxide presents a formation enthalpy more than three times higher than that of zirconium nitride ($\Delta_f H°_{ZrO2}$: -1100.6 kJ/mol [31] and $\Delta_f H°_{ZrN}$: -365.5 kJ/mol [32]), but presents a deposition rate four times lower than that of zirconium oxide [33], so the main issue here should be the result of the differences of thermal conductivity between the nitride and oxide compounds.

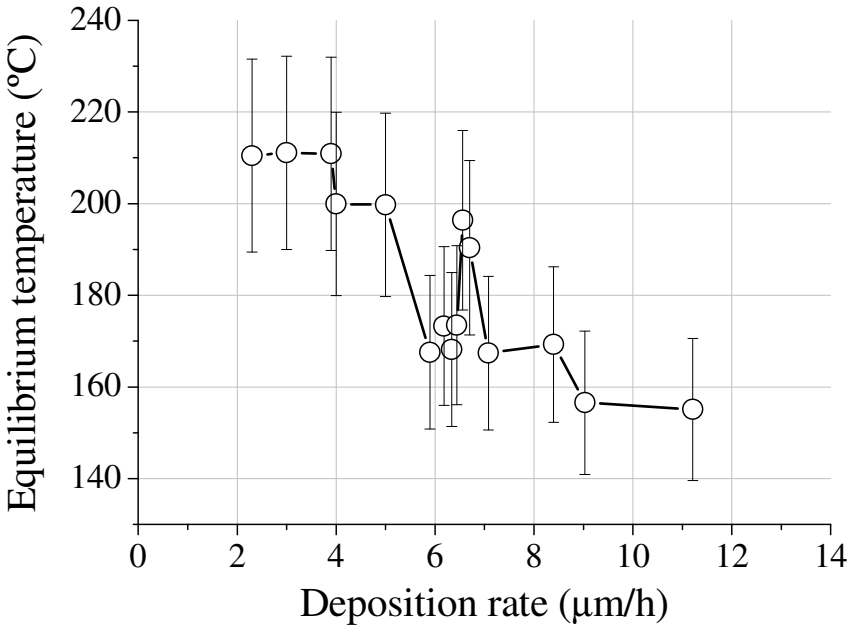


Fig. 2.10. Variation of the substrate equilibrium substrate temperature of the films as a function of the deposition rate for series 1. The error was estimated in 10 %.

Since the equilibrium temperature should be a consequence of the heating resultant from the adatom condensation (that depends on the formation enthalpy and deposition rate) and the heat loos by emitted radiation process, the lower thermal conductivity of zirconium oxide should present a major relevance on the decrease of substrate equilibrium temperature with the increase of the deposition rate.

2.6. Composition of the films

The atomic compositions of the as-deposited samples and the depth concentration profiles (in the growth direction) were measured by Rutherford Backscattering Spectrometry (RBS), performed with a beam energy of 1.4 MeV as well as 1.4 and 2 MeV proton beams to increase the accuracy in the oxygen signals. Two scattering angles were used: 140º (standard detector, IBM geometry) and 180º (annular detector), with tilt angles of 0º and 30º. A standard detector data was used due to the poorer resolution of the annular detector. The analyzed area was about 0.5x0.5 mm^2. In addition, for some samples, Particle Induced X-ray Emission (PIXE) measurements were performed to check for impurities. The data were analyzed with the IBA DataFurnace NDF v8.1l [34]. For the ^{14}N and ^{16}O data, cross sections given in [20] were used.

The first important fact that should be mentioned is that the results from the RBS simulations revealed a quite homogenous in depth composition profiles for all layers.

As a summary, figure 2.11. shows the obtained RBS spectra and simulations of a representative group of samples prepared with different reactive gas flows.

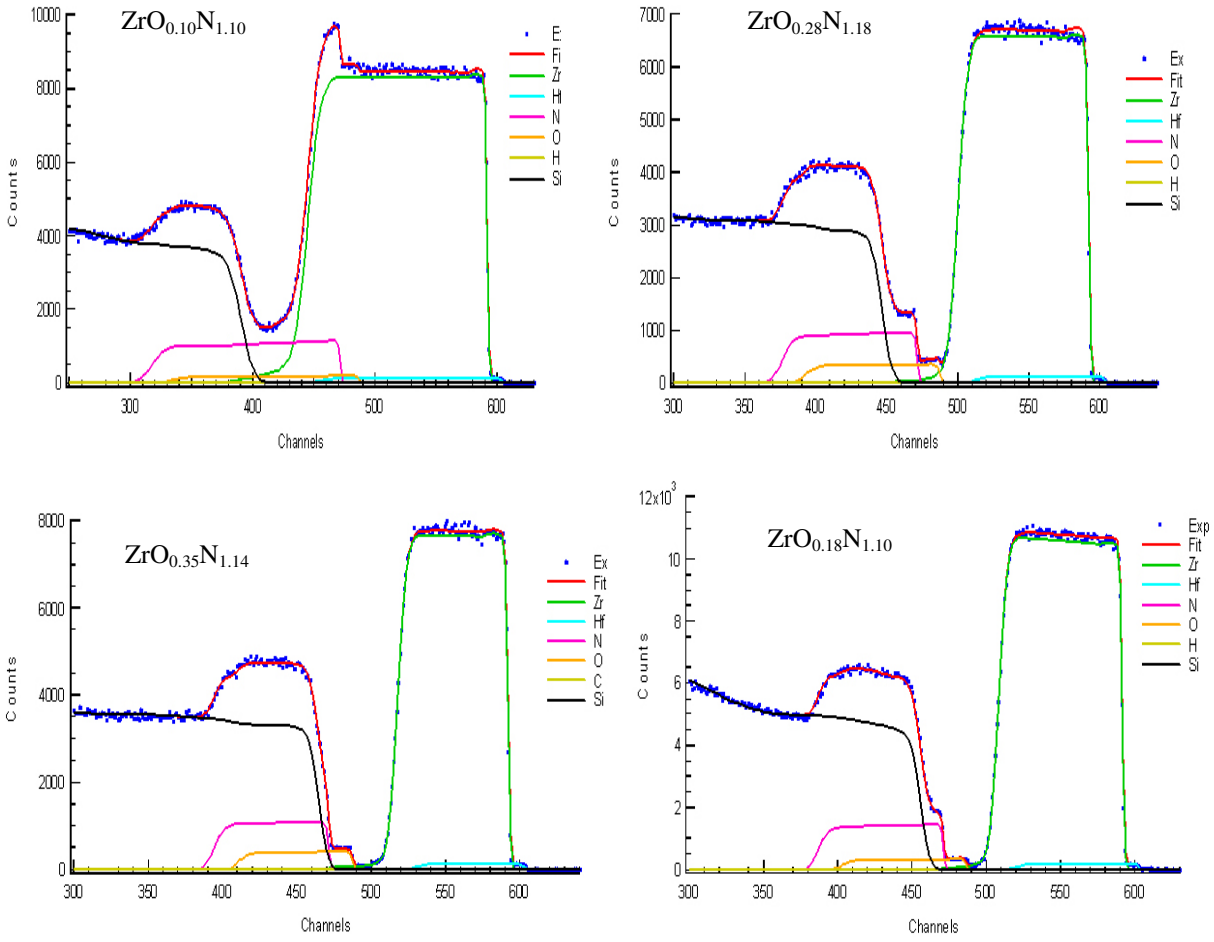


Fig. 2.11. RBS spectra obtained for the measurements of the series of samples prepared with different reactive gas flows.

Figure 2.12. shows a ternary diagram of the base group samples (series 1) prepared within the Zr-O-N system, showing the compositional location of all samples prepared within this series. The first interesting note that is worth mention is the position of the obtained samples. The diagram shows that they lye in a triangle that includes the well-known Zr_3N_4; ZrO_2 and ZrN, where the first two are actually occupying two of the triangle's vertices.

The third vertex of the triangle is located in a position that corresponds to sub-stoichiometric ZrN_y compounds, where y is close to 0.43 (corresponding to 30 at. % N and 70 at. % Zr). Also important to notice is the existence of a reasonable number of samples located in the vicinity of the Zr_2ON_2 compounds, lying in the composition line that connects ZrO_2 with ZrN-type compounds. A schematic representation of such a triangle is also presented in figure 2.13.

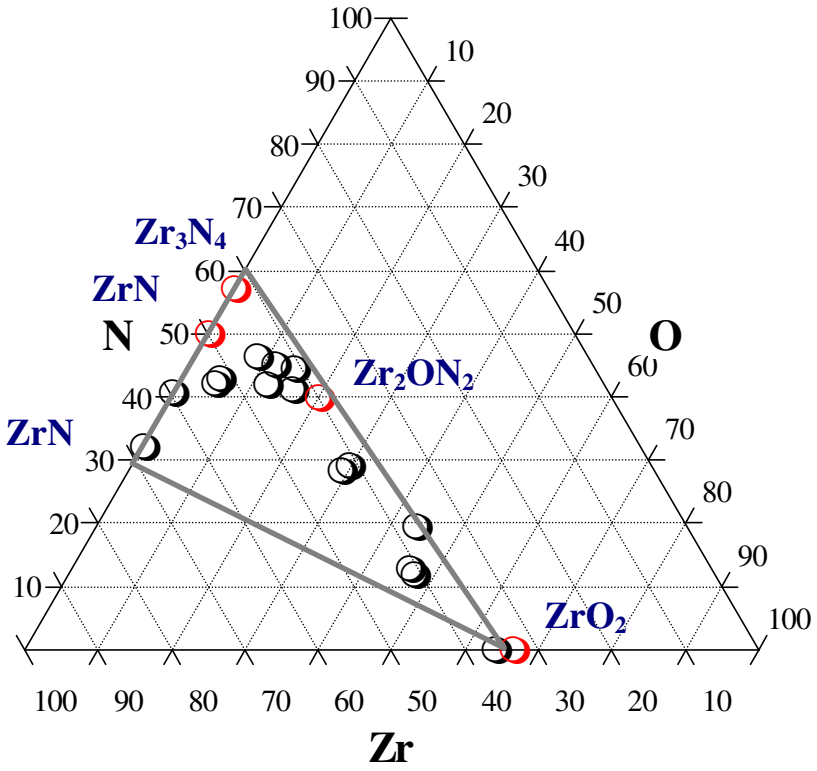


Fig. 2.12. Ternary diagram of the Zr-O-N samples from series 1. Red symbols present only the position of known Zr-based compound.

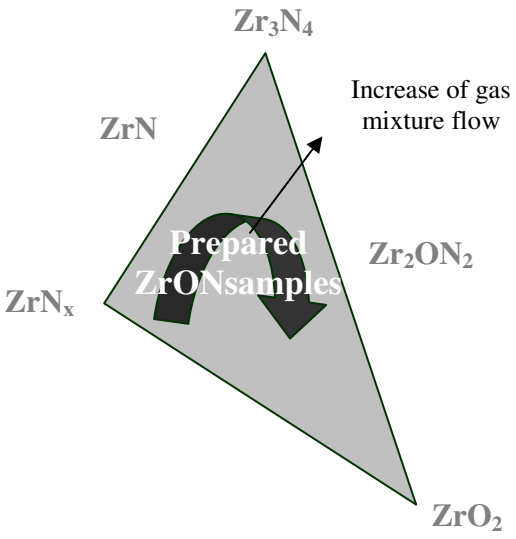


Fig. 2.13. Schematic representation of prepared samples (series 1).

These last two figures are a first important indication not only about the elemental composition of each sample (a fundamental factor to understand all the properties that will be analyzed throughout this work), but above all about, the possible compound-types that may be formed in the films, which will be then accurately investigated by crossing with both the results of X-ray diffraction (XRD) and X-ray photoelectron spectroscopy (XPS). Again these compound-types development will be a powerful tool to understand the different behaviours that will be under evaluation, but also to model the film growth, and especially the influence of oxygen, which, as it will be shown is of major importance for all these developments. Last, but not least, the distribution of compositions will firstly be used to further check the previously mentioned zones, trying to confirm or even extend the different growth regimes.

Although the important area of composition already present in such a triangle, it is clear that there is still an important part of the ternary diagram that is still unoccupied. This fact is the result of two major facts. First, the main purpose of this work was to study intrinsic coloured thin films, which means that beyond certain non-metal contents, the obtained samples revealed interference-like colourations, which are out of the main goal of the thesis. Secondly, it is also important to emphasize that a reactive gas mixture composed of nitrogen and oxygen was used. This induces some composition restrictions, namely because of very different chemical reactivity's of both gases.

In order to follow the concentration evolution as a function of the increase of reactive gas flow, and thus to be able to follow the chemical (and possibilities of compound-types development), figure 2.14. shows the variation of the atomic concentration of all elements as a function of the reactive gas mixture flow.

From this plot, the first conclusion to be drawn is that there is a continuous increase of the oxygen content of the coatings with increasing reactive gas flow, though a large amount of nitrogen is always present in the gas flow (the gas flow is composed of a mixture of N_2+O_2 with a 17:3 ratio). This is due to the already mentioned high affinity of metal atoms such as that of zirconium towards oxygen rather than to nitrogen [23,24]. Taking into account the available thermochemistry data for zirconium oxides and nitrides: a complete oxidation of the film would be expected as long as enough oxygen is available, since the formation of a metal–oxygen bond is energetically more favourable($\Delta H_f°_{ZrO2}$: -1100.6 kJ/mol [31]) than that of a metal–nitrogen

bond ($\Delta H_f°_{ZrN}$: -365.5 kJ/mol [32]). These results suggest that with the used deposition parameters, the kinetic of the reaction plays a dominant role.

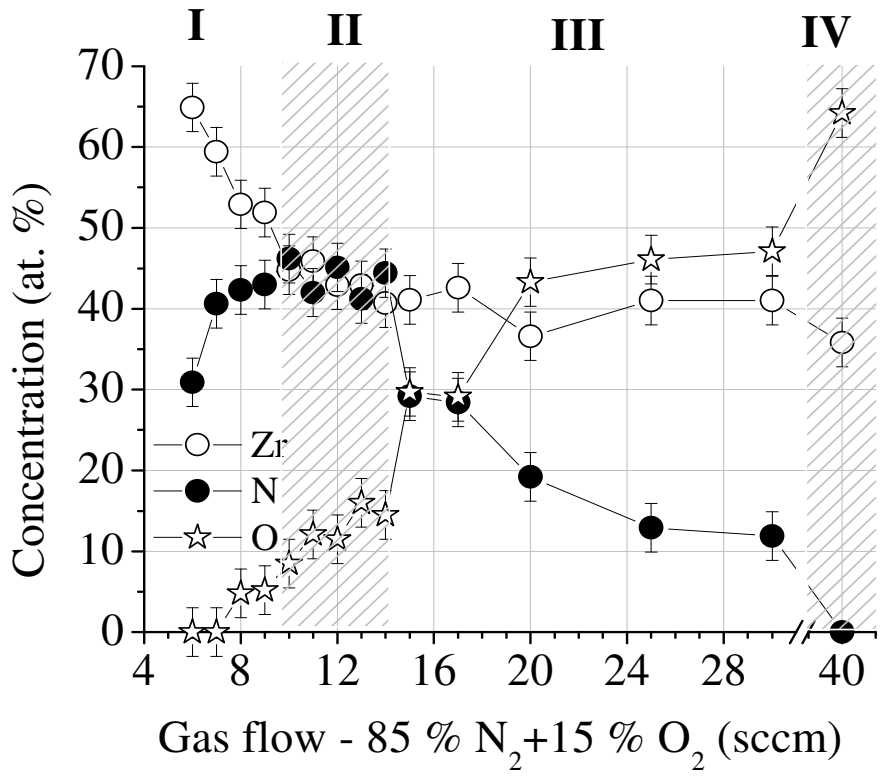


Fig. 2.14. Variation of the atomic concentration of the elements as a function of the reactive gas mixture flow, for the samples from series 1. An average of 5 at. % was estimated for the RBS concentration resolution.

Taking into account the previous zone division (see Fig. 2.5. and 2.7.), figure 2.14 confirms and clears out again those different zones division, but a closer look seems to reveal that it is possible to divide that previous zone III into two different ones. In fact, the last sample presented in all these graphs shows in figure. 2.14, that there is a significant change in the composition values, for all elements when compared with previous samples. This last sample (prepared with an amount of reactive gas flow of 40 sccm) presents an increase of the oxygen content of about 17 %, while the amount of Zr decreases of about 5 %, when compared to the previous sample in the plots (prepared with an amount of reactive gas flow of 30 sccm). To become even clear the difference of this sample (40 sccm) regarding those previous ones is the fact that practically no nitrogen was found in this sample within the resolution limitations of RBS, meaning that the uncertainty in N as well as in the others elements, would be around 5 at. %. Thus, and taking this into account, the composition results allow to make an update in the zone previously mentioned

three zone distribution, which will now include four distinct compositional regions, according to their particular compositional variations. This "new" region is now the result of a "refinement" of previous zone III that now excludes the sample prepared with a reactive gas flow of 40 sccm, which in its turn will be placed in the "new" zone IV.

In terms of a specific and detailed analyzes to the plot of Figure 2.14., the results show that the films (prepared with reactive gas flows below 10 sccm), reveals that the increase of reactive gas flows provokes an increase of the nitrogen content from about 31 at. % to ~43 at. % and a systematic decrease of the zirconium content from about 65 at. % down to about 52 at. %. The amount of oxygen within this region is relatively low, but increasing steadily up to about 6 at. %. Moreover, it is important also to note that the detailed analysis of figure 2.14 imposes a reactive gas flow of 10sccm the limit for zone I.

Beyond these absolute values of composition and their variations, it is particularly important to notice the ratios of the different elements, which may give the first indication about the particular tendency for compound formation. The values for such ratios are illustrated in figure 2.15.

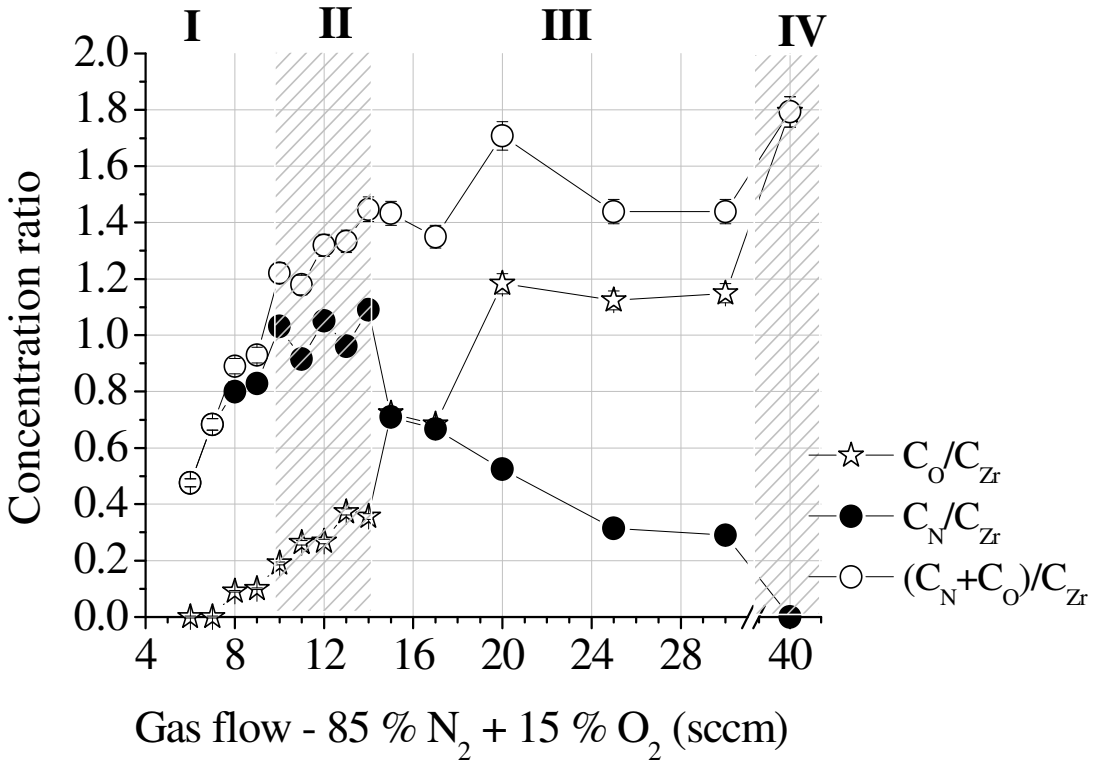


Fig. 2.15. Variation non-metals over the zirconium atomic ratios, C_O/C_{Zr}, C_N/C_{Zr} and $(C_N+C_O)/C_{Zr}$ as a function of the reactive gas mixture flow for the series 1. The uncertainty was determined by error propagation.

This figure, and for the films prepared within zone I, shows that all the non-metals to zirconium atomic ratios, C_O/C_{Zr}, C_N/C_{Zr} and $(C_N+C_O)/C_{Zr}$ are also increasing. Particularly noticeable is the increase of the C_N/C_{Zr} ratio, which approaches to 0.8, and thus providing evidences for some tendency of the deposition conditions to induce the formation of sub- and stoichiometric Zr-N-type compounds.

A comparison between these results and those of both deposition rate and target potential (Fig 2.5 and 2.7.b)), shows the possibility to establish some preliminary correlations. As shown previously in this text, these zone I samples presented the highest values of deposition rate (Fig. 2.5.) and the lowest values of target potential (Fig. 2.7.b)).

As illustrated by the composition results, the films are roughly sub-stoichiometric (even if taken into account both non-metals as illustrated by the $(C_N+C_O)/C_{Zr}$ ratio). At the target, a poor or partially poisoned surface appears when the poisoning rate is lower than the cleaning rate, inducing a high metal flux from the target. Since the formation rate of the compound film is limited by the impact rate and the use of the reactive gas atoms, a metal-rich, or sub stoichiometric, film is deposited [12], as illustrated in figure 2.16.

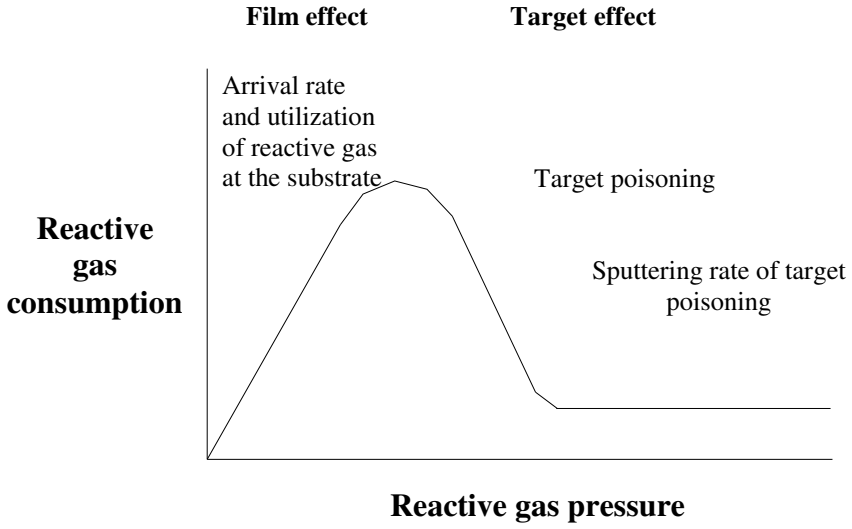


Fig 2.16. The origins of the reactive gas consumption. Reproduced from *Spencer et al.* [22].

Moreover, and still in zone I, the C_O/C_{Zr} ratio shows also a slight increase up to about 0.2 at a reactive gas flow of 10 sccm, due to the high reactivity of oxygen, inducing some important

changes in the film's bonding and structural features, as it will be shown latter in the text. As mentioned before, the films prepared within this first zone show apparent colours from metallic (silver like) towards golden tones, which is characteristic of a change from metal-type compounds to nitride-based compounds [35] and thus corroborating the obtained composition profile. Moreover, within this region, the first samples (reactive gas flows of 6 and 7 sccm) presented no detectable oxygen by RBS, indicating that with the used deposition parameters, the kinetic of the reaction plays the most significant role. Taking into account that the reactive gas mixture present in the reactor is composed of 85 % of nitrogen, this can be interpreted taking into account that in the time scale of the reactions. The arriving rate of the metal atoms doesn't allow a complete thermodynamical choice for reaction mechanism with theses partners, specially with the preferential thermodynamic partner, the oxygen [31,32]. Nevertheless, the kinetic of the reaction present a dominant role is this zone, on this basis, is expected that these samples present an atomic ratio of nitrogen to oxygen of 5.67 (gas mixture ratio O:N = 17:3). On this basis the samples prepared with reactive gas flows of 6 and 7 sccm, the simulated values for the oxygen amount would 4.6 and 6.1 at. %, respectively, which are close to the resolution of RBS. Figure 2.17 presents the C_O/C_N atomic ratio as a function of the reactive gas flow for the samples of series 1.

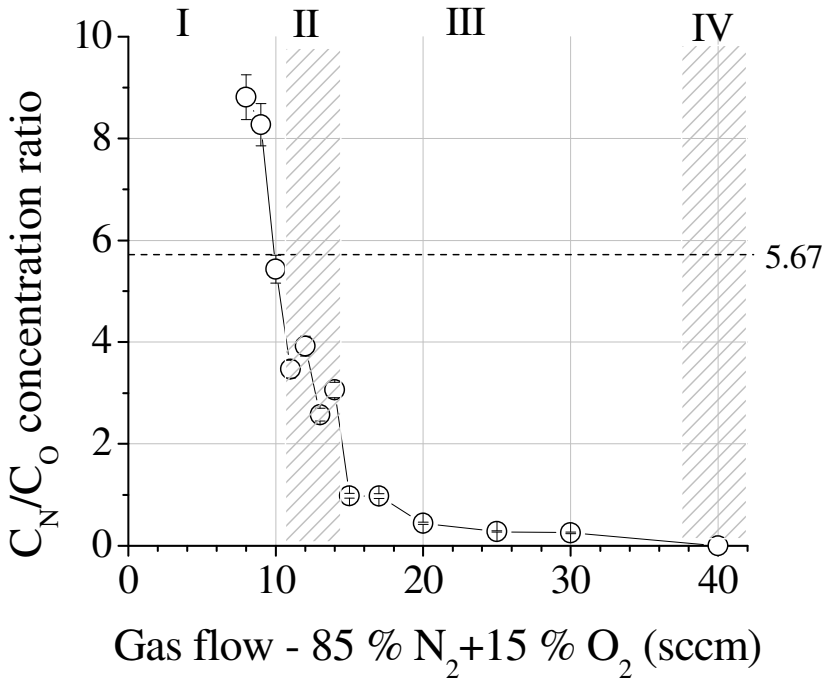


Fig. 2.17. Ratio C_O/C_N as a function of the reactive gas mixture flow for series 1. The uncertainty was determined by error propagation.

This figure shows that samples prepared within the first zone present an atomic ratio C_N/C_O higher than the "kinetic limit" of 5.67 (resulting from the ratio of both gases within the reactive gas mixture: O:N – 15 %: 85%). Taking into account the roughly sub-stoichiometric condition of these films (see Fig. 2.14.), this might be an unexpected result, meaning that not all available oxygen would be "deposited" in the film (even more if one keeps in mind the relatively high reactivity of oxygen towards zirconium). Although these apparent contradictions, the reason might be related with the RBS resolution, especially when small amount of light elements are involved. In fact, and taking as a reference the samples prepared with reactive gas flows of 8 and 9 sccm, the simulated values for the oxygen amount were 6.8 and 7.6 at. %, respectively, which are close to the technique resolution. A simple calculation based on the error margin (increase the oxygen amount about 3 at. % and thus reducing the nitrogen amount by the same quantity), would lead to an atomic ratio C_N/C_O close to 5 in both cases, and thus very close to that ratio expected for kinetic-dominating conditions. Anyway, with the increase of the oxygen amount, this "resolution problem" will tend to be more negligible and thus more representative of the real situation of the growing films.

For increasing gas flows ($\phi_{N2+O2} \geq 10$ sccm), elemental composition analysis (Fig. 2.14. and 2.15.) evidence the appearance of another zone, which is characterised by an approximately constant concentration of both zirconium and nitrogen for reactive gas flows up to 14 sccm, while the amount of oxygen increases slightly from ~12 at. % to 15-16 at. %. In this second zone, the C_N/C_{Zr} atomic ratio is also roughly constant and close to one, but the C_O/C_{Zr} atomic ratio increases from about 0.26 to 0.36-0.37 (Fig. 2.15)). The fact that the value of the C_N/C_{Zr} ratio is close to the unity, would, in a first approximation, induce some tendency to form stoichiometric ZrN compounds, but the significant amount of oxygen present (between 12 and 16 at. %), which, connected to its significant reactivity towards zirconium, will certainly play a decisive role in the phase formation, as well as in the bonding characteristics. One possibility is the increase of oxygen incorporation/substitution, in the zirconium nitride matrix [36], resulting in an oxygen doped over-stoichiometric zirconium nitride structure [37]. A detail analysis of this possibility will be made in the structural chapter (chapter IV). Nevertheless, the formation oxide or oxynitride compounds must be just regarded as a possibility. Another important fact is related with the sum of both non-metals over the metal atomic ratio, $(C_N+C_O)/C_{Zr}$. For the samples

within this zone II, this ratio increases from about 1.17 to 1.45, which is, basically, the result of the increase of oxygen content (see Fig. 2.14)).

Since the coatings are deposited at low deposition temperatures (below 210 ºC, less 14 % (in K) of the ZrN melting point [30], Fig. 2.9.) and with no film deposition bombardment (samples were prepared in grounded condition), it is most likely that the growing films do not present enough adatom mobility to assure phase segregations (nitride/oxides), thus reinforcing the possibility of having other types of compounds, such as over-stoichiometric nitrides, which may also result from the doping of growing compounds.

Another important point that is worth mention for the samples of zone II is related with the variation of the C_N/C_O atomic ratio, Fig. 2.17. This figure shows that these samples (and most predominantly those from zone III and IV) are below the "kinetic limit" (C_N/C_O = 5.67), reinforcing the idea that in these regimes, the kinetic parameters play no more the dominant role. Within zone II, there seems to be a transition behaviour between these two clear kinetic-thermodynamic behaviours. Following the already observed features in the composition plots (see Fig. 2.14. and 2.15.), the group of samples prepared within this second zone show relatively high values of that C_N/C_O atomic ratio (varying roughly between 3 and 5.4), and thus inducing a mixture of both behaviours or even a smooth transition between the two. This last possibility would then be consistent with a change between different compounds and crystalline phases. In conclusion, this first zone is characterized by an increase in both reactive elements, following consistently the increase of their flow rate – kinetics-dominated depositions.

In term of colour tones, the samples prepared within the zone II exhibited colours from red-brownish towards dark blue.

For samples deposited with reactive gas flows between 15 and 30 sccm - zone III, composition measurements (Fig. 2.14), showed that, similarly to what was observed in zone II, the zirconium concentration is still approximately constant (only few oscillations), but there is a clear decrease in the nitrogen concentration from about 44 at. % for the sample prepared with a reactive gas flow of 14 sccm to about 12 at. % for the sample prepared with 30 sccm. This significant decrease is followed by a notorious increase of the oxygen concentration from about 15 at. % for the sample prepared with 14 sccm to about 30 at. % for the 15 and 17 sccm samples, and from about 43 at. % to about 47 at. % for samples prepared with reactive gas flows varying from 20 to 30 sccm. Comparing these results with the plot of atomic ratios, Fig. 2.15, it can be

observed that these changes correspond to a substantial increase of the C_O/C_{Zr} atomic ratio, with a value close to 0.7 for the first samples of this zone (15 and 17 sccm), raising to a value of about 1.2 for the other samples. The values of the C_N/C_{Zr} ratio decrease significantly from 0.7 to ~0.3 as a consequence of the decrease of nitrogen concentration, but there is a roughly stabilization of the non-metal to metal atomic ratio, $(C_N+C_O)/C_{Zr}$ at a value close to 1.5. This evolution shows a very different behaviour in comparison to that of zone II, suggesting a possible change on the atomic arrangements and thus possible changes in both compound formation and crystalline structures. Taking into account both the C_N/C_{Zr} and C_O/C_{Zr} ratios, it is rather difficult to predict any kind of atomic compounds that may be formed with the three elements, at least from available information [36]. Anyway, the results of the non-metal to metal atomic ratio, $(C_N+C_O)/C_{Zr}$, may give some indication on different possibilities. The obtained ratio of ~1.5 might be an indication for the formation of different compounds beyond ZrN and ZrO_2.

Another good indication may come for the C_N/C_O atomic ratios plot, Fig. 2.17. It is particularly noticeable the case of the films prepared within this third zone, where the values of this atomic ratio are always below 1, meaning that oxygen is now playing the most important role. Regarding the surface colour tones, the samples prepared within this zone showed interference-like colours, loosing the characteristic intrinsic colour revealed by the samples prepared within the two previous regions.

Finally, the samples deposited with the highest values of the reactive gas flow (> 30 sccm) showed a stoichiometry close to that of zirconium oxide, ZrO_2, with non-detectable nitrogen by RBS (meaning that its content it is certainly very low, but it may go up to 5 at. %). This can be interpreted by the progressive replacement of nitrogen by oxygen within the matrix, due to its high reactivity together with its high partial pressure in the reactive gas mixture. The undetectable presence of nitrogen suggests that thermodynamic factors are now dominant with these deposition parameters. This is also clear from the plot of figure 2.14, where in spite of the large amount of nitrogen available in the gas atmosphere (let us keep in mind that a gas flow of 40 sccm in a 85 % N_2 + 15 % O_2 gas mixture such as the one used to prepare these coatings contains about 32 sccm of nitrogen!), the atomic ratio C_N/C_O is practically 0 (even considering the error margin of RBS).

In order to understand the role of kinetics and thermodynamics mechanisms occurring within the different sputtering modes (the four regions mentioned previously), different series of

coatings, with deferent deposition conditions were prepared. Moreover, with these different series of samples, it was a major goal to insure not only if the different composition features analyzed previously are still present, but above all, to study which parameters may influence these composition regions (if still present) or others that may appear. This study was also carried out in order to allow the widest range possible of experimental conditions and correlate them with the films properties (namely colour), trying to contribute to a better and easiest transpose of experimental work to industrial environments.

2.6.1. The role of the gas mixture composition

(Series 2: a series prepared with a gas mixture composed of 95 % N_2 + 5 % O_2)

First of all and in order to study some deposition parameters that may be varied not only in a laboratory scale but also in industrial environments, the role of the composition of the reactive gas atmosphere was characterized. Taking this experimental parameters scan as a start point, a second series was prepared in which the composition of the reactive gas mixture was varied. This second series was prepared using a reactive gas mixture composed of 95 % N_2 + 5 % O_2. This series was prepared taking as a ground basis the influence of the available oxygen within the reactive atmosphere. Again, the search for major or minor changes was the main objective, but now taking as start point the high reactivity of oxygen and also its significant importance, mainly as it was observed in zones II, III and IV form the first series. Figure 2.18.a) shows the elemental concentration variations for a set of samples prepared with a reactive gas mixture composed of 95 % N_2 + 5 % O_2 (series 2) as a function of the reactive gas mixture flow.

The first important point that needs to be referred is the relative differences in the elemental concentration variations. Contrarily to what has been observed for samples of series 1, this new series presents much smoother variations in the elemental concentrations, and thus the different zones will be relatively difficult to be quantified. Nevertheless, two points need to be clarified.

First of all is related with the region of reactive gas flows that was used. Taking into account the results from previous series, only intrinsic coloured films were deposited, which corresponded to zones I and II from series 1. The fact that the main goal of this work was to prepare intrinsic-type coatings resulted in the less important character to conduct a full scale study for this “new” series, which was roughly restricted to that intrinsic-like region. The second

point is related with the direct reading of the plots, which cannot be done in a straightforward manner due to the different composition of the reactive gas atmosphere.

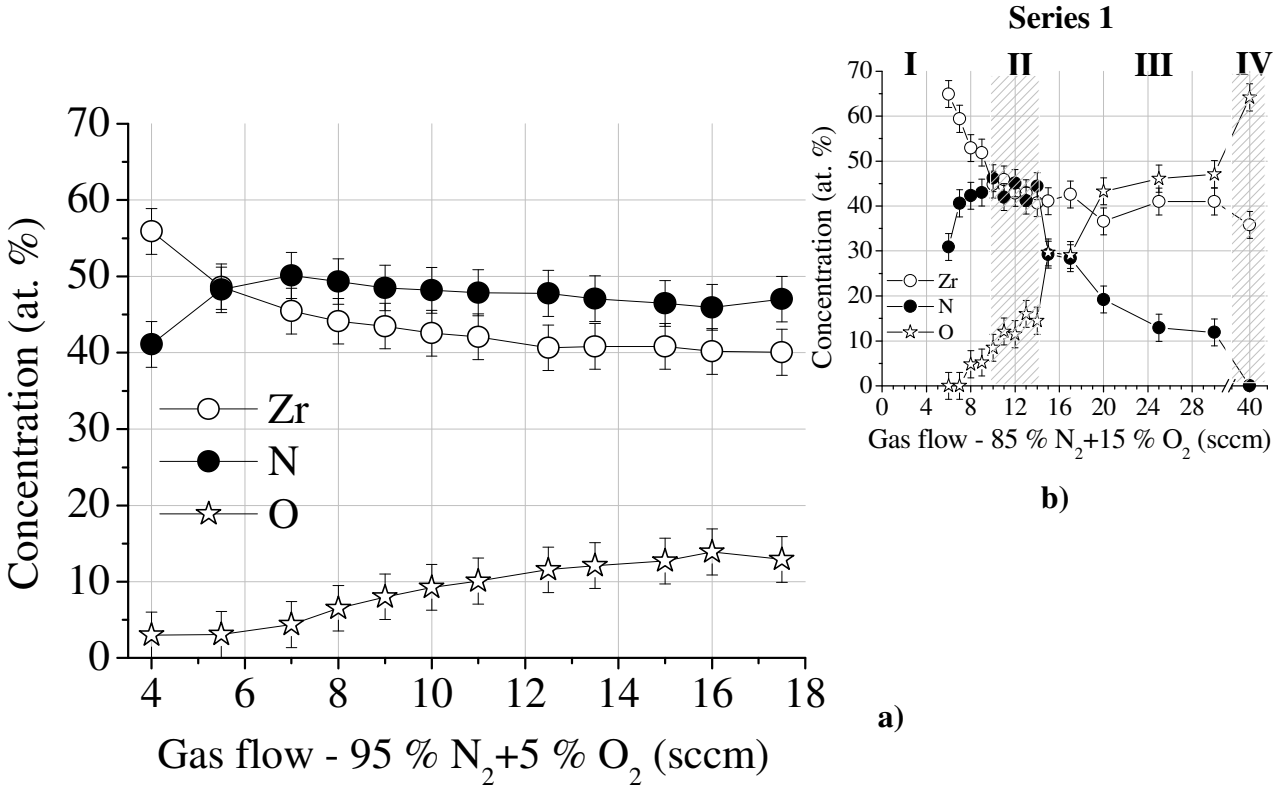


Fig. 2.18.a) Variation of the atomic concentration of the elements as a function of the reactive gas mixture flow, for the samples of series 2. **b)** For comparison purposes, the same plot is shown in the upper insert for the samples prepared with 85 % N_2 + 15 % O_2 (Fig. 2.14) – series 1. An average of 5 at. % was estimated for the RBS concentration resolution.

Beyond these important points, it is anyway clear that similar tendencies are observed. First of all, there is an initial decrease in the zirconium content and an increase in both nitrogen and oxygen. The main difference is that now these variations are smoother and relatively smaller. The zirconium content decreases about 20 % up to the sample prepared with 8 sccm (which seems to be the limit for the highest variations of all elements, although these variations keep occurring till the last samples, but less pronounced). On the other hand, series 1 showed a reduction of this same element content of about 30 % in zone I. Moreover, the increase of nitrogen content for series 2 is again smoother and less pronounced: 20 % for series 2 in comparison to those roughly 50 % that occurred within zone I of series 1. The variations of the oxygen content cannot be accurately analyzed due to the resolution problems of the RBS technique although it seems clear that it varies significantly in both cases. Again, it seems that

this element will act as one of the most important factors for the samples future behaviour. The less oxygen rich atmosphere is certainly playing a decisive role for these smoother variations, though the same tendencies of variation are kept. In order to better clarify whether the same zones of series 1 are present or if major changes occurred, figure 2.19.a) shows the plot of all concentration ratios.

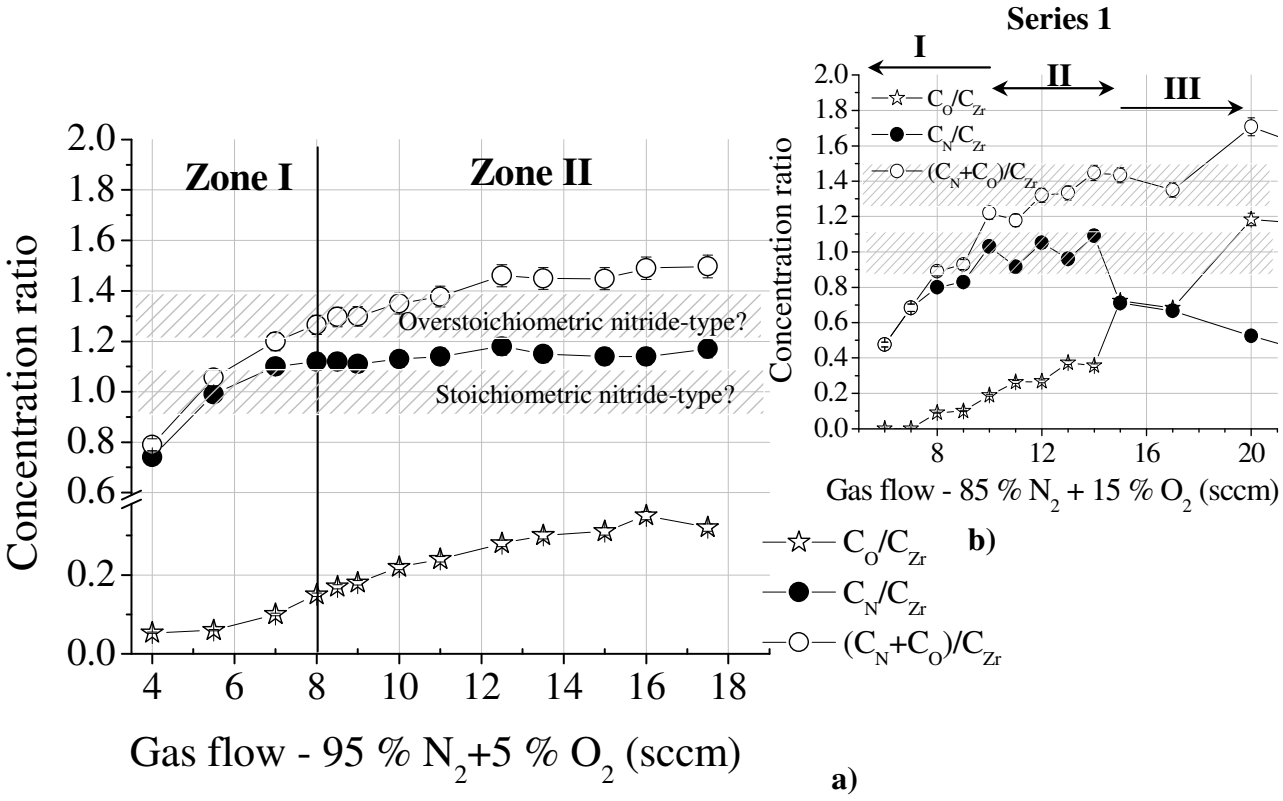


Fig. 2.19.a) Variation non metals over the zirconium atomic ratios, C_O/C_{Zr}, C_N/C_{Zr} and $(C_N+C_O)/C_{Zr}$ as a function of the reactive gas mixture flow for series 2 (The uncertainty was determined by error propagation.). **b)** For comparison purposes, the same plot is shown in the upper insert for the samples prepared with the 85 % N_2+15 % O_2 (see Fig. 2.14) – series 1, and for a similar region of gas flows.

A closer look to this plot shows that also from the atomic ratios, the division of films into different groups for this second series is again very difficult. Anyway, a closer look shows that similarly to what has been shown for the elemental composition analysis (Fig. 2.18.a)), the films prepared with reactive gas flows below 8 sccm presented also the largest change in the atomic ratios. Particularly noticeable is the increase of the C_N/C_{Zr} ratio, which approaches to 1.1, for the sample deposited with 8 sccm, but from that gas flow value on, this ratio seems to become approximately constant. Moreover, the ratio C_O/C_{Zr} is relatively low and thus there seems to be

some favourable condition to form some kind of stoichiometric ZrN compounds (with some possible oxygen inclusions).

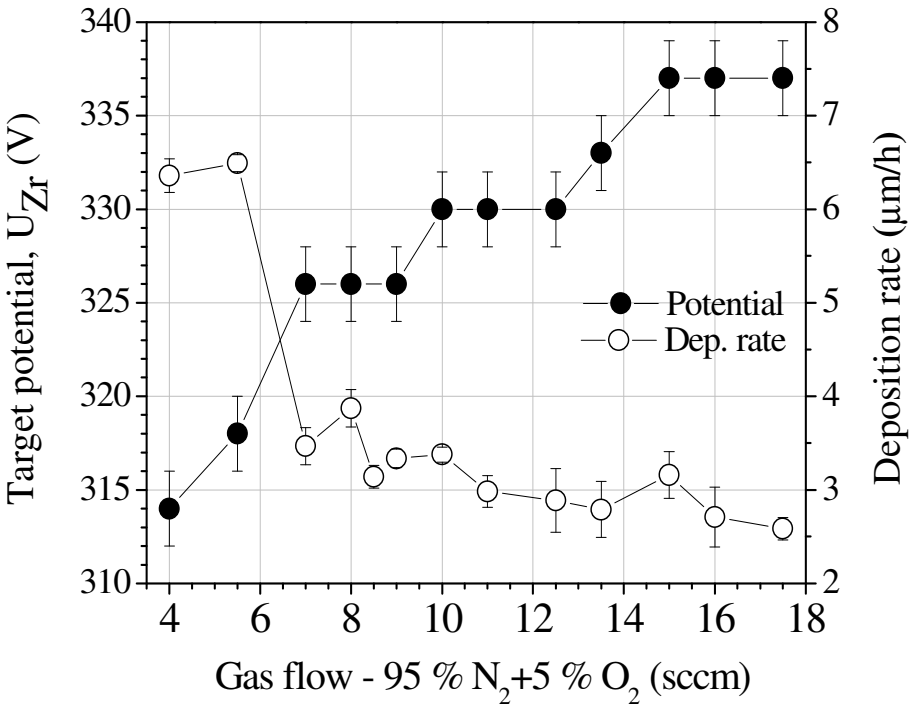
The films prepared with reactive gas flows of 8 sccm and higher, show a slow but systematic increase of oxygen (see Fig. 2.18.a)) and thus a smooth increase in the C_O/C_{Zr} atomic ratio. Although the C_N/C_{Zr} is kept approximately constant, the increase in the oxygen content results in a relatively high ratio of non-metallic over metallic elements, $(C_N+C_O)/C_{Zr}$), which increases also smoothly from 1.3 at 8 sccm to 1.5 for the sample prepared at 16 sccm. The almost no variation of nitrogen content (see Fig. 2.18)) and the reactively high over-stoichiometric condition of these films (if one takes into account the values of the ratio $(C_N+C_O)/C_{Zr}$), might be an indication for the possibility to form overstoichiometric compounds, which would then correlate to what has been referred for those zone II samples of series 1. Although not very clear (only two samples are present), there seems to be saturation of samples composition.

Nevertheless, it is important to emphasize that a similar trend also occurred in samples from series 1, where in both zones II and III this constancy in compositions was observed and then "new" increase of oxygen content was observed. That was the cases of samples prepared with 11 and 12 sccm (beginning of zone II) and 15 and 17 sccm and 25 and 30 sccm (from zone III – beginning and end) of that first series. Thus this constancy in this second series, and for the last two samples, should not be faced as definitive, but only as a possible beginning/end of another zone.

In order to extend the analysis of this second series and thus trying to search for a possible division of the samples into different growing zones, the target potential evolution as well as the deposition rates were also scanned. The results as depicted in figure 2.20.

For very low reactive gas flows (< 7 sccm), the sputtering process is clearly in the metallic regime, resulting in higher deposition rates and higher zirconium content. With further increase of the reactive gas mixture flow, the decrease of deposition rate, due to poisoning effect of the target, is also well correlated with the change of the concentration of non-metallic elements, as can be seen in figure 2.18.

Coherently, for these same low reactive gas flow samples, all the available gas is consumed and thus the target potential is roughly constant (U_{Zr} varies from 314 to 318 V), corresponding to the metallic mode regime. With the increase in the reactive gas flow there is an increase of the target potential and the deposition rate shows no significant changes.



Gas flow (sccm)	Thickness (μm)
4	6.4 +/- 0.2
5.5	6.5 +/- 0.1
7	3.5 +/- 0.2
8	3.9 +/- 0.2
8.5	3.1 +/- 0.1
9	3.3 +/- 0.1
10	3.4 +/- 0.1
11	3.0 +/- 0.2
12.5	2.9 +/- 0.3
13.5	2.8 +/- 0.3
15	3.2 +/- 0.3
16	2.7 +/- 0.3
17.5	2.6 +/- 0.1

Fig 2.20. Target potential and deposition rate as a function of the reactive gas mixture flow rate for series 2. The error bar for the deposition rate values was determinate by the maximum deviation to the average value. For the target potential, the error was estimated according to the maximum deviation observed during measurements (~2 V). For the sack of scientific accuracy and for further comparison purposes, the thickness values of the coatings are presented on the right-hand side of the figure.

This increases once more some attempt to clearly distinguish the samples in different zones, although a first group seems to appear for samples prepared with gas flows up to 7 or 8 sccm.

Beyond these differences in composition regions, a last point should also be discussed, concerning a comparison between these first two series of samples. A closer look to both plots of composition ratios (Fig. 2.15 and 2.19) shows an apparent unexpected incoherency. In fact, one should expect that the series deposited with a richer oxygen mixture (series 1) would present higher contents of this element for the same gas flows. By comparing the two series (Fig. 2.19), it is possible to observe that for low values of reactive gas flows, this is not the case. Series 1 (for samples deposited with the lowest reactive gas flow), present always less non-metal to zirconium ratios, C_N/C_{Zr} and C_O/C_{Zr}, in comparison to series 2. The ratio C_O/C_{Zr} for series 1 varies from non detectable to 0.10 (at 9 sccm), while for series 2 it varies from 0.05 (4 sccm) to 0.15 (8 sccm). The C_N/C_{Zr} for series 1 varies from 0.48 (at 6 sccm) to 0.83 (at 9 sccm), while for series 2 it varies from 0.74 (at 4 sccm) to 1.12 (at 8 sccm). Nevertheless the higher concentration of

nitrogen should be expected, since this coatings were deposited with a gas mixture richer in nitrogen (95 % N_2 + 5% O_2), the highest concentration of oxygen regarding to the series 1, it appears to be a contradiction. Comparing the deposition rates of booth series it may be possible to explain this apparent contradiction. Series 1 presents always higher values of deposition rate comparing to series 2. This result from the different erosion state of the target during the deposition of booth series.

A target with a higher sate of erosion induces a decrease of the flux density of sputtered zirconium arriving to the substrate, and hence, in the time scale of the reactions. Thus, the ratio between non-metal and zirconium atoms at the coating is higher. This induces an increase of the metalloid content in the coatings. These results reinforce the idea that the kinetic parameters, for samples deposited with low flows of the reactive gas, play a dominant role. Otherwise the series deposited using a much richer oxygen mixture (series 1) should present a higher amount of oxygen. For higher flows the differences become less visible, as a consequence of the already mentioned decrease of kinetic factors dominance and increasing importance of thermodynamic ones. The decreasing role of the kinetic parameters for the samples from series 2 is also confirmed by the decrease of C_O/C_N ratio with the increase of the reactive gas mixture flow, Fig. 2.21.

Again, the difficulties to measure accurately the low amounts of oxygen in the first samples are contributing for the differences in the obtained ratios. Moreover, and due to the very low amounts of oxygen within the gas mixture, it is somehow expected that for very low flows, the amounts of oxygen in the film can vary slightly from those expected taking into account the kinetic dominant factor. Anyway, one might say that the sample prepared with a reactive gas flow of 8 sccm is, as previously anticipated, in a zone transition. In fact below this gas flow, the samples present very high ratios C_N/C_O, while from this value on, the values tend to decrease significantly, pointing for a change from kinetics to thermodynamic-dominant growing factors.

In summary, it can be claimed as a general conclusion that in spite of the different gas ratios, the prepared samples show different growing regions, which depend strongly on the particular compositions, and manly on the predominance of one of two factors: kinematic and thermodynamic.

Lower oxygen containing gas flows induce much smoother transitions in composition of the samples, which is reflected in the samples surface aspect.

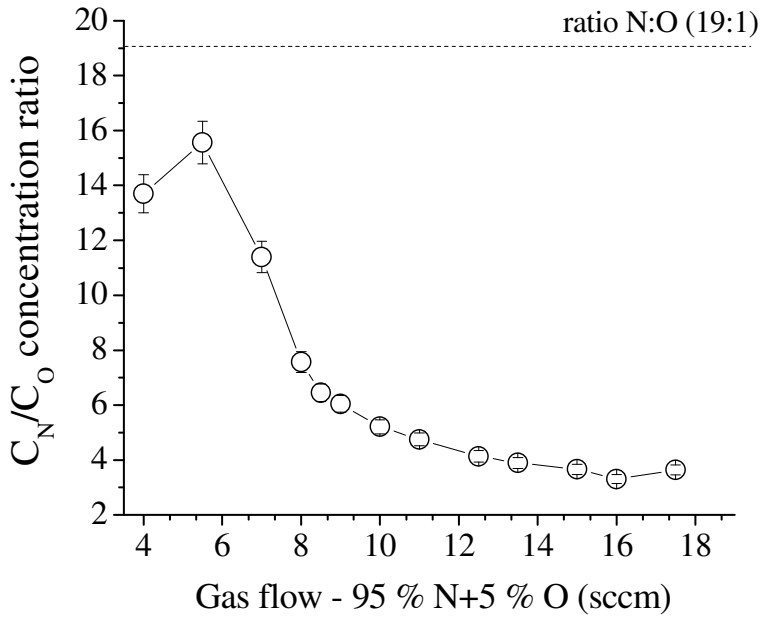


Fig. 2.21. Ration C_O/C_N as a function of the reactive gas mixture flow for the series 2. The uncertainty was determined by error propagation.

In fact, samples from this second series revealed the same colour transitions as referred previously for series 1, but with a clear smoother transition and much wider tones pallet (although keeping the same main colour regions).

2.6.2. The role of the ion bombardment

(Series 3: a series prepared with a bias voltage of – 70 V)

In order to check if the same structural transitions are occurring when the grounded condition (no ionic bombardment during deposition) is replaced by a moderate ion bombardment condition (use of a negative bias voltage), a series of films was deposited with a bias voltage of -70 V applied to the substrates. This series allowed to study whether the energetic ion bombardment was capable to significantly influence the atomic bonds and thus the different structural features previously shown, or if most of these features were maintained. The gas mixture that was used was that of 17:3 nitrogen:oxygen ratio (in fact, the same that was firstly presented in this chapter). The samples prepared under these conditions will be referred as series 3 throughout the text. As before for series 2, the deposition parameters were selected to obtain intrinsic colours and so this series was prepared with gas flow varying only up to 14 sccm.

Figure 2.22. shows the variation of the atomic concentration of the elements as a function of the reactive gas mixture flow.

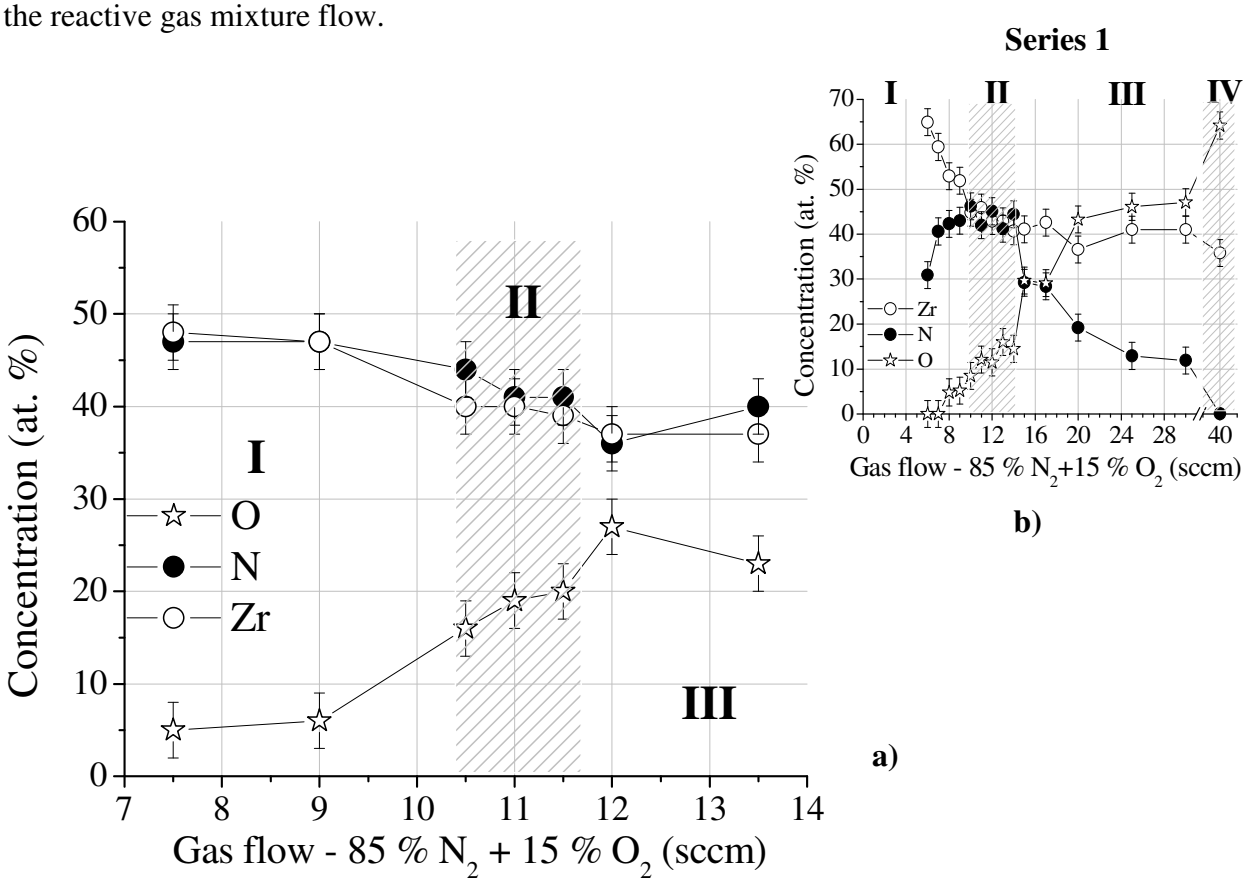


Fig. 2.22.a) Variation of the atomic concentration of the elements and deposition rate as a function of the reactive gas mixture flow (samples prepared with a bias voltage of – 70 V). An average of 5 at. % was estimated for the RBS concentration resolution. **b)** For comparison purposes, the same plot is shown in the upper insert for the samples prepared with the samples in a grounded condition, and for a similar region of gas flows.

The first note that is worth notice is that this figure shows that it is possible to divide again the films into distinct compositional regions (coherently with what has been claimed for the first series within a similar window of gas flows). For reactive gas flows below 10.5 sccm (zone I), composition analysis revealed a small increase of both the oxygen content and the C_N/C_{Zr} ratio (see Fig. 2.23.a)), with a small decrease of zirconium content. In this zone the samples exhibited colour appearances from bright yellow to golden yellow. In the second zone (from 10.5 sccm to 11.5 sccm) there is an abrupt increase of oxygen content, from about 6 at % for the sample

deposited with a gas flow of 10.5 sccm to ~16 at % for the sample deposited with a gas flow of 11.5 sccm.

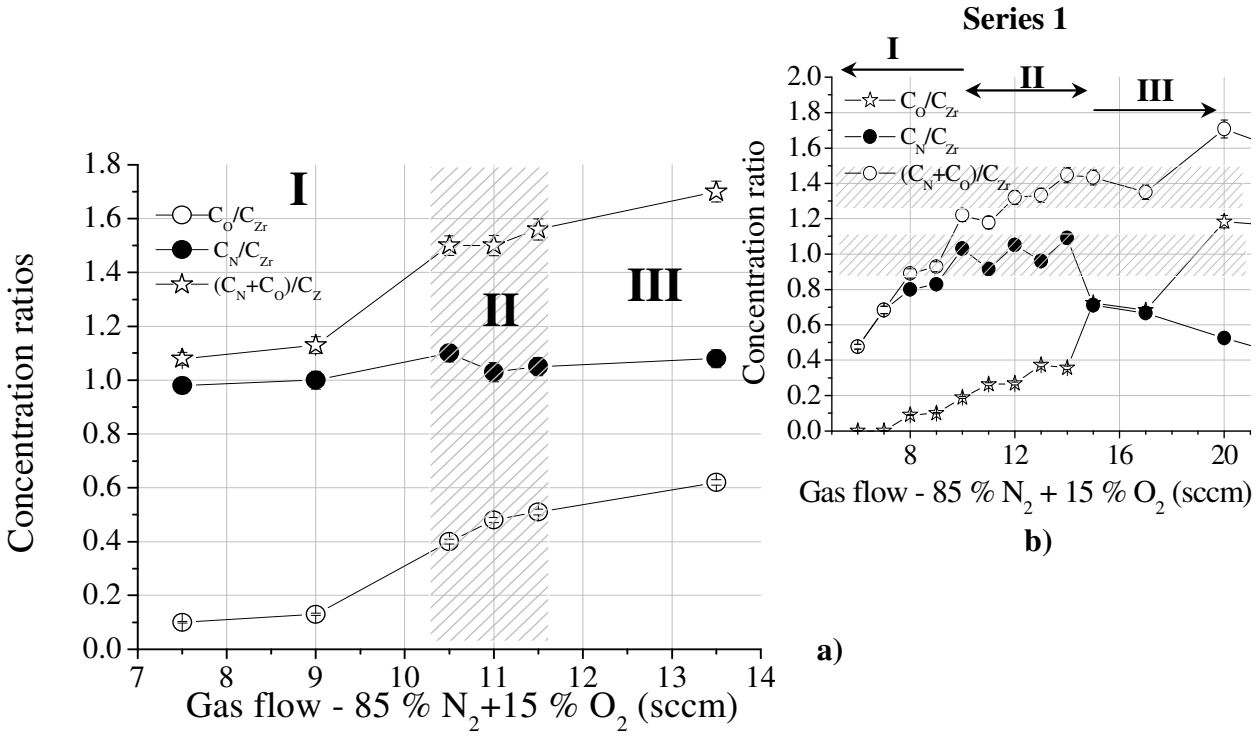


Fig. 2.23.a) Variation of the atomic ratios, C_O/C_{Zr}, C_N/C_{Zr} and $(C_N+C_O)/C_{Zr}$ as a function of the reactive gas mixture flow for samples prepared with a bias voltage of – 70 V - series 3. The uncertainty was determined by error propagation. **b)** For comparison purposes, the same plot is shown in the upper insert for the samples prepared with the 85 % N_2+15 % O_2 (see Fig. 2.14) – series 1, and for a similar region of gas flows.

This increase is associated with a decrease of nitrogen content from about 44 at % (sample prepared with a gas flow of 10.5 sccm), to 41 at % for the sample deposited with a gas flow of 11.5 sccm. In this zone, the film colour changes to red-brownish for the sample deposited with 10.5 sccm, and dark blue at higher flow rates (11.5 sccm).With further increase of the reactive gas flow (zone III), where the sample prepared with a gas flow of 13.5 sccm presents a less pronounced dark blue, there is another increase of oxygen content ratio, C_O/C_{Zr}, keeping approximately constant the C_N/C_{Zr} ratio, Fig. 2.23.a). Related again with figure 2.22.a), and beyond the already mentioned similarities, there are still non negligible changes that should be referred. The first one to be noticed is the apparent shift in the limits of the different zones, which is particularly noticeable in the limit of zone II that seems to be shifted to lower gas flows, when compared to series 1.

Anyway, and much more important than the gas flow itself, are the changes in the concentration ratios, Fig. 2.23.a). This figure shows that this third series presents higher values of metalloid content when compared with the grounded series, and, for similar compositional zones. Particularly noticeable is the increase of the C_O/C_{Zr} atomic ratio at higher gas flows. This series presents an atomic ratio C_O/C_{Zr} varying from 0.4 (sample prepared with 10.5 sccm) to around 0.6 (sample deposited with 13.5 sccm), whilst series 1 presented values of this ratio varying from around 0.18 (10 sccm) to less than 0.4 (14 sccm). For series 3, the C_N/C_{Zr} ratio is approximately constant ~ 1.1, which is about the same observed for series 1. The higher amount of oxygen in this third series, where ion bombardment was used, appears to be a contradiction, since oxygen is expected to reveal preferential resputtering when compared to nitrogen [19], caused by the lower bond strength of the Zr-O with respect to that of Zr-N [38]. One possible explanation for this behaviour could be related with the fact that the samples of this series (series 3) where prepared in rotation mode (7 rpm), and static in the case of series 1. During the "shadow zone", i.e., when the substrates are not completely parallel to the target, there is a decrease of the rate of zirconium atoms arriving to the already deposited coating, inducing higher non-metal content in the coatings. This effect is particularly sensitive to oxygen due to the high chemical affinity of oxygen with zirconium regarding the nitrogen [32]. This fact associated to the decrease of deposition rate for the samples deposited with highest reactive gas flow (Fig. 2.25), may be responsible for the higher content of oxygen in the coatings for this series. Regarding the deposition condition; the rotation mode, explain also the very low values for the deposition rate of this series, that varies from around 2.2 to 0.9 μm/h. Another factor that could play an important role in the deposition rate and in films composition is the state of erosion of the target, it must remembered that the samples of the first series were made with a new target, and so present high deposition rate and for correspondent reactive gas flows a lower metalloid content.

Figure 2.24 presents the values of the ratio C_O/C_N as a function of the reactive gas mixture flow for series 3. Similarly to the other series, when going from the first zone to the second one, there is a substantial decrease of the C_N/C_O ratio, revealing values much lower than those of the "kinetic limit" of 5.67, reinforcing the idea that kinetic parameters are playing a less important role.

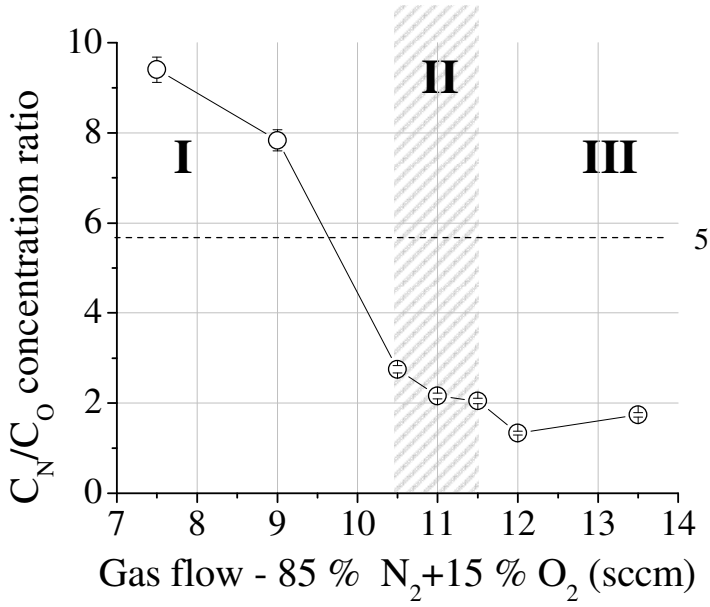
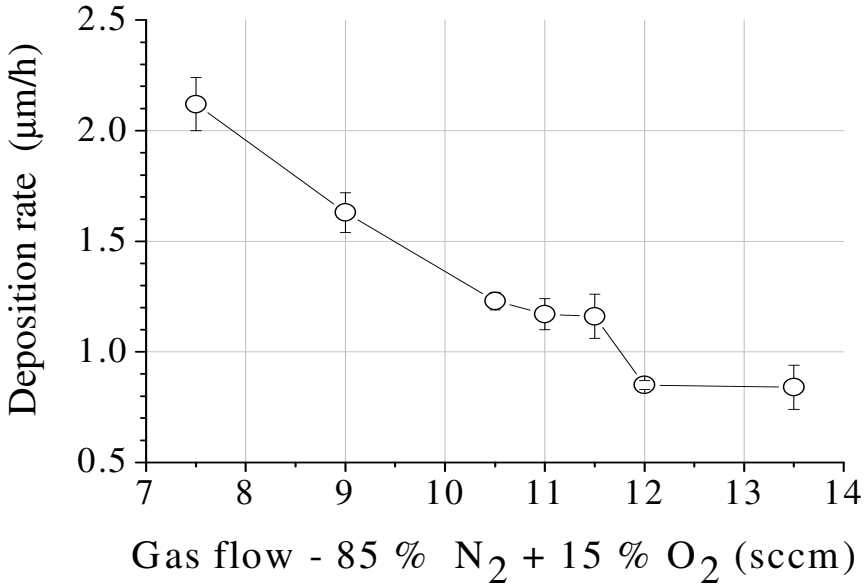


Fig. 2.24. C_O/C_N atomic ratio as a function of the reactive gas mixture flow for samples from series 3. The uncertainty was determined by error propagation.

The existence of a C_N/C_O ratio higher than 5.67 for the firth two samples, should be again explain by the resolution limits of the RBS technique.

Finally, the variation of the deposition rate, figure 2.25., shows that the continuous increase of the target poisoning is again inducing a decrease of this characteristic of the films.



Gas flow (sccm)	Thickness (μm)
7.5	2.1 +/- 0.1
9	1.6 +/- 0.1
10.5	1.2 +/- 0.05
11	1.2 +/- 0.05
11.5	1.2 +/- 0.1
12	0.9 +/- 0.1
13.5	0.9 +/- 0.1

Fig. 2.25. Variation of the deposition rate as a function of the reactive gas mixture flow for samples from series 3. . The error was determined by the maximum deviation to the average value. For the sack of scientific accuracy and for further comparison purposes, the thickness values of the coatings are presented on the right-hand side of the figure.

2.6.2. The role of the gas injection mode

(Series 4: a series prepared with pulsed injection of oxygen – RGPP ("*R*eactive *G*as *P*ulsing *P*rocess"))

In order to deeply analyze this oxygen influence issue, another series was also prepared in which this element was introduced separately from nitrogen, but in a pulsed manner (Reactive Gas Pulsing Process – RGPP) for deeper analysis of this gas feed system see [39-41]. This last series allowed to establish some conclusions about main influences of oxygen, and mainly if the target poisoning has a major effect on film's bonding and structural features, or if it is mainly the oxygen content (and others of course) that rules most of the different behaviours. The pulsed introduction of oxygen is carried out in order to maintain its constant consumption, avoiding undesirable drawbacks such as those of target poisoning and consequently a wider range of composition and thus colours pallet.

In order to compare the RGGP series (series 4) with the other gas mixture series, it must be remembered that this series was prepared using a constant nitrogen flow of 10 sccm and an oxygen flow corresponding roughly to a variation of this parameter varying roughly from ~0.5 to 2.5 sccm. Figure 2.26.a) presents the atomic concentrations of the films as a function of the duty cycle (T_{on}/T). The first observation that can be drawn is that this series presents a different but expected variation tendency.

The first observation to be notice is the very smooth composition evolution with increasing of the duty cycle (T_{on}/T), showing an almost constant increase of the oxygen content associated to a decrease of nitrogen and zirconium content. Similar to series 3, there is no metallic region (i.e. a metal rich coating) since these coatings were made with sufficient nitrogen flow to deposit close stoichiometric zirconium nitride coatings. On this basis, these films present no initial increase of all elements like in zone I in the series 1 and 2. With a closer look to figure 2.26.a) it is possible to observe that for duty cycles lower than 0.5, there is an increase of oxygen content from ~7 ($T_{on}/T = 0.17$) to ~14 at. % ($T_{on}/T = 0.5$). Associated to this increase, there is a decrease of zirconium and nitrogen content from ~47 to 44 at. % and 46 to 42 at. %, respectively.

Regarding the films deposited with duty cycles varying from 0.5 to 0.67, there is a roughly stabilization of all elements contents. With further increase of the duty cycle ($T_{on}/T = 0.83$) there is an increase of the oxygen content from ~15 ($T_{on}/T = 0.67$) to ~19 at. % ($T_{on}/T = 0.83$)

associated to a decrease of nitrogen content from ~41 ($T_{on}/T = 0.67$) to ~37 at. % ($T_{on}/T = 0.83$), without any substantial changes in zirconium content.

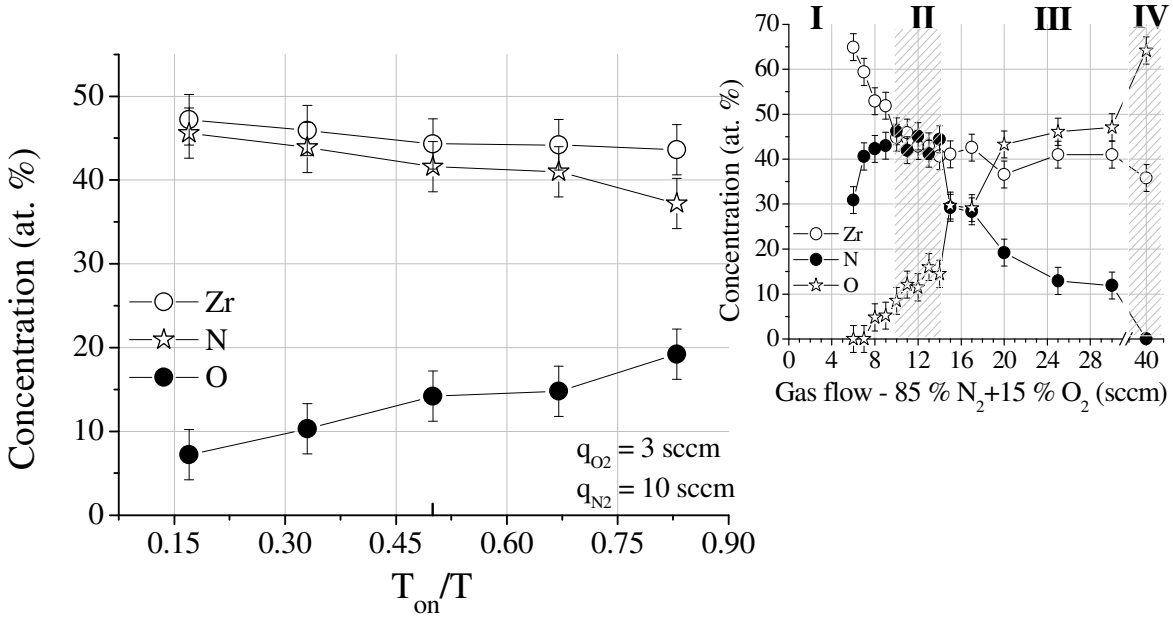


Fig. 2.26.a) Variation of atomic concentrations as a function of the duty cycle - series 4. An average of 5 at. % was estimated for the RBS concentration resolution. **b)** For comparison purposes, the same plot is shown in the upper insert for the samples prepared with the 85 % N_2 + 15 % O_2 – series 1 (see Fig. 2.14).

Regarding the surface colour tones, the samples prepared within this zone showed gold yellow colour in a small increase in redness.

Figure 2.27.a) shows the plots of the variation of all atomic ratios as a function of the duty cycle. This plot shows that, similarly to what has been observed in the gas mixture series, one may divide the prepared samples in different groups, but with lees accuracy, since this films present a much smoother compositional evolution. The first zone (zone I), corresponding to the samples deposited with duty cycles lower than 0.5, is characterized by a constant increase of C_O/C_{Zr} and $(C_O+ C_N)/C_{Zr}$ ratios, associated to a very smooth decrease of C_N/C_{Zr} ratio, suggesting a substitution of nitrogen for oxygen, as already refereed for other series.

In the second zone, corresponding to the coatings deposited with duty cycle faring from 0.5 to 0.67, the coatings appears to present an almost constancy of the $(C_O+ C_N)/C_{Zr}$ ratio close to 1.3, showing only a very smooth increase of C_O/C_{Zr} ratio, associated to an also very smooth decrease of C_N/C_{Zr} ratio. The last zone (zone III), corresponding to the film deposited with a duty

cycle of 0.83, there is an increase of C_O/C_{Zr} ratio from 0.33 to 0.44, associated with a decrease of C_N/C_{Zr} ratio from 0.93 to 0.85, with a $(C_O+ C_N) /C_{Zr}$ ratio close to 1.3.

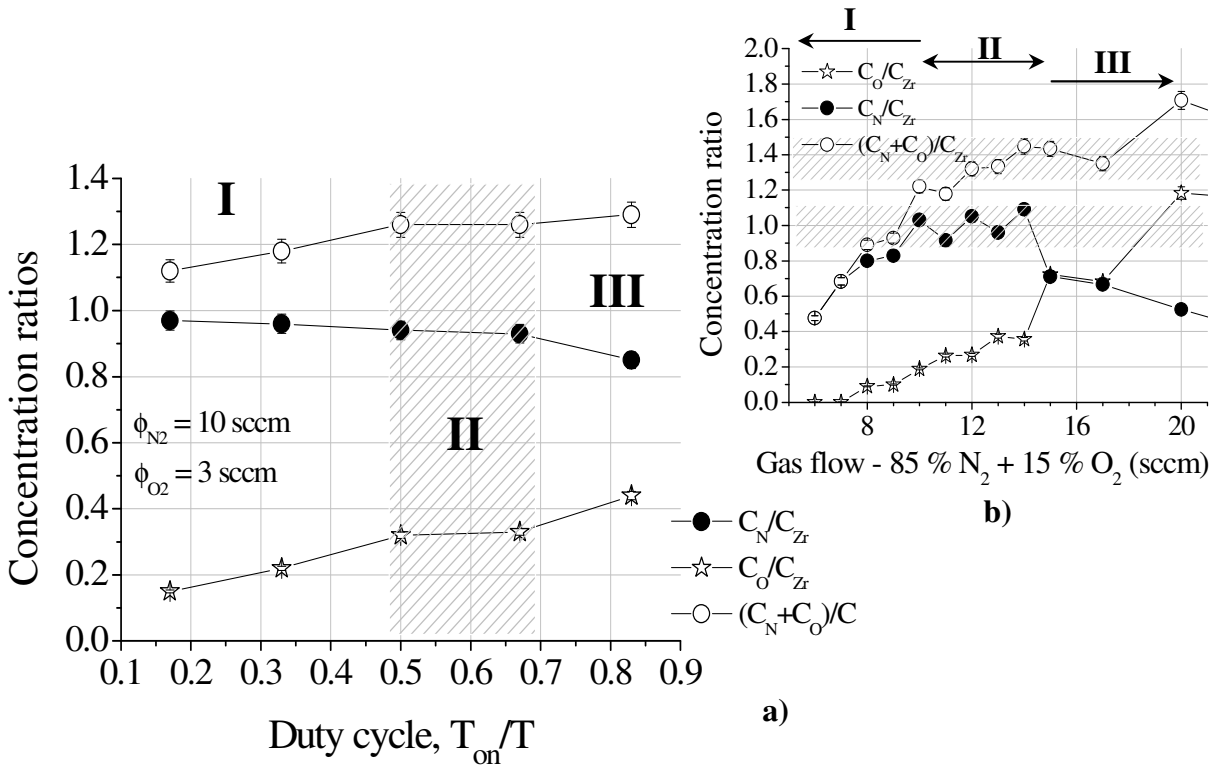
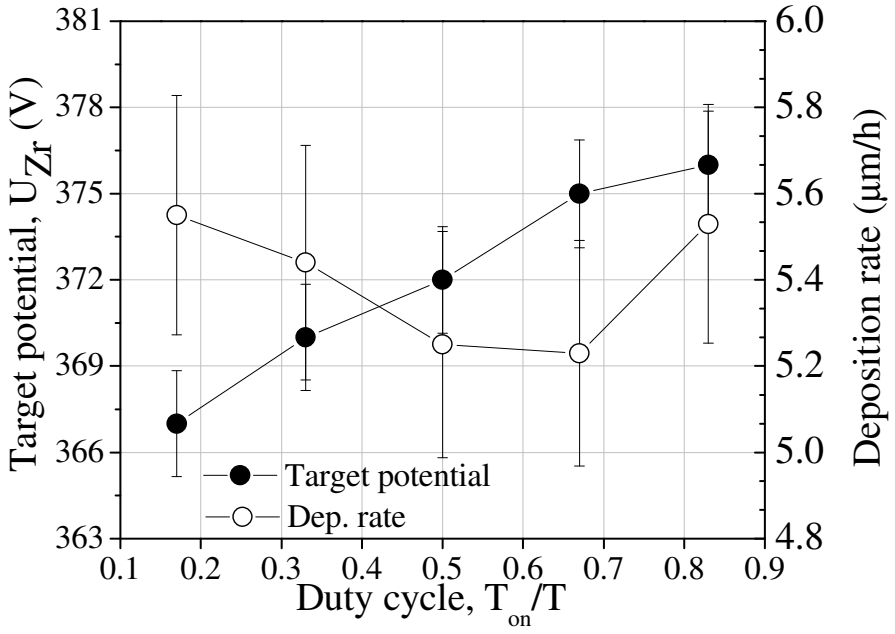


Fig. 2.27.a) Variation non metals over the zirconium atomic ratios, C_O/C_{Zr}, C_N/C_{Zr} and $(C_N+C_O)/C_{Zr}$ as a function of the duty cycle. The uncertainty was determined by error propagation. **b)** For comparison purposes, the same plot is shown in the upper insert for the samples prepared with the 85 % N_2+15 % O_2 (see Fig. 2.14) – series 1, and for a similar region of gas flows.

This compositional evolution opens the possibility of another phase formation, as we will se later on in this thesis. Regarding the surface colour tones, the samples prepared within this zones present a colour change from red-brownish to dark blue.

Figure 2.28. shows the plot of the target potential and deposition rate as a function of the duty cycle. This plot shows a roughly constant deposition rate of ~5.4 μm/h associated to a small increase of target potential from ~ 366 V to 376 V. This lower level of target poisoning of this system should be responsible for the almost constant values of the deposition rate. These two factors together should explain the smoothness of the compositional variation.

Furthermore, this plot shows that it is possible to observe that this series present a lower increase of the target potential (< 10 V) comparing with the series 1, within similar zones (zone I and II).



Duty cycle	Thickness (μm)
0.83	2.8 +/- 0.1
0.67	2.6 +/- 0.1
0.50	1.8 +/- 0.1
0.33	1.8 +/- 0.1
0.17	1.4 +/- 0.1

Fig. 2.28. Target potential and deposition rate as a function of the duty cycle, for the series 4. The error bar for the deposition rate values was determinate by the maximum deviation to the average value. For the target potential, the error was estimated according to the maximum deviation observed during measurements (~2 V). For the sack of scientific accuracy and for further comparison purposes, the thickness values of the coatings are presented on the right-hand side of the figure.

This lower level of target poisoning, which induces a more constant deposition rate, should result from the fact that the pulsing of oxygen allows the system to work in equilibrium between the poisoning rate of the target and the cleaning rate, resulting in a lower level of target poisoning and consequentially highest and more constant deposition rate.

2.7. Conclusions

The previous analysis allows a better understanding of the relationship between the depositions parameters and the compositions of the coatings. The first conclusion that can be draw is that the reactive sputtering deposition method of zirconium oxynitride coatings is a rather complex system. Several deposition parameters/conditions play an important role in the relation

between the kinetic parameters and the thermodynamics ones, that will influence the final composition of the coatings, and consequently in the colours of the films. The main issue about the deposition of zirconium oxynitride coatings for decorative applications is controlling the rate of metallic atoms arriving to the substrate *versus* the thermodynamic affinity of the metalloids with zirconium. On this basis the reactive gas flow and/or oxygen partial pressure play a dominant role in the final composition of the coatings. Analyzing all the deposited series is possible to conclude that the increase of reactive gas flow and/or oxygen partial pressure induces a decrease of the kinetics role and increases the thermodynamics ones, leading to an increase of the oxygen content of the coatings. Nevertheless the dominant role of the gas mixture and/or oxygen partial pressure plays a dominant role in the composition of the coatings it is necessary to clarify the importance of secondary conditions that influence the final composition of the coatings. Comparing the first two series is possible to observe that not only the reactive gas mixture present an important role in the final composition of the films but also the state of erosion of the target. Sputtering an erased target, regarding to a new one, induce a lower rate metal atoms arriving to the substrate and a higher metalloid content of the coatings is observed. Another deposition condition that could play an important role in the composition of the coatings is the use of the "rotation mode". It was observed that rotation of the substrate holder induce a higher concentration of non metal content, specially oxygen, in the coatings. Regarding the RGPP system is possible to conclude that the introduction of pulsed oxygen decrease target poisoning effect and open new opportunities to obtain a wider range of coatings composition

2.8. References

[1]- S. Hofmann, Thin Solid Films 191 (1990) 335.

[2]- G. Lemperière, J. M. Poitevin, Thin Solid Films 111 (1984) 301.

[3]- S. Berg, T. Larsson, C. Nender, H. O. Blom, J. Appl. Phys. 63 (1988) 887.

[4]- X. Chu, S. A. Barnett, M. S. Wong, W. D. Sproul, J. Vac. Sci. Technol. A 14 (1996) 3124.

[5]- L. J. Meng, M. P. Dos Santos, Thin Solid Films 250 (1994) 26.

[6]- A. Billard, C. Frantz, Surf. Coat. Technol. 59 (1993) 41.

[7]- W. D. Westwood, S. Maniv, P. J. Scanlon, J. Appl. Phys. 54 (1983) 6841.

[8]- S. Berg, H. O. Blom, T. Larsson, C. Nender, J. Vac. Sci. Technol. A 5 (1987) 202.

[9]- J. Heller, Thin Solid Films 17 (1973) 163.

[10]- J. Affinito, R.R. Parsons, J. Vac. Sci. Technol. A 2 (1984) 1275.

[11]- F. Shinoki, A. Itoh, J. Appl. Phys. 46 (1975) 3381.

[12]- I. Safi, Surf. Coat. Technol. 127 (2000) 203-219.

[13]- H. Schiller, U. Heisig, G. Beister, K. Steinfelder, J. Strumpfel, C. Korndorfer, W. Sieber, Thin Solid Films 118 (1984) 255.

[14]- A. Kinbara, E. Kusano, S. Baba, J. Vac. Sci. Technol. A 10 (1992) 1483.

[15]- D. K. Hohnke, D. J. Schmatz, M. D. Hurley, Thin Solid Films 118 (1984) 301.

[16]- A. H. Eltoukhy, B. R. Natarajan, J. E. Greene, T. L. Barr, Thin Solid Films 69 (1980) 229.

[17]- T. Abe, T. Yamashina, Thin Solid Films 30 (1975) 19.

[18]- André Anders, Thin Solid Films 502 (2006) 22-28.

[19]- M. Ohring, *The Materials Science of Thin Films*, Academic press Inc., San Diego, 1992.

[20]- A. R. Ramos, A. Paúl, L. Rijniers, M.F. da Silva, J.C. Soares, Nucl. Instr. And Meth. in Phys. Res. B 190 (2002) 95.

[21]- J. R. Bird, J. S. Williams, eds., *Ion Beams for Materials Analysis*. Academic Press, Sydney, 1989.

[22]- A. G. Spencer, R. P. Howson, R. W. Lewin, Thin Solid Films 158 (1988) 141.

[23]- N. Martin, R. Sanjines, J. Takadoum, F. Lévy, Surf. Coat. Technol. 142-144 (2001) 615.

[24]- S. H. Mohamed, O. Kappertz, J. M. Ngaruiya, T. Niemeier, R. Drese, Wakkad, M. Wuttig, Phys. Stat. Sol. (a) 201 (2004) 90.

[25]- J. Adachi, K. Kurosaki, M. Uno, S.Yamanaka, Journal of Alloys and Compounds 432 (2007) 7.

[26]- Byung-Koog Jang, Surf. Coat. Technol. 202 (2008) 1568.

[27]- http://en.wikipedia.org/wiki/Zirconium_nitride (January 2008)

[28]- http://www.webelements.com/webelements/compounds/text/Zr/N1Zr1-25658428.html (January 2008).

[29]- http://www.webelements.com/webelements/compounds/text/Zr/O2Zr1-1314234.html (January 2008).

[30]- http://en.wikipedia.org/wiki/Zirconium_oxide (January 2008).

[31]- D. R. Lide, *Handbook of Chemistry and Physics*, 85th Edition ed. CRC Press: Florida, 2004.

[32]- H. J. Goldschmidt, *Interstitial Alloys*, London: Butterworths, 1967.

[33]- F. Vaz, P. Carvalho, L. Cunha, L. Rebouta, C. Moura, E. Alves, A.R. Ramos, A. Cavaleiro, Ph. Goudeau, J.P. Rivière, Thin Solid Films 469-470 (2004) 1.

[34]- N. P. Barradas, C. Jeynes, R. P. Webb, Appl. Phys. Lett. 71 (1997) 291.

[35]- A. Rizzo, M. A. Signore, L. Mirenghi, D. Dimaio, Thin Solid Films 515 (2006) 1486.

[36]- D. I. Bazhanov, A. A. Knizhnik, A. A. Safonov, A. A. Bagatur'yants, M. W. Stoker, A. A. Korkin, J. Appl. Phys. 97 (2005) 044108.

[37]- P. Carvalho, F. Vaz, L. Rebouta, L. Cunha, C.J. Tavares, C. Moura, E. Alves, A. Cavaleiro, Ph. Goudeau, E. Le Bourhis, J. P. Rivière, J. F. Pierson, O. Banakh, J. Appl. Phys. 98, (2005) 023715

[38]- D. Sherman, D. Brandon, *Handbook of Ceramic Hard Materials*, Wiley-VCH, New Jersey, 2000.

[39]- N. Martin, J. Lintymer, J. Gavoille, J.M. Chappé, F. Sthal, J. Takadoum, F. Vaz, L. Rebouta, Surf. Coat. Technol. 201 (2007) 7720.

[40]- N. Martin, J. Lintymer, J. Gavoille, J.M. Chappé, F. Sthal, J. Takadoum, F. Vaz, L. Rebouta, Surf. Coat. Technol. 201 (2007) 7727.

[41]- N. Martin, J. Lintymer, J. Gavoille, J.M. Chappé, F. Sthal, J. Takadoum, F. Vaz, L. Rebouta, Surf. Coat. Technol. 201 (2007) 7733.

Chapter 3

Structural features

3.1. Introduction

The term structure is used as a commonly accepted concept in materials engineering, although many systems are more or less nanoscaled in nature. Due to the nature and characteristics of PVD processes, the structural properties of thin films are, in general, strongly dependent of the deposition parameters, such as deposition rate, deposition temperature, gas (working and reactive ones) pressures, impurities, ion bombardment etc. Thin films prepared by sputtering (such as those from this thesis) can range, in structural terms, from polycrystalline towards quasi-amorphous, depending on the composition of deposited materials and, above all, on specific preparation conditions such as those mentioned above. In the policrystalline case, the orientation of the grains (with or without texture) may strongly influence the film's behaviour. The phenomenon of texture in thin films prepared by PVD techniques is very frequently observed and, its characterization allows establishing relations not only with the deposition process but also with the properties revealed by the deposited thin films.

Deposition of functional thin films (which may range from protective to decorative, among other types), with a few microns in thickness, is a common technology to improve the performance of tools, dies, or moulds for many different applications [1], but also to improve the surface appearance of several decorative parts or even jewellery objects. In fact, coloured films on high-quality consumer products, such as eyeglass frames, wristwatch casings and wristbands, are becoming more and more attractive, providing to these everyday-life objects both scratch-resistance and protection against corrosion, while enhancing their appearances lending their surfaces attractive colorations. Starting with thermally activated chemical vapour deposition (CVD), different methods have been developed including several variants of plasma-assisted physical vapour deposition techniques (PVD).

The important issue for the future is not which deposition technology is used, but instead which properties can be achieved at which production cost. This is where the need for microstructural design becomes important. Generally, thin films, and in particular the decorative ones, prepared by various deposition techniques and conditions, exhibit a very wide variety of microstructures, resulting from internal variations in terms of grain size, crystallographic orientation, lattice defects, texture, and surface morphology as well as phase composition. The recent review by *Petrov et al.* [2] clearly shows the microstructural evolution during film growth. These thin film materials are generally single or multi-phase polycrystals with a typical crystal

size ranging from a few nanometres (1–50 nm) to several hundreds in, at least, one direction. Thus, they can be layered (micro- or nanostructured in one dimension), or they can consist of a columnar (nanostructured in two dimensions) or equiaxed nanostructure (nanostructured in three dimensions) [3].

Gradients or inhomogeneities over the film thickness are typically present by design or through process determination. In the case of functional coatings, the synthesis is also driven by the industrial demand for low-temperature deposition, especially plasma-assisted methods. Obviously, thermodynamic equilibrium is not obtained during this kind of deposition. It is noteworthy that many of the nitride, oxide, and, carbide coatings produced for the engineering and manufacturing industry, are highly relevant for the microelectronics field. This applies for example to diffusion barriers and contact layers (e.g., TiN, TaN) and gate oxides from transition metals. Developments in all applications will benefit from a closer interaction of the different fields, e.g., for controlling film texture, defect density, and purity.

Nevertheless, the structurally and/or compositionally designed thin films (such as the decorative ones, referred in this work) grown by plasma assisted vapour deposition, are often in a non-equilibrium state [3], e.g., characterized by compressive stresses, small grain sizes in the nanometre range, or metastable phases.

Advanced surface engineering design approaches have led to the development of coating materials with unique property combinations, e.g., surface appearance combined with relatively high hardness and wear/corrosion resistance, or chameleon-like frictional self-adaptation [4]. It should be appreciated that while the number of coating material systems explored is growing rapidly, they share a few basic structural types for conceptual design. As the microstructural complexity grows with number of chemical elements present in which structure, future progress will require knowledge based design concepts of the coatings used. Present research is in a stage of knowledge construction that intends to search for possible understanding of thin film structural evolution and thus materials development.

3.2. Characterization Techniques - X-ray diffraction (XRD)

X-rays are electromagnetic radiation of wavelength in the range of 0.1 to 100 Å, and result from the collision of fast electrons with a metallic target. Often, X-rays are also called *Röntgen radiation* since they were discovered by the German physicist Wilhelm Conrad Röntgen, in 1895. Since X-rays have wavelengths in the same order of magnitude of the interatomic distances within materials structures, it is a powerful non-destructive technique to study the crystalline structure solids, including lattice constants and geometry, identification of unknown materials, orientation of single crystals, and preferred orientation of polycrystals, defects, stresses, etc.

Braggs's Law

Diffraction occurs when monochromatic X-rays interact with a regular structure, whose repeat distance is about the same as the wavelength of the first ones.

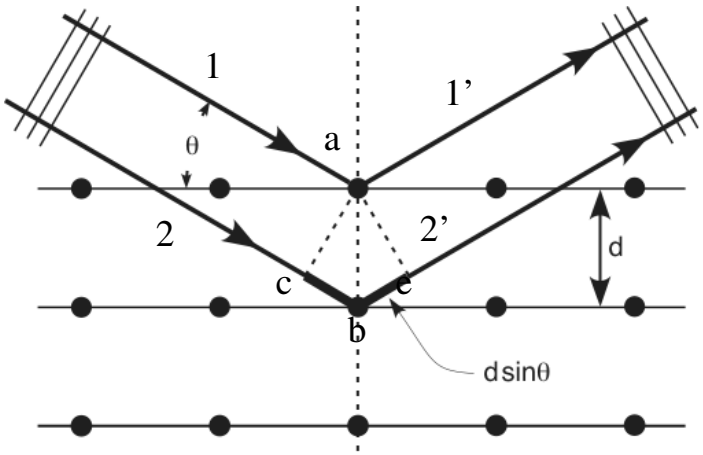


Fig. 3.1. Bragg's diffraction condition for a reflection of x-rays in two planes of atoms in a solid.

For constructive interference between two waves, a certain geometric configuration is needed. X-rays 1 and 2 are reflected by the atoms *a* and *b* (Fig. 3.1) and the path difference between them will be:

$$cb + be = 2\,d\sin\theta \qquad \text{(Eq. 3.1)}$$

For constructive interference between these waves, the path difference must be an integral number of the wavelength, leading to the Bragg equation:

$n\lambda = 2d\sin\theta$ (Eq. 3.2)

n is an integer that represents the diffraction order, λ is the wavelength of the radiation (in our case it was used a Cu anode and the wavelength of the two components is 1.54056 Å for Cu $K_{\alpha 1}$ and 1.544390 Å for Cu $K_{\alpha 2}$), *d* is the interatomic spacing and θ is the diffraction angle.

The use of X-ray diffraction methods to study thin films has some drawbacks. The high penetrating power of X-rays results that with typical incident angles, their path length through films is too small to produce diffracted patterns with sufficient intensity and, rather than the film, the scattered X-ray signal of the substrate, sometimes, dominates. This could be avoid selecting appropriated substrates, were the diffraction patterns of the substrate could be clearly identified and separated from the diffraction patterns of the thin film. In the case of this work, monocrystalline silicon (100) was used as the substrate material due to its clearly distinct diffraction peaks.

Different experimental X-ray diffraction methods were used to analyze the samples produced in this work:

Bragg-Brentano geometry

In Bragg-Brentano or θ/2θ geometry, for etch value of the incident angle θ (angle between the X-ray beam and the sample surface) the detector is synchronised in the 2θ angle position, and the intensity of the diffracted X-ray beam is registered. This geometry is illustrated in figure 3.2.

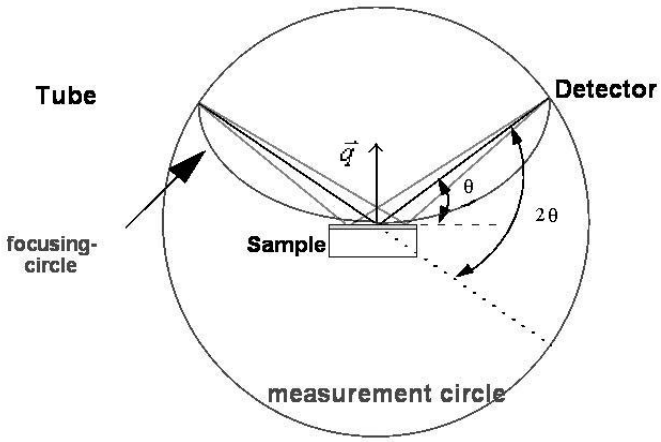


Fig. 3.2. Schematic representation of the *Bragg-Brentano geometry*

With this type of geometry only the crystallographic plans that are parallel to the surface will be in Bragg condition.

Glancing Incidence X-ray Diffraction (GIXD)

With this type of geometry, parallel, monochromatic X-ray beams fall on the sample surface at a fixed angle of incidence ω (see Fig .3.3.) and the diffraction profile is recorded by detector scan only.

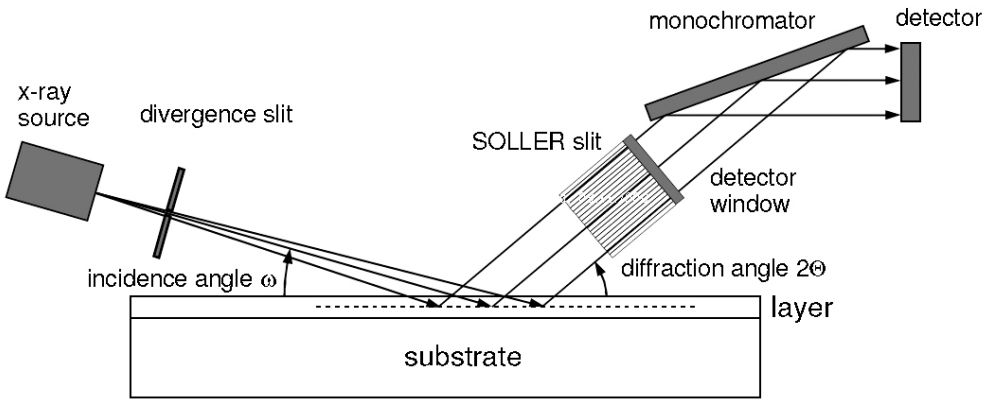


Fig. 3.3. Schematic diagram of grazing incidence X-ray diffractometry (GIXRD), 2θ Bragg angle, ω angle of incidence.

The major advantage of this technique is that allows observing diffraction patterns of crystallographic plans that are not parallel to the sample surface. This becomes a very useful technique to be used when poorly crystallized phases are present and to study the material's texture phenomena, as well.

Results and discussion

3.3. Structure analysis of prepared films

In order to follow the influence of the chemical composition in the structural features of the films, a detailed structural characterization was carried out in all prepared films.

3.3.1. Series 1 (85 % N_2 + 15 % O_2 gas mixture)

Following the previous characterization described on chapter 2, where four different composition zones were observed, the first structural inspection done was to confirm if those composition differences corresponded to different structural arrangements. Figure 3.4 shows the X-ray diffraction patterns for some samples prepared within series 1, corresponding to the four different composition zones.

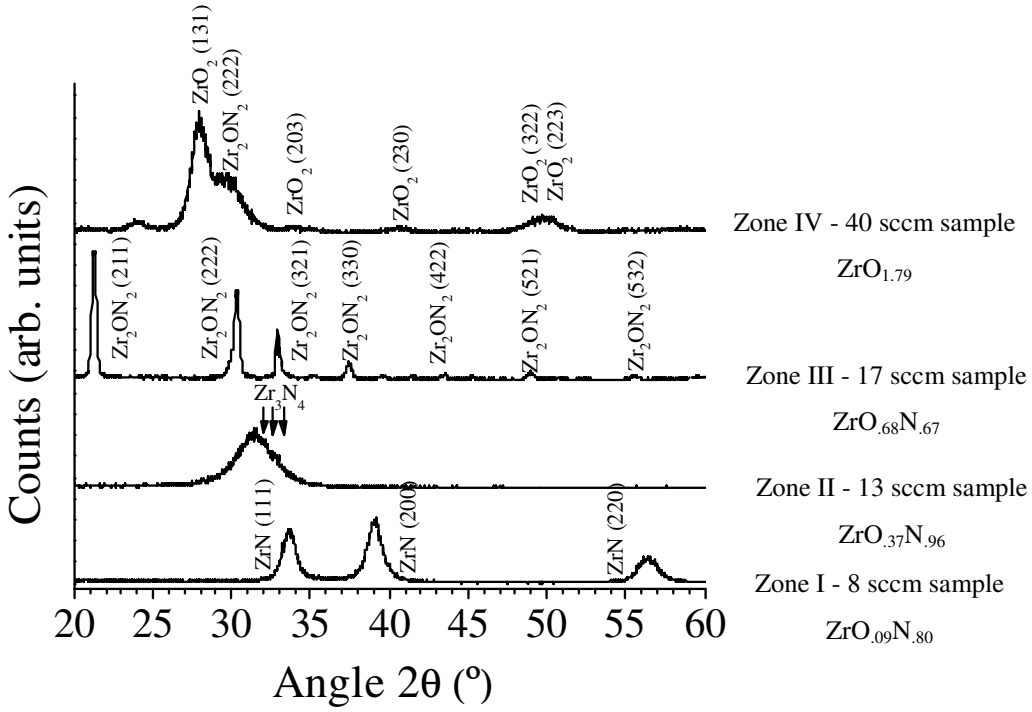


Fig. 3.4. XRD patterns for samples from the four different zones of series 1.

This figure shows that in fact the changes in composition induced by the variation of the deposition parameters (the mixed gas flow rate in this first series of samples), result in different structural arrangements of the films, and thus with a major importance for all the properties that will be studied in this work. A detailed analysis of all samples within each of the different zones was thus carried out.

For films within composition zone I, which revealed composition ratios, C_N/C_{Zr} up to ~0.8 and $(C_N+C_O)/C_{Zr}$ ~ 0.9, the XRD patterns (Fig. 3.5.) revealed that the films crystallize in a B1-NaCl-type crystal structure, typical of ZrN films [5,6], with a progressive change on the preferential growth from (111) to (200) with increasing reactive gas flow.

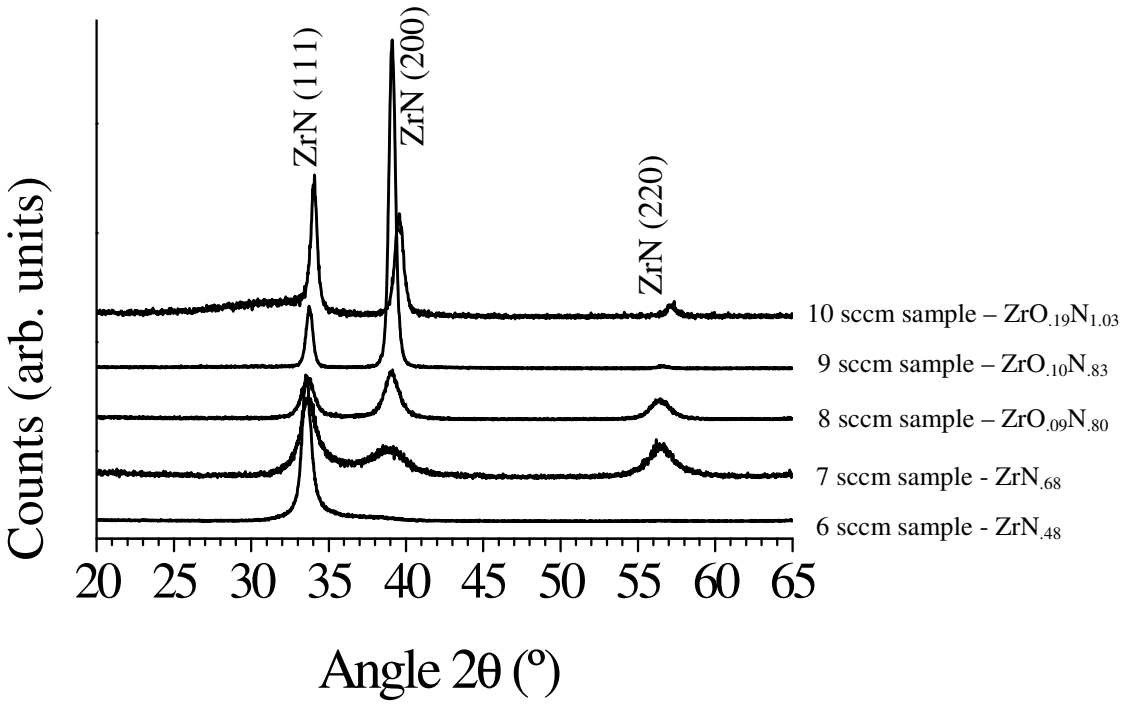


Fig. 3.5. XRD patterns for ZrO_xN_y films laying in the composition zone I.

The peaks intensity ratio ($I_{200}/(I_{200}+I_{111}+I_{220})$) is plotted in figure 3.6., where is possible to observe that this ratio increases from ~0 for the sample prepared at 6 sccm to ~0.5 at 8 sccm and about 0.9 at 9 sccm. This texture change has long been the subject of extensive research. For the growth of transition metal nitrides by reactive sputter deposition, the interplay and competition among several interrelated surface reaction and diffusion processes determine film growth kinetics, surface morphology, film microstructure and texture [2]. It has been shown that kinetic parameters such as the ion-to-metal flux ratio play a decisive role for its variation [7,8]. In the case of absence of ion bombardment, such as the case of this series, results suggest that the preferred orientation is determined by the overall lowest energy plane, which comes from a critical competition between the residual strain and surface energy [9]. In the *fcc* structure (200) plane has the lowest surface energy while the (111) plane has the lowest strain energy [9].

In general, all the DC sputtered ZrN_y thin films deposited under these conditions show strong <111> preferred orientations compared to ZrN powders, where the (200) intensity is the highest as the N/Zr ratio approaches to stoichiometry. In the literature, the (200) preferential orientation is also associated to high nitrogen partial pressures [10].

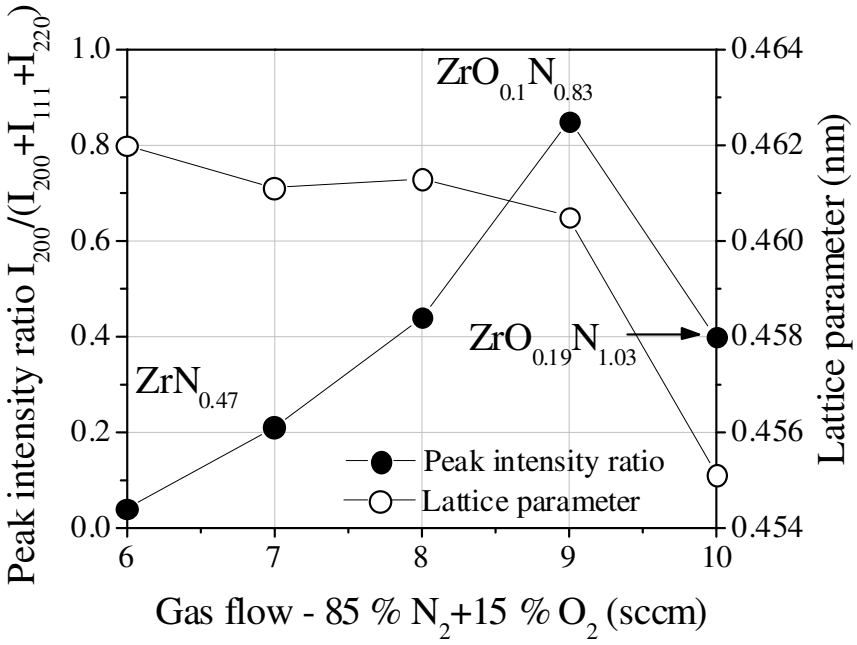


Fig. 3.6. Variation of the peak intensity ratio and lattice parameter as a function of the reactive gas flow, for the films laying in zone I - series 1.

Although (200) planes represent the most stable planes resulting from the minimum surface energy, the film growth by DC sputtering is highly dynamically controlled, so that (111) planes, with faster growth rate, dominate [11]. This is the case of this work for the films prepared with low gas flows [12]. One possible explanation of the orientation change from <111> to <200> orientation within zone I is that the continuous approach of composition towards stoichiometric condition ($(C_N+C_O)/C_{Zr}$ tending to one) brings the system closer to its thermodynamically stable condition, and thus favouring the (200) growth.

Mahieu et al. [13] stated that the change from <111> to <200> orientation can also be the result of distinct growth modes, such as the microstructure changes according to Thornton's zone model [14]. In fact, the increase in flow rate, and the consequent changes in the deposition rate, are inducing these different morphological growth features and textures.

This <200> orientation reveals a significant decrease for the sample prepared with the highest gas flow (10 sccm), where the (111) peak is already the most intense one. This "sudden" change might be a direct result of the excess of atomic species (N and/or O) to form the NaCl-type ZrN(O)structure (let us remind that this sample as a composition of the type $ZrO_{0.19}N_{1.03}$).

The growth rate of grains with (200) orientation is then inhibited further due to the lattice distortion or interstitial site occupancy by the excess nitrogen and/or oxygen atoms. In fact, for a

fcc NaCl structure, growth of (200) orientation needs more coalescent energy than <111> orientation [15] and therefore, for films prepared with the highest flows and developing this *fcc*-type structure (zone I), crystallization becomes difficult and the (200) orientation tends to disappear from the X-ray pattern. This is also the case observed in a series of ZrN_y films prepared with increasing nitrogen gas flows, see figure 3.7.

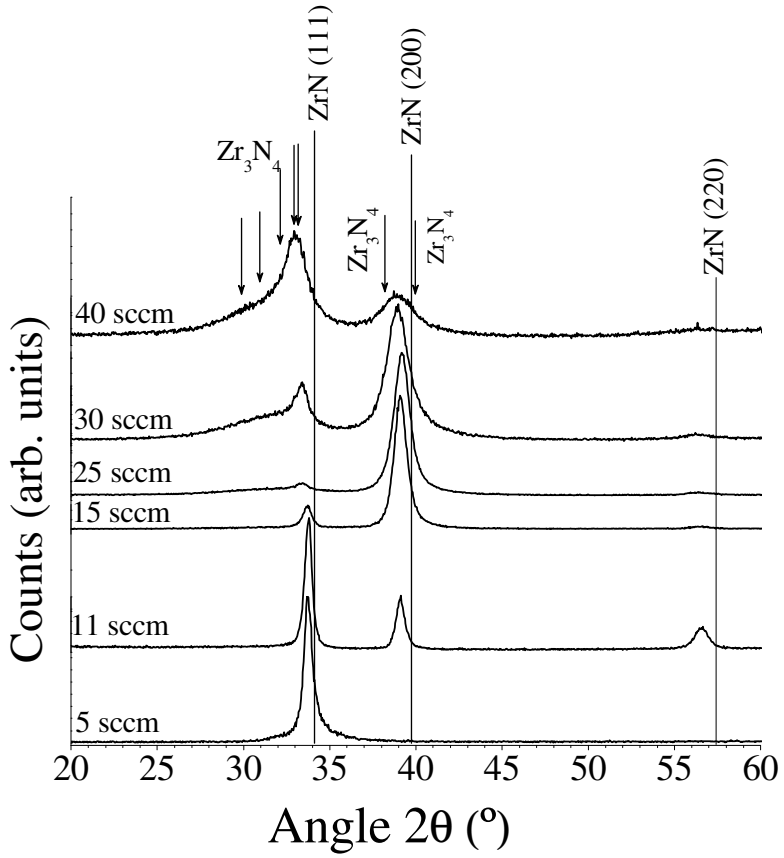


Fig. 3.7. XRD patterns for ZrN_y films for different values of nitrogen flow.

First, and revealing the same preferential growth change tendency, the ZrN_y films show a <111> preferential growth, which then changes to <200>. For very high nitrogen flows (40 sccm sample), the <200> preferential growth decreases and changes to <111> texture. Similarly as stated before, the growth rate of (200) grains is inhibited due to the lattice distortion or interstitial site occupancy by the excess of nitrogen atoms. Nevertheless, the binary ZrN_y system presents a similar texture evolution when compared with the ternary ZrO_xN_y system, although the reactive gas flows values, for which the texture changes occur, are quite different. Regarding the

oxynitride system (series 1) at 9 sccm of the gas mixture flow (Fig. 3.5) the (200) is already dominant areas in the binary system ZrN_x at 11sccm of nitrogen flow the dominant family of planes still are the (111) crystalline plan (Fig. 3.7).

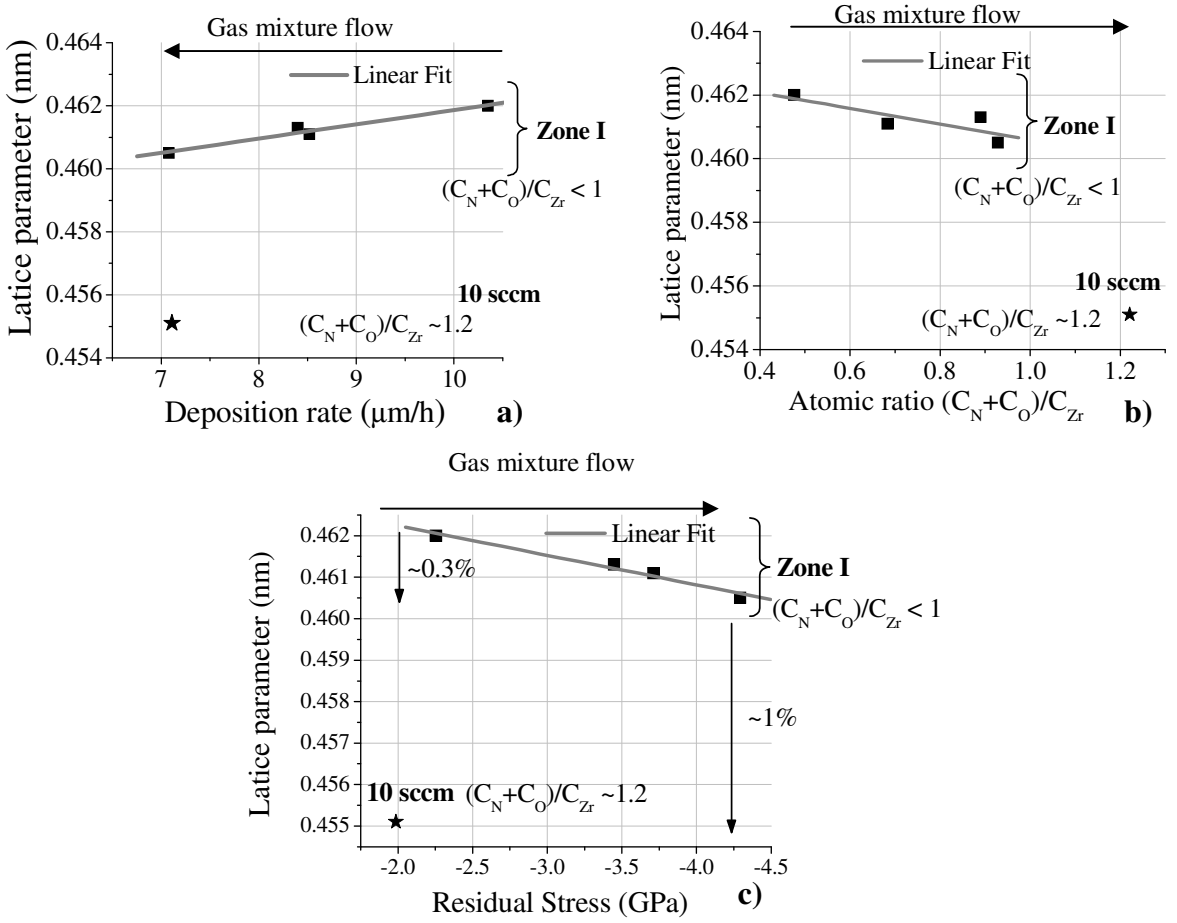


Fig. 3.8. a) Lattice parameter versus deposition rate; **b)** lattice parameter versus non- metal to zirconium atomic ratio for ZrO_xN_y films and **c)** lattice parameter versus compressive residual stress.

The increase of the $(I_{200}/(I_{200}+I_{111}+I_{220}))$ intensity ratio for the zirconium oxynitride samples from series 1 – zone I, is also associated to a decrease of around 0.3 % of the lattice parameter. Figure 3.8. shows plots of this lattice parameter variation as a function of deposition rate (Fig. 3.8a)), atomic ratios (Fig. 3.8b)) and residual stresses (Fig. 3.8.c)) – for details on stresses analysis, please see chapter 7). The graphs show that the samples of zone I have a slight decrease in the lattice parameter as a function of the increase in both the atomic ratio and residual stresses, and a increase with the increase of the deposition rate. Regarding the evolution

with the residual stresses, it should be expected that their increase should lead to an increase of lattice parameter due to the "*atomic peening*" mechanism. This mechanism results from the bombardment of the growing film by atoms or ions at low temperature deposition, $T_s/T_m < 0.25$, (T_m: melting point; T_s: substrate deposition temperature) resulting in a volumetric distortion of the lattice [16]. Since in the plane of the thin film the expansion is not possible, due to the link between the film and the substrate [17], this causes an expansion only in the perpendicular direction of the surface of the substrate, leading to a lattice parameter increase [18]. This is not the case of these oxynitride films, which means that the decrease of lattice parameter should not result from the residual stress.

These coatings show a decrease of the deposition rate and an increase of the metalloid content until, a metalloid to zirconium ratio close to one, with the increase of the reactive gas flow. It is expected that the decrease of the deposition rate and the approximation to the stoichiometric conditions should lead to a better arrangement of the adatoms decreasing the lattice disorder, and decreasing the lattice parameter.

Nevertheless, this figure shows also that a major change occurred in the sample prepared with a gas flow ratio of 10 sccm, as in fact observed already in the composition variation (Fig. 2.15, chapter 2). This sample (deposited with 10 sccm of the reactive gas flow) present a significant decrease of the lattice parameter (~1 %) regarding the samples lying in the first compositional zone (6 sccm< gas mixture flow < 9 sccm). This reveals that this sample is already in a transition zone as in fact observed in the composition plots from chapter 2. This significant decrease of the lattice parameter should result from two factors: the decrease of the compressive residual stress (Fig 3.8.c)) and/or the increase of zirconium vacancies in the increase of the metalloid contend (Fig. 3.8.c)). *F. Lévy et al*. reported a decrease of the lattice parameter in nearly all of the overstoichiometric titanium nitride thin films [19], and the evolution of the optical properties suggested that the defects are both Ti vacancies and N interstitials [20,21].

Regarding the X-ray diffractograms for films prepared with reactive gas flows between 10 and 14 sccm – zone II (Fig. 3.9), the results suggest the development of a crystalline structure that does not match with that of fcc ZrN, revealing a smooth transition from *fcc*-NaCl type structure of zone I towards a new one.

The reduced number of diffraction peaks with a significant broadening cannot allow a fully accurate indexing of this structure. The broadening of the peak at $2\theta \approx 32.2°$, which would

correspond to the (320) plane of the oxygen doped *orth*-Zr_3N_4 structure, could result from the small grain size and/or some reduction of the crystalline volume fraction of the coating, or even to a superposition of several peaks predicted in this region for this structure.

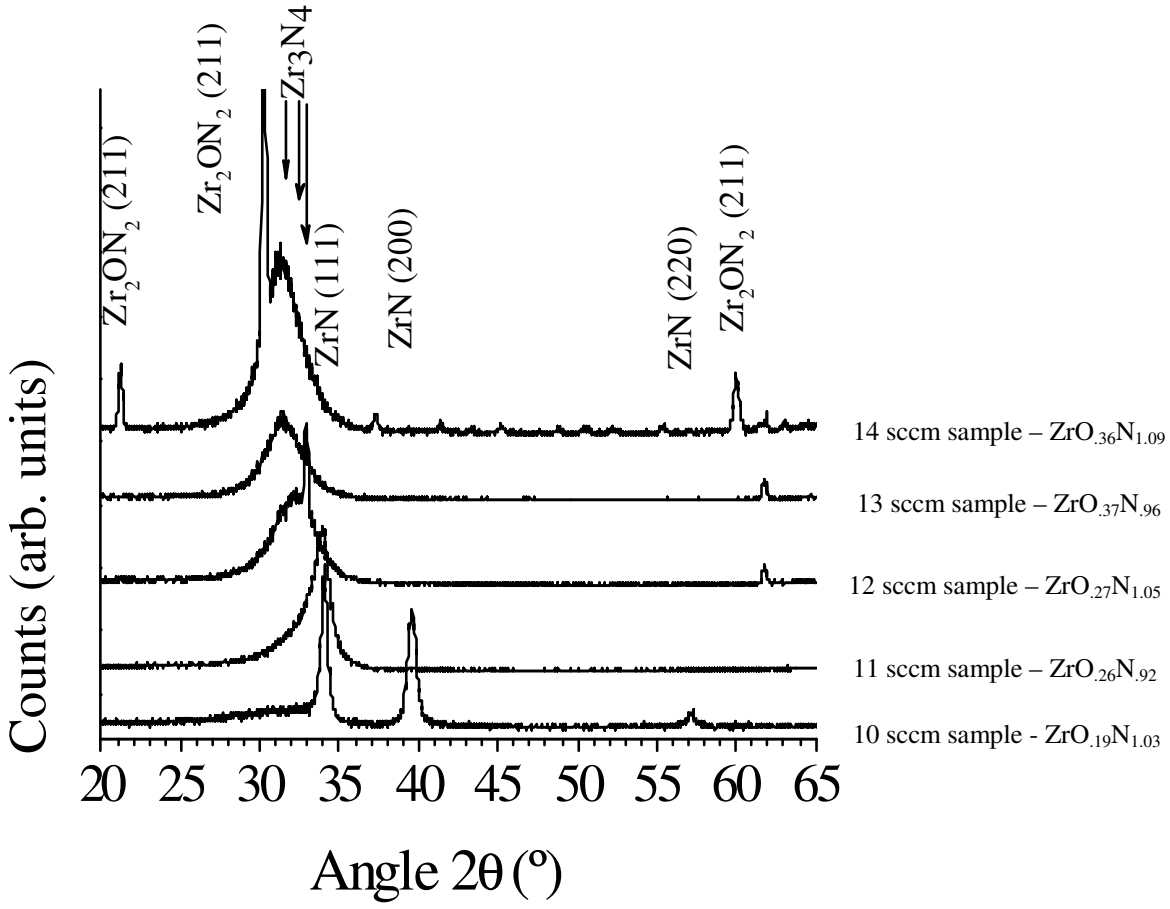


Fig. 3.9. XRD patterns for ZrO_xN_y films laying in composition zone II.

The possibility of having a mixture of both *fcc*-ZrN(O) and a different type of structure (*orth*-Zr_3N_4) must be assumed, specially for the firth two samples in this zone, as suggested by the large tail observed in the diffraction peak between 30 and 33º. Moreover, for the sample prepared with the highest flow within this zone (14 sccm), the indexing of the peak located at $2\theta \approx 32.2º$ to a (111) peak of a ZrN-type structure is very unlikely, since its shift relatively to the ICDD standard position is too large (about 2º).

Similarly, the results obtained for the ZrN_y system (Fig. 3.7), show that not only the preferential growth change behaviour is the same, but also the shape of the diffraction peaks at the highest nitrogen flows (30 and 40 sccm) are similar to those of zone II. *Lévy* and co-authors

[22] have noticed similar behaviour on magnetron sputtered ZrN_y thin films, claiming that for $y > 1.27$ the XRD diffraction patterns suggest the development of a particular structural arrangement consisting on a mixture of defect-rich *fcc*-ZrN and poorly crystallized *orth*-Zr_3N_4. Nevertheless, it is important to notice the differences in the gas flows that are needed to trigger these structural changes, which are significantly higher for the ZrN_y system (it seems to start only at 30 and 40 sccm, in comparison to 10 for the ZrO_xN_y system (see Fig. 3.5 and 3.7). It is thus clear that oxygen is playing a fundamental role on this behaviour, indicating that this "early" phase change in the ZrO_xN_y system could be the result of some kind of "catalytic" effect of oxygen atoms incorporated in the nitride lattice. This oxygen doping, which is also facilitated by the low mobility of impinging species ate the growing film – low temperature and unbiased conditions, would then lead to the formation of an oxygen doped zirconium nitride phase (also with possible nitrogen interstitials), resulting in a structure close to that of *orth*-Zr_3N_4 [23], as claimed by other authors in the ZrN_y system. The diffraction peak at $2\theta \approx 32.2^{\circ}$ would then correspond to the (320) plane of the oxygen doped *orth*-Zr_3N_4 type structure or even to a mixture of several peaks. Other authors have already indicated the shift of the (111) peak of the ZrN (NaCl type phase) towards smaller angles for films prepared with high nitrogen flows [24-27], which resulted in the development of a poorly crystallized *orth*-Zr_3N_4 phase.

From figure 2.15 (chapter 2) it was also observed that the ratio C_N+C_O/C_{Zr} in this zone varies between ~ 1.2 and 1.4, and the atomic ratio C_N/C_{Zr} is close to 1, much lower than that of Zr_3N_4 compound [24-27,28]. This might be again a sign that, if the Zr_3N_4-type phase is developed, it probably involves oxygen. The ZrN_y system (Fig. 3.7.) only reveals a clear ZrN-type structure for these amounts of gas flow (pure nitrogen). According to some authors, this *orth*-Zr_3N_4 phase is formed as a result of cell expansion by incorporation of nitrogen (and oxygen) atoms in interstitial positions [23,29-31]. Other authors have described it as a relaxed NaCl structure with some Zr vacancies [24,25].

The development of over-stoichiometric type of structures in metal nitrides has being discussed for some time in literature, and it is known and widely accepted that there is a tendency towards an increased stability of heavier transition metals, when chemical bonds are established, that correspond to highest oxidation states. This fact is due to relativistic effects [32]. For example, in the case of Zr and Hf nitrides, this enhanced stability of the +4 oxidation state in comparison to the common +3, allows the coexistence of the metallic nitride, MN

(oxidation state +3) and insulating M_3N_4 (oxidation state +4) phases [23]. For zirconium oxynitrides prepared by PVD techniques or by nitridation of ZrO_2, the higher oxidation state (+4) is stabilized [23]. As a result, the stoichiometry of the oxynitrides tends to a "mixture" of ZrO_2 with Zr_3N_4, rather than the constant development of a fcc ZrN-type phase (doped or "pure") [23]. This might be a strong possibility within he films prepared within this zone II. A close look into the XRD diffraction spectrums of the sample produced with a mixture flow rate of 14 sccm, is possible to observe that not only the oxygen doped *orth*-Zr_3N_4 phase is observed but also another phase the γ-Zr_2ON_2. The peak at $2\theta \approx 30°$, which would correspond to the most intense (222) plane, the peak at $2\theta \approx 21.5°$ to the (211) plane and the peak at $2\theta \approx 60.5°$ to the (622) plane. This coating, as we will se later on in this work, represents a transition sample between two compositional and structural zones showing a crystalline structure resulting from a mixture of the *orth*-Zr_3N_4 and the γ-Zr_2ON_2 structure.

With further increase of the reactive gas flow (films prepared with gas flows varying from 15 to 30 sccm), the composition has shown an abrupt increase of the oxygen content (chapter 2, Fig. 2.14), as well as on the particular ratios C_N/C_{Zr} and C_O/C_{Zr} (chapter 2, Fig. 2.15). These changes are also well correlated with the formation of another structure, which is easily observed by the change in the diffraction patterns (Fig. 3.10), if compared to those of films from zone I and II (Fig. 3.5. and Fig. 3.9.).

With the deposition conditions of zone III (gas flows from 15 up to 30 sccm), the diffraction patterns (Fig. 3.10) correspond to a cubic structure, which can be indexed to that of γ-Zr_2ON_2 (ICDD card Nº 48-1635) [33-35]. An analysis of film composition ratios shows that the ratio C_N/C_{Zr} in the films from zone III decreases from about 0.7 down to approximately 0.3, and that C_O/C_{Zr} increases from about 0.7 in the first two samples to about 1.2 for the last ones. Taking into account that in stoichiometric Zr_2ON_2 compound, the ratios C_N/C_{Zr} and C_O/C_{Zr} are 1 and 0.5, respectively, it is concluded that the films within zone III have different atomic arrangements within the cubic lattice, where again oxygen is playing a fundamental role. In fact, oxygen is always in excess, in contrast with the deficiency of nitrogen, providing some evidence that the films may have significant lattice substitution/replacement in the nitrogen positions.

Clarke et al. [36] claimed that this structure (cubic Bixbyite-type crystal structure [37]) is similar to that of fluorite-type from cubic ZrO_2, in which one-fourth of anion positions are unoccupied and two-thirds of the remaining oxygen atoms are replaced by nitrogen atoms.

This arrangement means that in most oxynitrides nitrogen and oxygen atoms are statistically disordered, and M_2N_2O can be formally considered as a M_2X_3-type compound [36]. For this group of samples, this could explain the formation of the Zr_2ON_2 structure with a stoichiometry varying from $ZrO_{0.72}N_{0.71}$ (15 sccm) to $ZrO_{1.15}N_{0.29}$ (30 sccm).

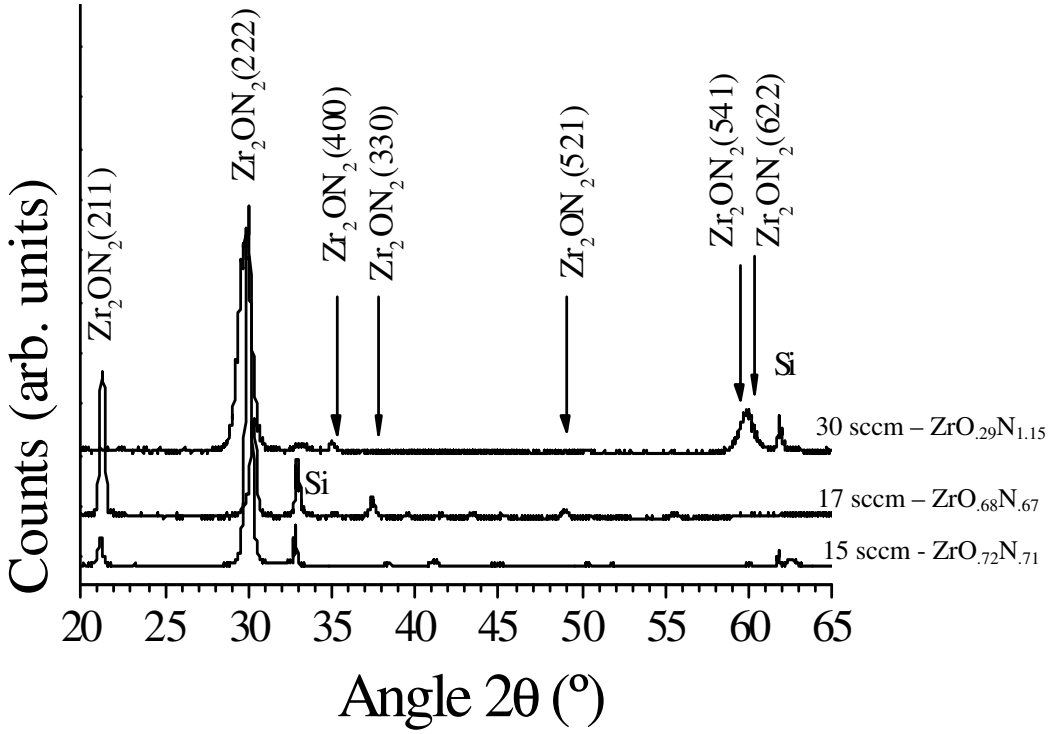


Fig. 3.10. XRD patterns for ZrO_xN_y films from composition zone III.

In fact, figure 2.15 shows that the ratio $(C_N+C_O)/C_{Zr}$ varies between 1.4 and 1.5 (with one of the films presenting a value of about 1.7), which is very close to that of the Zr_2ON_2 compound (1.5). This fact provides some evidence for this "intermixing" of nitrogen and oxygen within the lattice.

Regarding the samples deposited with the highest reactive gas mixture flows (zone IV) and with a stoichiometry close to zirconium dioxide (C_O/C_{Zr} is about 1.8), X-ray diffractograms confirmed the oxide phase formation (Fig. 3.11), revealing the existence of a monoclinic-zirconium oxide phase, *m*-ZrO_2 (ICDD card Nº37-1484). This is somewhat expected since similar behaviour was also observed when preparing ZrO_x films, as shown in the diffractograms of figure 3.12.

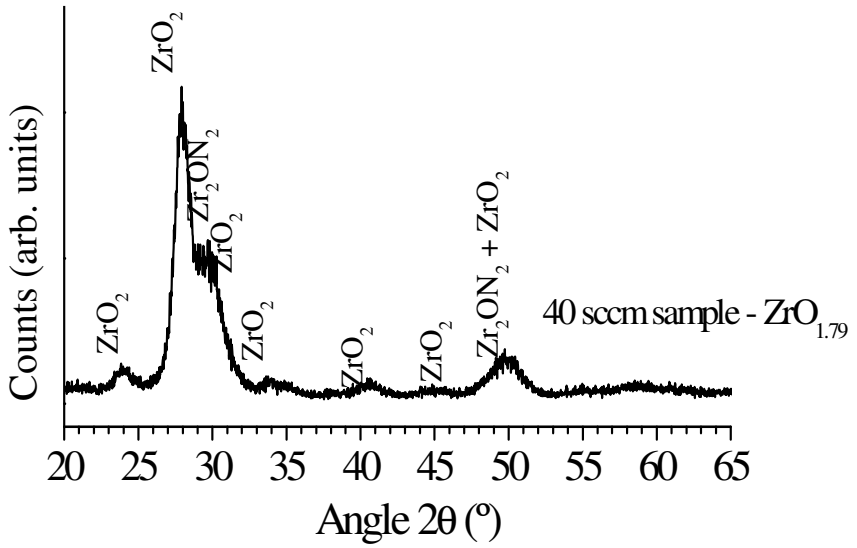


Fig. 3.11. XRD patterns for a ZrO_xN_y film from composition zone IV.

Figure 3.12. shows that the evolution of the diffraction patterns from the ZrO_x system is basically the change from an oxygen doped Zr lattice (hcp type), towards that of monoclinic ZrO_2.

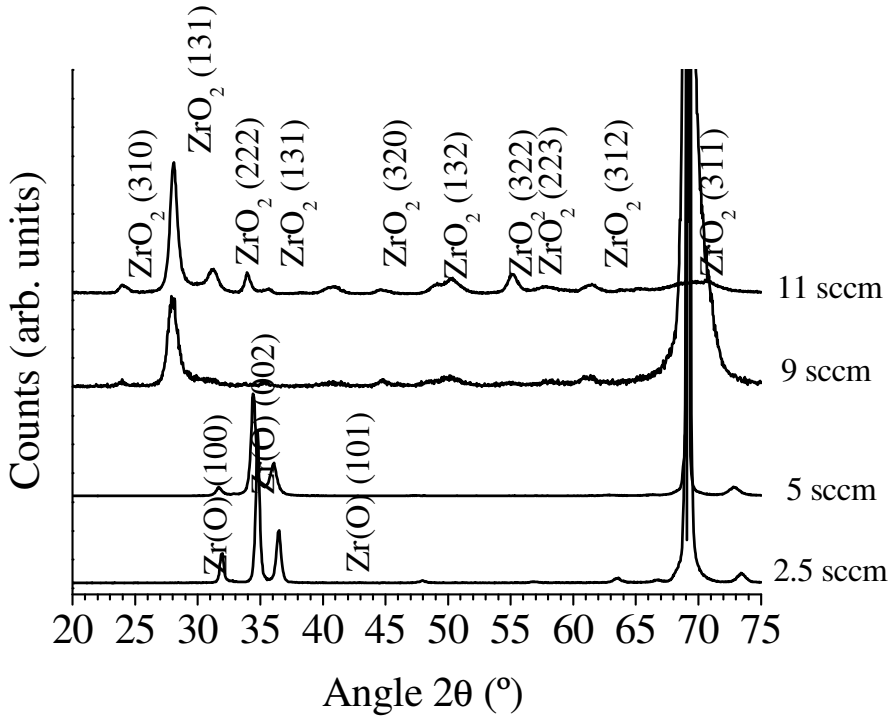


Fig. 3.12. XRD patterns for the ZrO_x thin films.

Nevertheless the coating deposited with 40 sccm presents the same structure as the coating deposited using only oxygen as a reactive gas, there are some differences that should be referred. The sample deposited using the reactive gas mixture of nitrogen and oxygen requires less oxygen flow than the one deposited using only oxygen. The sample deposited with gas mixture, was produced with an oxygen flow of 6 sccm (40×0.15) and the sample deposited with 5 sccm of oxygen doesn't present any traces of zirconium oxide phase. The main reason for this is that with 5 sccm of oxygen the system is running in metallic mode, presenting high deposition rate and low target potential (see fig. 2.7.b).

In conclusion it appears that the there is a good correlation between the composition and crystalline structure evolution, were it is also possible to distinguish deferent's structural zones that present the same "transitional" samples between which zone.

3.3.2. Series 2 (95 % N_2 + 5 % O_2 gas mixture)

Similarly to what has been done for composition analysis (chapter 2), this sub-chapter will be devoted to scan the different structural features that were developed within the different series of samples.

Figure 3.13 presents the XRD diffraction patterns evolution for the series of samples prepared with the gas mixture 95 % N_2 + 5 % O_2 (series 2). Let us just recall that this series, for films prepared with reactive gas flows below 8 sccm, presented noticeable the increase of the C_N/C_{Zr} ratio, which approaches to 1.1, keeping this ratio approximately constant for higher values of the reactive gas flow. Associated to this evolution is the systematic increase of oxygen content of the films. Regarding the films deposited with higher reactive gas flows the films show a slow but systematic increase of the C_O/C_{Zr} atomic ratio leading to an increase of the $(C_N+C_O)/C_{Zr}$) ratios which approaches 1.5 for the sample prepared at 16 sccm.

From this figure it is possible to observe that, similarly to what has been observed for composition, the samples present also the same structural evolution as those from series 1, going from a *fcc*-ZrN type structure to a Zr_3N_4-type orthorhombic phase with the last sample presenting a mixture of *orth*-Zr_3N_4 and γ-Zr_2ON_2 structures. The results from glancing geometry experiments (GIXRD) shown in figure 3.14 further attest this behaviour, while a very broad peak around 56º has also appeared [12]. The diffraction peak at $2\theta \approx 32º$ should correspond to the

(320) plane of the oxygen doped Zr_3N_4-type structure or even to a mixture of several peaks predicted in this region for this structure, and the peak at $2\theta \approx 56^\circ$ could relate or be a mixture of diffraction peaks predicted for the Zr_3N_4-type structure in the region $54^\circ < 2\theta < 56^\circ$ [28].

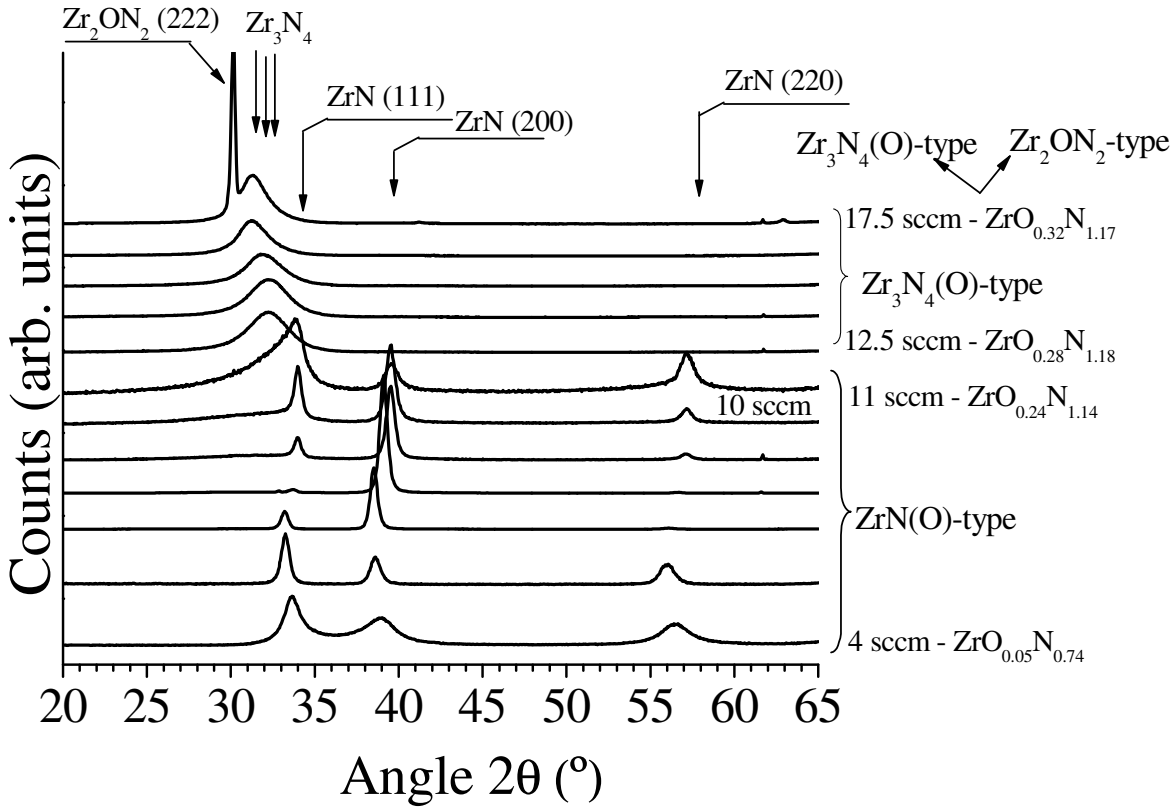


Fig. 3.13. XRD patterns for ZrO_xN_y films from series 2 as a function of the gas mixture flow.

The diffractograms (see Fig 3.13) reveal that the transition from one crystalline-type structure to the other although occurring in a similar way regarding the samples of the series 1, involve always a significant number of samples, which in fact is quite consistent with the composition results that also varied in similar ways. As already referred in chapter 2 this series present a smoother compositional change when compared to the films of series 1, this is also reflected in the crystalline evolution of these coatings. A closer look into figure 3.13 is possible to observe that the samples deposited with reactive gas flow between 4 and 11 sccm, which present a metalloid to zirconium ratio varying from ~0.8 to ~1.4, still present the *fcc*-ZrN phase. Nevertheless the last sample of this region (11 sccm) presents a large tail in the region $30^\circ < 2\theta < 33^\circ$. Comparing the relationship between the composition and crystalline structure of

the first and second series, is possible to conclude that the crystalline changes occurs at different metalloid to zirconium ratio.

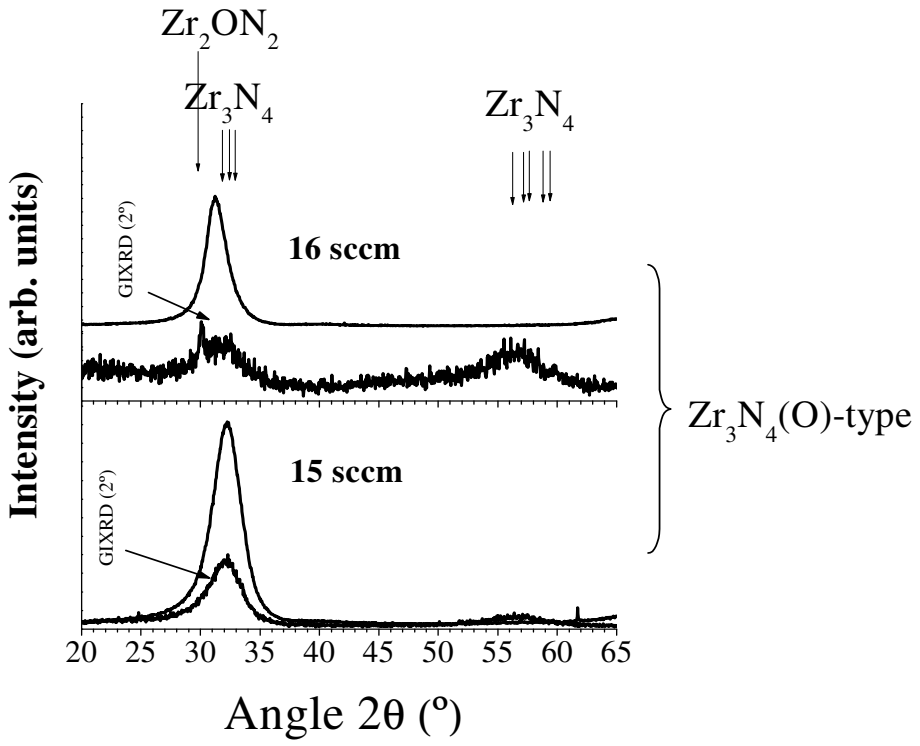


Fig. 3.14. Conventional (XRD) and glancing (GIXRD) geometry patterns for two different ZrO_xN_y films of the series 2 that showed the $Zr_3N_4(O)$ phase development.

Regarding the series 1, the sample that still presents the (111) ZrN plane (11 sccm) with a large tail between 30 and 33º, present a $(C_N+C_O)/C_{Zr}$ ~ 1.2, and the sample of the series 2 that present similar diffraction patterns (11 sccm) present an $(C_N+C_O)/C_{Zr}$ ~1.4, but presenting less oxygen content. The sample of the series 1 present an C_O/C_{Zr} ~ 0.3 where the correspondent sample of the series 2 present ~ 0.2. It should be expected that the higher of metalloid content should promote the formation of the over-shtoichiometric Zr_3N_4 phase, but in this case the transition sample between the ZrN(O) structure to the over-shtoichiometric $Zr_3N_4(O)$ structure happens at different non-metal to zirconium ratios in the two series. This could reinforce the idea that oxygen is acting as a "catalyser" in the formation of the meta-stable phase *orth*-$Zr_3N_4(O)$.

Figure 3.15. shows the texture coefficient and the lattice parameter as a function of the reactive gas flow for the series 2. Again in good coherence with series 1, the evolution of the

peak intensity ratio ($I_{200}/(I_{200}+I_{111}+I_{220})$), is characterized by an initial increase and then followed by a decrease of this parameter (Fig. 3.15.).

For very low values of reactive gas flow (<8 sccm) the <111> orientation decrease continuously and the (200) becomes the dominant growth. With further increase of the reactive gas flow there is another change on the preferential orientation with the decrease of <200> preferential orientation.

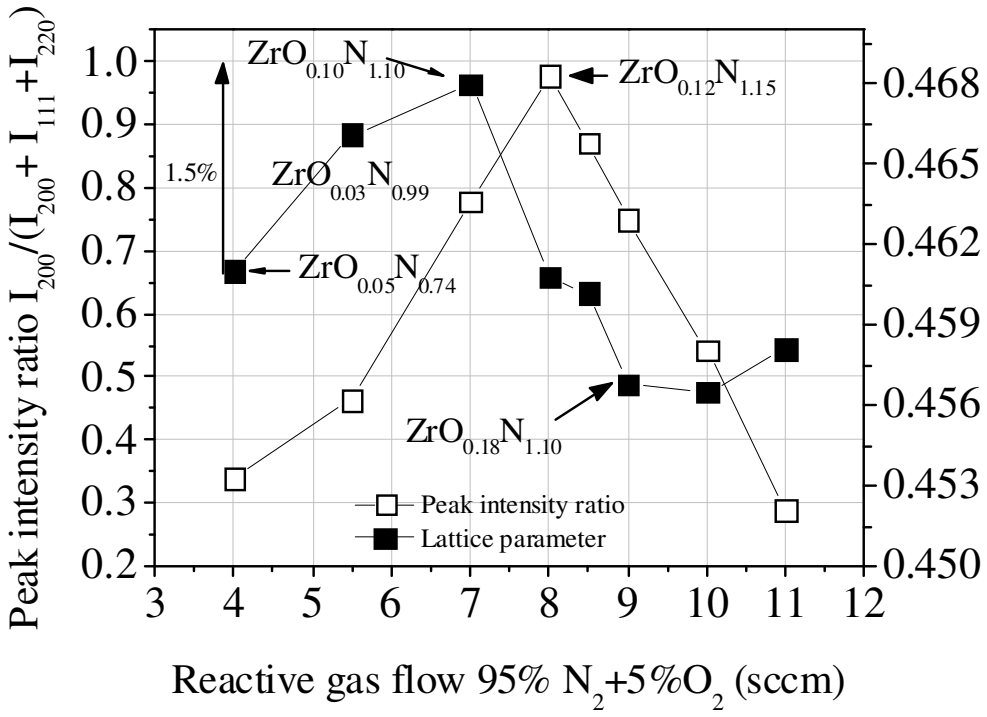


Fig. 3.15. Variation of the peak intensity ratio and lattice parameter as a function of the reactive gas flow, for the in the films laying in zone I - series 2.

In fact for a reactive gas flow of 10 sccm, this peak intensity ratio is already below 0.6, which shows that the films are mostly randomly oriented. Nevertheless, the preferential orientation evolution presents quite similar evolution but there are some non-negligible differences that should be referred. In series 1, the peak intensity ratio ($I_{200}/(I_{200}+I_{111}+I_{220})$) increases until the reactive gas flows of 9 sccm (Fig. 3.6). This sample presents a sub-stoichiometric condition when the texture coefficient of the series 2 increases until the reactive gas flow reaches 8 sccm. In this case the sample presents an over-stoichiometric condition. Nevertheless, this could result only because the rate of evolution of the crystalline structure of the series 1 is higher. It must be remembered that the sample deposited with 9 sccm of the series

1, already presents the large tail between 30 and 33º, and presents a peak intensity ratio ($I_{200}/(I_{200}+I_{111}+I_{220})$) close to 0.4 (Fig. 3.6). Looking to the similar XRD diffraction pattern for series 2 it is the sample deposited with a higher reactive gas flow rate (10 sccm), which presents a random orientation with a peak intensity ratio ($I_{200}/(I_{200}+I_{111}+I_{220})$) close to 0.5, see Fig. 3.15.

Regarding the evolution of the lattice parameter there is also some non-negligible changes between the series 1 and series 2. The most remarkable one is the significant increase of the lattice parameter (~1.5%) going from the sample deposited with a reactive gas flow rate of 4 sccm to the sample produced with 7 sccm, whereas in the first series there were an initial decrease of about 0.3% of this parameter. This difference should result from the different compositional values of the two series in this zone. In this series (series 2), in contrast with series 1, the coatings composition goes from a sub-stoichiometric to an metalloid to zirconium ratio close to 1.2, with a C_N/C_{Zr} ratio varying from ~0.7 to ~1.1. The insertion of nitrogen and oxygen in interstitial positions should explain the increase of the lattice parameter [6]. Another factor that could also play an important role in is this initial increase of the lattice parameter is the increase of the compressive residual stress from ~ 1.4 GPa for the sample deposited with a reactive gas flow of 4 sccm to ~5.4 GPa for the sample deposited with 7 sccm. The decrease of the lattice parameter for the samples deposited with reactive gas flows higher than 7 sccm, should also result from de decrease of the compressive residual stress that goes from ~5.4 GPa (7sccm) to ~2.4 GPa (9sccm).

In order to understand the similarities and differences between both series, a detailed analysis was carried out by comparing samples of the both series, with similar composition. Figure 3.16. presents the XRD diffraction patterns of two samples deposited with different gas mixtures (95 % N_2 + 5 % O_2 - 19/1 ratio and 85 % N_2 + 15 % O_2 17/3 ratio), but with similar elemental compositions, and a ZrN diffraction pattern for reference proposes.

A close look to these diffraction patterns shows that both samples present the same characteristic ZrN peaks, with just small differences. The sample deposited with the gas mixture 95/5 presents a more pronounce broadening of the diffraction peaks and a lower $I_{200}/(I_{200}+I_{111}+I_{220})$ ratio. These differences should result mainly from the different non-metal/metal atomic ratios. The lower metalloid to zirconium ratio should induce a higher lattice disorder explaining the bordering of the XRD diffractions patterns of series 2 sample. Regarding the a lower $I_{200}/(I_{200}+I_{111}+I_{220})$ ratio of the sample deposited with 4 sccm (series 2) as already

referred the approximation to the stoichiometric condition brings the system closer to its thermodynamically stable condition, and thus favouring the (200) growth.

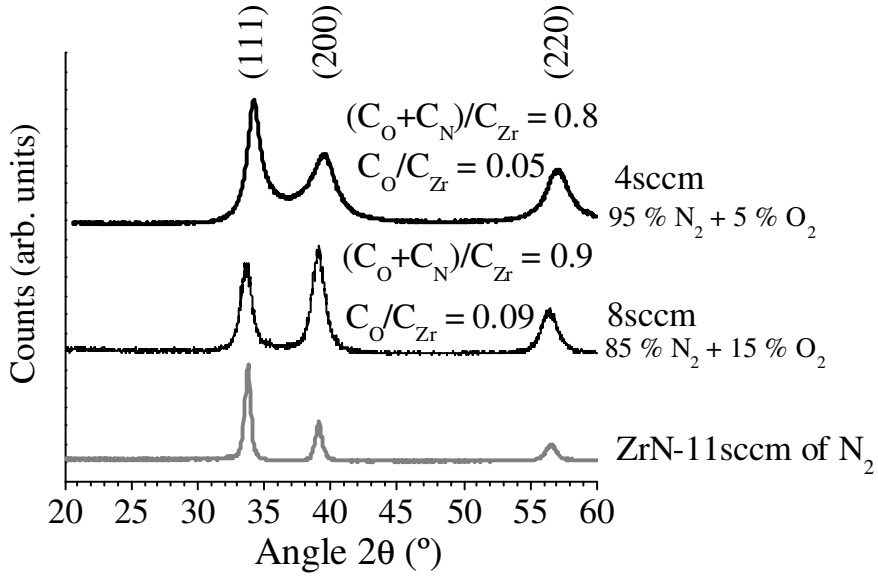


Fig. 3.16. XRD patterns for ZrO_xN_y films, prepared with different reactive gas mixtures: zone I, but similar atomic compositions.

Furthermore, comparing two more samples from both series (now those from the *orth*-Zr_3N_4(O) zone) with similar composition the same similarities appear again (Fig. 3.17.), revealing that composition is a key factor for the crystallinity/texture phenomena.

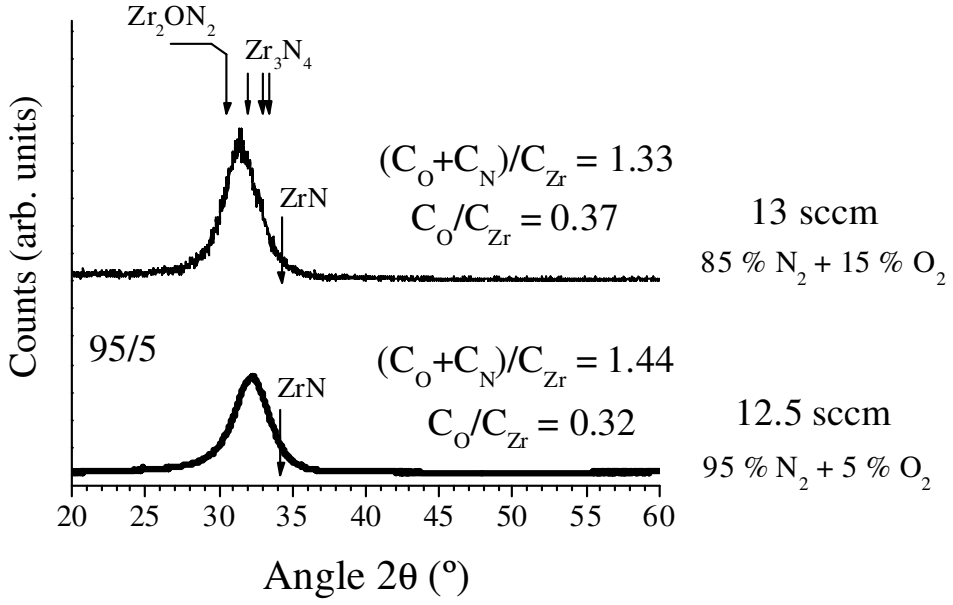


Fig. 3.17. XRD patterns for ZrO_xN_y films, prepared with different reactive gas mixtures: zone II.

Anyway, it is worth notice that the sample prepared using the 85/15 gas mixture presents a small shift to lower angles of the diffraction peak compared with the sample deposited with the gas mixture 95/5, which could also the reflect the small composition differences between the two samples (higher amount of oxygen of this coating, and the progressive formation of the γ-Zr_2ON_2 structure). A close look into this figure ((Fig. 3.17)) is also possible to observe that the sample deposited with 13 sccm (series 1) present a less crystalline structure regarding the other sample (12.5sccm- series 2) this could be a consequence of the significant differences in the deposition rate values. The sample of the series 1 presents a deposition rate close to 7 μm/h whereas the sample of the series 2 presents a value close to 3 μm/h. The high value of deposition rate of series 1 sample should induce a higher lattice disorder. Regarding the X-ray diffractograms for films deposited with higher reactive gas flows in both series (Fig. 3.18.) – the Zr_2ON_2-type films, the same similarities appeared. Once again it is clear that beyond the different gas mixtures, similar compositions give origin to similar crystalline structures, presenting a mixture of *orth*-Zr_3N_4 (O) and Zr_2ON_2 crystalline structures. The presence of extra γ-Zr_2ON_2 peaks in the XRD diffractograms of series 1 sample (14 sccm) is probably due to the higher oxygen content of this coating.

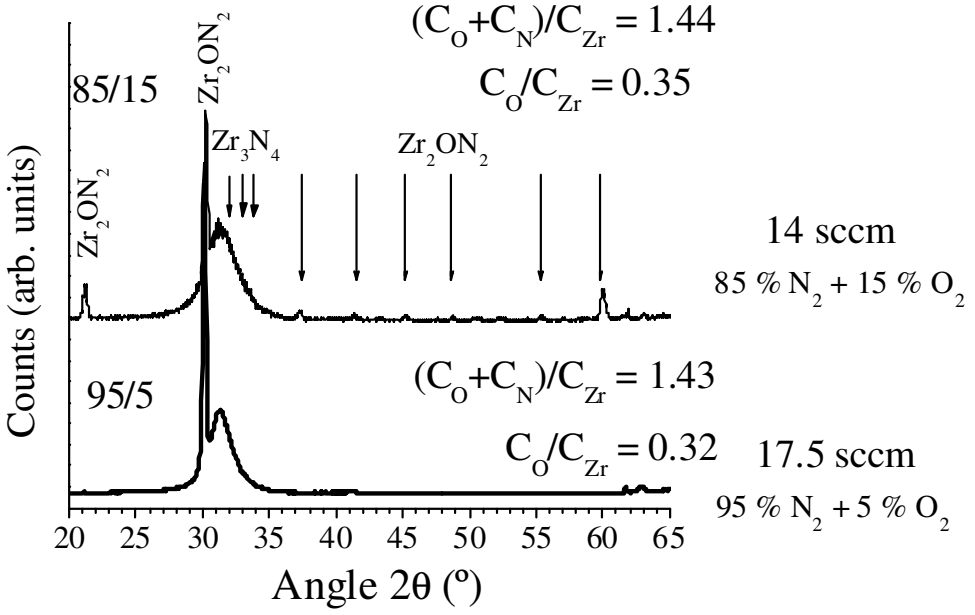


Fig. 3.18. XRD patterns for ZrO_xN_y films prepared with different reactive gas mixtures: zone III.

As shown above, beyond small differences, these results indicate a strait correlation between composition and crystalline structure, meaning that controlling the composition allows to "predict" the crystalline phase to be formed and thus tailoring a material's properties according to specific needs.

3.3.3. Series 3 (85 % N_2 + 15 % O_2 gas mixture - biased samples)

Figure 3.19 shows the XRD diffraction patterns for the different samples prepared within series 3 (using the 85% (N_2)/15% O_2 gas mixture and a bias voltage of -70V). The first observation that can be draw is that in this series, although prepared using ion bombardment during film's growth, the crystalline structure evolution is similar when compared to the other two non-biased series.

For the samples deposited with the lowest values of gas flow (< 10.5 sccm), results reveal the formation of the same *fcc*-ZrN structure, again with some changes in the preferential orientation.

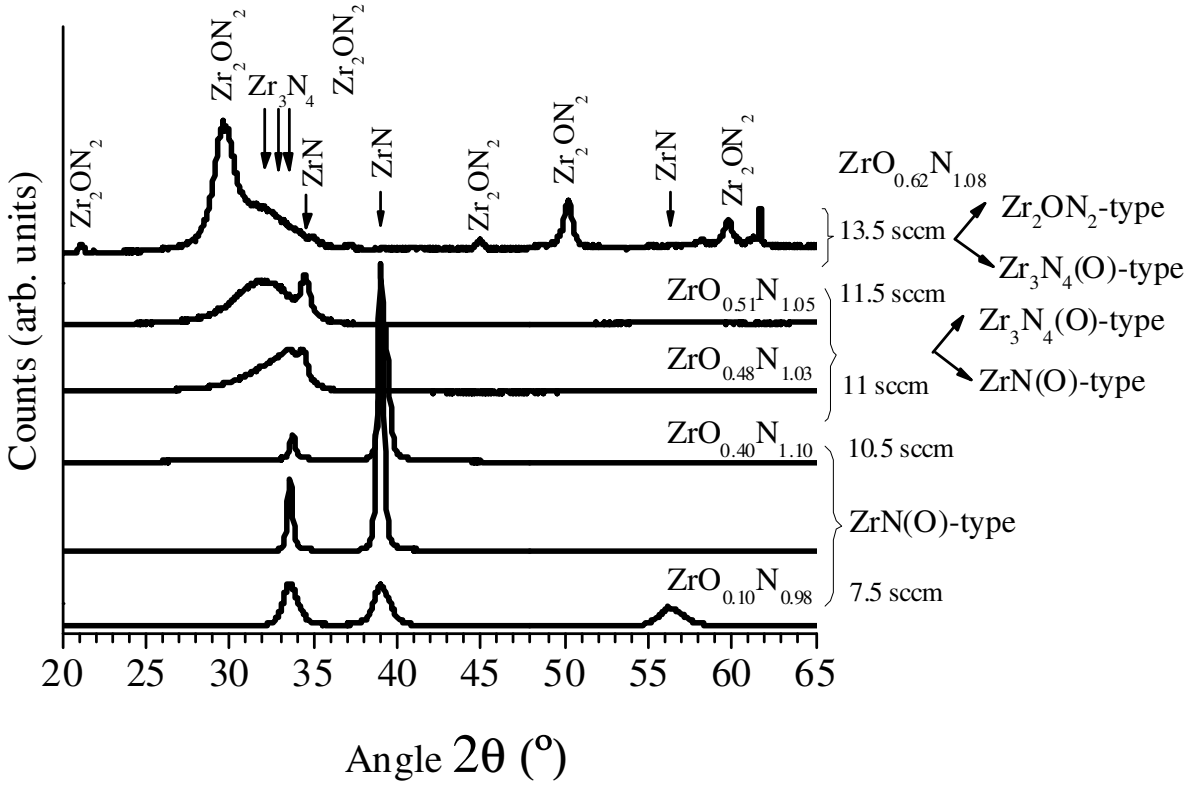


Fig. 3.19. XRD patterns for ZrO_xN_y films from series 3 as a function of the gas mixture flow.

Figure 3.20 presents the peak intensity ratio ($I_{200}/(I_{200}+I_{111}+I_{220})$) for the samples deposited with reactive gas flow up to 11 sccm, were the only crystalline phase observed is the *fcc*-ZrN. Nevertheless the ion bombardment should promote the (200) orientation [6], is possible to observe that the preferential growth evolution (Fig 3.20) is very similar to that one observed in the others 2 series deposited without ion bombardment, when samples with similar composition are compared. The initial increase of the reactive gas flow provokes a (200) preferential growth. Similarly to the other series with further increase of the reactive gas flow (11sccm) there is another change in the preferential orientation, were the (111) orientation becomes dominant again.

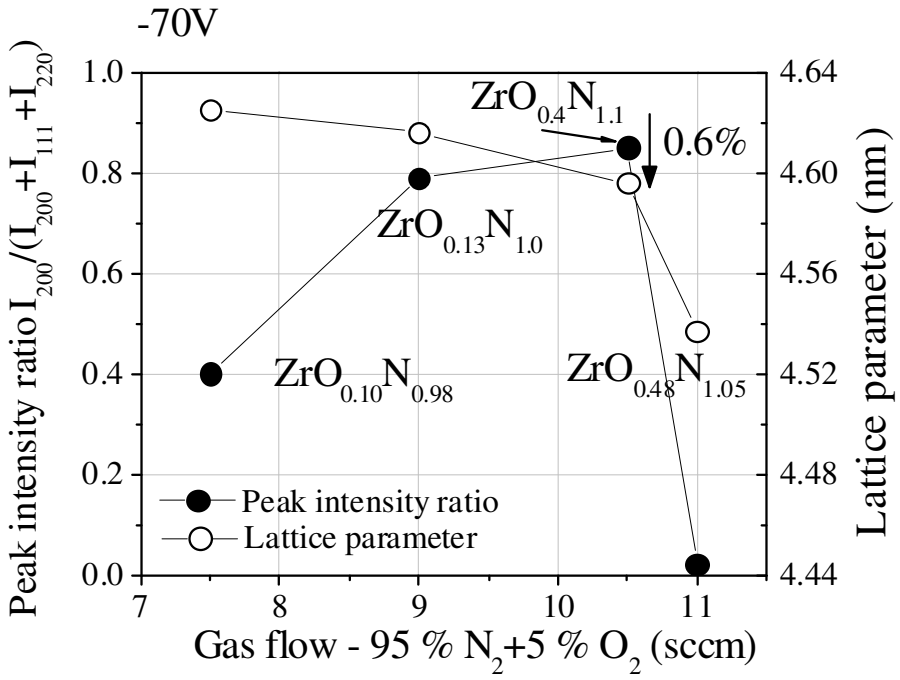


Fig. 3.20. Variation of the peak intensity ratio and lattice parameter as a function of the reactive gas flow, for the in the films laying in zone I - series 2.

Figure 3.20 also presents the lattice parameter of the samples deposited with reactive gas flow lower than 11.5 sccm. In this graphic it is possible to observe a decrease of the lattice parameter of around 0.6 % within the samples that only present the *fcc*-ZrN phase (<11 sccm). This decrease of lattice parameter should result from the decrease of the compressive residual stress from ~3.3 GPa for the sample deposited with 7.5sccm until ~1.4 GPa for the sample deposited with 10.5 sccm of the reactive gas flow. Looking to the sample deposited with a 11 sccm reactive gas flow (Fig 3.19.), once more the formation of the large tail between 30º and

33º, accompanies a substantial decrease of the lattice parameter, indicating that this sample, like in the other series, corresponds to a transition sample between the dominant *fcc*-ZrN structure zone and the dominant orthorhombic Zr_3N_4(O) structure zone.

Although following similar tendencies, there are non-negligible differences that must be referred. The most remarkable one is the co-existence of the *fcc*-ZrN phase and the *orth*-Zr_3N_4(O) structure (see Fig. 3.21). The series 3 sample deposited with 11 sccm presents two clear distinct peaks one concerning the (111) *fcc*-ZrN and the other it is a broad peak associated to the formation of the *orth*-Zr_3N_4(O) phase.

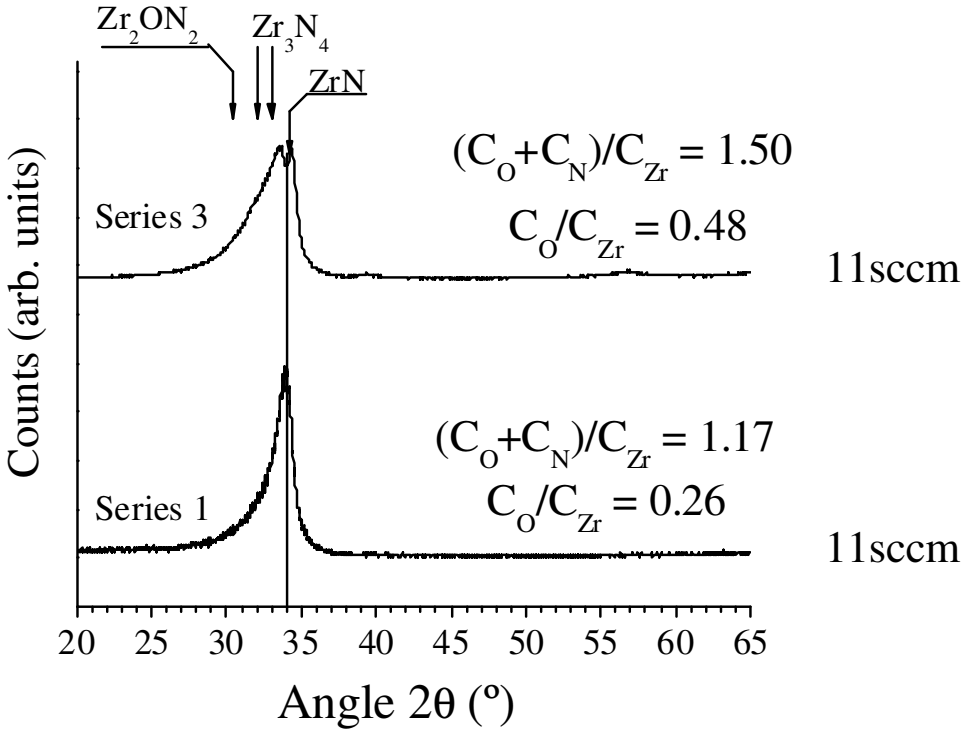


Fig. 3.21. XRD patterns for ZrO_xN_y films, for samples deposited with 11sccm, for the series 1 and 3.

This co-existence of both structures is even clearer with the sample deposited with 11.5 sccm reactive gas flow (see Fig. 3.22). In this series (series 3) the sample deposited with 11.5 sccm presents a clearly visible peak correspondent to the diffraction on <111> planes of the *fcc*-ZrN ($2\theta \approx 34º$) and the characteristic very broad peak near $2\theta \approx 32º$ (Fig. 4.22), whereas the series 1 sample deposited with 12 sccm doesn't present any traces of the *fcc*-ZrN structure. One possible explanation for this phase segregation is the applied bias voltage (-70 V). Ion bombardment

favours atomic diffusion by transferring their kinetic energy to the lattice, leading to the formation of the most stable material [24], which in this case is *fcc*-ZrN. Nevertheless the ion bombardment should also promote preferential re-sputtering of oxygen regarding the nitrogen [38], inducing a decrease of oxygen content in the coatings. But, as it was already referred, this is not the case for these coatings. On this basis, it is not clear that the ion bombardment is the only "responsible" factor for the observed phase segregation. Another possibility is the deposition conditions already refereed, the rotation mode (7 rpm). When the substrates are not parallel to the target, the rate of zirconium atoms arriving to the already deposited coating is lower, inducing a lower metal to non-metals ratio. These conditions are equivalents to a deposition made with a higher reactive gas flow.

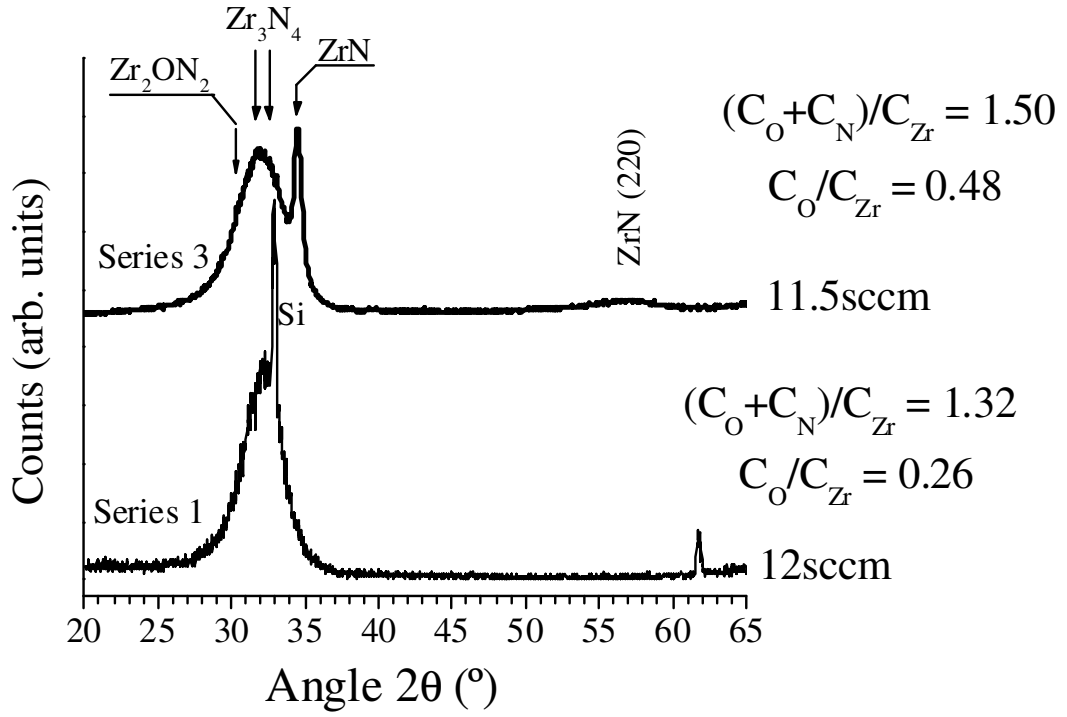


Fig. 3.22. XRD patterns for ZrO_xN_y films, of the samples deposited with 11.5sccm (series3) and 12 sccm (series 1) reactive gas flow.

On this basis, it is possible that the rotation mode could promote a non-homogenous coatings concerning the composition and, consequentially, non-homogenous in crystalline structure. With a further increase of the reactive gas flow it is noticed that the coatings present a crystalline

structure that results from a mix between the *orth*-Zr_3N_4(O) and γ-Zr_2ON_2 structures, flowing the same tendency as in previous series.

3.3.4. Series 4 (samples prepared with oxygen pulsing – RGPP)

As mentioned previously in chapter 2, one of the biggest problems in preparing thin films is related with the poisoning of sputter targets [39-42]. This poisoning provokes a significant decrease in the deposition rate (a serious problem in industrial production) as well as an increasing difficulty to have a wide and smooth range of compositions available. The "doping" of a target surface changes the sputtering yield and consequently the composition of incoming particles towards the part to be coated is different. This is one of the most undesired phenomena in industry. During the course of this work, a new deposition method was investigated in order to search for some attenuation of this undesired effect. Such method is the pulsing of one of the reactive gases (oxygen in the case) using RGPP. It should be reminded that during the deposition of this series of samples, series 4, and due to the selected deposition conditions, the increase of the measured target potential was systematically lower (<10 V) which induced a more constant deposition rate, comparing with the sample produced in series 1. Consequentially this series presents a smoother increase of the C_O/C_{Zr} ratio, associated to an also very smooth decrease of C_N/C_{Zr}.

Figure 3.23 presents XRD diffraction patterns for samples prepared with different duty cycles (ratio between T_{on} and T).

The first conclusion that is possible to draw from the results presented in this figure is that the structural evolution is similar to the previous ones. The samples change from a *fcc*-ZrN type structure, to a mixture between the *orth*-Zr_3N_4(O) and γ-Zr_2ON_2-type structures. In the previous cases, the XRD diffraction patterns revealed that in the first zone, the films crystallized in a *fcc*-ZrN structure, with an initial increase and then decrease of the ($I_{200}/(I_{200}+I_{111}+I_{220})$) ratio.

Regarding this RGPP series, results show that the first changes in the preferential growth towards <200> does not occur (Fig. 3.24), which is most certainly the result of the particular set of parameters that were selected.

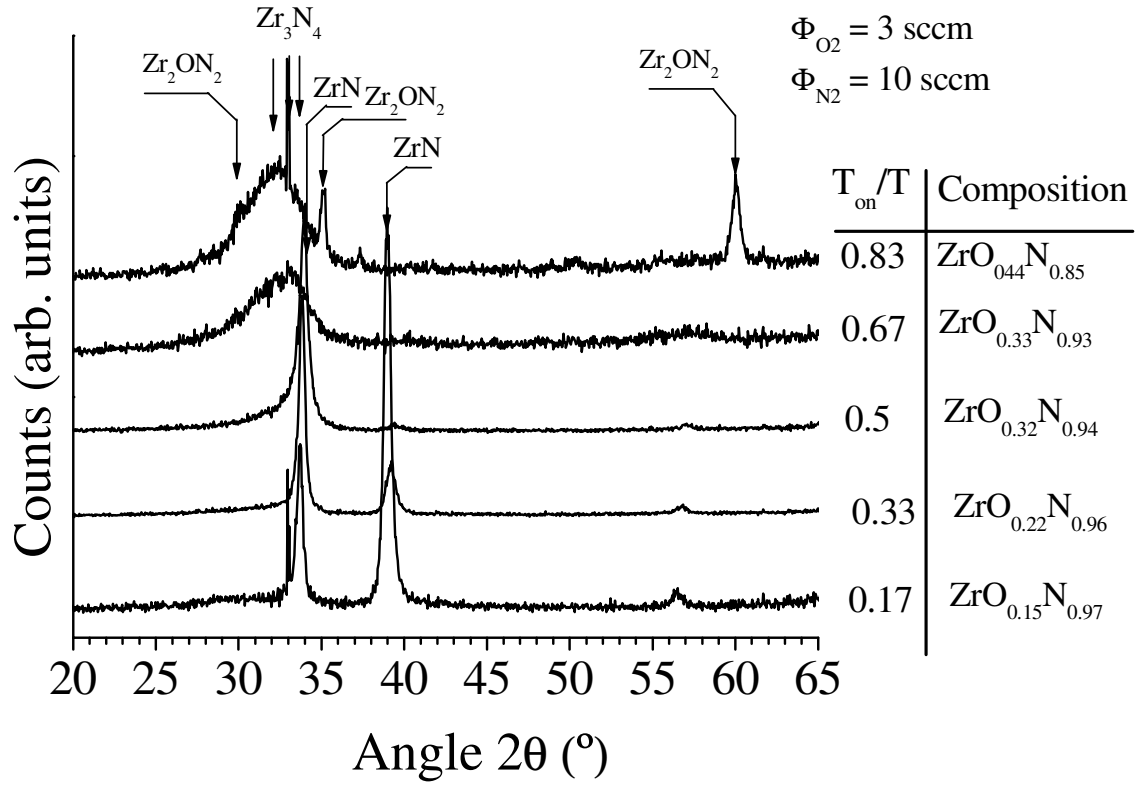


Fig. 3.23) XRD patterns for ZrO_xN_y films as a function of duty cycle, for the series 4.

The films presented no metallic regime, since they were already deposited with sufficient reactive gas flow to deposit coatings with $(C_N+C_O)/C_{Zr}$ ratio close to one (see Fig. 3.24.). The series 4 samples present a decrease of the (200) preferential growth (Fig. 3.24), with the increase of the duty cycle, and the consequential increase of oxygen content.

Associated to the decrease of $(I_{200}/(I_{200}+I_{111}+I_{220}))$ ratio is the decrease of ~0.6 % of the lattice parameter values (Fig. 3.24). This decrease should result from the decrease of compressive residual stresses from ~ -3.8 (T_{ON}/T=0.17) to ~2 GPa (T_{ON}/T=0.5), with the increase of the oxygen content (see Fig. 2.26.a).

Regarding the sample deposited with a duty cycle of 0.67, results show the same tendency to change the structure towards poorly crystallized oxygen doped *orth*-Zr_3N_4, as observed in previous series.

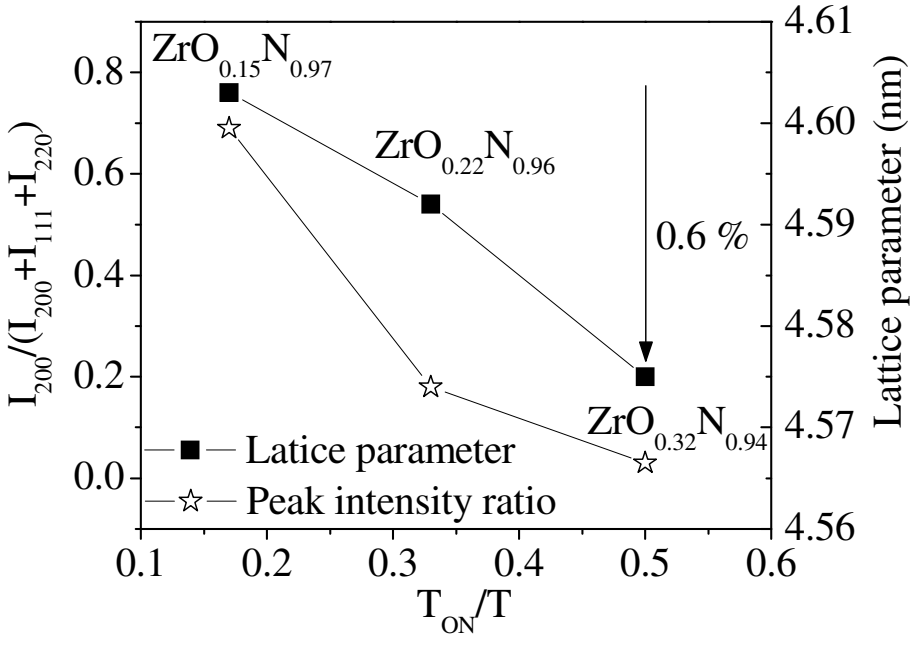


Fig. 3.24. Variation of the peak intensity ratio and lattice parameter in the films lying in zone I and II, as a function of the duty cycle, for the serie 4.

For the highest duty cycles, the coatings present a mixture of γ-Zr_2ON_2 and *orth*-Zr_3N_4(O) structures, also similar to the previous series.

Figure 3.25 shows the XRD diffraction patterns of a sample from series 1 (deposited with a gas mixture flow of 9 sccm) and from a sample deposited with the RGPP system, using a duty cycle of 0.17. From this figure, it is possible to observe that for low reactive gas flows and for low duty cycles the two systems present similar diffraction patterns. The sample deposited with the gas mixture presenting a more pronounced <200> preferential growth. Comparing the results from ($I_{200}/(I_{200}+I_{111}+I_{220})$) intensity ratio for these two samples (Fig. 3.6 and 3.24), it is possible to observe that the sample deposited with the reactive gas flow of 9 sccm (series 1) presents a ($I_{200}/(I_{200}+I_{111}+I_{220})$) intensity ratio close to 0.9, whereas the sample deposited with the RGPP system presents, for this parameter, a value close to 0.7. This difference could result from small differences in composition of the samples, since one is sub-stoichiometric (series 1 sample) and the other (deposited with the RGPP system) is over-stoichiometric.

Furthermore, figure 3.25 also shows that the XRD diffraction pattern of the sample from series 1, presents a small shift to lower diffraction angles in comparison to the sample deposited with the RGPP system.

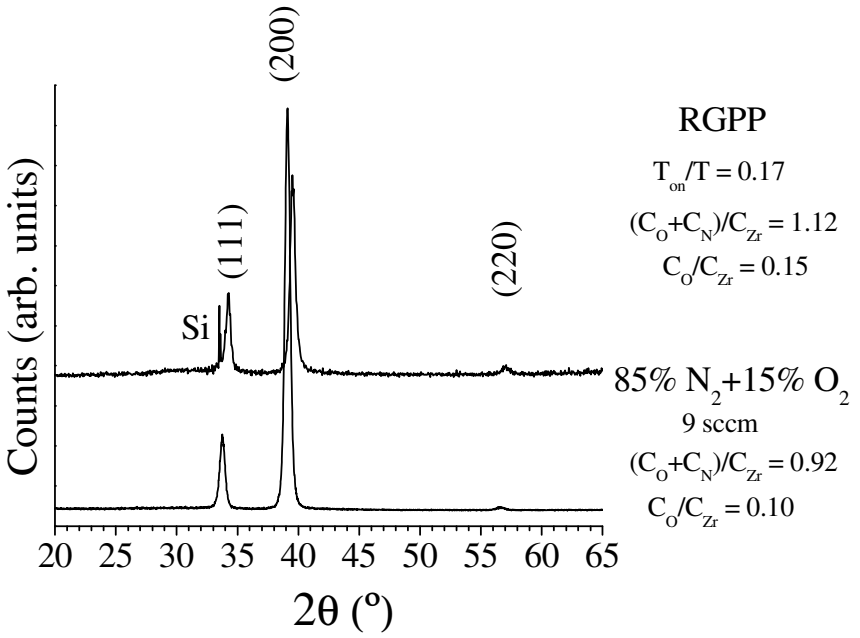


Fig. 3.25. XRD patterns for ZrO_xN_y films, for a sample from series 1 - zone I (deposited with 9 sccm), and a sample prepared by RGPP - duty cycle of 0.17.

This could result from the different compressive residual stress values. In fact, the sample deposited with the gas mixture presents residual stress close to 4.7 GPa and the sample deposited using the RGPP system presents a compressive residual stress of ~ 3.8 GPa.

In order to further search for differences between the series produced with the RGPP and gas mixture system, figure 3.26 presents the XRD diffraction patterns of a sample from series 1 (using a gas mixture flow of 12 sccm) and from a sample deposited with RGPP system using a duty cycle of 0.67.

From this figure, it is possible to observe that these samples, with similar compositions, have similar structural features. Both present a very broad "peak" between 2θ ~28º and 2θ ~36º that should represent a mixture of γ-Zr_2ON_2 and *orth*-Zr_3N_4(O) structures. Nevertheless, the sample prepared by RGPP shows also a very broad peak at 2θ ~57º, which is not present in the sample prepared with the gas mixture, and should correspond to the (220) ZrN plane. The presence of this peak, associated to a possible contribution of the (111) peak of *fcc* zirconium nitride phase in the zone between 2θ ~28º and 2θ ~36º, may indicate tha this sample, deposited with the RGPP system, still present traces of *fcc*-ZrN. Comparing the composition of the these two coatings (Fig. 2.24) is possible to observe that the RGPP sample presents a higher oxygen

content regarding the sample deposited using the gas mixture system, although still present the some traces of the *fcc*-ZrN structure.

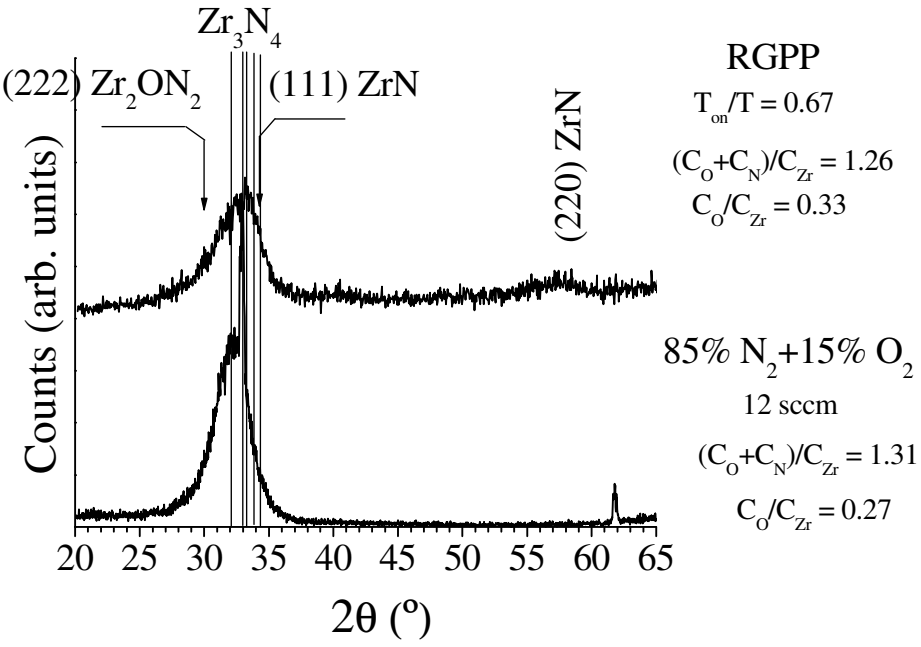


Fig. 3.26. XRD patterns of ZrO_xN_y films, for a sample from series 1 - zone II (deposited with 12 sccm), and a sample prepared by RGPP – duty cycle of 0.67.

This could indicate that introduction of pulsing oxygen flow may have similar effect in the composition of the coatings than the rotation mode, promoting non-homogeneous coatings in composition and consequently in structure. In the T_{on} period with the higher oxygen partial pressure the coatings could be more oxygen rich than in the T_{OF}. Although this factor should be avoid by decreasing the period of the pulsing.

Finally, and for the highest flows and duty cycles, some differences were also observed. Figure 3.27 show the XRD diffraction patterns of a sample from series 1 (deposited with 14 sccm) and the sample deposited with RGPP, using a duty cycle of 0.83.

In this figure is possible to observe that both samples present a mixture between γ-Zr_2ON_2 and *orth*-Zr_3N_4(O) structures, but probably with different volume fractions of each. In the sample deposited using the RGPP system, it is possible to observe several peaks associated to the γ-Zr_2ON_2 phase, whereas in the sample deposited with the gas mixture system, only the most intense peak is observed. This higher number of diffraction peaks could represent a higher crystalline fraction of the γ-Zr_2ON_2 phase. One possible explanation is the higher amount of

oxygen in the film deposited with the RGPP system (~20 at. % - see Fig. 2.26a) compared with the sample deposited using the gas mixture system (~16 at. %, see Fig. 2.13). As already referred in this thesis, with the increase of the oxygen content there is an increase of the crystalline volume fraction of the γ-Zr_2ON_2 crystalline phase.

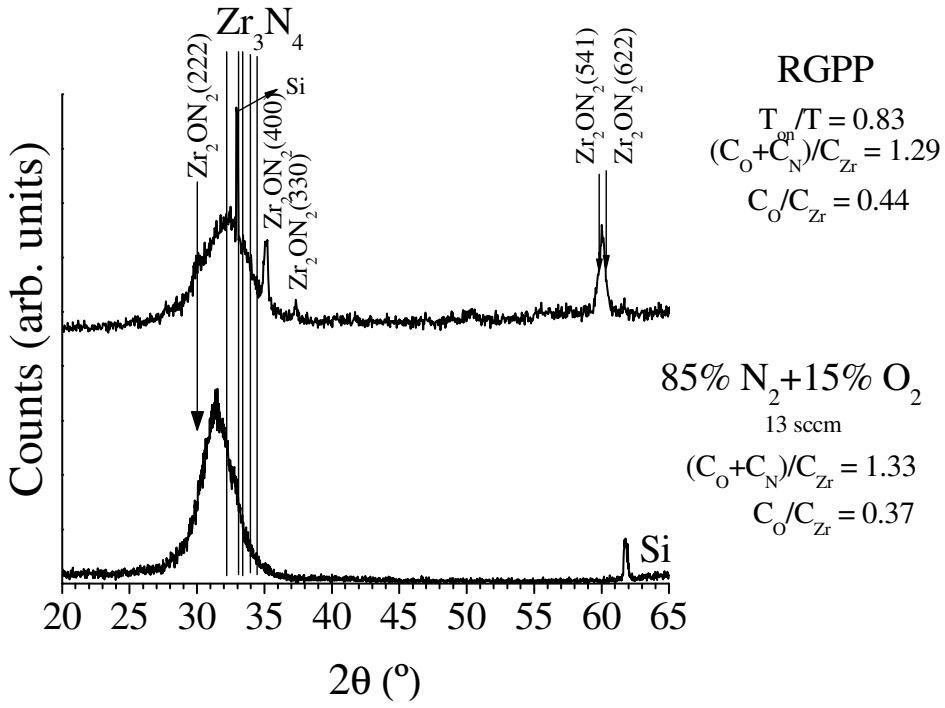


Fig. 3.27. XRD patterns for ZrO_xN_y films for a sample from series 1 - zone III 14 sccm, and a sample prepared by RGPP – duty cycle of 0.83.

3.4. Conclusions

The different regions observed taking into account, firstly the variations in the film's elemental concentrations (chapter II), was also observed in the structural evolution of the coatings. Structural characterization of the ternary system ZrO_xN_y revealed a strong dependence of the film texture on the oxygen content, exhibiting a change from a *fcc* B1 Nacl-type films for low gas flows (low oxygen contents) to develop a structure that might be similar to that of *orth*-Zr_3N_4, with oxygen inclusions, at intermediate gas flows (intermediate oxygen contents). For relatively high gas flows or duty cycle (high oxygen amounts), the films exhibited only crystalline structures that were indexed as oxynitride (γ-Zr_2ON_2) and oxide phase (*m*-ZrO_2).

3.5. References

[1]- B. North, Surf Coat Technol. 106 (1998) 129.

[2]- I. Petrov, P.B. Barna, L. Hultman, J.E. Greene, J Vac Sci Technol A (5) (21) (2003) 117.

[3]- P.H. Mayrhofer, C. Mitterer, L. Hultman, H.Clemens, Progress in Materials Science 51 (2006) 1032.

[4]- A.A. Voevodin, J.S. Zabinski, Thin Solid Films 370 (2000) 223.

[5]- Chuan-Pu Liu, Heng-Ghieh Yang, Thin Solid Films 444 (2003) 111.

[6]- D. Pilloud, A.S. Dehlinger, J.F. Pierson, A. Roman, L. Pichon, Surf. Coat. Technol.174-175 (2003) 338.

[7]- I. Ivanov, P. Kazansky, L. Hultman, I. Petrov, J.-E. Sundgren, J. Vac. Sci. Technol. A 12 (1994) 314.

[8]- P.J. Kelly, R.D. Arnell, J. Vac. Sci. Technol. A 16 (1998) 2858.

[9]- J. Pelleg, L.Z. Zevin, S. Lungo, N. Croitora, Thin Solid Films 197 (1991) 117.

[10]- J.V. Ramana, S. Kumar, C. David, A.K. Ray, V.S. Raju, Mater. Lett. 43 (2000) 73.

[11]- M.M. Larijani, N. Tabrizi, Sh. Norouzian, A. Jafari, S. Lahouti, H. Haj Hosseini, N. Afshari, Vacuum 81 (2006) 550.

[12]- P. Carvalho, F. Vaz, L. Rebouta, L. Cunha, C. J. Tavares, C. Moura, E. Alves, A. Cavaleiro, Ph. Goudeau, E. Le Bourhis, J. P. Rivière, J. F. Pierson, O. Banakh, J. Appl. Phys. 98 (2005) 023715-1-8.

[13]- S. Mahieu, G. Winter, D. Depla, R. De Gryse, J. Denul, Surf. Coat. Technol. 187 (2004) 122.

[14]- J.A. Thornton, Am. Rev. Mater. Sci. 7 (1977) 239.

[15]- J. E. Greene, J.-E. Sundgren, L. Hultman, I. Petrov, D. B. Bergstrom, Appl. Phys. Lett. 67 (20) (1995) 2928

[16]- K. Reichelt,. X. Jiang, Thin Solid Films 191 (1990) 91.

[17]- N. Durand, K.F. Badawi, Ph. Goudeau, Thin Solid Films 275 (1996) 168.

[18]- O. Knotek, R. Elsing, G. Krämer, F. Jungblut, Surf. Coat. Technol. 46 (1991) 265.

[19]- F. Lévy , P. Hones, P.E. Schmid, R. Sanjinés, M. Diserens, C. Wiemer, Surf. Coat. Technol. 120-121 (1999) 284.

[20]- P.E. Schmid, M. Sato Sunaga, F. Lévy, J. Vac. Sci. Technol. A 16 (1998) 2870.

[21]- L.E. Toth, *Transition Metal Carbides and Nitrides*, Academic Press, New York, 1971.

[22]- R. Lamni, E. Martinez, S.G. Springer, R. Sanjinés, P.E. Schmid, F. Lévy, Thin Solid Films 447-448 (2004) 316.

[23]- D.I. Bazhanov, A.A. Knizhnik, A.A. Safonov, A.A. Bagatur'yants, M.W. Stoker, A.A. Korkin, J. Appl. Phys. 97 (2005) 044108.

[24]- L. Pichon, T. Girardeau, A. Straboni, F. Lignou, P. Guérin, J. Perrière, Appl. Surf. Sci. 150 (1999) 115.

[25]- L. Pichon, T. Girardeau, A. Straboni, F. Lignou, J. Perrière, J.M. Frigerio, Nucl. Instr. Meth. Phys. Res. B 147 (1999) 378.

[26]- H. M. Benia, M. Guemmaz, G. Scmerber, A. Mosser, J. C. Parlebas, Appl. Surf. Sci. 200 (2002) 231.

[27]- H. M. Benia, M. Guemmaz, G. Scmerber, A. Mosser, J. C. Parlebas, Appl. Surf. Sci. 211 (2003) 146.

[28]- D. Gall, S. Kodambaka, M.A. Wall, I. Petrov, J.E. Greene, J. Appl. Phys. 93 (2003) 9086.

[29]- J. P. Dauchot, S. Edart, M. Wautelet, M. Hecq, Vacuum 46 (1995) 927.

[30]- M. Yoshitake, T. Nosaka, A. Okamoto, S. Ogawa, Jpn. J. Appl. Phys. 32 (1993) L113.

[31]- B. O. Johansson, H. T. G. Hentzell, J. M. E. Harper, and J. J. Cuomo, J. Mater. Res. 1 (1986) 442

[32]- P. Pyykko, Chem. Rev. 88 (1988) 563.

[33]- M. Lerch, J. Mater. Sci. Lett. 17 (1998) 441.

[34]- H. Wiame, M.-A. Centeno, S. Picard, P. Bastians, P. Grange, J. Eur. Ceram. Soc. 18 (1998) 1293.

[35]- I. Milosev, H. H. Strehblow, M. Gaberscek, B. Navinsek, Surf. Interface Anal. 24 (1996) 448.

[36]- S. J. Clarke,C. W. Michie, M. J. Rosseinsky, J. Sol. Stat. Chem. 146 (1999) 399.

[37]- E. Fuglein, R. Hock, M. Lerch, Z. Anorg, Allg. Chem. 623 (1997) 304.

[38]- M. Ohring, *The Materials Science of Thin Films*, Academic Press, San Diego, 1992.

[39]-W.D. Sproul, M.E. Graham, P.J. Rudnik, M.-S. Wong, Surf. Coat. Technol. 89 (1997) 10.

[40]- A. Kinbara, E. Kusano, S. Baba, J. Vac. Sci. Technol. A 10 (1992) 1483.

[41]- H. Schiller, U. Heisig, G. Beister, K. Steinfelder, J. Strumpfel, C. Korndorfer, W. Sieber, Thin Solid Films 118 (1984) 255.

[42]- I. Safi, Surf. Coat. Technol. 127 (2000) 203.

Chapter 4

Binding Characteristics

4.1. Introduction

The deposition of thin films by physical vapour deposition (PVD) technologies has been used for different applications in several technological fields due to the wide range of material combinations and, therefore, the significant number of possible property gradients. In terms of specific examples of synthetic materials used in these above mentioned applications, the transition metal oxide thin films, MeO*x*, are frequently applied in several optical devices such as antireflection and dense wavelength multiplexing devices and switchable windows [1,2]. These applications are enabled by the excellent mechanical properties of oxide-based films together with a good chemical stability, high index of refraction, and wide optical band gap.

On the other hand, transition metal mononitrides such as ZrN, TiN, and HfN are used as refractory compounds. They exhibit a wide number of exceptional physical properties, including their relatively high hardness, high melting point, chemical stability, and corrosion resistance [3]. The exceptional physical properties of refractory materials may be understood by taking into account that the binding mechanism comprises three bonding types: metallic, covalent, and ionic [4,5]. For a careful and systematic investigation of this combination of properties, experimental investigations using techniques such as X-Ray photoelectron spectroscopy, which probes the electronic density of states (DOS), are of great interest [6]. In fact, it is known that the non-vanishing DOS at the Fermi energy is responsible for the metallic conductivity of ZrN. *K. Schwarz et al.* [7] reported that the particular electronic structure of ZrN consists of a low-lying N 2*s* band followed by the *p- band*, which manly originates from N 2*p* states, but with significant contribution from Zr 4*d* orbitals. The covalent interactions between Zr *4d* and N *2p* orbitals result in the high hardness and high melting point.

The next band is primarily derived from Zr 4*d* states and, thus, it is denoted as *d band*, which, in the case of ZrN, overlaps the p-band. Between the "*p band*" and "*d band*" there is a minimum in the DOS at eight valence electrons. From this minimum, the DOS steadily increases until all nine valence electrons of ZrN are accommodated and so, the Fermi energy, E_F, lies in the "*d band*" with a relatively high DOS. Due to these properties, ZrN is widely used in several technological domains, such as mechanical rotation tools [8], cryogenic thermometers [9], Josephson junctions [10], gates in MESFET transistor technology [11] and in Cu/Si contacts [12].

In spite of the large amount of bibliographic references available on these mononitrides, there are clearly very few studies on nitrides of elements of the group IV with the composition Me_3N_4 (where Me represents the transition metal). In this respect, zirconium and hafnium nitrides show an interesting transformation in electronic structure when composition changes from MeN to Me_3N_4. This transformation is followed by a significant variation in their optical and electrical properties. It is also important to note that these changes from MeN metallic-type compounds towards the insulating Me_3N_4-type phase are not easily achieved, mainly due to the relatively low reactivity of nitrogen towards the metallic element [13]. Nevertheless, Me_3N_4 meta-stable phases have been observed, especially when using implantation or low energy ion-beam bombardment coupled with sputtering [14]. One question that may arise is the possibility to tailor the film bond characteristics between those of metallic nitrides, MeN, and those with high ionic bonding character. An approximation that is currently being investigated is the oxygen addition to the group IV elements. Examples on TiN [15,16], TaN [17] WN [18], NbN [19], FeN [20] and ZrN [21-23] are under intensive research and the available results show that the tailoring of the behaviour of the material from metallic-type to insulating-type by addition of the oxygen atoms to the metallic MeN matrix, seems to be an interesting approach.

4.2. Characterization techniques

Fourier Transform Infrared Spectroscopy (FTIR)

Fourier transform spectroscopy is a technique where the spectra are collected based on measurements of the temporal coherence of a radioactive source, using time-domain measurements of the electromagnetic radiation or other type of radiation. Electromagnetic radiation is a travelling wave of orthogonal electric and magnetic fields, whose intensities vary in time. Its propagation it is described by the wave equation, which is derivable from Maxwell's equations. One of the mathematical processes that describes the resolution of a time-varying wave into its constituent frequencies, independent of what form the dispersing instrument takes, it is the *Fourier decomposition of the waves* [24]. The intensity *versus* time function it is transformed into the intensity *versus* frequency spectrum. The observation and measurement of the radiation absorbed or emitted by atoms and molecules can provide information about their identity and structure and their chemical environment [24]. A spectrum may contain discrete lines and bands and perhaps a continuum.

Fourier Transform Infrared Spectroscopy (FTIR) deals with the infrared region of the electromagnetic spectrum, and exploits the fact that molecules have specific frequencies at which they rotate or vibrate corresponding to discrete energy levels. By interpreting the infrared absorption spectrum, the chemical bonds in a molecule can be determined. FTIR spectra of pure compounds are generally so unique that they are like a molecular "fingerprint". While organic compounds have very rich and detailed spectra, inorganic compounds are usually much simpler (including here most of the cases of thin films).

The infrared (IR) region of the electromagnetic spectrum can be divided into three regions: i) the near-, ii) mid- and iii) far- infrared, regarding to the visible spectrum. The far-infrared, ranging from approximately 400 to 10 cm^{-1}, corresponds to low energy radiation and may be used for rotational spectroscopy. The mid-infrared, ranging from approximately 4000 to 400 cm^{-1}, may be used to study the fundamental vibrations and associated rotational-vibrational structure. This was the selected region of the infrared spectrum that was used to perform the analysis of the samples studied in this thesis, since it allows to detect fundamental vibrations of solid materials. The higher energy near-IR, approximately 14000 - 4000 cm^{-1}, can excite harmonic vibrations. Infrared spectroscopy exploits the fact that molecular bonds vibrate at characteristic frequencies, (see Fig. 4.1.), depending on the elements and the type of bonding.

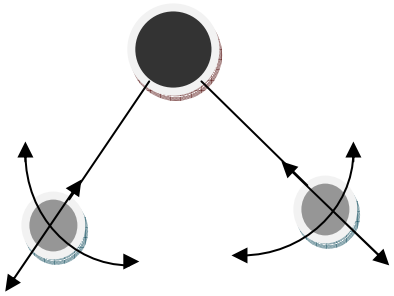


Fig. 4.1. Examples of vibrational modes of water molecule.

A particular bond can give rise to several types of vibration modes, occurring at specific frequencies. According to quantum mechanics, these frequencies correspond to the ground state (lowest frequency) and several excited states (higher frequencies). One bond can be excited, increasing its frequency of vibration, by absorbing photons. For any specific transition between

two states, the energy difference must be equal to the energy of absorbed light. Since the energy of these transitions between molecular vibrational states are in the same order of magnitude of the energy of the photons of the infrared region, the infrared spectroscopy is one of the most appropriated techniques to identify different types of bonds. After collecting the infrared spectrum of a sample, by passing a beam of infrared light through the sample, is possible to determine how much energy was absorbed at each wavelength. Analysis of these absorption characteristics reveals details about the molecular structure of the sample. Nevertheless, the important potential of this technique is not useful for conductive samples since free electrons should absorb all the energies in the IR region.

Raman spectroscopy

Raman spectroscopy is a spectroscopic technique that can also be used to study vibrational, rotational, and other low-frequency modes occurring in a material. It relies on inelastic scattering, or Raman scattering of monochromatic light, usually from a laser in the visible, near-infrared, or near-ultraviolet range. The inelastic scattering of light by matter was predicted, on theoretical grounds, by Brillouin (1922) and by Smekal (1923). The first experimental observation of the inelastic scattering of light was made by Raman and Krishnan (1928).

The Raman effect arises when a photon is incident on a group of atoms and interacts with the electric dipole of the two bonded atoms resulting in a interaction of vibrational and/or rotational motions of molecules with the electromagnetic radiation. In Raman scattering, the energies of the incident and scattered photons are different.

Energy transfer model and Scattering processes

According to quantum theory, a molecular motion can have only certain discrete energy states. A change in state is thus accompanied by the gain or loss of one or more quanta of energy ($\Delta E = h\nu$, were h is Planck's constant and ν the classical frequency of molecular motion). In a simple elastic scattering process a quantum of electromagnetic energy is created at the same time that an identical one is annihilated. In an inelastic light-matter process, such as the Raman effect, the quantum of electromagnetic energy created is not identical to the annihilated one and there is a net change in the state of the bonded atoms. Considering that before the interaction of the radiation with the system there are n_1 photons, each one with energy $E = h\nu_1$, were ν_1 is the

frequency of the incident monochromatic radiation, and the molecule has energy E_i. The interaction of the radiation with the molecule leads to annihilation of one photon of energy $h\nu_1$, creation of a new photon of energy $h\nu_s$, and the transition of the molecule to a state with E_f. The radiation now consists of $(n_1 - 1)$ photons of energy $h\nu_1$ and one photon of energy $h\nu_s$. In the overall process, energy must be conserved an thus $E_{f_i} = h(\nu_1 - \nu_s)$ or $\nu_s = \nu_1 - \nu_{f_i}$. However, the energy $h\nu_1$ does not correspond to any electronic transition energy and the photon of energy $h\nu_1$ is not absorbed in the strict spectroscopic sense, as there is no conservation of energy in this stage of the process [25]. The role of the incident radiation is rather to perturb the molecule and open the possibility of spectroscopic transitions rather than direct absorption. If $h\nu_1$ approaches an electronic transition energy, enhancement of the scattered intensity is observed. Scattering processes involve at least two quanta of energy acting simultaneously in the light-matter system. For classification purposes in this energy transfer model it is convenient to induce N, defined as the total number of incident photons involved in a single scattering act, i.e., the number of incident photons annihilated. The Raman scattering process involves two photons overall, one incident and one scattered, so that N + 1 = 2. For Raman scattering, if the created photon is less energetic than the annihilated one, the scattered light presents lower frequency than that of the incident light ($E_f > E_i$ then $\nu_s = \nu_1 - \nu_M$), and we have Stokes Raman scattering [25,26]. If the created photon is more energetic than the annihilated one ($E_f < E_i$), the Raman frequency will be higher than that of the laser ($\nu_s = \nu_1 + \nu_M$) and the anti-Stokes spectrum will be produced. The Stokes and anti-Stokes spectra contain the same frequency information. The scattering processes occur in 10^{-14} seconds or less and are illustrated in figure 4.2. The laser frequency ν_1 reappears as the relatively strong Rayleigh line, and the lower intensity Raman "sidebands" are the result of inelastic scattering. It should be emphasized that Raman effect comprises a very small fraction, about 1 in 10^6, of the incident photons.

Raman frequencies can be measured relatively to that of the excitation frequency ν_1, thus the Raman frequencies will then appears at $\pm\nu_1$. Typically, a vibrational frequency has a value of the order of 10^{12} s^{-1}, dividing the vibrational frequency by the velocity of light is expressed in cm s^{-1}. Raman scattered light is frequency-shifted with respect to the excitation frequency, but

the magnitude of the shift is independent of the excitation frequency. This "Raman shift" is therefore an intrinsic property of the sample. The frequency of a vibrational mode depends on molecular structure and environment, atomic mass, bond order, dopants, molecular geometry and hydrogen bonding (if present).

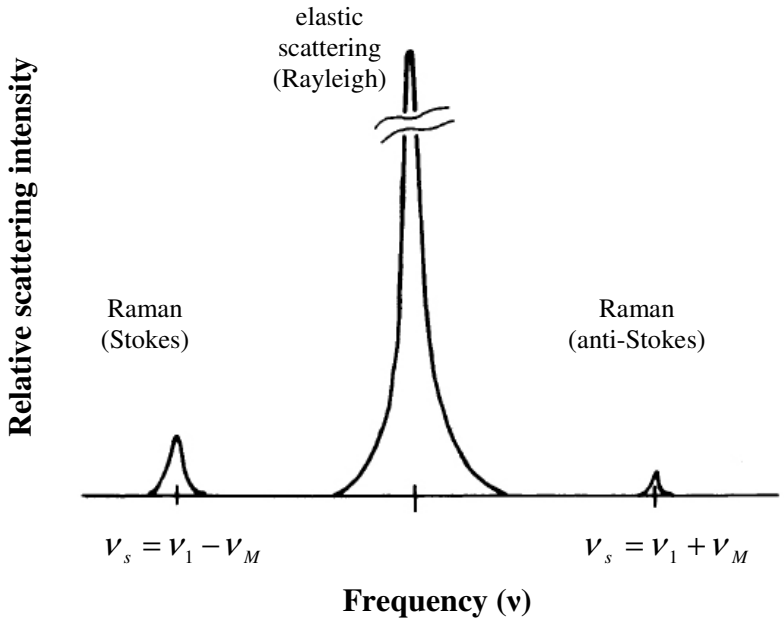


Fig. 4.2. Raman and Rayleigh scattering of excitation at a certain frequency [26].

All these parameters affect the vibrational force constant which, in turn, dictates the vibrational energy. The relative intensity of a Raman band is correctly obtained by integration over the entire spectral profile [27]. Not only the Raman spectral frequency shifts, or, simply, wave numbers can give information of the material analysed but also the shape or profile of a Raman band.

Raman Selection Rules and Intensities.

A simple classical electromagnetic field description of Raman spectroscopy can be used to explain many of the important features of Raman band intensities. The effect of the electric field on a molecule is to polarize the electron distribution. If the electric field is not too strong, it will induce an electric dipole moment given by: $\vec{\mu} = \alpha\vec{E}$, were α represents the polarizability of the molecule. This induced dipole moment then emits a photon, leading to either Raman or Raleigh scattering. Raman scattering occurs because a molecular vibration can change the polarizability.

This change is described by the polarizability rule for a Raman-active vibration. This change in polarizability during the vibration is given by the equation:

$$\partial\alpha/\partial Q \neq 0 \qquad \text{(Eq. 4.1)}$$

were Q is the normal coordinate of the vibration and α represents the polarizability of the molecule [27].

The scattering intensity is proportional to the square of the induced dipole momentum, that is to the square of the polarizability derivative $\left(\partial\alpha/\partial Q\right)^2$. If a vibration does not significantly change the polarizability, then the polarizability derivative will be near zero, and the intensity of the Raman band will be low.

X-ray Photoelectron Spectroscopy (XPS)

X-ray Photoelectron Spectroscopy is also known as Electron Spectroscopy for Chemical Analysis (ESCA), and is a widely used technique to investigate the chemical composition of the surface of materials, as well as their bonding states. In order to apply this technique, the samples have to support ultra-high vacuum conditions. This technique was developed in the middle of the 1960's by Kai Siegbahn and his research group at the university of Uppsala, Sweden. This technique is based on the photoelectric effect [28], consisting on the emission of electrons (photoelectrons) from a surface of a material that is being irradiated by photons, see Fig. 4.3.

The energy of X-rays photons is enough to eject electrons from most of the energy levels, including the core levels, putting the atom in an unstable energetic state. The atom returns to the fundamental state by different ways. One of them is the emission of X-ray (or other) photons, but the technique does not analysis the radiation emitted from the sample, so this process does not perturb the XPS analysis. The detector is only electron sensitive.

The energy of the emitted photoelectrons is used for XPS analysis. Another process resultant from the interaction of X-ray radiation with the sample, is the emission of Auger electrons, where an electron occupies a vacancy in a lower energy band (see Fig. 4.3). The photon emitted, resultant from this transition, is absorbed by another electron. The energy of the photon may be enough to cause ionization.

This mechanism “disturbs” the XPS analysis since the detector cannot discriminate photoelectrons from Auger electrons. Nevertheless, since electrons Auger do not depend on the

initial X-Ray photon energy, but only by the band energy difference, by using two X-rays sources with different energies it is possible to distinguish the photoelectrons from the Auger electrons.

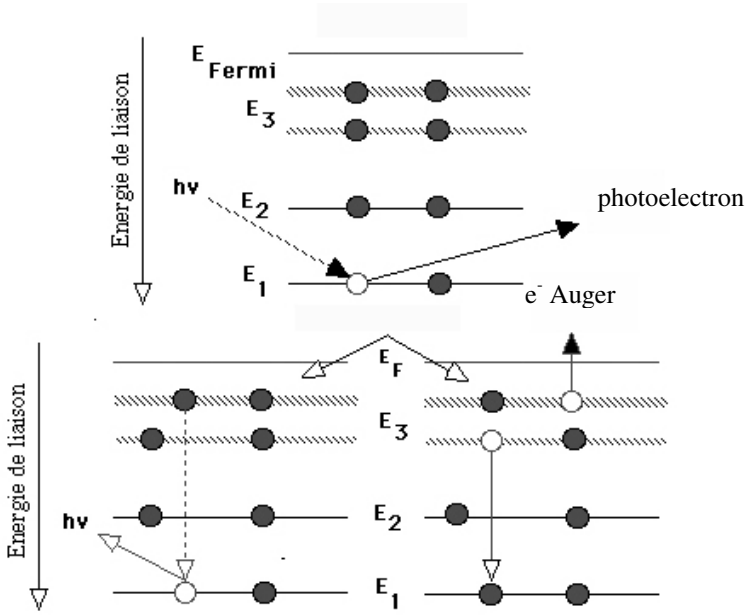


Fig. 4.3. Scheme of electron photoemission resultant from the interaction of X-ray radiation with the sample

The kinetic energy of the emitted photoelectron depends on two parameters: The X-ray photon energy and the binding energy of the atoms. The first one only depends of the X-ray source and the second depends on the type and chemical environment of the atom. On this basis, by knowing the X-ray source energy and the kinetic energy of emitted photoelectron, it is possible to determine its binding energy. These energies are related by the equation:

$$K_e = (E_{X-ray}) - (\text{Binding Energy}) - \psi \qquad \text{(eq. 4.2)}$$

where K_e is the photoelectron kinetic energy, (E_{X-ray}) the energy of the X-ray photons and ψ the spectrometer work function.

Since the binding energies of the outer shell electrons depend strongly on the bonding states of the atom, it is possible to identify the elements present and their chemical state. This allows characterizing chemically the top of the surface of any solid supporting high vacuum, being it

insulator or conductor. Although these advantages, this technique allows only a very small limited depth of analysis (around 10 nm, see Fig. 4.4.) that results from the mean free patch of photoelectrons in matter, since X-rays penetrate much more deeply.

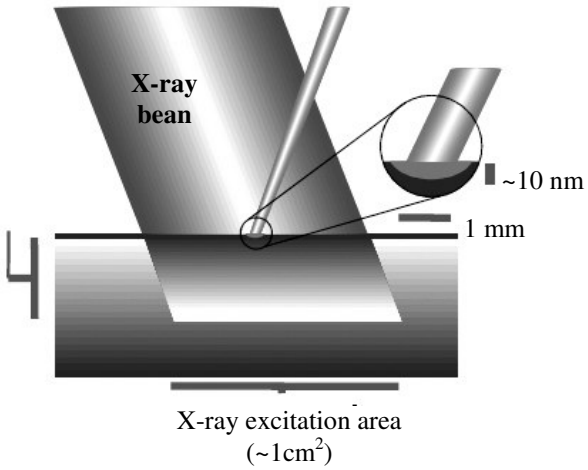


Fig. 4.4. Scheme of depth of the analysed area.

Due to the very low depth of analysis, XPS is a very sensitive technique to any surface contamination and/or degradation, and it is usually necessary to sputter clean the material's surface.

The XPS peaks position (binding energy) of an element may change by a few of eV (or tenth of eV) due to a change in the chemical bonding of that element; this effect is called the *chemical shift*. The value of the shift, and its variation to lower or higher energies, depend on the chemical environment. Although, there is a generic rule that says that the binding energy increases if the atom is bonded to a more electronegative element.

XPS spectrum of some elements shows that emission from some core levels does not give rise to a single photoemission peak, but a closely spaced doublet. When electrons are emitted from an atom with unpaired spins in a valence orbital, they interact with the unpaired spins. Interaction depends upon the spin of the electron left in the orbital with the hole. Since the *d* and *p* orbital's have non-zero orbital angular momentum (l = 2 and 1 respectively), there will be coupling between the unpaired spin and orbital angular momentum. For example the electronic configuration of the initial state of the Zirconium is $(1s)^2(2s)^2(2p)^6(3s)^2(3p)^6(4s)^2(3d)^{10}(4p)^6(5s)^2(4d)^2$. The removal of an electron from the 4 sub-shell by photo-ionization

leads to a $(4d)^1$ configuration for the final state - since the *d*-orbital have non-zero orbital angular momentum ($l = 2$), there will be coupling between the unpaired spin and orbital angular moment. In this case, the resultant angular momentum arise from the single hole in the *d*-shell; a *d*-shell electron (or hole) has $l = 2$ and $s = 1/2$, which again gives permitted *j*-values of 3/2 and 5/2 with the latter being lower in energy. This spin-orbit splitting is of course not evident with *s*-levels ($l = 0$), but is seen with *p*, *d* and *f* core-levels which all show characteristic spin-orbit doublets.

Electron Energy Loss Spectroscopy (EELS)

Electron Energy Loss Spectroscopy (EELS) is a surface technique that has been extensively used for qualitative identification of compounds [29]. The process is very simple; in EELS a material is exposed to a beam of electrons with a known, narrow range of kinetic energies. Scattering processes experienced by signal electrons on their way out comprise multiple elastic and inelastic collisions. While elastic scattering occurs via interaction of the projectile with the screened Coulomb potential of individual atomic nuclei, inelastic scattering comes about through deceleration in a polarization field of the sea of weakly bounded solid state electrons [30]. Different types of inelastic excitations are distinguished: i) bulk or volume excitations, where the polarization field is the response of an unbounded medium to the incoming projectile [31-33]; ii) surface excitations decaying within a few angstroms at both sides of the solid/vacuum interface [34-37] and; iii) intrinsic excitations where the polarization field is caused by screening of the suddenly appearing core hole, when an Auger or photoelectron is liberated from an atom [38]. The emitted signal electrons are decelerated in this polarization field [30].

Some of the most common processes that can originate electron energy loss are plasmon losses and collective electronic excitations of the lattice of the solid, which can be resultant from de bulk or from the surface of the analysed material.

EELS is a technique which is sensitive to changes in both the occupied and unoccupied densities of states [39-40] and probes the electronic density of states in the material [39,40,41]. This spectroscopy can be performed in either transmission or reflection mode. In the transmission mode, high-energy electrons (10 - 2000 eV) impinge on a thin sample and those scattered inelastically, while passing through the sample, are energy analyzed. In the reflection mode (REELS), backscattered electrons are energy analyzed [42].

Results and discussion

4.3. Bonding characteristics of the prepared films.

4.3.1. Fourier Transform Infrared Spectroscopy (FTIR)

In order to further investigate the different compositional and structural zones observed in the previous sections, detail infrared spectroscopy (FTIR) studies were carried out. The main point to be searched in this chapter is that one related with the type of bonds that are formed in the films. In short terms, the main goal is to confirm whether the differences in composition and structural arrangements are prompted by differences in the types of bonds that are formed during the film growth, or if by the contrary these differences in composition and structural arrangements have no direct correlation with the types of bonds that are formed.

As the films structure change from zirconium nitride (*fcc*-ZrN and *orth*-Zr_2N_3) towards γ-Zr_2ON_2 and finally to *mon*-ZrO_2, discontinuous changes, as well as smooth and continuous ones, are expected to be detected in the infrared spectra. This comes because any static and/or dynamic change in the structure that should, in principle, lead to a variation in the phonon behaviour, and thus the analysis of the wave-number, intensity and line width evolution of the whole spectra as a function of gas flow, is expected to give insight into the structural changes. Such analysis is known as hard mode spectroscopy, in opposition to the analysis of directly involved modes, and it is a powerful method for the analysis of phase changes.

Further, in this kind of mixed systems, the spectra are the consequence of both short- and long-range ordered regions and chemically ordered regions. Then, the selection rules are relaxed because of the disorder, off-centre atomic shifts, presence of chemically ordered regions and/or local symmetry and an assignment of each mode becomes highly complex. It is why the observed broad peaks are rather labelled as bands. Furthermore, and for clarification purposes, the whole detailed analysis (intensity, line-width and frequency position) is not shown here, but rather the most pertinent features which reveal/confirm the chemical/structural changes already referred in previous chapters (chapters 2 and 3) occurring at the films as the gas flow changes (and consequently their composition and structure).

FTIR measurements were carried out in the transmission mode for studying the chemical bonding configuration of the films. The spectral shape is ruled by two different mechanisms, i.e. absorption due to vibration species involved in the sample, and to multiple reflections of the beam throughout the thin film. The absorption mechanisms prevail in the spectral region below

1500 cm^{-1}. In transmittance, vibration modes cause absorption of the beam across the sample, leading to downward oriented peaks. Above 1500 cm^{-1}, the prominent spectral feature is due to the interference of partial beams reflected successively at the front (film/air) and rear (film/substrate) interfaces of the layer [43].

Figure 4.5. shows the transmission spectra (in the range 400 to 3000 cm^{-1}) of selected samples belonging to the four different zones presented in previous chapters.

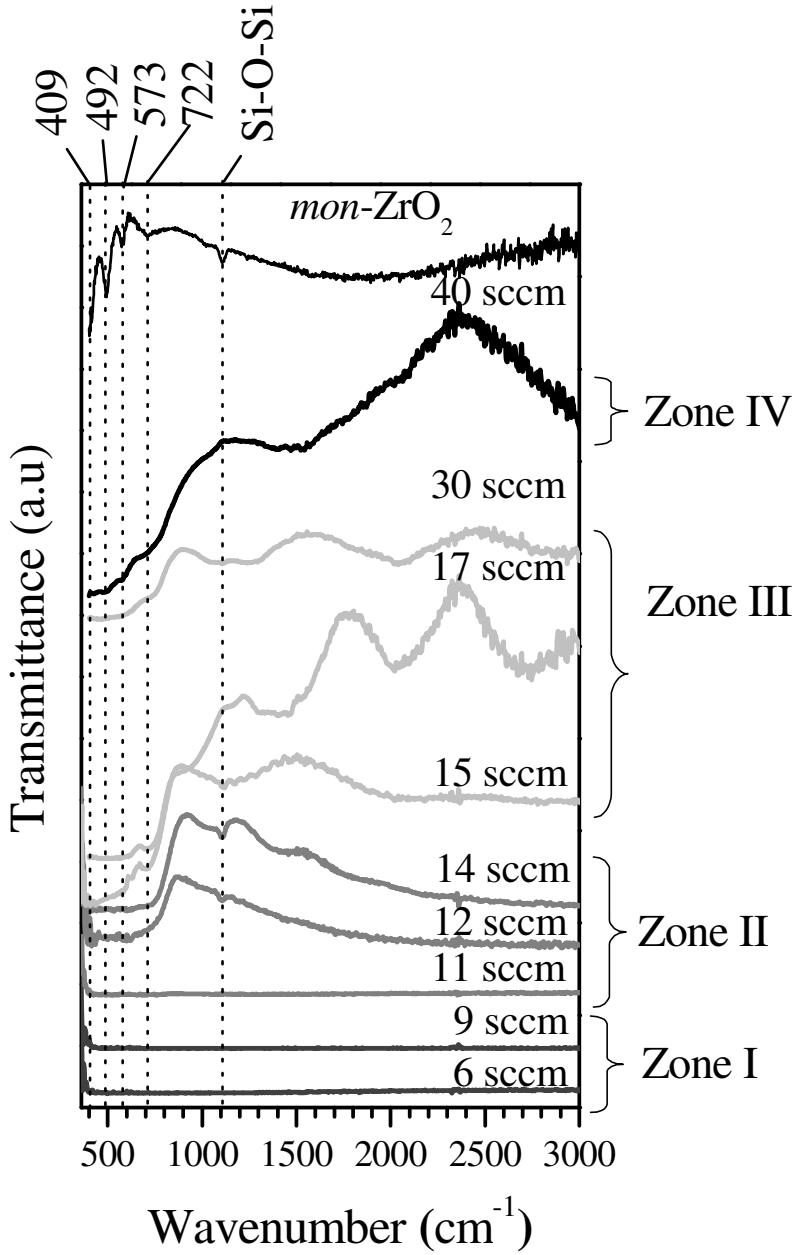


Fig. 4.5. FTIR spectra of samples from series 1. For comparison purposes, a "pure" ZrO_2 sample is also presented (prepared with only O_2 as reactive gas).

The first conclusion that may be drawn form this figure, is that similarly to what has been observed in the composition and structural analysis, also in terms of the types of bounds developed by the films, the four different zones give rise to some important changes. Regarding the samples prepared within zone I (samples revealing an *fcc*-ZrN type structure, with a sub- and closely stoichiometry condition), results show a typical metallic-like behaviour, with no transmission in the infrared (IR) region. As we will see in the study of the electronic structure of these samples, they present a clear non-vanishing of the *d* band near the Fermi level. These free electrons should explain the optical behaviour in the IR region. Similar to metals, the free electrons should absorb all the energies in the IR region.

Regarding the samples from the second zone, there is a change in the infrared optical response of the coatings with the abrupt increase of transmission around 800 cm^{-1} with an overlapping of the typical IR behaviour of the samples from zone I for lowest wave numbers, see figure 4.5. This evolution is a good indication that the absorption mechanisms are changing due to the changes in the electronic structure of the coatings going from zone I through zone II, as we will se later on in this chapter.

Regarding the already mentioned possibility of having a very thin amorphous oxide tissue within the structural arrangement of the samples from this zone II, results are far from being conclusive. In fact it should be expected that some features would appears for wave numbers lower than 600 cm^{-1}, similar to the result obtained for the "pure" ZrO_2 sample (see Fig 4.5). As it can be observed in figure 4.5, it is quite difficult to claim it, thus reinforcing the possibility to have the oxygen doping the Zr_3N_4 structure. Moreover, the sample deposited with a reactive gas flow of 14 sccm shows a broad band near 1050 cm^{-1}. This feature is probably due to the Si–O stretching mode due to the interfacial SiO_2 (from the oxidize Si surface) [44].

Zone III, present a similar abrupt increase of transmission around 800 cm^{-1}, regarding the zone II, but at lower wavenumbers a new band appears close to 720 cm^{-1}. *Neumayer et al*. [45] attributed this band to Zr-O vibrations. The appearance of this band should be associated to the increase of oxygen content of the coatings lying in this zone (zone III) regarding the samples of from zone II.

For the spectrum of the ZrO_2 sample, three main absorption features are visible at wave numbers 409, 492, 573 and 722 cm^{-1}. These peaks are characteristic of the formation of ZrO_2 films, in good agreement with the results reported by *Neumayer et al*. [45].

This mode structure is still partially observed in the film prepared with a gas flow of 40 sccm. From the comparison of these results with those of the ZrO_2 reference sample, it can be assumed that the crystal structure of the film is of monoclinic-type, which is consistent with the XRD measurements.

4.3.2. Raman spectroscopy

In order to further clarify the structural evolution of zirconium oxynitride, specially in what concerns to the samples from zone II (where XRD seems to indicate the presence of an oxygen doped Zr_3N_4 orthorhombic-type structure (see Fig. 3.9, chapter 3), as well as to further attest the different composition and structural zones already referred, Raman spectroscopy has been used as a local probe of the of the oxynitride samples (namely those from series 1). The selected samples belong to the first three compositional and structural zones. The selection of the samples were based on the propose of clarifying the existence or not of an amorphous oxide phase and further study the structural evolution already described in chapter 3. On this basis, no samples lying in the last zone (zone IV-40 sccm) were analysed.

Moreover, and even after the compositional and structural characteristics analysis, one question still remains: *is there a thin amorphous oxide phase, probably within the grain boundaries, in the samples the samples prepared within zone II*? Since Raman spectroscopy allows to study crystalline or amorphous samples, it appears again to be a good choice to answer this question.

Raman measurements were performed at room temperature with a Dilor triple monochromator, equipped with a liquid nitrogen cooled charge couple device (CCD) detector, with a resolution better than 1 cm^{-1}. The excitation line, 514.5 nm, of an argon ion laser was focused onto the sample using a ×100 MS Plan objective of an Olympus Microscope BHSM, in a backscattering geometry. The spectra were obtained with a measured power of about 10mW on the sample, during an integration time of 120 s, over the range 80–1200 cm^{-1}.

To correlate the changes in Raman spectra of all samples, each spectrum was normalized to the total scattering intensity. To analyse the changes due the deposition parameters, the “true” line shape of the spectra must be found. To recover this line shape, the position and the widths of the scattered bands, a least squares best fit with five Lorentzian profiles was performed. In order to compare the evolution of structural modifications in ZrO_xN_y samples, the spectra of ZrN and

ZrO_2, deposited in the same chamber, are depicted in figure 4.6.b. and c, respectively. The analysis of the evolution of the Raman signal, with the variation of gases flow, will be centred on two aspects: the first one will be the changes in the spectral shapes; the second a quantitative analysis based on band or peak position and the relative intensities of some of the detected peaks.

In zirconium nitride, first order Raman scattering is forbidden as a consequence of selection rules. However due to disorder, induced by the deposition technique, the translation symmetry is lost, and thus all the modes can participate in the scattering. Raman spectra will be an "image" of the Density of Vibrational States (DVS) [46].

Raman spectrum of zirconium nitride (see Fig 4.6.b)) is dominated by an asymmetric band centred at around 500 cm^{-1}, and in the low frequency region by the presence of two bands centred at around 165 and 220 cm^{-1}, reflecting the material's DVS. In the low frequency range, the bands are attributed to the disorder of single phonons and second order processes. For higher frequencies the presence, and the asymmetry, of the bands is due to the superposed contributions of disorder of optical phonons and second order combination of acoustic and optical processes [47]. Figure 4.6.a) shows the Raman spectra of the coatings deposited with reactive gas flow lower than 11 sccm, indexed to the first zone (see Fig. 2.14, chapter 2 and Fig. 3.5, chapter 3).

The absence of sharp and well-defined peaks should be attributed to the local structural disorder of the prepared films. Furthermore, the spectral shape of zirconium oxynitride samples (Fig. 4.6.a)) resents some similarities with the spectrum of zirconium nitride (Fig. 4.6.b)) It can be seen that in the region below 300 cm^{-1}, two bands occur, which possess positions close to the bands observed in the spectrum of as-deposited ZrN (see 4.6.b)). For frequencies higher than 300 cm^{-1}, the presence of a large band extended up to frequencies around 800 cm^{-1}, although with noticed lower intensity when compared with the band of the ZrN spectrum (see Fig. 4.6.b)) is observed.

With the increase of the reactive gas flow from 6 to 10 sccm, with the consequent increase of metalloid content already described, the spectral shape continues to change and a shoulder located at around 420 cm^{-1} starts to appear, as can be seen in figure 4.6.a). Associated to this spectral evolution, there is also the zone of higher wave lengths, where an overlapping of low frequency range features and a transformation to a asymmetrical band centred at ~170 cm^{-1} is also observed for the sample deposited with 10 sccm (see Fig. 4.6.a))

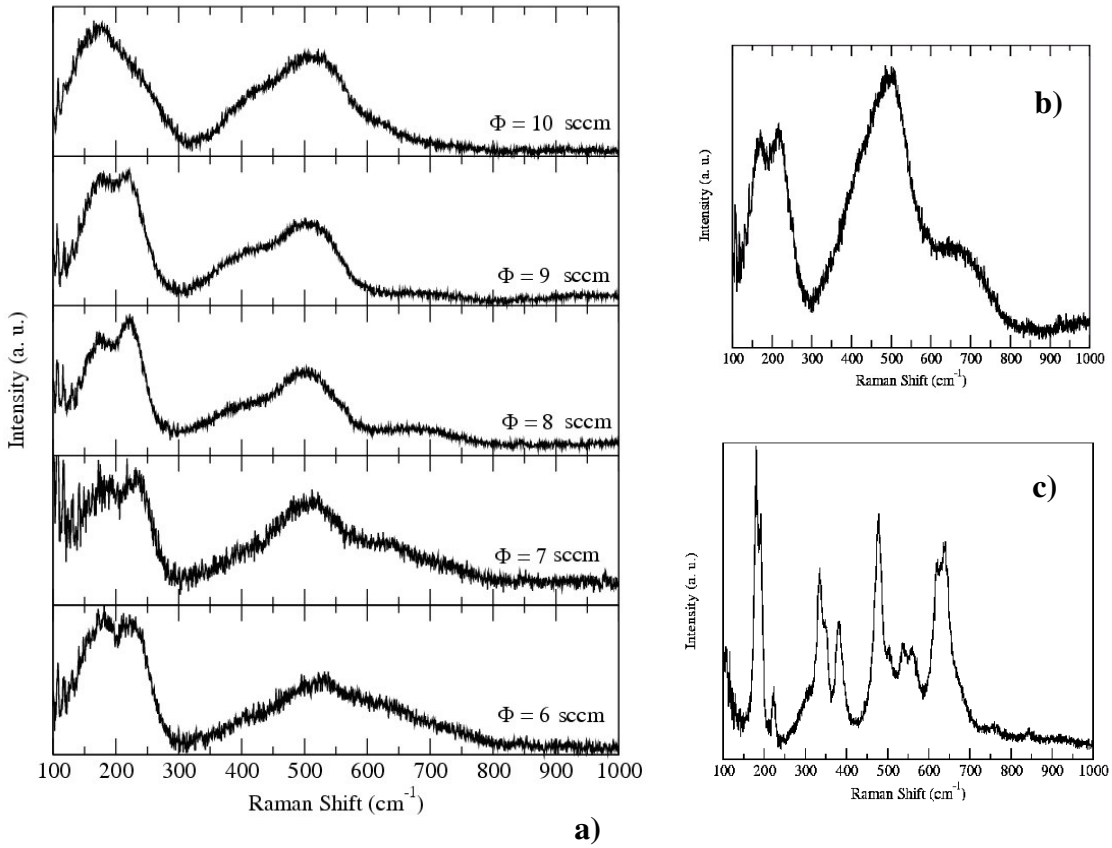


Fig. 4.6. Raman spectra **a)** of films as a function of reactive gases flow rate, from 6 to 10 sccm; **b)** Zirconium Nitride and **c)** Zirconium Oxide.

In accordance with the observed in composition and structural features, a considerable change of the spectral shape occurs for reactive gas flows between 11 and 13sccm, as can be seen in the spectra depicted in figure 4.7. From this figure, it is possible to observe that the number of visible bands increases with the appearance of new bands in the region between 250 and 300 cm^{-1}, and also in the region between 400 and 700 cm^{-1}.

For flow rates higher than 13 sccm, another modification of the spectral shape is observed. In the present case, the reduced number of visible Raman bands seems closely related to the overlap of bands in the region between 200 and 400 cm^{-1} and the decrease in intensity of the band located at 640 cm^{-1}.

In consequence the spectra are dominated by a large band centred around 460 cm^{-1}. In all the spectra presented in figure 4.7, some of the features appear in positions close to the expected frequencies of modes belonging to monoclinic zirconium oxide. Nevertheless, the presence of broad bands, indicative of local disorder, could be due to a non-stoichiometric phase of ZrO_xN_y-

type structure and to a poorly crystallized *orth*-Zr_3N_4(O) structure, as in fact already discussed in chapter 3.

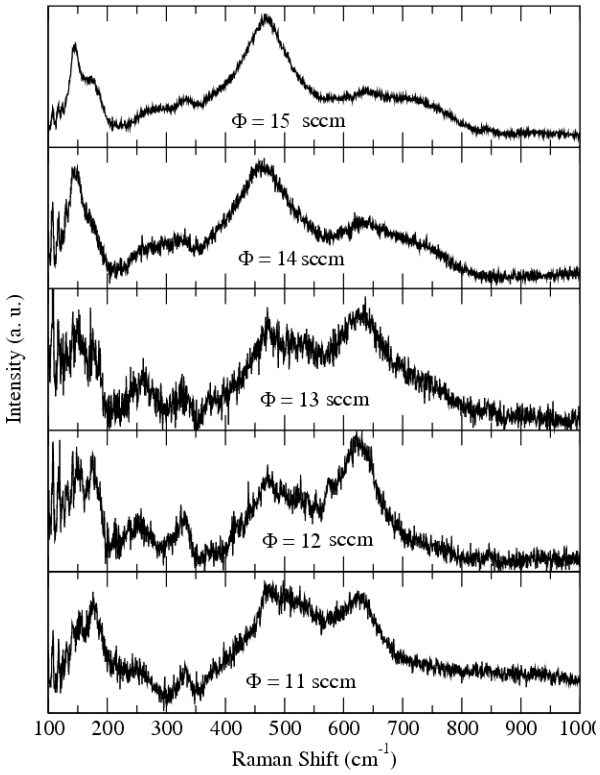


Fig. 4.7. Raman spectra of films as function of reactive gases flow rate, from 11 to15 sccm.

In order to clarify all these changes, figures 4.8. and 4.9 present the fitting results of the position for some bands, which have been chosen to perform a qualitative study: two bands situated in the low frequency range, centred around 167 and 220 cm^{-1}; and two bands situated at higher frequencies, centred around 475 and 680 cm^{-1}.

As it can be observed in both figures (Fig. 4.8 and 4.9), it is possible to divide the evolution of the band position in three zones, and correlate the observed behaviour with the observations that have been discussed for composition and structural features.

The observed shifts in band position could be attributed to film stresses, to non-stoichiometry of the deposited films and to changes in local structural arrangements, resulting from the deposition conditions itself.

The Raman features reinforce the already division of the compositional and structural zones. Nevertheless, the sample deposited with 14 sccm is indexed in the previous chapters as lying in the second zone. Although this sample was indexed in compositional and structural evolution as

zone II, it represents a transition sample between zone II and zone III, showing a crystalline structure resulting from a mixture of *orth*-$Zr_3N_4(O)$ and the γ-Zr_2ON_2 structures.

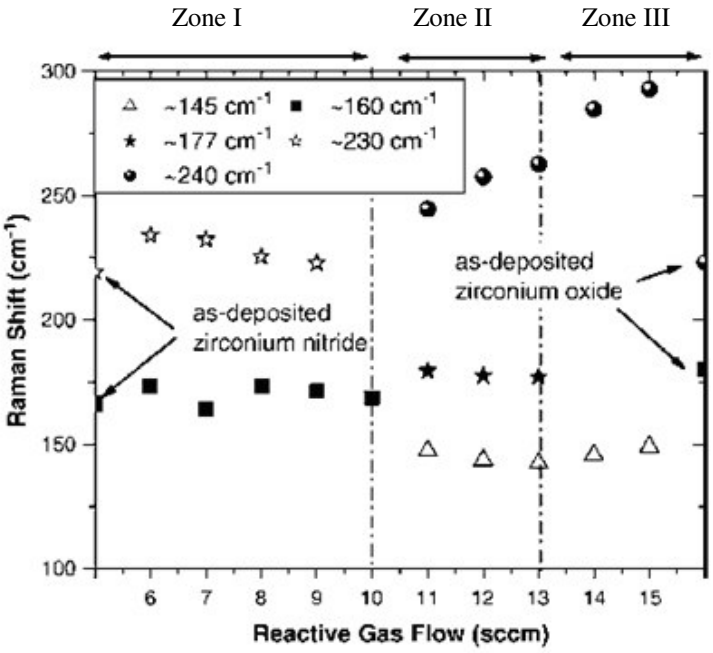


Fig. 4.8. Variation of the Raman shift of low frequency bands, as function of reactive gases flow rate.

Looking at figure 4.8 it is possible to observe that two new bands appear (~150 and ~250cm^{-1}) for the samples deposited with reactive gas flows between 11 and 13 sccm, when compared with the samples deposited with gas mixture flows lower than 11 sccm. These bands appear in Raman sift positions quite different from those observed for zirconium oxide (see Fig. 4.8), questioning again the possibility of having a very thin amorphous oxide phase in these samples.

Figure 4.9 presents the variation of Raman shift of high frequency bands, as function of reactive gases flow rate. For the samples from the first region, the incorporation of oxygen in zirconium nitride lattice is expected, as well as the substitution of nitrogen atoms by oxygen ones, and consequently the appearance of new bands in Raman spectra is expected: the shoulder located at ~400 cm^{-1} and a large band located at ~690 cm^{-1} (see Fig. 4.9). These bands are present for flow rates higher than 8 sccm, but they vanish for flow rates equal to 10 sccm. The observed shifts for the bands located at ~240 and ~480 cm^{-1}, to higher and low frequency respectively, cannot be attributed only to compressive stress, but also to lattice dynamics.

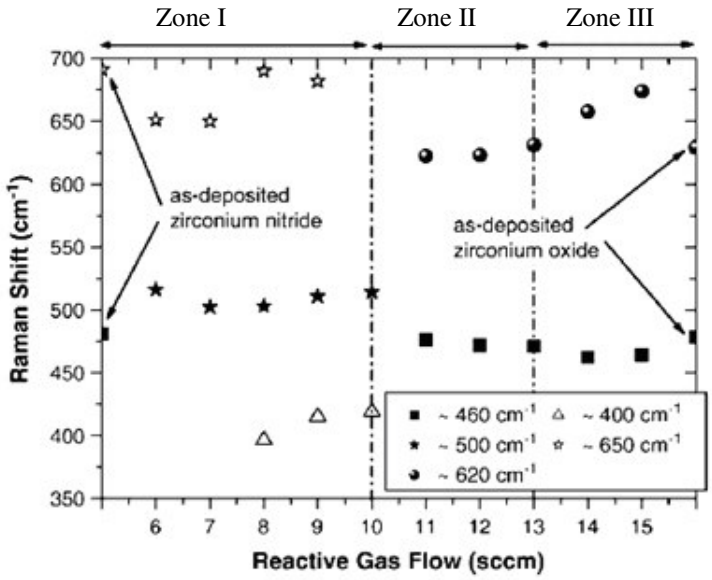


Fig. 4.9. Variation of the Raman shift of high frequency bands, as function of reactive gases flow rate.

The effect of increasing oxygen content from ~10 (10sccm) to close to 30 at. % (15sccm) on Raman spectra is clearly seen in zone III, with the continuous shift to higher energy of the band located close to 600 cm^{-1} (see Fig. 4.9). This shift evolutes to higher energy, which values, are quite different from those observed for zirconium oxide. Questioning once more time the possibility of formation of a very thin oxide phase.

4.4. Electronic structure and oxidation state

4.4.1. X-ray Photoelectron Spectroscopy (XPS)

In order to explain the electrical and optical behaviour of the samples, detailed electronic structure characterization was performed. This characterization includes X-ray Photoelectron Spectroscopy valence band and core analysis and correlate them with the compositional and structural features.

X-ray photoelectron spectroscopy (XPS) - Preparation of the samples

Both XPS core and valence band spectra were recorded after successive sputtering-clean processes with Ar^+ ions (3.5 kV, 30º incidence), until a stationary compositional regime was reached. Spectra were obtained in the ΔE constant mode with 50 eV energy steps. Shirley

algorithm was applied for background subtraction [48]. In order to eliminate the "charging effect" in the XPS analysis, all spectra where the N 1s peak was clearly observed were calibrated to N 1s position - 396.2 eV. This peak position is referred in literature as the energy of the N 1s peak in ZrO_xN_y [49,50]. Anyway, this is not the "ideal" calibration, since the N 1s energy peak should be different in ZrN, Zr_3N_4 and ZrO_xN_y states. This choice results from two factors: i) the inexistence of Ar peaks in some of the sputter-cleaned samples and, ii) the surface oxide degradation of the samples. The peak located at E_B ~ 396.2 eV is referred in the literature as representative of Zr-N bonds in Zr_3N_4 phase [51,52], and to the Zr-O-N bond type in ZrO_xN_y compounds [53,54]. Since zirconium and nitrogen can present similar ionic valences in zirconium oxynitride and in the Zr_3N_4 form [50], the selected calibration should be the most adequate choice. The oxide coating (zone IV) was calibrated to the Ar $2p_{3/2}$ - 242.6 eV and N 1s - 396.2 eV.

X-ray photoelectron spectroscopy (XPS) -Valence Band

Figure 4.10 shows experimental XPS valence band spectra for representative samples lying in the different compositional and structural zones previously identified (chapter 2 and 3). Assuming that there is no shift in the position of the Fermi energy, the valence band spectra characteristics of those four zones can be derived. The spectra are dominated by the Zr 4*p* levels, but the O 2*s,* N 2*s* and molecular orbitals associated with O2*p*/N2*p* and Zr 4*d* valence levels can also be observed. *Bazhanov at al.* [55] already reported that the valence band top in zirconium oxynitride is formed mainly by N 2*p* orbitals, while the valence band bottom is composed of O 2*p* orbitals, and that the conduction band in zirconium oxynitride structures consists predominantly of Zr 4*d* orbitals, with also a significant contribution of Zr 4d states to the valence band, indicating that the Zr–(O)N bonds in this compound have a significant covalent character.

The first important observation is that the Zr 4*p* levels in the oxide zone (zone IV) appear chemically shifted by ~ 3.5 eV to higher binding energy with respect to the nitride (zone I). This shift is most likely due to the increase of the ionic character of the bonding. Moreover, some authors have claimed that the Zr *4p* peak of zirconium oxide present a shift of ~ 4 eV to higher binding energies regarding to the metal [56,57]. In nitrides, the Zr 4*p* core level exhibits an energy shift towards higher binding energy, being of about 1.5 eV in the case of Zr_3N_4-type films, if compared to the value of metallic zirconium [58].

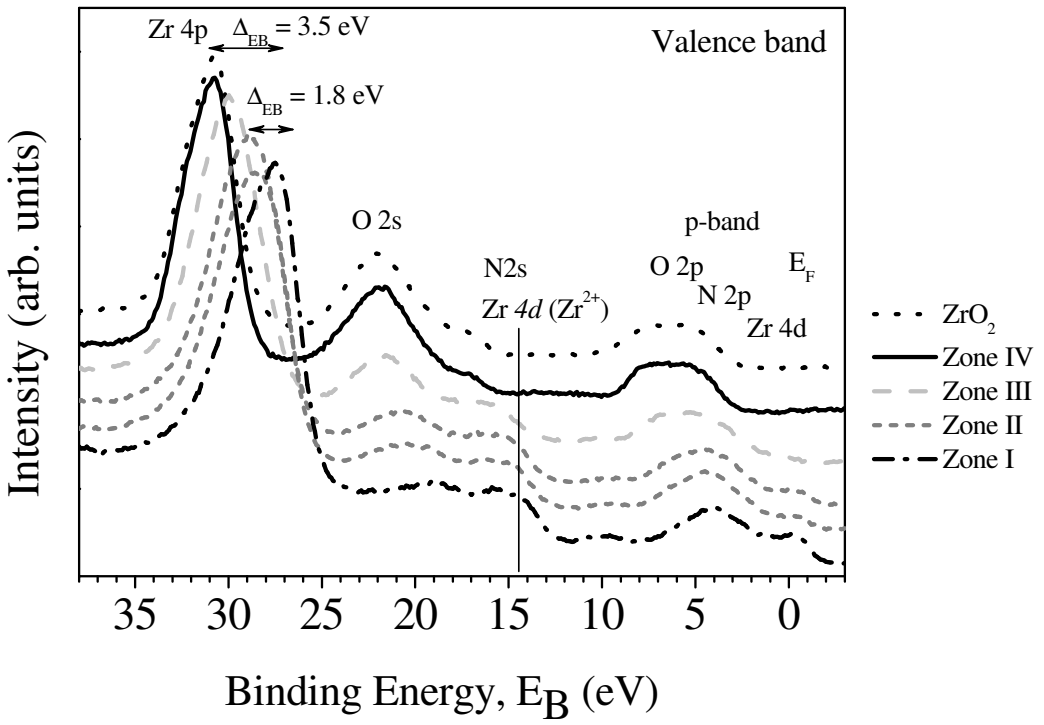


Fig. 4.10. XPS valence band spectra for representative samples lying in the different zones previously identified for the series 1.

Associated with this shift of the Zr levels, there is also a decrease of the band at the Fermi level, until it disappears for samples lying in zone III (oxynitride-type films zone), and a parallel growth of a broad band at energies between 3 and 8 eV. This could indicate a progressive transfer of zirconium 4*d* valence electrons to the O 2*p* and N 2*p* bands, until the complete depopulation of the *d-band*, the films becoming therefore insulator-type. Associated to the decrease of the *d band* at the Fermi levels is the decrease in intensity of the N 2*s* peak and an increase of the O 2*s,* from films within zone I to those in zone IV. This variation is the result of films variation from N to O dominant. The difference in energy of the *2s* peaks (N *2s* and O *2s*) reflects the increase of the nuclear charge, which results in contracted orbitals and lower-lying energy levels [59].

Also from figure 4.10 it is possible to determine the energy gap between the top of the valence band and the Fermi level of ~5eV (energy distance between the *p* band and Fermi level) for the films corresponding to zones III and IV, reinforcing the idea of a progressive tendency to form insulating-type films. This could be interpreted from the large energy difference between

the O 2*p* and N 2*p* bands and the *nd* orbitals that promotes an intrinsic gap between the *p* and *d* bands in the material. In contrast to fcc zirconium nitride (films within zone I), which is a metallic conductor, monoclinic zirconium oxide (and corresponding films from zone IV) is an insulator, with an electronic configuration of $4d^0$ valence electrons located in the O 2*p*-derived band at energies between 4 and 11 eV, with a large energy difference between the 2*p* and the *nd* orbitals originating an intrinsic band gap [59].

Finally, figure 4.10 also shows that the *p*-band is sifting to higher energies, followed by an increase of the O2*s* band. This could indicate that the hybridization between the Zr 4*d* and O2*p* is increasing regarding to the Zr 4*d* and N 2*p* hybridization. In order to clarify this issue, figure 4.11 shows the subtraction spectrum between pairs of consecutive zones.

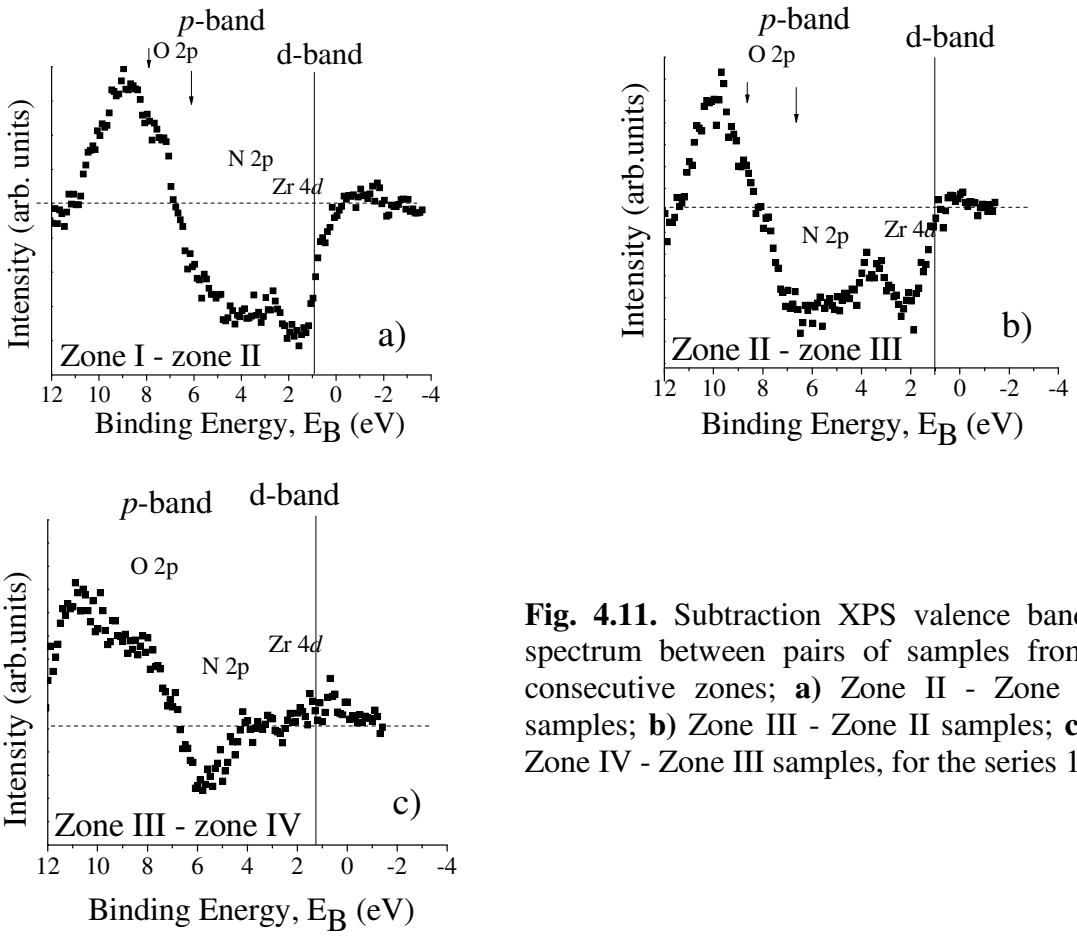


Fig. 4.11. Subtraction XPS valence band spectrum between pairs of samples from consecutive zones; **a)** Zone II - Zone I samples; **b)** Zone III - Zone II samples; **c)** Zone IV - Zone III samples, for the series 1.

Plots from figures 4.11.a) and b) show that there is a constant reduction of the Zr 4*d* and N 2*p* bands, followed by an increase of O 2*p* band. According to previous studies [60-63], this evolution can be qualitatively interpreted as an increase of the transference of *d*-electrons from

the band at the Fermi level to states between 6 and 9 eV in the O 2*p* band, together with a reduction of transference of *d*-electrons at the Fermi level to the N 2*p* band, which would be the consequence of the oxygen increases in the first three zones. Again, this behaviour can be well correlated with the decrease of the metallic and covalent character of the binding mechanisms and an increase of the ionic character, confirming the progressive change form nitride-type coatings (zone I) to oxide-type ones (zone IV).

These changes in the electronic structure will have a significant effect in the electrical and optical behaviour of the samples, as it will be shown later on in this thesis. Regarding the last plot (Fig. 4.11.c)) where the difference between the spectra of zone III and IV is presented, it can be observed that there is no significant changes in the *d* band at the Fermy level, since the Zr 4*d* band is already completely depopulated. Moreover, there is a reduction of the N 2*p* band and an increase of the O 2*p* band, being again a sign of the increase in the ionic character of the binding mechanisms with the increase of the oxygen content.

X-ray photoelectron spectroscopy (XPS)-Core level

One of most common sources of errors in XPS interpretation comes from surface contamination. *Foord et al.* [64] studied the absorption of oxygen on polycrystalline zirconium and they suggest that oxygen absorbs dissociatively at 300 K and is immediately incorporated into the first few atomic layers of the solid. In the case of zirconium oxynitrides, this contamination layer is normally zirconium oxide, which may lead to a misunderstanding in the identification of chemical states. In order to overcome this problem, a sputter-cleaning procedure was adopted in this work. The ion bombardment of the ternary system ZrO_xN_y causes the preferential sputtering of oxygen and nitrogen, inducing a metal rich surface, promoting the appearance of sub-stoichiometric phases were zirconium is in a oxidation state lower than +4. In fact, *Wiame et al.* [65] claimed the formation of several different zirconium sub-oxide phases. In order to minimize this problem, a moderate energy sputtered cleaning process was performed with Ar^+ ions (3.5 kV, 30º incidence), during relatively large periods of time (up to 200 minutes), until a compositional stationary regime was achieved. It is however worth noticing that even after this cleaning process there was still some surface degradation (Fig. 4.12), due to the high reactivity of oxygen with zirconium and the deposition parameters. The inexistence of ion bombardment induces less dense coatings, favouring the superficial oxide degradation.

M. Del Re et al. already reported oxidised coatings through all the bulk for unbiased samples due to the high porosity of the coatings [66].

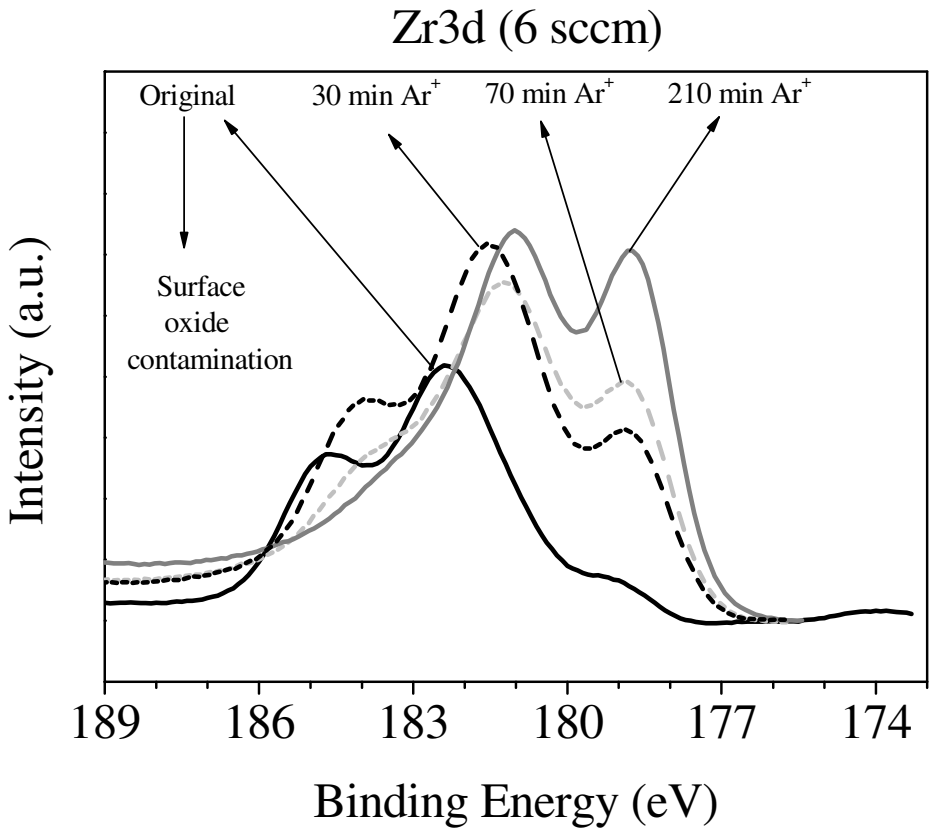


Fig. 4.12. XPS Zr 3d spectra for the sample of the series 1 deposited with 6 sccm of the reactive gas flow, with deferent's sputtering cleaning times.

Figure 4.12 shows the XPS Zr 3d spectra for different sputtering-cleaned times, for the sample prepared within zone I (gas flow of 6 sccm). Some oxide degradation at the surface still remains, even after 210 min of sputter cleaning. The erosion rate estimated due to the Ar^+ bombardment is between 0.1-0.5 Å/min, and thus on this basis, the 210 minutes of sputter cleaning should correspond to ~10 nm erosion, which is less than 1 % of the film thickness. The superficial oxide degradation is also visible in the composition results from XPS, obtained for the samples after the steady state has been reached by sputtering (Fig. 4.13). Nevertheless the Ar^+ bombardment induces a preferential sputtering of oxygen and nitrogen, the analysed area by XPS for all the films shows more oxygen than that of the "bulk" measured by RBS (Fig. 2.11 and a 2.12, chapter 2).

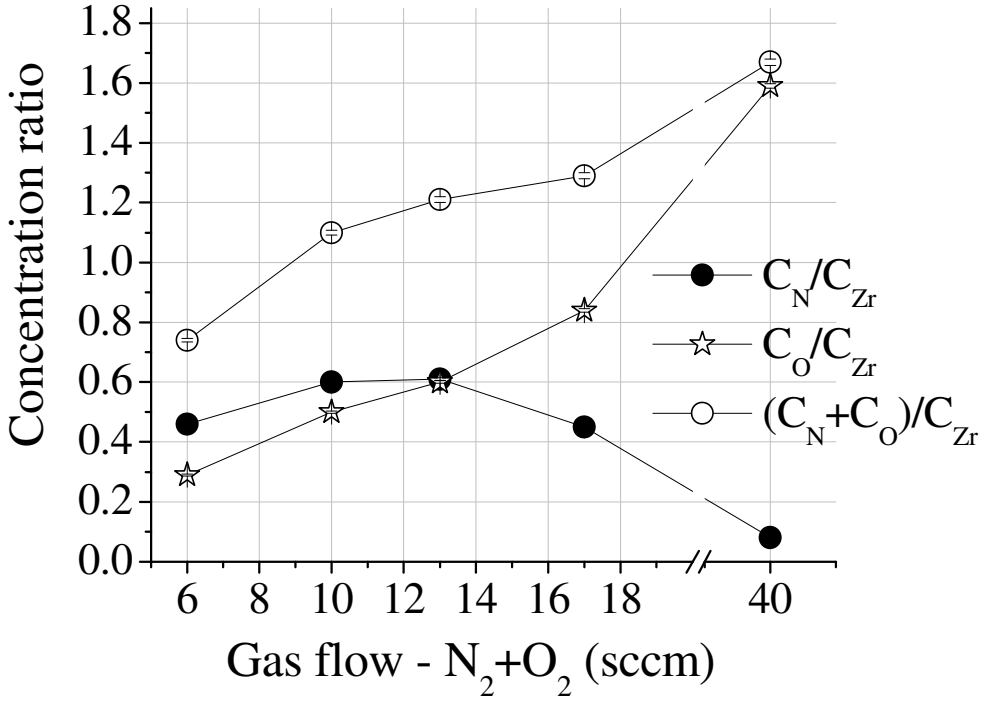


Fig. 4.13. XPS calculated metalloid over the zirconium atomic ratios, C_O/C_{Zr}, C_N/C_{Zr} and $(C_N+C_O)/C_{Zr}$ as a function of the reactive gas flow. The results were obtained after the steady state has been reached by sputter-cleaning. The error was determined by error propagation.

Figure 4.14. shows the Zr *3d* spectrum for selected samples prepared within each of the four zones, and a Zr *3d* spectrum of a *monoclinic*-ZrO_2 subjected to the same sputtering treatment (3.5KV, 30º), for reference. The high number of species of Zr with different oxidation states, induced by the ion bombardment or proper states of the film, does not allow an accurate deconvolution of the Zr 3*d* XPS spectra obtained to show the presence of zirconium in different chemical states; nitride, oxynitride and oxide [53, 66, 67].

The Zr $3d_{5/2}$ peak at ~178.8 eV corresponds to Zr-N [65], and the related peak located at E_B ~ 181.5 eV is commonly attributed to ZrO_xN_y [57]. The last peak is close to 182.5 eV, which is commonly observed for ZrO_2 compounds [65]. It must be noticed that the Zr *3d* spectrum of the sample deposited with 40 sccm of the reactive gas present a very similar spectum regarding the reference sample of *mon*-ZrO_2, confirming that the Zr $3d_{5/2}$ peak at 182.5 eV represents a zirconium oxide phase [65].

Another relevant feature coming from figure 4.14 is related with the reduction of the ZrN phase contribution, when going from samples within zone I towards those of zone III. The ZrN

contribution completely vanishes for the samples within zone IV. This fact is consistent with the XRD analysis, where no traces of ZrN phase were observed in zone IV.

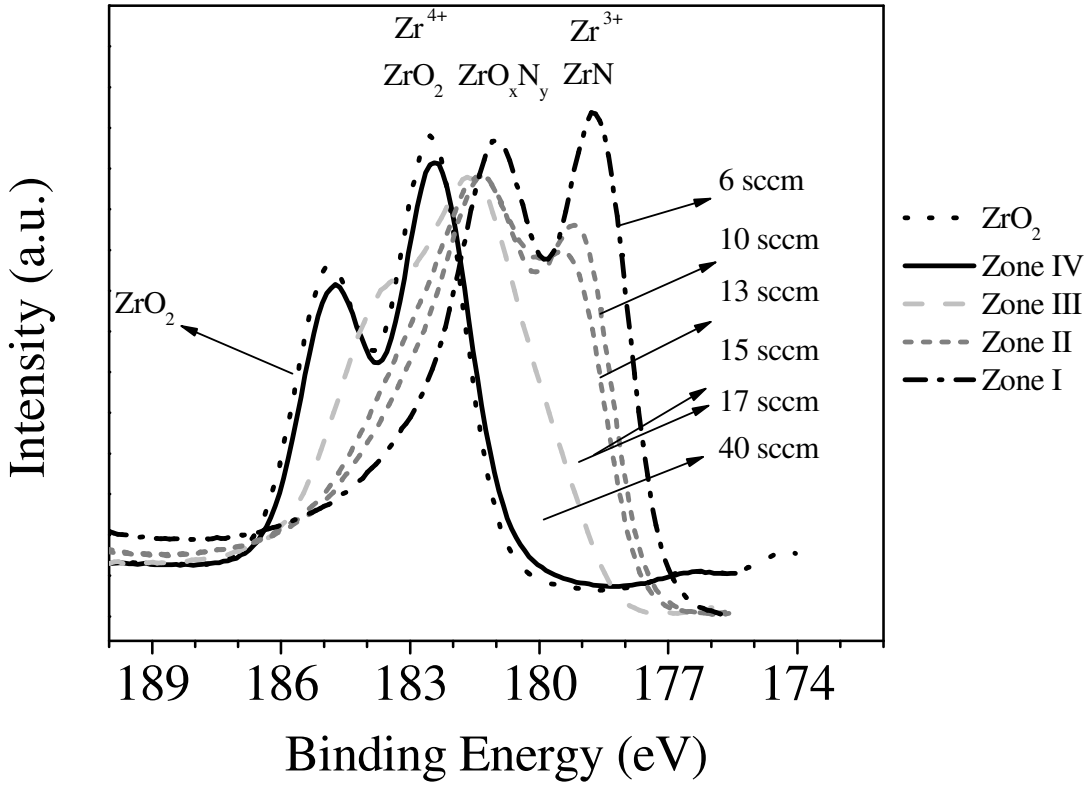


Fig. 4.14. Zr *3d* spectrum for selected samples prepared within each of the four zones from series 1, and a Zr *3d* spectrum of a *mon*-ZrO_2 sample.

Together with the reduction of the ZrN contribution, Figure 4.14 also shows a shift of ~0.5 eV of that ZrN peaks to higher binding energies. This shift to higher binding energies of a core-electron is correlated to the change in the ionic valences induced by the chemical environment [68,69]. *J.M. Sanz et al.* proposed that for nitride compounds, the XPS binding energy shift is due to the increase of oxygen that is incorporated within the nitride matrix [70], which is consistent with the case of this work, where an increased oxygen amount is found when going from zone I to zone IV. With increasing oxygen content and the consequent continuous depopulation of the *d* band at the Fermi level, the core electrons of zirconium will be more tightly attracted by the protons of the nuclei, which cause an increase of the binding energy of core electrons.

From figure 4.14 it is also clear that beyond the Zr-N bonds, another important contribution for the overall behaviour of the samples in zones II and III, comes from a different kind of

zirconium bonding: the so-called oxynitride-type bonding, Zr-O-N. Regarding this contribution, it must be stated that it could represent several contributions resulting from different zirconium chemical environments with slightly different O and N contents. It is, therefore, extremely difficult to index this contribution either to actual films bonds or to surface contaminations. *Milošev et al.* [50] claimed the later possibility, since the formation of several different zirconium sub-oxides (Zr_2O, ZrO, Zr_2O_3 and ZrO_2) can occur during the interaction of zirconium with oxygen [52,56]. Nevertheless, it is difficult to accurately propose the origin of these oxides. In recent works, *Grafouté et al.* [71] reported by Mössbauer spectrometry that, in FeON system, the environments of metal sites in these oxynitride films must be modelled by means of a binomial distribution of oxygen atom as first neighbours and are surrounded both by nitrogen atoms and at least one atom of oxygen or oxygen or vacancies.

It is also worth mentioning that this Zr 3d doublet, referred here as "oxynitride component", is also pointed by *Prieto et al.* [67] to be representative of Zr-N bonds correspondent to over-stoichiometric zirconium nitride: Zr_3N_4. This is probably due to the fact that zirconium presents similar chemical states in both insulating phases of oxynitride and over-stoichiometric zirconium nitride (Zr_3N_4). *Bazhanov et al.* [55] reported that, in oxynitrides, the higher (+4) oxidation state is stabilized, such as the case of Zr_3N_4.

Figure 4.15 shows the N *1s* spectra for selected samples prepared within each of the four zones. The oxide degradation of the analysed area is also reflected in the shape of the N 1s spectrums. The dominant peak corresponding to nitride (ZrO)-N^{3-} in ZrO_xN_y oxynitride appears at a lower binding energy (396.2 eV), regarding to the characteristic N 1s nitride peak, which normally appears at 397.8 eV [50]. This fact might be the result of the already referred oxide degradation of the analysed area or representing the characteristic binding energy of the (ZrO)-N^{3-} in ZrO_xN_y oxynitride phase. The sample representative of zone IV only presents a residual N 1s signal, also consistent with the composition and structural analysis.

Others authors claimed that in zirconium oxynitride, the N 1s spectrum contains not only the peak at E_B ~ 396.2 eV, but also another one at E_B ~ 400.1 eV [64,72]. In our case, the sputtered cleaned samples showed no evidences of other peaks at higher energies. However some of the "non-cleaned samples" (gas flows of 6, 10 and 13 sccm), present a secondary peak at ~ 400 eV (Fig. 4.16).

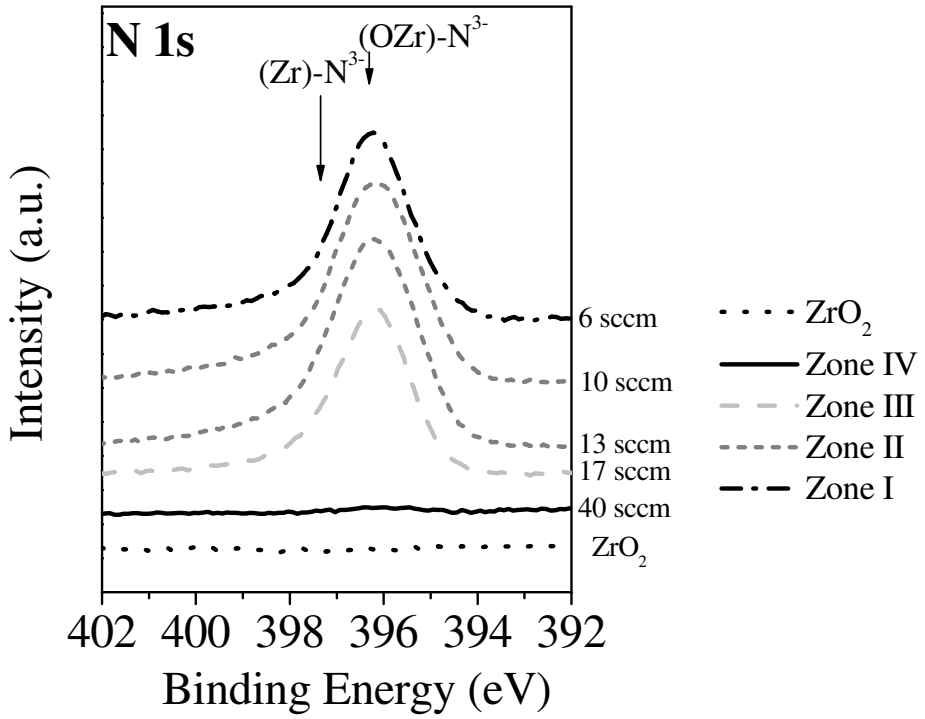


Fig. 4.15. N *1s* spectra for selected samples (series 1) prepared within each of the four zones, from series 1.

The intensity of this signal is not correlated with composition of the films, and it is fully and very soon removed by the sputtering cleaning process. This species as been detected previously [73] in a Zr electrode, when oxidized by electrochemical surface nitriding with LiCl–KCl–Li_3N, since no special care was taken to avoid surface oxidation of the sample after electrolysis. *Milošev et al.* [50], working on ZrN exposed to atmosphere, found tree components of the N 1s spectrum: the main nitride peak at 397.3 eV; a peak at lower binding energies (~396.3 eV) attributed to an "oxynitride peak" and a third peak at higher binding energies (~400 eV), which was also indexed to an "oxynitride peak".

Nevertheless, after the surface sputter-cleaning the "oxynitride peak at 400 eV" in the nitrogen signal disappeared and only the main nitride peak remained. Similar results on TiN coatings were obtained by several others authors [74-76]. On this base it is possible to suggest that the N 1s peak at ~400 eV should result from the surface contamination and not a characteristic peak of N 1s spectra in the ZrO_xN_y ternary system.

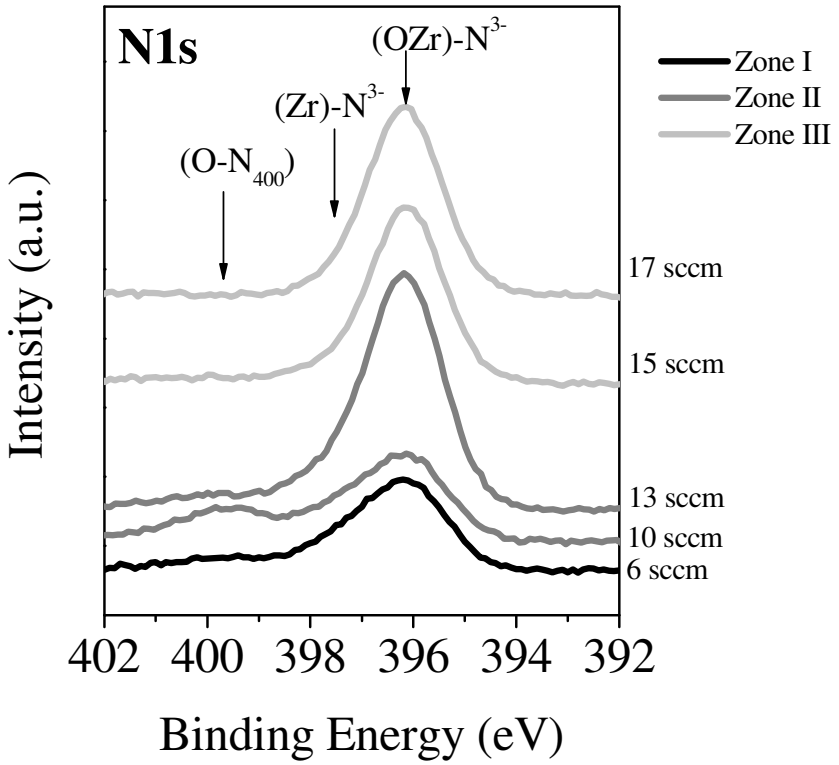


Fig. 4.16 N 1s spectrums for the selected "non sputtered cleaned" samples, from the series 1.

Figure 4.17 presents the O 1s spectrums for the representative samples in each of the four zones. From these results it is possible to observe that the O 1s spectrum presents a clear increase in intensity, due to the increase of oxygen content. Associated to the intensity increase is a shift of this O 1s peak to higher binding energies. This shift was also observed by *Signore et al.* [77], when studying zirconium oxynitride thin films. These authors observed a shift to higher energies, not only in the O 1s spectrums but also in the N1s peak. In this work, this was not the case since the binding energy scale was calibrated by the N 1s peak at E_B ~ 396.2 eV. *Signore* and co-authors claimed that the shift to higher energies of the N 1s peak should result from the nitrogen replacement by oxygen in the Zr-N network [77]. Similar results were obtained by *Mössbauer* spectrometry on FeON films [71]. These authors claimed a partial substitution of nitrogen atoms for oxygen atoms in the nitride network and that the oxynitride film does not contain any oxides phases.

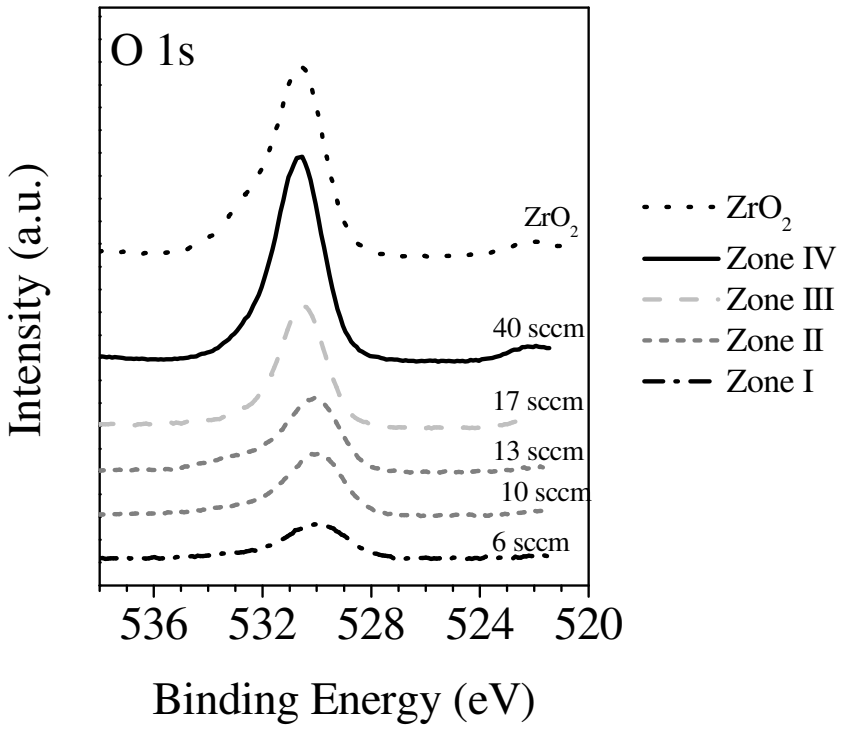


Fig. 4.17. O 1s spectrums for the representative samples in each of the four zones, from series 1.

Due to a higher electronegativity of oxygen in comparison to that of nitrogen, the valence electrons of N atoms will move further from nuclei by surrounded O atoms. As a result, the core electrons will be attracted more tightly by the protons in the nuclei. Analogously, the binding energy of O 1s also increases by the decrease of surrounded N atoms [77].

4.4.2. Reflection Electron energy loss spectroscopy (REELS)

Surface-sensitive spectroscopies such as X-ray photoelectron spectroscopy (XPS), are powerful tools to study the electronic structure of a given material, namely the valence band region, although they cannot give information about energy loss processes and multiple scattering effects, which will determinate the optical properties of a given material, namely the colour. On this basis REELS analysis were performed to study the energy loss mechanisms of electrons with the surface of the coatings namely; plasmon losses, intra and interband transitions.

Reflection electron energy loss spectroscopy (REELS) studies were performed using a electron gun, fitted at the analysis chamber. The energy of the excitation electron beam was 1500 eV and the kinetic energy of reflected electrons was measured with a hemiespherical analyser at

20 eV of pass energy. Under these experimental conditions, the full width at half maximum of the elastic peak was 0.8 eV. Losses have been normalized by the area of the elastic peak.

Figure 4.18 presents the REELS spectra of representative samples (series 1) from each of the fours zones, which contains a sharp and intense zero-loss peak, representing electrons that have passed through the specimen without losing energy through inelastic scattering. The low-loss region (up to about 40 eV energy loss) is dominated several broader peaks which arise from inelastic scattering of incoming electrons by valence or conduction electrons in the surface of the coating.

The first important observation that can be taken from the figure is the continuous decrease of the low-energy loss, observed in the 1-3 eV region, when going from the films within zone I to those in zone III. In fact, there is a complete vanishing in the samples prepared within the last zone (zone IV), see figure 4.18 marked with an ellipse.

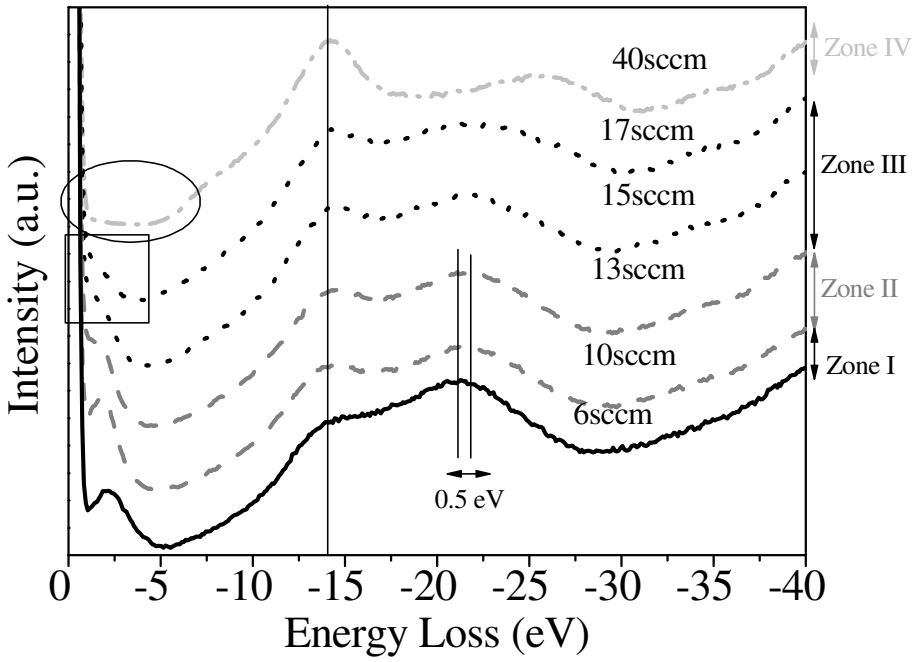


Fig. 4.18. REELS spectra of representative samples (from series 1), for each of the four zones.

Regarding the origin of this feature, there is actually some controversy among the authors who previously observed it. *G. R. Greagry et al.* [78] claimed that this low-energy loss feature in the 1-3 eV region is due to transitions from filled to empty states of the Zr 4*d* shell, resulting

from the presence of zirconium in an oxidation state lower than +4. A similar feature has also been observed in the loss spectra of titanium oxides [79,80]. Meanwhile, some authors [81-83] have pointed out that, in fact, optical transitions between pure *d*-states are forbidden. However, the so called *d-band* is originated mostly by the Zr 4*d* orbitals, but has also some admixing of *s* and *p* states [84]. For this reason, *G. R. Gregory et al.* [78] claimed that it is difficult to expect a strict selection rule applied to this transition. Others authors [85,86] have associated the spectral feature to a plasmon related to the *d*-electrons, and shifted down by the strong interband *p-d* coupling at higher energies (≈ 8 eV). The reason for its high intensity is the weak interband damping in this region due to the low *p*-character of the states at the Fermi level [85]. *P. Prieto et al.* [86] supported this point of view. According to these authors, the peak at 2.5 eV in the spectrum of the energy loss function (ELF),

$$ELF \propto -\omega \,\mathrm{Im}\left[1/\hat{\varepsilon}(\omega)\right] = -\omega \frac{\varepsilon_2(\omega)}{\varepsilon_1^2(\omega) + \varepsilon_2^2(\omega)} \qquad \text{(eq. 4.3)}$$

(where $\varepsilon_1(\omega) = \mathrm{Re}\,\hat{\varepsilon}(\omega)$ and $\varepsilon_2(\omega) = \mathrm{Im}\,\hat{\varepsilon}(\omega)$ are the real and imaginary parts of the frequency-dependent dielectric function $\hat{\varepsilon}(\omega)$), corresponds to a collective plasmon-type excitation. Regardless the specific origin of this loss features, either intra-band transitions or *d*-electron plasmon, this result confirm the already referred continuous depopulation of the *d*-band. A closer look into the plot (see figure 4.18 marked with a rectangle) reveals a small feature in this low energy region for the samples lying in the third zone (oxinitride zone). It implies that even for this zone (zone III) there must be some amount of zirconium with oxidation state lower than +4. Anyway, it must be also mentioned that this could result from the sputter-cleaning process and not from the coating it self. Regarding the samples lying in the oxide zone (zone IV), that presented a small peak at ≈ 9 eV, *G. R. Corallo et al.* [78] claimed that one of the loss features associated with the O 2*p* initial state could be the shoulder at about 9.5 eV. For the samples that present the loss feature at low energies, 2.5eV, (zones I, II, III), it is also possible to observe the presence of two other loss features: i) one close to 14 eV and ii) another close to 22 eV, with an increasing shift towards lower energies. Regarding the loss feature at about 14 eV, there are three different interpretations given by different authors. *J. M. Sanz and co-workers* and *G. Marletta et al.* [87,87] attributed this peak to an excitation involving O 2*p* electrons and empty Zr 5*s-p* states. Other authors assigned this energy loss to a bulk plasmon [86,89-91]. *G. R. Corallo and*

co-workers [78] attributed it to a transition between the oxygen 2*p* and 3*s* levels, since the energy loss does not change with zirconium oxidation state, as would be expected from a plasmon loss due to the changing valence-band electron concentration. Since the energy position of this loss feature does not change when going from the coatings lying in the nitride zone to the oxide zone, with the consequential change in the zirconium oxidation state, transition between the oxygen 2*p* and 3*s* levels, appears to be the most probable explanation.

Regarding the peak ≈ 22 eV, again there is a controversy between different authors. Most of the published works [81,82,85,92] assigned this peak to a bulk plasmon, assuming that not only the Zr 4*d* and Zr 5*s,* but also the N 2*p* and N 2*s* electrons behave like free ones. However, *P. Prieto et al.* do not accept this explanation and claim that the 22 eV energy loss corresponds to *p-d* transitions [i.e., VB (N 2*p*+Zr 4*d*) → CB (Zr 5*sp*N 3*s*), where VB and CB mean valence and conduction bands, respectively]. The peak at ≈ 22eV in the spectra of samples from the first two zones (samples prepared with gas flow varying from 6 to 13 sccm), present an overall broadening, together with a small shift of about 0.5 eV, and a change in the relative intensity of the two components of the double peak at ≈ 14 and ≈ 22 eV.

P. Prieto and co-workers [86] already observed this evolution comparing the inelastic scattering cross section of insulating Zr_3N_4 with that of conductive ZrN. This could reinforce the already reported conclusion concerning a change of the crystalline structure from fcc-ZrN to orth-Zr_3N_4, when going from samples within zone I and II, respectively. The peak at ≈ 26 eV is assigned to a bulk plasmon by *G.R. Corallo et al.* and *J. Frandon et al.* [78,89], based on the fact that the free electron (Drude) model predicts a plasmon energy of 25 eV, if one assumes the participation of 12 electrons/mol. However, this assumption is contested by *P. Prieto et al.* [86] since, in their opinion, the O 2*s* electrons should not behave as free electrons. These authors claim that this loss feature should result from transitions between the O 2*p* VB states and the Zr 5*sp* CB.

4.5. Conclusions

The variations observed in the FTIR spectra as a function of reactive gas flow are in good correlation with the previous measurements, in particular with the different regions defined by the compositional and structural analysis.

Raman study show that line shapes continuously change with the variation of the material composition in good agreement with the compositional and structural zones previously reported. The observed changes reflect the modifications in local arrangements induced by the increase of oxygen content in the films. The appearance of new bands in spectra reflect also the changes in the local structure, with the formation of the *orth*-$Zr_3N_4(O)$ and γ-Zr_2ON_2 phase. Regarding the possibility of having an oxide phase, Raman study although does not disclose this possibility doesn't show any clear evidence of this hypotheses.

XPS valence band show that the electronic structure of zirconium oxynitride is ruled by the Zr 4*p* levels, but the O 2*s,* N 2*s* and molecular orbitals associated with O 2*p*/N 2*p* and Zr 4*d* valence levels can also be observed.. Going from zone I to zone IV, the films present a progressive transfer of zirconium 4*d* valence electrons to the O 2*p* and N 2*p* bands, with a shift to lower energies of the "*p band"*, until the complete depopulation of the *d-band* where the films become an insulator-type material.

XPS core level show that the ternary system ZrO_xN_y, present zirconium in three different oxidation sates, correspondents to zirconium attributed to Zr-N, ZrO_xN_y/Zr_3N_4 and ZrO_2 compounds. Showing a reduction of the ZrN phase contribution, when going from samples within zone I towards those of zone III until completely vanishes for the samples within zone IV.

REELS studies show that in the visible region, the coatings present a continuous decrease of the plasmon loos when going from the films within zone I to those in zone III until a complete vanishing in the samples prepared within the last zone (zone IV).

4.6. References

[1]- H. K. Pulker, *Coatings on Glass, Thin Films Science and Technology,* Elsevier, Amsterdam, 1984), Vol. 6, pp. 343-417.

[2]- H. Bach and N. Neuroth, *The Properties of Optical Glass*, Springer, Heidelberg, 1995, pp. 263-388.

[3]- S. T. Oyama, *Chemistry of Transition Metal Carbides and Nitrides*, Blackie Academic & Professional, New York, 1996, pp. 215-309.

[4]- J.-L. Calais, Adv. Phys. 26 (1977) 847.

[5]- K. Schwarz, CRC Crit. Rev. Solid State Mater. Sci. 13 (1987) 211.

[6]- A. Neckel, lnt. J. Quantum Chem. 23 (1983) 1317.

[7]- K. Schwarz, H. Ripplinger, A. Neckel, Z. L. Phys. B 48 (1982) 79.

[8]- D. F. Arias, Y. C. Arango, A. Devia, Appl. Surf. Sci. 253 (2006) 1683.

[9]- T. Yotsuya, M. Yoshitake, T. Kodama, Cryogenics 37 (1997) 817.

[10]- K. Schwarz, A. R. Williams, J. J. Cuomo, J. H. E. Harper, H. T. G. Hentzell, Phys. Rev. B 32 (1985) 8312.

[11]- M. Wautelet, J. P. Dauchot, F. Debal, S. Edart, M. Hecq, J. Mater. Res. 11 (4) (1996) 825.

[12]- Y. Igarashi, T. Yamaji, S. Nishikawa, Jpn. J. Appl. Phys. 29 (1990) L2337.

[13]- R. A. Andrievski, J. Mater. Sci. 32 (1997) 4463.

[14]- L. Pichon, T. Girardeau, A. Straboni, F. Lignou, P. Guérin, J. Perrière, Appl. Surf. Sci. 150 (1999) 115.

[15]- J. M. Chappé, N. Martin, J. Lintymer, F. Sthal, G. Terwagne, J. Takadoum, Appl. Surf. Sci. 253 (2007) 5312.

[16]- F. Vaz, P. Cerqueira, L. Rebouta, S. M. C. Nascimento, E. Alves, Ph. Goudeau, J. P. Rivière, K. Pischow, J. de Rijk, Thin Solid Films 447-448 (2004) 449.

[17]- H. Le Dréo, O. Banakh, H. Keppner, P.-A. Steinmann, D. Briand, N.F. de Rooij, Thin Solid Films 515 (2006) 952.

[18]- N. M. G. Parreira, N.J.M. Carvalho, F. Vaz, A. Cavaleiro, Surf. Coat. Technol. 200 (2006) 6511

[19]- M. Fenker, H. Kappl, O. Banakh, N. Martin, J.F. Pierson, Surf. Coat. Technol. 201 (2006) 4152.

[20]- M. Grafouté, C. Petitjean, C. Rousselot, J.F. Pierson, J.M. Grenèche, Scripta Materialia 56 (2007) 153.

[21]- P. Carvalho, F. Vaz, L. Rebouta, L. Cunha, C. J. Tavares, C. Moura, E. Alves, A. Cavaleiro, Ph. Goudeau, E. Le Bourhis, J. P. Rivière, J. F. Pierson, O. Banakh, J. Appl. Phys. 98 (2005) 023715.

[22]- R. Franchy, Surf. Sci. Rep. 38 (2000) 195.

[23]- F. Vaz, P. Carvalho, L. Cunha, L. Rebouta, C. Moura, E. Alves, A.R. Ramos, A. Cavaleiro, Ph. Goudeau, J. P. Rivière, Thin Solid Films 469-470 (2004) 11.

[24]- S.P. Davis, M. C. Abrams, James W. Brault, *Fourier Transform Spectrometry*, Elsevier Inc., 2001.

[25]- Derek albert Long, The Raman Effect in *A unified Treatment of the Theory of Raman Scattering by Molecules*, John Wiley and Sons, 2002, pg 7.

[26]- George Turrell, Jacques Corset, *Raman Microscopy developments and applications*, Elsevier, 1996, pg 4.

[27]- Derek albert Long, The Raman Effect in *A unified Treatment of the Theory of Raman Scattering by Molecules*, John Wiley and Sons, 2002, pg 18.

[28]- A.Einstein, Ann. Physik.17 (132) (1905) 1921.

[29]- L. J. Allen, S. D. Findlay, A. R. Lupini, M. P. Oxley, S. J. Pennycook, Phys. Rev. Letters 91 (10) (2003) 105503-1.

[30]- Wolfgang S. M. Werner, Surf. Interface Anal. 35 (2003) 347.

[31]- L.D. Landau, E.M. Lifshitz. *Quantum Mechanics: Non Relativistic Theory* (3rd edn). Pergamon Press: Oxford, 1977.

[32]- D.R. Penn, Phys. Rev. B 35 (1987) 482.

[33]- Ding Z-J. *PhD Thesis*, Osaka University, Japan, 1990.

[34]- R.H. Ritchie. Phys. Rev. 106 (1957) 874.

[35]- E.A. Stern, R.A. Ferrell. Phys. Rev. 120 (1960) 130.

[36]- F. Yubero, S. Tougaard, Phys. Rev. B 46 (1992) 2486.

[37]- K.L. Aminov, J.B. Pedersen. Phys. Rev. 63 (2001) 125 412.

[38]- S. Hűfner, *Photoelectron Spectroscopy*. Springer: Berlin, 1995.

[39]- R. Ludeke, L. Esahi, Surf. Sci.47 (1975) 132.

[40]- E. Bauer, Z. Phys. 224 (1969) 19.

[41]- D. F. Cox, G. B. Hoflund, Surf. Sci. 151 (1985) 202.

[42]- G. R. Corallo, D. A. Asbury, R. E. Gilbert, G. B. Hoflund, Phys. Rev. B 18 (1987) 9451.

[43]- M. Klanjšěk Gunde, M. Maček, Phys. Stat. Sol. (a) 183 (2) (2001) 439.

[44]- C.A. Wert, R.M. Thomson, Physics of Solids, McGraw-Hill Series in Materials Science and Engineering, McGraw-Hill, Book Co, New York, NY, 1964.

[45]- D.A. Neumayer, E. Cartier, J. Appl. Phys. 90 (2001) 1801.

[46]- A.N. Christensen, O.W. Dietrich, W. Kress, W.D. Teuchert, Phys. Rev. B 19 (1979) 5699.

[47]- A. Cassinese, M. Iavarone, R. Vaglio, M. Grimsditch, S. Uran, Phys. Rev. B 62 (2000) 13915.

[48]- QUASES-Tougaard Inc. Available from: www.quases.com.

[49]- M. Del Re, R. Gouttebaron, J.-P. Dauchot, P. Leclère, G. Terwagne, M. Hecq, Surf. Coat. Technol. 174-175 (2003) 240.

[50]- I. Milošev, H. H. Strehblow, M. Gaberscek, B. Navinsĕk, Surf. Inter. Anal. 24 (1996) 448.

[51]- Briggs, M.P, Seah (Eds.), *Practical Surface Analysis by AES and XPS*, John Wiley and Sons, Chichester and New York, 1983.

[52]- S. Tsunekawa, K. Asami, S. Ito, M. Yashima, T. Sugimoto, Appl. Surf. Sci. 252 (2005) 1651.

[53]- I. Milošev ,H.-H. Strehbtow , B. Navinšek, Thin Solid Films 303 (1997) 246.

[54]- K. A. Gruss, T. Zheleva, R. F. Davis, T. R. Watkins, Surf. Coat. Technol.107 (1998) 115.

[55]- D.I. Bazhanov, A.A. Knizhnik, A.A. Safonov, A.A. Bagatur'yants, M.W. Stoker, A.A. Korkin, J. Appl. Phys. 97 (2005) 044108.

[56]- C. Morant, J. M. Sanz, L. Galán, L. Soriano, F. Rueda, Surf. Sci. 218 (1989) 331.

[57]- C. Palacio, J. M. Sanz, J. M. Martnez Duart, Surf. Sci. 191 (1987) 385.

[58]- J. M. Sanz, L. Soriano, P. Prieto, G. Tyuliev, C. Morant, E. Elizalde, Thin Solid Films 332 (1998) 209.

[59]- A. Delin, O. Eriksson, R. Ahuja, B. Johansson, M. S. S. Brooks, T. Gasche, S. Auluck, J. M. Wills, Phys. Rev. B 54 (1996) 1673.

[60]- P. Prieto, A. Fernández, L. Soriano, F. Yubero, E. Elizalde, A.R. González-Elipe, J.M. Sanz, Phys. Rev. B 51 (1995) 17984.

[61]- P. Prieto, Ph.D. Thesis, Universidad Autónoma de Madrid, 1992.

[62]- L. Porte, Solid State Commun. 50 (1984) 303.

[63]- J. Lindström, L.I. Johansson, A. Callenas, D.S.L. Law, A.N. Christensen, Phys. Rev. B 35 (1987) 7891.

[64]- J. S. Foord, P. J. Goddard, R. M. Lambert, Surf. Sci. 94 (1980) 339.

[65]- H. Wiame, P. Grange, M.-A. Centeno, S. Picard, P. Bastians, P. Grange, J. Eur.Ceram. Soc.18 (1998) 1293.

[66]- M. Del Re, R. Gouttebaron, J.-P. Dauchot, P. Leclère, G. Terwagne, M. Hecq, Surf. Coat. Technol. 174-175 (2003) 240.

[67]- P. Prieto, L. Galán, J. M. Sanz, Phys. Rev. B 47 (1993) 1613.

[68]- W.E. Swartz Jr., D.M. Hercules, Anal. Chem. 43 (1971) 1774.

[69]- W.E. Swartz Jr., K.J. Wynne, D.M. Hercules, Anal. Chem. 43 (1971) 1884.

[70]- C. Morant, J. M. Sanz, L. Galan, Phys. Rev. B 45 (1992) 1391.

[71]- M. Grafouté, C. Petitjean, C. Rousselot, J.F. Pierson, J.M. Grenèche, Scripta Materialia 56 (2007) 153.

[72]- W.E. Swartz Jr., D.M. Hercules, Anal. Chem. 43 (1971) 1774.

[73]- T. Goto, H. Ishigaki, Y. Ito, Mat. Sci. Eng. A 371 (2004) 353.

[74]- C. Ernsberger, J. Nickerson, A. E. Miller, J. Moulder, J. Vac. Sci. Techno1. A 3 (6) (1985) 2415.

[75]- K. S. Robinson, P. M. A. Sherwood, Surf. Interface Anal. 6 (1984) 261.

[76]- M. J. Vasile, A. B. Emerson, F. A. Baiocchi, J. Vac. Sci. Techno1. A 8 (1) (1990) 99.

[77]- M.A. Signore, A. Rizzo, L. Mirenghi, M.A. Tagliente, A. Cappello, Thin Solid Films 515 (2007) 6798.

[78]- Gregory R. Corallo, Douglas A. Asbury, Richard E. Gilbert, Gar B. Hoflund, Phys. Rev. B 18 (1987) 9451.

[79]- V. E. Henrich, R. L. Zeiger, Phys. Rev. B 23 (1982) 6280.

[80]- M. C. Burrell, N. R. Armstrong, J. Vac. Sci. Techonol. A 1 (1983) 1831.

[81]- B. M. Biwer, S. L. Bernasek, Surf. Sci. 167 (1986) 207.

[82]- I. R. Strydom, S. Hofmann, Vacuum 41 (1990) 1619.

[83]- D. W. Lynch, C. G. Olson, J. H. Weaver, Phys. Rev. B 11 (1975) 3617.

[84]- P. Blaha, K. Schwarz, Int. J. Quantum Chem. 23, 1535 (1983).

[85]- Pflüger, J. Fink, K. Schwarz, Solid State Commun. 55 (1985) 675.

[86]- P. Prieto, F. Yubero, E. Elizalde, J. M. Sanz, J. Vac. Sci. Technol. A 14 (6) (1996) 3181.

[87]- J. M. Sanz, M. A. Banön, E. Elizalde, F. Yubero, J. Electron Spectrosc. Relat. Phenom. 48 (1989) 143.

[88]- G. Marletta, S. Pignataro, Chem. Phys. Lett. 124 (1986) 414.

[89]- J. Frandon, B. Brousseau, F. Pradal, Phys. Status Solidi B 98 (1980) 379.

[90]- P. Camagni, G. Samoggia, L. Sangaletti, F. Parmigiani, N. Zena, Phys. Rev. B 50 (1994) 4292.

[91]- K.-O. Axellson, K.-E. Keck, B. Kasenmo, Surf. Sci. 164 (1985) 109.

[92]- W. K. Schubert, R. N. Shelton, E. L. Wolf, Phys. Rev. B 24 (1981) 6278.

Chapter 5

Electronic properties

5.1. Introduction

Best known for many outstanding physical properties such as high hardness, low electrical resistivity and aesthetically pleasing gold coloration, zirconium nitride (ZrN) is a IVB-V compound that exhibits desirable properties for a variety of industrial and consumer applications. In fact, this "particular" thin film-type material shows metallic as well as covalent properties, exhibiting a unique combination of characteristics that allow them to be serious candidates for a wide range of high-technology applications [1-6]. Beyond these technological applications, that can range from several examples in metallurgy, aeronautics, electronics and medicine, where it is used to protect and to decrease wear in a variety of components, there are also the more specific cases of fundamental research, where this nitride revealed to be a subject of grate interest [7,8]. Metallic properties correspond to electrical conductivity and metallic reflectance and covalent bonding properties correspond to high melting point, high hardness and brittleness, and excellent thermal and chemical stability. ZrN is also a superconductor with a transition temperature, T_c, of 10 K [9]. Its metallic band structure is manifested in the golden colour of the crystal itself [10]. On the contrary, the "overstoichiometric phase of zirconium nitride, Zr_3N_4, is a metastable phase, insulating and almost transparent [11]. *Juza et al.* [12] are credited with the discovery of the metastable phase of ZrN, in 1964, by ammonolysis of zirconium tetraiodide. This higher nitride phase is a semiconductor with a calculated band gap of 2.2 eV [13]. Other research groups claimed for this compound an optical band gap of 3.1 eV [14].

In previous chapters, it was presented a detailed analysis concerning the composition structure and electronic behaviour of the zirconium oxynitride system. In order to correlate these features with the electronic properties of the films, an analysis of the films resistivity was carried out, which allowed to understand how the previous differences in film behaviours (see chapters 1 through 4) are influencing the films properties. Moreover, the characterization that will be shown in this chapter will allow the establishment of limits for practical applicability of devices coated with these materials, providing new areas of application and supplying criteria for new materials design for specific applications. This knowledge will be of major importance to understand the electrical behaviour of the material and the nature of the metallic-to-insulating transition with increasing oxygen concentration. The main focus of this work is given to the understanding of the different phases that are formed in ZrO_xN_y ternary systems in comparison with those that are characteristic of ZrO_x and ZrN_y binary systems.

Electrical resistivity

The *Electrical resistivity* of a material describes how much it resists the flow of electricity. This property does not depend on the physical dimensions of the material. The resistivity of a material ρ is related with a local applied electric field ($\vec{E}$) and the resultant current density ($\vec{j}$) by the following expression:

$$\vec{E} = \rho \vec{J} \qquad \text{(eq. 5.1)}$$

The resistivity of a material depends on the temperature, but for a specific temperature corresponds to the proportionality coefficient between the electric field and the current density. Being $\vec{J}$ and $\vec{E}$ vectors ρ is, in general, a tensor. This means that the current does not necessary flow in the direction of the electric field. In the case of isotropic and homogeneous materials, it is assumed that ρ is a scalar.

Band structure and Conductivity

A useful way to visualize the difference between conductors, insulators and semiconductors is to plot the available energies for electrons in the materials. When two identical atoms are far apart, their electronic levels are not mutually affected. If two atoms are close enough, their atomic orbitals split since electrons must occupy different energies (ΔE) due to Pauli Exclusion principle. As the number of atoms is increased to a very large number, the levels are so numerous and so close together that we can no longer distinguish the individual levels as show in figure 5.1. We can regard the N atoms as forming an almost continuous *band* of energy levels. This produces a number of molecular orbitals proportional to the number of atoms.

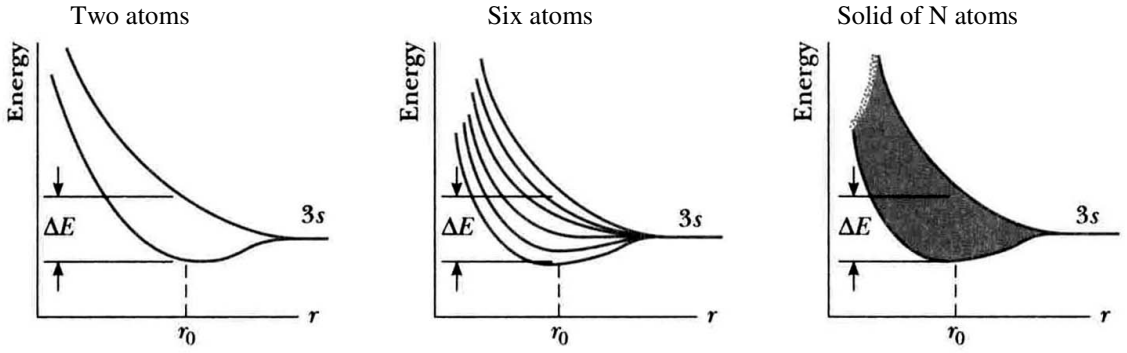


Fig. 5.1. Splitting of 3s levels when; a) two atoms are brought together; b) six atoms are brought together; c) N atoms are brought together.

The situation described above represents the ground state of sodium metal. Adding energy to the system (thermal or electrical, for example), the electrons may move from the filled states to any of the empty states. In this particular case (3*s* energy band of sodium), electrons from the partially full 3*s* band can absorb a small amount of energy and move to empty 3*s* states within the 3*s* band, or they can absorb a larger amount of energy and move to the 3*p* band.

Fermi-Dirac distribution allows describing how these bands are "filled" with electrons. Fermi-Dirac distribution is strongly dependent on temperature (*T*), and is express by the equation 5.2.

$$f_{FD}(E) = \frac{1}{e^{(E-E_F)/KT} + 1} \qquad \text{(Eq. 5.2)}$$

where E_F is called the Fermi energy.

Figure 5.2. shows the Fermi-Dirac temperature dependence.

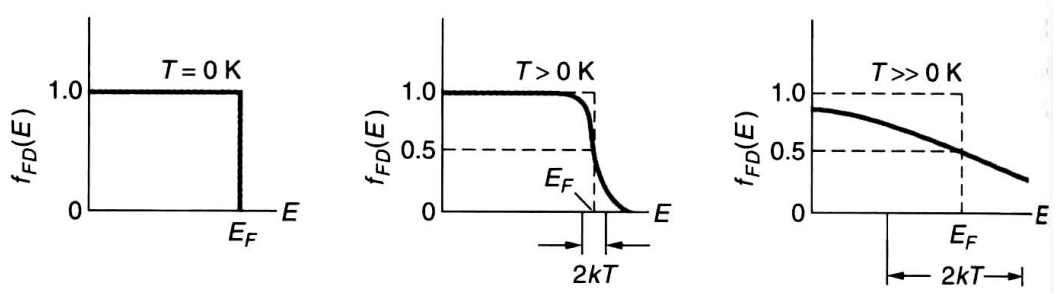


Fig. 5.2. Temperature dependence of Fermi-Dirac function.

For electrons in a metal E_F depends on electron density of the material, which doesn't change much with temperature. For, some materials, notably semiconductors, the density of the conduction electrons can change significantly with temperature, and thus E_F in these materials is temperature dependent.

Conductors

At absolute zero temperature, all levels in conduction band below the Fermi energy E_F are filled with electrons, while all levels above E_F are empty. Electrons are free to move into "empty" states of conduction band with only a small electric field, leading to high electrical conductivity.

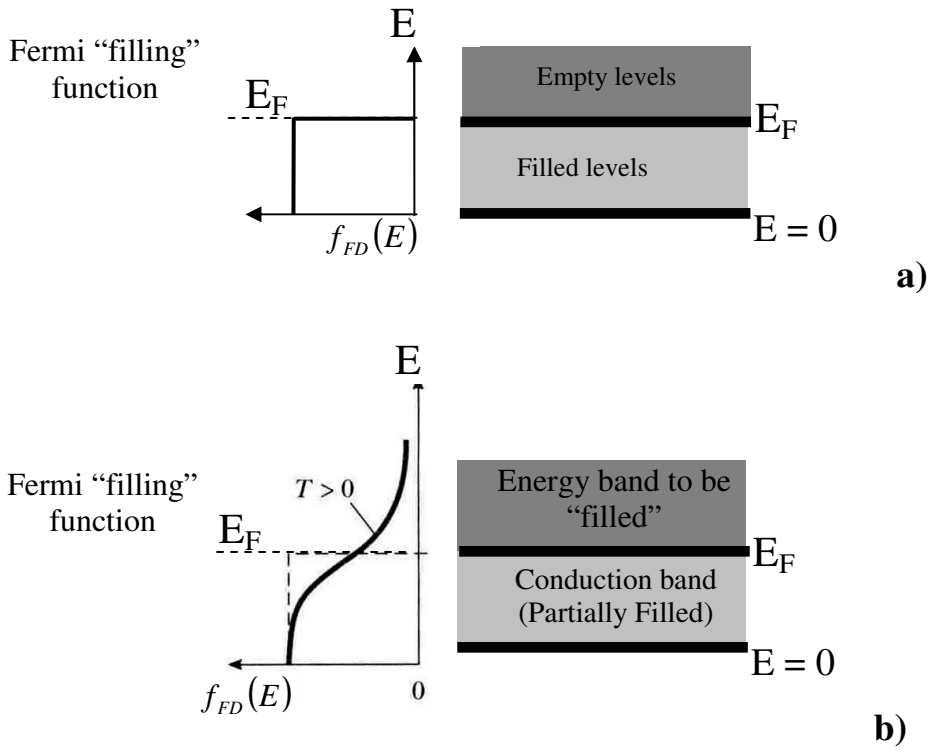


Fig.5.3. a) Detail of a half-filled band at T = 0, showing the Fermi-Dirac distribution of the left: **b)** Band structure of a metal at T > 0, showing the Fermi-Dirac distribution of the left.

The energy difference between the conduction band and the valence band may be overcome by many sources: thermal energy (room temperature, 300 K, is equivalent to 0.025 eV), photonic energy (Infrared, visible, ultraviolet, X-rays, gamma rays), and incident particles, i.e. protons, neutrons or electrons. The transition rate depends on the number of filled states below the Fermi level and the number of empty states above the Fermi level.

Insulators

A material in which one band is completely full and the next higher completely empty is a poor conductor. We refer in this case to a gap between the energy bands, and the Fermi energy lies somewhere in the gap, as shown figure 5.4.

At absolute zero temperature, the valence band is filled with electrons and the conduction band is empty, leading to zero conductivity. As the temperature is raised, the shape of the Fermi-Dirac distribution function changes (see Fig. 5.2); if the energy gap E_g between the valence band and the conduction band is large compared with KT, there will be few electrons thermally excited from the valence band to the conduction band.

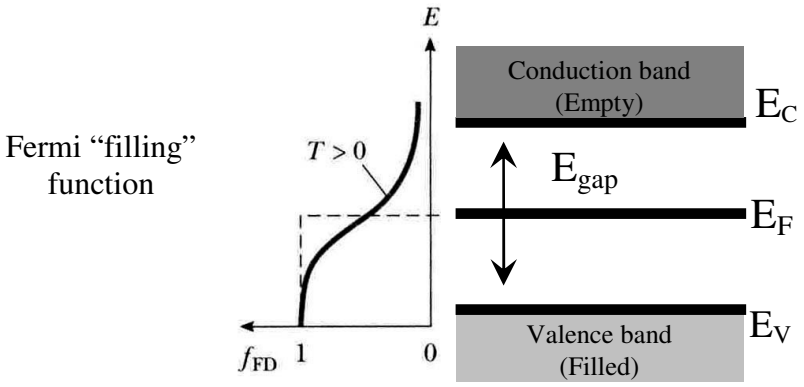


Fig. 5.4. Band structure in which E_F lies in the gap between bands.

There are many electrons in the valence band but there are few empty states for them to move through, so they do not contribute to the electrical conductivity. In the conduction band there are many empty states, but at ordinary temperatures there are so few electrons in that band that their contribution to electrical conductivity is very small.

Semiconductors

When a material has the basic structure of an insulator, but with a much smaller energy gap between the valence and the conduction band the behaviour becomes quite different, and these materials are known as *semiconductors*. Figure 5.5 shows a band structure representation for a semiconductor. At zero absolute temperature, the valence band is filled with electrons and the conduction band is empty, leading to zero conductivity.

At higher temperatures, thermal excitation across the energy gap between the valence and the conduction band is relatively probable leading to measurable electrical conductivity. Although the value of room-temperature Fermi-Dirac distribution function is nearly zero in the conduction band (in fact, it is so close to zero that it cannot be correctly scaled in figure 5.5. it is not exactly zero). At ordinary temperatures, there are few electrons in the conduction band and few empty states accessible to them, so the electrical conduction is relatively easily. In fact, in an ordinary sample containing about 10^{20} atoms, there may be 10^{11} conduction electrons in a semiconductor, 10^{20} in a conductor, and none in an insulator.

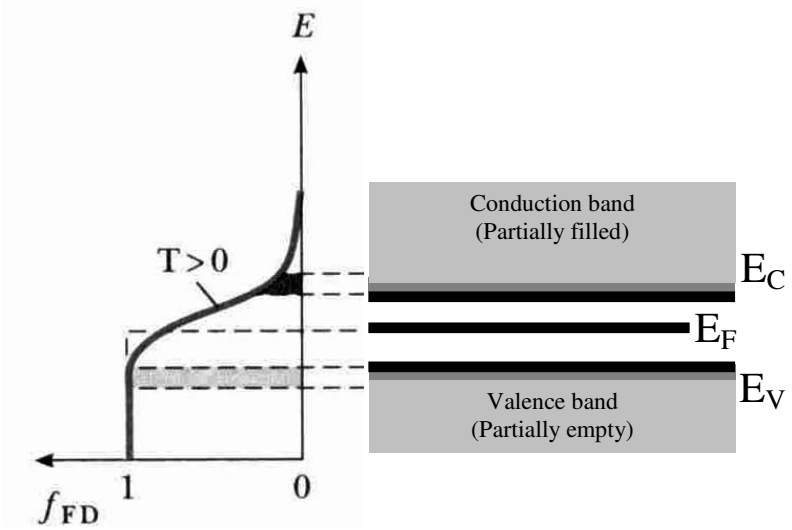


Fig. 5.5. Band structure of a semiconductor. The gap between bands is much smaller than in an insulator, so there is now a small population of the conduction band.

There are also many empty states in the valence band, so that some of the electrons in the valence band can also contribute to the electrical conductivity by moving about through those states. Since all the electrons in the conduction band came originally from the valence band, the number of vacancies in the valence band is exactly equal to the number of electrons in the conduction band. Thus, the values of (E_V - E_F) must be exactly equal to the values (E_C- E_F), and so the Fermi energy must be at midpoint of small energy gap between conduction and valence bands.

The thermal excitation across the energy gap between the valence and the conduction band is relatively probable leading to measurable electrical conductivity. Semiconductors depends more strongly on the temperature regarding the electrical conductivity then conductors and insulators.

5.2. Characterization techniques

Two point technique I-V curves

The resistivity of a thin film can be obtained by the same method used to measure electrical resistivity of a cooper bar [15], but considering now that *l* is the distance between the aluminium evaporated contacts, *h* is the thickness of the coating and *w* is the width of the aluminium evaporated contacts, see figure 5.6. A voltage source applies a voltage, *V*, across the rectangular shape coating area, causing an electrical current, *I*, to flow through the film.

Alternatively, an electrical current source could force a current through the coating, while a voltmeter, in parallel with the current source, would measure the voltage induced across the sample film.

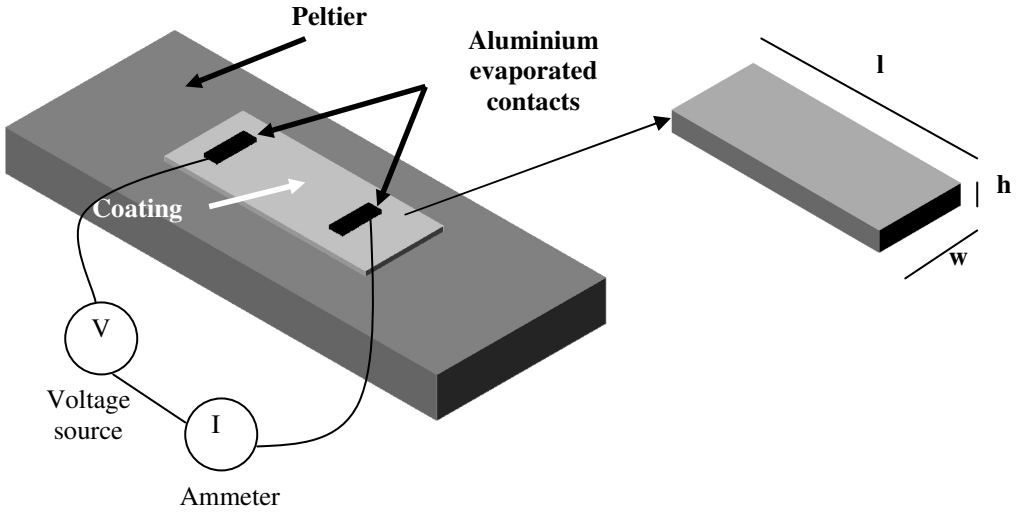


Fig. 5.6. I-V technique for measuring the resistivity of a coating.

The amount of current, *I*, that flows through the bar is measured by the ammeter, which is connected in series with the bar and voltage source. The voltage drop across the ammeter should be negligible.

In this particular case, since the analysed area of the coating may be assumed to have a rectangular shape, the electrical resistivity is obtained by the following expression:

$$\rho \equiv \frac{Vwh}{Il}; \qquad \text{(eq. 5.3)}$$

were V is the voltage measured by the voltmeter, we l is the distance between the aluminium evaporated contacts, h is the thickness of the coating, w is the width of the aluminium evaporated contacts and I the current flowing through the coating.

In spite of the simplicity of this technique to measure electrical resistivity, there is usually some resistance between the contact wires and the material or inherent to the measuring equipment itself. This additional resistance is responsible for obtaining resistivity values higher than the real values of the tested material. Because of this problem, the experimental error is relatively smaller if it is used to measure the electrical resistivity of high electrical resistivity or insulating materials, where the electrical resistivity is several orders of magnitude higher than that one of the contacts.

Four point probe technique - Van der Pauw geometry

The Vander Paw geometry is a general four-point probe resistivity measurement technique that allows measurements on samples of arbitrary shape, with no need to measure all the physical dimensions of the sample [16]. The Van der Pauw technique, due to its simplicity, is widely used in the semiconductor industry to determine the resistivity of uniform samples [17,18].*Van der Pauw* technique uses a thin-plate sample, containing four very small ohmic contacts placed on the periphery, preferably in the corners, of the plate (see Fig. 5.7.).

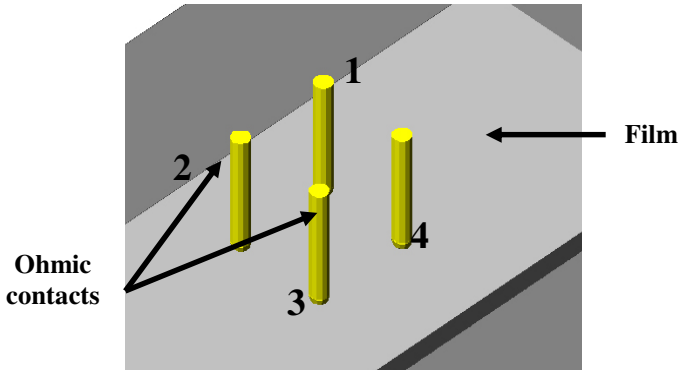


Fig. 5.7. Schematic of a Van der Pauw configuration.

The objective is to determine the sheet resistance, R_S. Van der Pauw demonstrated that there are actually two characteristic resistances R_A and R_B, associated with the corresponding terminals shown in figure 5.8, related to the sheet resistance R_S through the Van der Pauw equation:

$$e^{\left(-\pi R_A / R_S\right)} + e^{\left(-\pi R_B / R_S\right)} = 1 \qquad \text{(eq. 5.4)}$$

which can be solved numerically for R_S.

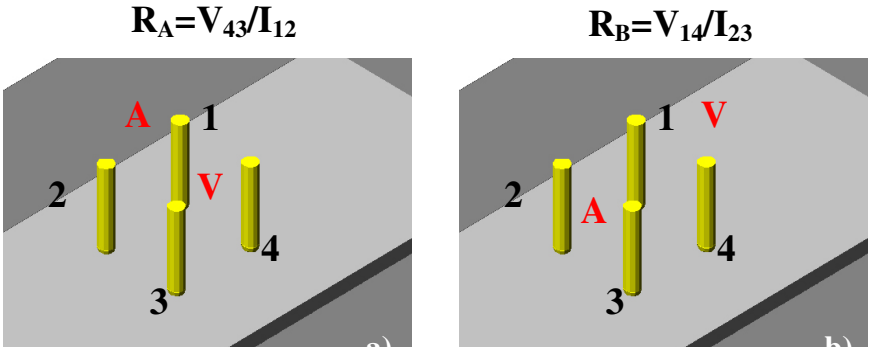


Fig. 5.8 Schematic of a Van der Pauw configuration used in the determination of the two characteristic resistances R_A and R_B.

The bulk electrical resistivity (ρ) can be calculated by multiplying the sheet resistance (R_S) by the thickness of the coating. To obtain the two characteristic resistances, a dc current, I, is applied into contact 1 and out of contact 2 and the voltage V_{43} is measured between contact 4 and 3, as shown in figure 5.8.a). This procedure is followed by a similar one, applying the current I into contact 2 and out of contact 3 while the voltage V_{14} is measured between 1 and 4, see figure 5.8.b). R_A and R_B are calculated using Ohms law.

The use of this technique is restricted by some conditions that must be fulfilled:

- The sample must have a flat shape of uniform thickness.
- The sample must be homogeneous and isotropic.
- The sample must not have any isolated holes.
- All four contacts must be located at the edges of the sample.
- The area of contact of any individual contact should be at least an order of magnitude smaller than the area of the entire sample.

Results and discussion

5.3. Electrical behaviour of the zirconium oxynitride coatings

Following both the composition and bonding characteristics evolutions, the ZrO_xN_y films properties show, as well, a wide range of different behaviours, as it can be observed by the evolution of the electrical resistivity at room temperature, as a function of the reactive gas flow (see Fig. 5.9). The results correspond to the films from series 1.

From this plot, the first conclusion to be drawn is that the evolution of the electrical resistivity evidences the existence of different zones as well, although it seems also clear that there are some important differences if the resistivity is directly correlated with the composition and bonding features. First, there seem to be only three major zones in comparison to the already claimed four for the other characteristics. In addition, the electrical resistivity of the films prepared within zone II, present a variation of this property of about thirteen orders of magnitude, although the composition within this zone has shown to be varying only slightly (see chapter 2, Fig. 2.14). Anyway, the XRD patterns showed some important variations, which may induce some explanations for this large variation of resistivity within a similar material.

In terms of specific analysis, the films from zone I, (present a sub-stoichiometric condition and XRD patterns typical for ZrN), revealed relatively low values of resistivity, ranging from

~ 20 μΩ.cm for "pure" Zr to values around 200 μΩ.cm for the oxynitride films, which allows to index these films as of a "roughly" metallic-type.

These values are also consistent with those in the literature for both Zr and ZrN films [19-21]. In this zone, the XPS valence band spectrum (see Fig. 4.12) showed non-vanishing of the *d* band near the Fermi energy with an overlapping between the *d* and *p* bands. This non-vanishing DOS at the Fermi energy should explain the metallic conductivity of these coatings [22]. *Schwarz et al.* [23] claimed that this overlapping of *p* and *d* bands is a sign of metallic-type materials. Moreover, the films prepared within this zone presented a small increase of resistivity with increasing temperature (Fig. 5.12.), which can be also ascribed to the non-vanishing DOS at the Fermi energy.

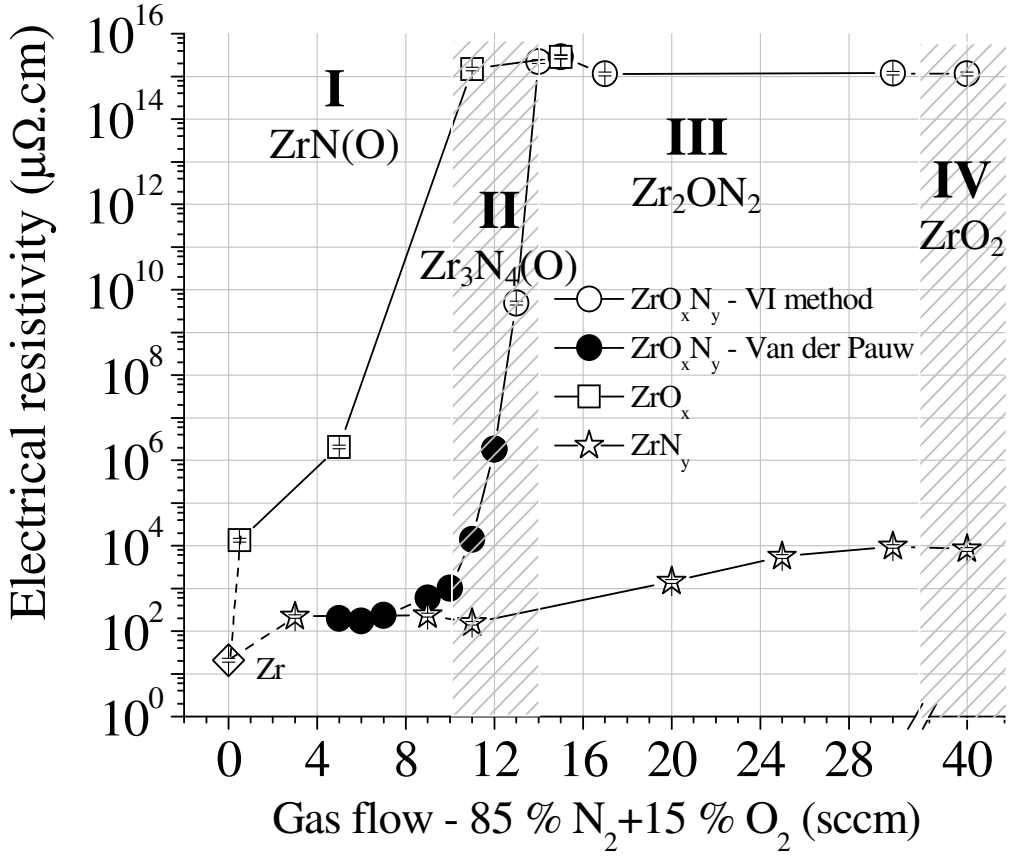


Fig. 5.9. Electrical resistivity variation at room temperature as a function of the reactive gases, for the oxynitride, nitride and oxide series. The error bar was determinate by maximum deviation to the average value.

Figure 5.10. presents the evolution of films electrical resistivity as a function of non-metal to zirconium ratio.

This figure shows that the evolution of resistivity is in good agreement with the different zones (regimes) analysed before, revealing that composition influences the film properties, as in fact it is also demonstrated for all films characteristics, such as the structural evolution. Important also to note is that the films from zones III and IV reveal very similar values of resistivity, which is the result of their insulating nature. Both ZrO_2 and Zr_2ON_2 are known to be of insulating-type, even more if we take into account the most probable doping of this last one with oxygen (let us remind that the composition of the samples from zone III are deviating significantly from that of Zr_2ON_2, with the increasing predominance of oxygen, see chapter 2, Fig. 2.14).

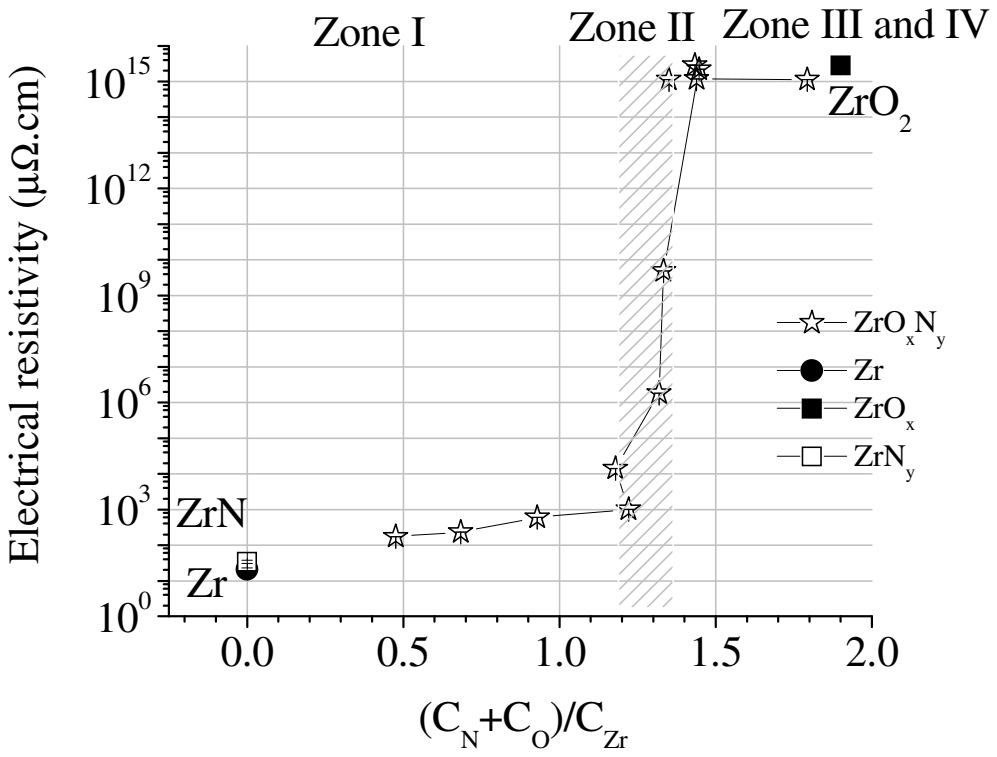


Fig. 5.10. Variation of film resistivity for the films as a function of non-metal to zirconium ratio. For comparison purposes, the resistivity of Zr, ZrN and ZrO_2 films is also plotted. The error bar was determinate by maximum deviation to the average value.

The films allocated in zone II, where an oxygen doped Zr_3N_4-type phase was indexed (see chapter 3, Fig. 3.9), associated with the development of over-stoichiometric nitride compounds (see chapter 2, Fig. 2.14 and 2.15), show the most interesting behaviour. The resistivity is

varying from low metallic-type values (few hundreds of μΩ.cm) at the lower gas flows, to high – insulating-type ones (between 10^{10} and 10^{15} μΩ.cm) at the highest gas flows. The composition analysis for the samples within this second zone (Fig. 2.14 and 2.15) shows only slight changes in the N and Zr content, and the main important change correspond to the O content, which varies from ~9 at. % to about 15 at. %, with the $(C_N+C_O)/C_{Zr}$ varying from 1.22 to about 1.45. Moreover, and although, the XRD data allowed the indexing of an oxygen doped Zr_3N_4 phase, some traces of the previous ZrN phase seem also to be present, especially for the first two samples of this zone, as it is evidenced by the significant peak broadening within the samples of this zone (see chapter 3, Fig. 3.9). Therefore, the significant increase of resistivity in this zone might be resultant from the progressive change of an oxygen-doped ZrN-type structure towards a nitrogen+oxygen rich phase similar to that one of Zr_3N_4. Several authors reported a significant increase of electrical resistivity of ZrN thin films, when the C_N/C_{Zr} ratio is approximately 1.2–1.3, which results in the change of the structure of the films from a metallic-type ZrN to an insulating-type Zr_3N_4 phase [19,20,24,25]. This increase of electrical resistivity cannot be attributed exclusively to the increase of oxygen (Fig. 2.14 and 2.15) and the consequent increase of the ionic character of the bonds, since there is a similar oxygen increase in zone I (Fig. 2.14 and 2.15), but with almost no effect in the electrical resistivity. *Chappé et al*. [26] claimed that the increase of oxygen content and the increase of ionic bonding character are responsible for the smooth increase of electrical resistivity in the transition between a nitride and oxide sputtering regimes for the TiO_xN_y system.

The behaviour of the resistivity in nitrides is a very complex subject, depending not only on composition but also on parameters such as crystalline structure, morphology and density, among others [21,24,27]. In fact, *Chuan-Pu Liu* and co-workers [24] reported that zirconium nitride coatings with rock salt structure (such as the samples within zone I) and similar composition as the samples from zone I and II of this work, revealed electrical resistivity varying roughly between 10^3 and 10^5 μΩ.cm. In the case of the zirconium oxynitrides that are object of study in this thesis, the changes in compositional and structural features from zone I to zone II resulted in an increase of the electrical resistivity of about seven orders of magnitude (from ~10^3 to 10^{10} μΩ.cm, see Fig. 5.9). It is the electronic structure correlated to the compositional and structural features that explains the evolution of resistivity. The XPS valence band plots (Fig. 4.12 and 4.13) allowed to observe a decrease of the *d* band near the Fermi level, associated with an

increase of the 2*p* band. This result indicates an increase of the ionic bond character and thus an increasing tendency to increase the electrical resistivity of the films, with a non-completed vanishing of the *d* band. *Prieto et al.* [28] claimed that the change from metallic to insulating electrical behaviour results from the complete depopulation of the *d* band just below the Fermi level, due to the large transference of Zr *d* electrons to nitrogen. In the same line, *J. M. Sanz* and co-workers [25] claimed that the opening of a band gap in over-stoichiometric zirconium nitride compounds, developing the Zr_3N_4-type phase of zone II, could correspond to a percolation transition. The incorporation of nitrogen atoms prevents the formation of Zr-Zr paths, so that the conduction band minimum becomes determined by Zr-N anti-bonding states, and the valence band maximum becomes determined by N *2p* bonding states. Furthermore, these authors also claimed that the intensity of the *d*-band at the Fermi level of zirconium nitride (ZrN_y) depends linearly on the average nitrogen content (y). The density of electrons per atom of zirconium (i.e. nd) could vary linearly according to the formula nd = 4-3y, with a complete suppression of the *d*-band for y = 1.33 (i.e. in the presence of a Zr_3N_4-type compound).

In the case of this work, the complete depopulation of the *d* band is not observed. Nevertheless the observed incomplete depopulation of the *d* band could result form the sputtering cleaning process. This argument is reinforced by the observed negative slope in the Arrhenius plot, as will see later in this chapter. A “real” non-complete depopulation of the *d* band should result in an opposite electrical behaviour with temperature, and a decrease of electrical conductivity with increasing temperature should be observed.

Another important fact is that the samples lying in zone II, although presenting a significant increase of the resistivity with increasing gas flow, show no significant changes in the activation energies (Fig. 5.11.).

The activation energies were calculated assuming a linear behaviour in an Arrhenius plot of the conductivity as a function of the inverse temperature [26]. The approximately constant low values of the activation energy regarding the samples from this second zone (prepared with gas flows from 11 to 14 sccm), associated with the continuous increase of electrical resistivity, can be explained with the decrease of free career concentration and/or mobility. The continuous increase of oxygen content in the Zr_3N_4 insulating phase could explain the constancy of the electrical conductivity activation energies and the increase of the electrical resistivity as it follows. Taking into account the composition plots (Fig. 2.14), it is possible to observe that

zirconium and nitrogen still dominate in this region, with oxygen content lower than 15 at. %. It is expected that a "pure" Zr_3N_4 phase presents a higher density of states near the Fermi level than a $Zr_3N_4(O)$ phase.

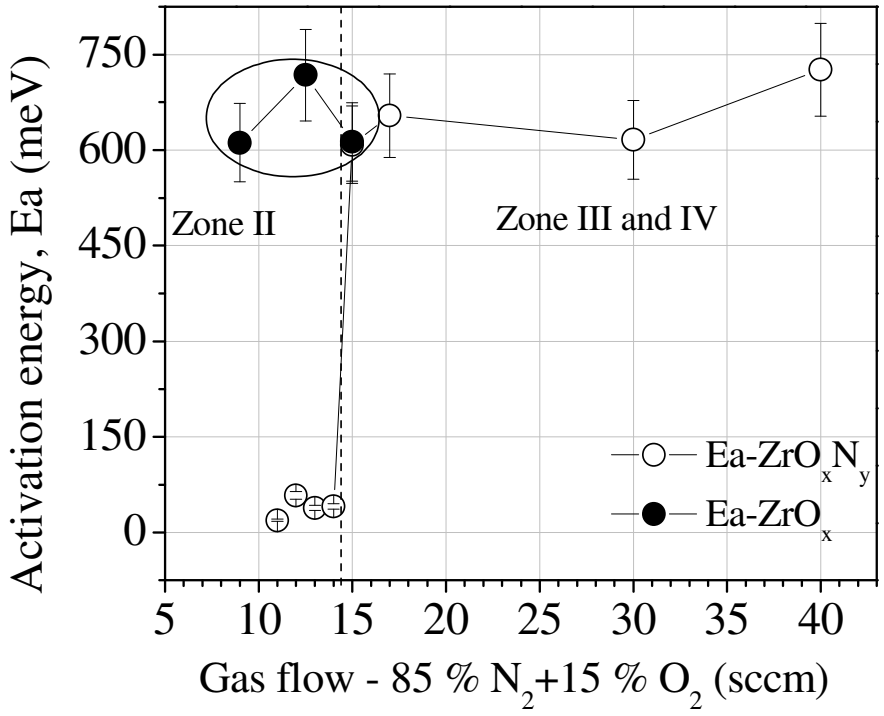


Fig. 5.11. Electrical conductivity activation energies, E_a, as a function of the reactive gas flow for samples from zones II, III and IV. The error bar was determined by maximum deviation to the average value.

The presence of oxygen will induce a shift of the *p* band to lower energies, with the consequent transfer of part of the Zr *d* electrons near the Fermi level to the O *p* band and the concomitant decrease of transference to the N *p* band. Thus, it is expected that the lowest activation energy of the electrical conductivity should correspond to electronic transitions from states closer to the Fermi level, which for zirconium oxynitride correspond to states in the N 2*p* bands. The XPS analysis (see chapter 4) confirms that, although there is an increased transference of *d* electrons to the O 2*p* band and a decreased transference to the N 2*p* bands, there isn't a complete depopulation of the N *2p* band. On this basis, it is possible to assume that the energy of the electrons available for electrical conductivity (in the N 2*p* band) is the same in the samples deposited with reactive gas flows between 11 and 13 sccm, giving rise to approximately constant values of activation energy, but with a decrease in their concentration (and possibly on the mobility too) that results in a lower conductivity.

Regarding the "transition" sample between zone II and zone III (sample deposited with a reactive gas flow of 14 sccm), which presents a mixture of both Zr_3N_4 and γ-Zr_2ON_2 structures, it was expected an increase of the activation energy due to the formation of the γ-Zr_2ON_2 insulating phase, with a higher band gap energy. *Bazhanov et al.* [29] claimed that the calculated DOS for the orthorhombic Zr_3N_4 structure shows the semiconductor character of the material with the Fermi level located inside the energy band gap of 0.68 eV. The same authors claimed an energy band gap of 1.5 eV for the Zr_2ON_2 Bixbyite-type crystal structure [29]. The reason for the constant activation energy of the conductivity regarding this sample should result from the percolation effect within the compound with the lowest activation energy, the Zr_3N_4 structure.

The plot of the electrical resistivity as a function of the temperature (Fig. 5.12) also confirms the particular behaviour of the samples from zone II. Although with resistivity values nine orders or magnitude higher than the first sample within this zone, the sample deposited with 14 sccm shows no significant decrease of resistivity with the temperature.

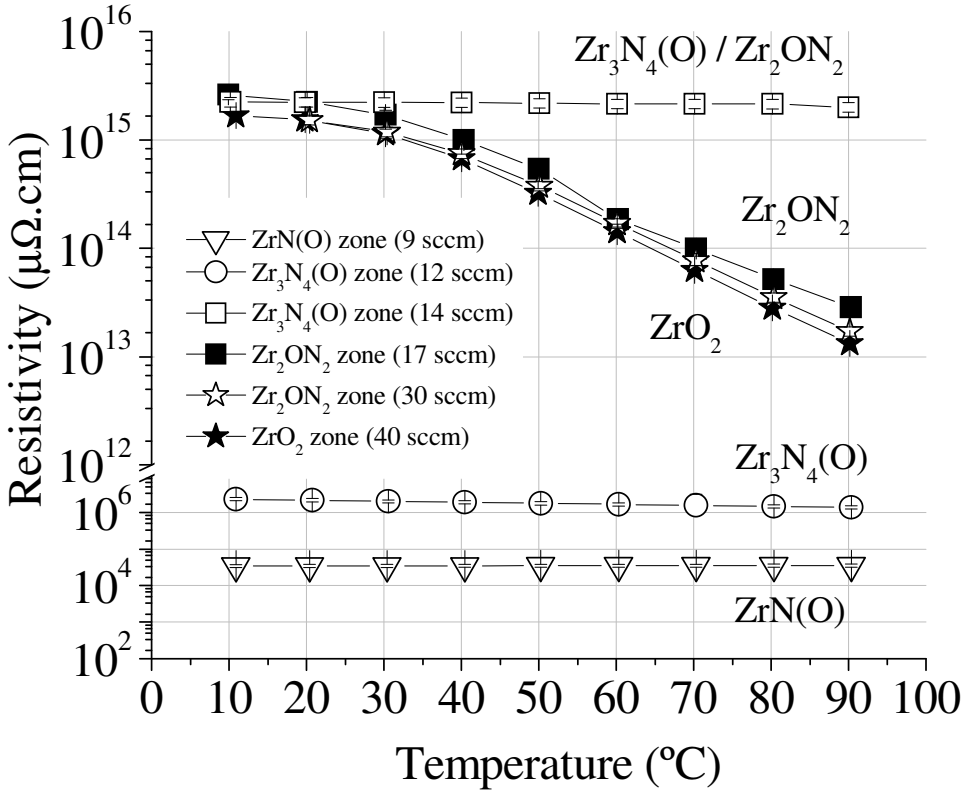


Fig. 5.12. Electrical resistivity evolution as a function of temperature. The error bar was determined by maximum deviation to the average value.

Comparing the evolution of the electrical resistivity of the zirconium oxynitride coatings with the zirconium nitride coatings (Fig. 5.9) it is possible to observe that the zirconium nitride coatings present only a small and smooth increase of the electrical resistivity with the reactive gas flow (N_2). This difference is due to the fact that these films show a dominant conductive phase (ZrN) and only a residual insulating phase, *orth*-Zr_3N_4 (see Fig. 3.7, chapter 3).

Within zones III and IV, the amount of oxygen is already significant and it is enhanced the tendency to have highly insulating phases, such as Zr_2ON_2 and ZrO_2. Therefore, the films tend to be of insulating type. In these zones the samples show high values of the electrical resistivity (Fig. 5.10) and the conductivity is thermally activated (Fig. 5.12), similar to what happens in the case of zirconium oxide films. With the formation of the insulating phases of Zr_2ON_2 and ZrO_2 and the progressive formation of a gap between the *p* and *d* bands, there is a thermal activated transport mechanism (Fig. 5.12). The activation energy for electrical conduction (E_a) is a function of the electronic energy levels of the chemically interacting atoms and hence of the emerging band gap [30]. As already discussed in chapter 4 the samples lying in the third an forth zone show a complete depopulation of the *d* band at the Fermi level, with a continuous shift to higher energies of the *p* band, that explains the electrical characteristics of the samples.

Following the same tendencies observed in all the characteristics that were previously analysed in this thesis, also the electrical properties show notorious similarities within all prepared series, if similar composition and structural behaviours are present. An example of such similarities are the results obtained for the samples prepared within series 2 (the one prepared with a gas mixture composed of 95 % N_2 + 5 % O_2). Figure 5.13. presents the variation of the electrical resistivity as a function of the reactive gas flow for that series 2.

From the observation of this graph, the main conclusion that might be drawn is that there is in fact a great similarity of behaviours with the films from series 1, although one must take into account that in series 2 only the first two zones were observed. Results of this late series revealed quite similar variation ranges, which are again between few hundreds of μΩ.cm to MμΩ.cm values. This shows again a systematic transition between metallic-type films towards insulating ones with increasing gas flow. Similarly to what has been observed in the previous series of samples, the distinct compositional and structural behaviours occurring within the different zones can also be correlated with the resistivity values (taken at room temperature). The initial low

values of resistivity should be again related with the "roughly" metallic nature of the films, which revealed close stoichiometric ZrN(O) compositions (see Fig. 2.18, chapter 2).

The increase of resistivity for the films prepared with reactive gas flows higher than 7 sccm should be explained by the decrease of the metallic bond contribution and the transition from oxygen-doped ZrN towards a nitrogen-oxygen rich phase, similar to that of *orth*-Zr_3N_4.

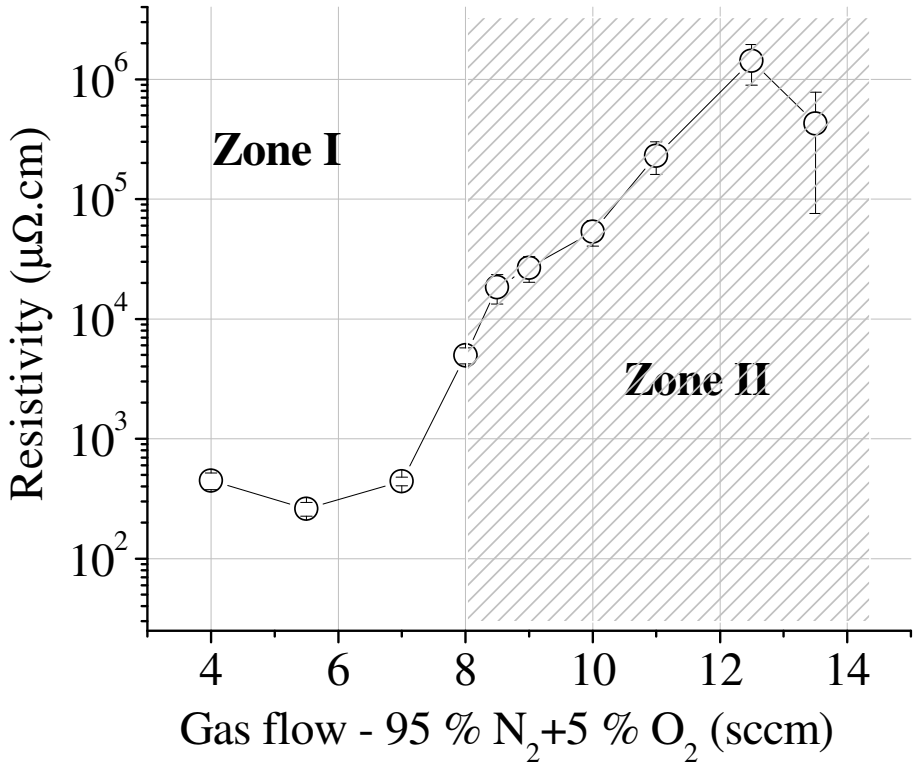


Fig. 5.13. Variation of film resistivity as a function of the reactive gas flow, for the samples from series 2. The error bar was determined by maximum deviation to the average value.

As already explained, the decrease of the metallic bond contribution can be described by a model of bonding of metal (oxy)nitrides. Accordingly, higher C_N/C_{Zr} and C_O/C_{Zr} atomic ratios result in a higher consumption of the free *d* electrons from zirconium atoms and thus fewer free *d* electrons are available for conduction. This reduction of the number of free electrons decreases the metallic bond contribution and increases the covalent Zr-N and ionic Zr-O bonds [21], thus increasing the electrical resistivity. Similar to what has been shown for the samples from series 1, the transition between a *fcc*-ZrN structure towards insulating *orth*-Zr_3N_4(O) type phase induces an increase of activation energy of the films (see Fig. 5.14).

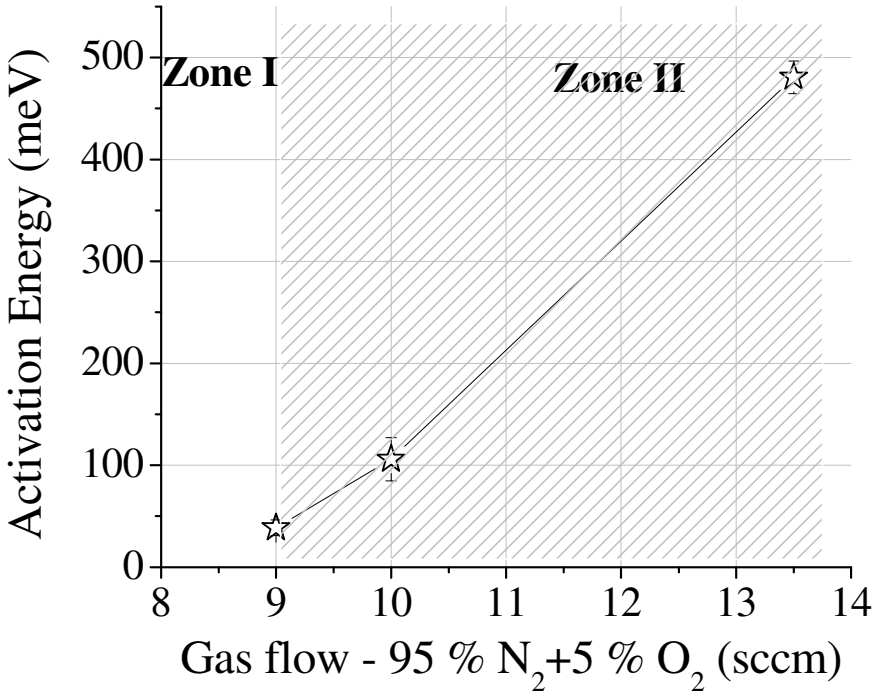


Fig. 5.14. Variation of film activation energy as a function of the reactive gas flow, for the series 2. The error bar was determined by maximum deviation to the average value.

Finally, and in order to confirm that the films' behaviours are mostly rolled by their particular compositions and structural features, another series of films was tested for the electrical behaviour. This series was that one prepared with the reactive gas pulsing process (RGPP), whose results indicate that, beyond some possible small influence, it is most likely to be the film's characteristics that induce the most relevant differences in the films behaviour.

Figure 5.15. presents the variation of the electrical resistivity as a function of the duty cycle for the samples prepared within this RGPP series. This plot shows that once again, the evolution of resistivity may be divided in different zones (regimes). Zone I, which shows films of a "roughly" metallic-type (low resistivity values), correspond to the films that, similarly to what was observed in the previous series, developed a *fcc* ZrN-type phase. This group of films is then followed by a set of others (duty cycles above 0.50 - zone II) that revealed relatively higher resistivity values, which in fact are within the same order of magnitude of those from the other two series revealing similar compositional and structural features.

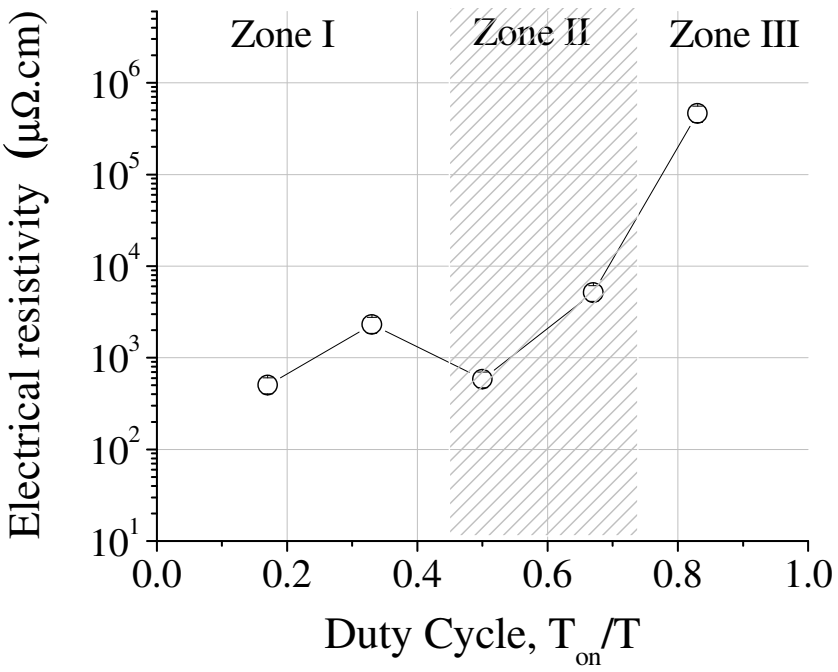


Fig. 5.15 Variation of film electrical resistivity as function of the duty cycle (samples from series 4).

5.4. Conclusions

The zirconium oxynitride films electrical behaviour present straight correlation between the crystalline and electronic structure. The initial low values of resistivity were found to be related with the roughly metallic nature of the films, with compositions between that of Zr and sub-stoichiometric ZrN(O). For higher reactive gas flows (zone II) the resistivity of the films increased, which can be explained by the decrease the metallic bond contribution and the formation of oxygen-doped ZrN crystalline phase towards a nitrogen+oxygen rich phase, similar to that of Zr_3N_4. Particularly noticeable was the result of electrical resistivity of films for intermediate gas flows (oxygen content between about 8 to 15 at. % - zone II films), where in spite of almost no changes in Zr and N contents, the resistivity values increased about twelve orders of magnitude (~10^3 to ~10^{15} μΩ.cm). The structural and bonding changes were found to be in accordance with these changes. Regarding the last two zones, the coatings present high electrical resistivity and the conductivity is thermally activated.

5.5. References

[1]- K. Schwarz, A. R. Williams, J. J. Cuomo, J. H. E. Harper, H. T. G. Hentzell, Phys. Rev. B 32 (19865) 8312.

[2]- L. Wang, M. Yin, Y. Zhu, Surf. Interf. Anal. 35 (2003) 814.

[3]- P. Panjan, B. Navinšek, A. Cvelbar, A. Zalar, I. Milošev, Thin Solid Films 298 (1996) 281.

[4]- L.C. Zang, C. L. Liang, S. K. Cheung, N. W. Cheung, J. Vac. Sci. Technol. B 5 (1987) 1716.

[5]- W. D. Sproul, J. Vac. Sci. Technol. A 4 (6) (1986) 2874.

[6]- P.J. Martin, R. P. Netterfield, W. G. Sainty, Vacuum 32 (1982) 359.

[7]- H.M. Benia, M. Guemmaz, G. Schmerber, A. Mosser, J. C. Parlebas, Catalysis Today 89 (2004) 307.

[8]- J. Adachi, K. Kurosaki, M. Uno, S. Yamanaka, Journal of Alloys and Compounds 432 (2007) 7.

[9- L.E. Toth in *Transition Metal Carbides and Nitrides,* Academic Press, New York, 1971.

[10]- W. Y. Ching, Yong-Nian Xu, Lizhi Ouyang, Phys. Rev. B 66 (2002) 235106.

[11]- M. Yoshitake, T. Yotsuya, S. Ogawa, Jpn. J. Appl. Phys. 31 (1992) 4002.

[12]- V. R. Juza, A. Gabel, H. Rabenau, W. Klose, Allg. Chem. 329 (1964) 136.

[13]- P. Prieto, F. Yeubero, E. Elizalde, J. M. Sanz, J. Vac. Sci. Technol.14 (1996) 3181.

[14]- L. M. Atagi, J. A. Samuels, D. C. Smith, D. M. Hoffman, Mat. Res. Coc. Symp. Proc. 410 (1996) 289

[15]- ASTM Standard D 257 in *Standard Method for DC Resistance of Conductance of Insulating Materials*, Annual Book of ASTM Standards Vol.10.01, American Society of Testing Materials, Philadelphia, 1993, pp.103-119.

[16]- L. J. van der Pauw, Philips Res. Rep, 13 (1958) 1.

[17]- L. J. Van der Pauw, Philips Tech. Rev. 20 (1958) 220.

[18]- A. Bartels, J. Appl. Phys. 15 (1995) 4271.

[19]- H.M. Benia, M. Guemmaz, G. Scmerber, A. Mosser, J. C. Parlebas, Appl. Surf. Sci. 200 (2002) 231.

[20]- H.M. Benia, M. Guemmaz, G. Scmerber, A. Mosser, J. C. Parlebas, Appl. Surf. Sci. 211 (2003) 146.

[21]- D. Pilloud, A. S. Dehlinger, J. F. Pierson, A. Roman, L. Pichon, Surf. Coat. Technol. 174 -175 (2003) 338.

[22]- I. Milošev, H.-H. Strehbtow, Navinsek, Thin Solid Films (1997) 246.

[23]- K.Schwarz, H. Ripplinger, A. Neckel, Z. L. Phys. B 48 (1982) 79.

[24]- Chuan-Pu Liu, Heng-Ghieh Yang, Thin Solid Films 444 (2003) 111.

[25]- J. M. Sanz,, L. Soriano, P. Prieto, G. Tyuliev, C. Morant, E. Elizalde, Thin Solid Films 332 (1998) 209.

[26]- J.-M. Chappé, N. Martin, J.F. Pierson, G. Terwagne, J. Lintymer, J. Gavoille, J. Takadoum, Appl. Surf. Sci. 225 (2004) 29.

[27]- H.B. Bhuvaneswari, I. Nithiya Priya, R. Chandramani, V. Rajagopal Reddy, G. Mohan Rao, Cryst. Res. Technol. 38 (12) (2003) 1047.

[28]- P. Prieto, L. Galán, J. M. Sanz, Phys. Rev. B 47 (1993) 1613.

[29]- D.I. Bazhanov, A.A. Knizhnik, A.A. Safonov, A.A. Bagatur'yants, M. W. Stoker, A. A. Korkin, J. Appl. Phys. 97 (2005) 044108.

[30]- Sodky H. Mohamed , André Anders, Surf. Coat. Technol. 201 (2006) 2977.

Chapter 6

Optical properties

6.1. Introduction

Colour results from the interaction of visible light with materials surface, both extrinsically and intrinsically. The intrinsic interaction results from electrons in materials selectively absorbing (and reemitting such as the case of metals) and reflecting the incident light. The light leaving materials with deficient visible spectra is observed as having colour. Since the main objective of this thesis is the development of decorative intrinsic colour films, in this study, the emphasis is placed on the origins of intrinsic colours in oxynitride thin films, including here the influence of several of the film's deposition parameters as well as the particular compositional and structural features developed in the films.

Light is absorbed through many absorption mechanisms, in which the absorption results from the response of both optical phonons and outermost electrons to the incoming electromagnetic radiation. The absorption processes are categorized into four types of mechanisms [1]:

i. Reststrahlen absorption;
ii. absorption due to impurities;
iii. interband transition;
iv. free-carrier absorption.

Figure 6.1 shows a schematic of the optical absorption spectrum as a function of the energy of the photons.

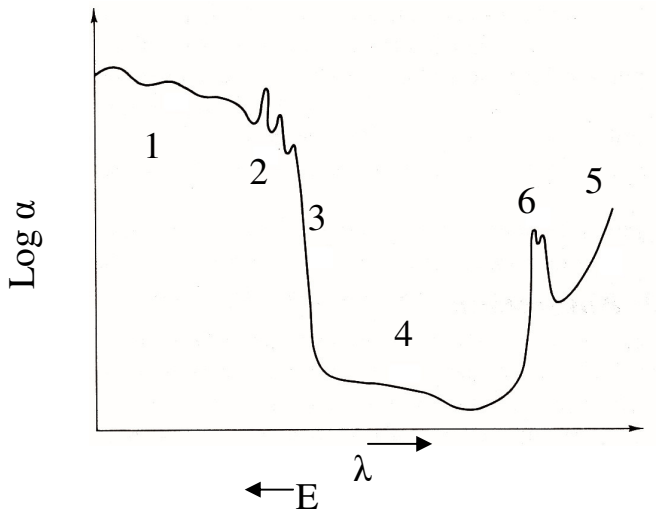


Fig. 6.1. Different types of optical absorption phenomena; (1) transitions of high-lying bands, (2) excitons, (3) fundamental absorption (valence-band-to-conduction-band transition), (4) impurity absorption, (5) free-carrier absorption and (6) Reststrahlen absorption.

Reststrahlen absorption

Reststrahlen absorption happens typically in the infrared region and results from the response of optical phonons to the electromagnetic wave. With a frequency comparable to that of the lattice vibration, the incident electric field induces the vibration of two opposite charges in the transverse direction. The vibration in the transverse optical mode generates the strongest absorption, called *Reststrahlen* absorption, and causes the reflection of the remaining light (mostly in the infrared region) called *Reststrahlen* reflection [1].

Interband transition (valence-band-to-conduction-band transition)

When a photon impinges the material, the valence electrons at the ground state absorb photons of threshold energy and then cross the band gap to an empty conduction band [2]. In a perfect crystal, having a filled valence band and a totally empty conduction band with a forbidden gap between them, the absorption process is ruled by the interband transition mechanism. Interband transitions can be further split into direct and indirect transitions. Both direct and indirect interband transitions must involve a third particle (e.g., a phonon) in addition to the electron and photon in order to account for the momentum transfer [3].

Figure 6.2. shows the difference between the absorption behaviour of indirect and indirect semiconductor.

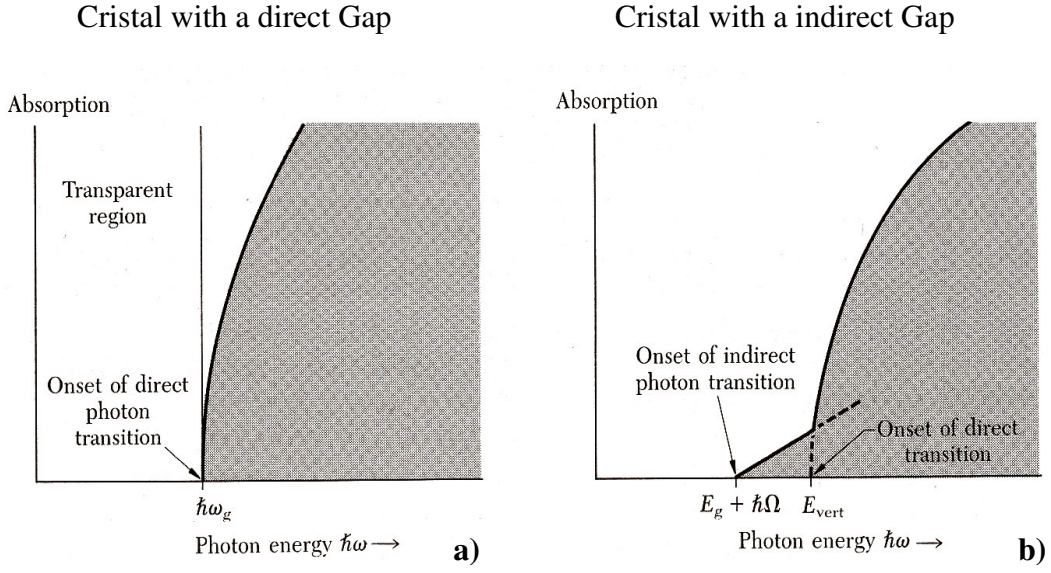


Fig. 6.2. The absorption edge of; **a)** a direct semiconductor and **b)** indirect semiconductor.

From this picture it is clear that indirect transitions require a modification of the density of states since in the energy of the lattice vibrations (phonons) is involved in the transition process. The phonon is either created by the absorption process or, if the temperature is high enough, it is already thermally excited in the crystal.

Colour created from this process depends on the magnitude of the energy gap [4]. With band gaps larger than the highest energy in the visible region (3.5 eV), the materials become transparent since there is no absorption of visible light. Materials with band gaps smaller than 1.7 eV (lower limit of visible region of the electromagnetic spectrum) are opaque and blackish due to the absorption of the whole spectrum of visible light wavelengths.

Absorption due to impurities

In imperfect crystals, there is the formation of extra energy levels, located in a small region around defects. This causes that valence electrons require photons with less energy, regarding the perfect crystals, to go to higher energy levels. For instance, diamond that is colourless but becomes yellowish with nitrogen doping [5]. In this case, nitrogen acts as a donor, creating an energy level at 1.4 eV above Fermi level, although the required for a direct transition between the valence and conduction band is approximately 4 eV. Therefore, the diamond absorbs energy ranging from blue to violet and transmits yellow and green. In case of adding some boron atoms this element will act as an acceptor and the empty state is originated at approximately 0.4 eV above the Fermi level. The diamond is then able to absorb light in red region and appears bluish. Moreover, in most minerals, colouring comes from the presence of transition metals [4].

Free-carrier absorption

When a photon impinges a material with a partially filled valence band, the electromagnetic radiation excites the free carriers from the original ground states to unfilled higher energy states, located immediately above the Fermi energy level. Therefore, these carriers absorb light with a wide range of energy including the visible region. Excited electrons could dissipate their extra energy in form of heat, due to the collisions with the lattice vibrations or in the form of photons when return to lower energy states, leaving the material surface as the observed reflected light. Due to the selection rules, the electron paths going to higher energy levels may differ from the paths returning to ground states and so, the observed colour may not correspond to the absorbed

light [4]. The Drude model, which is the application of kinetic theory to electrons in a solid, can describe the response of free carriers to the electromagnetic radiation [6]. In the theory developed by Drude, every metal contains a huge number of free electrons, which he treated as a gas, the electrons having an average kinetic energy equal to the average kinetic energy of the atoms and molecules of the substance. It assumes that the material contains immobile positive ions and an "electron gas" of classical, non-interacting electrons of density n, each of whose motion is damped by a frictional force, due to collisions of the electrons with the ions, characterized by a relaxation time τ.

However, this model represents an oversimplification and is in fact incorrect in several ways, but it is still a very useful conceptual model to understand the electrical resistivity and to make rough estimates of some physical properties, namely the response of a conductive material to electromagnetic radiation. This response is represented in terms of the refractive index, *n*, and the extinction coefficient, *k*.

The refractive indexes (*n*) represent the ratio of light velocity in vacuum and in the medium, while the extinction coefficient (*k*) indicates the exponential decrease of the light wave intensity during the propagation in the medium and strongly depends on the conductivity of the materials. Both terms are described together as the complex refractive index, *N*. This Drude model correlates the complex refractive index with the number of free electrons, N_e, the electronic charge, *e*, angular frequency, ω, and an effective mass, m_e as follows:

$$N = n + ik = 1 - \frac{4\pi N_e e^2}{m_e \omega^2} \qquad \text{(eq. 6.1)}$$

Accordingly, the free-carrier response as a function of frequency can be discussed in terms of the refractive index (*n*) and extinction coefficient (*k*).

The plasma frequency ω_p is the critical frequency separating a highly reflecting and totally transparent region and is correlated with the density of free electrons as fallows [7]:

$$\omega_e^2 = \left(\frac{4\pi N_e e^2}{m_e} \right) \qquad \text{(eq. 6.2)}$$

with m_e being the effective mass and N_e the number of conduction electrons per unit volume (i.e. the concentration).

With respect to the damping factor, $1/\tau$, and plasma frequency of free carriers, ω_p, the behaviours are separated into three frequency regions [8,9]:

- $0 < \omega < 1/\tau$: the region where the light wave frequency is less than the reciprocal of the collision time. The excited carriers collide freely with crystal lattices dissipating their energy in form of heat.
- $1/\tau < \omega < \omega_p$: the region where light frequency is between the damping constant $1/\tau$ and the plasma frequency. The excited carriers dissipate their energy not through collision but through re-emission, giving rise to reflected light. Although some absorption may occur resulting from some collisions between the freely oscillating electrons and crystal lattice.
- $\omega > \omega_p$; For light frequency higher than the plasma frequency, light propagates through a medium with almost no attenuation since the electrons cannot respond fast enough to screen it.

In specific terms, the colour of a conductive-type material results from the reflected light and is described by the reflection coefficient or reflectivity, *R*, [6,9,10]. Reflectivity is the ratio of the reflected energy over the incident energy of the electric field. With normal incidence of light, the reflectivity is expressed as a function of material properties as:

$$R = \left| \frac{1-N}{1+N} \right|^2 \qquad \text{(eq. 6.3)}$$

replacing the complex refractive index, N, by the equation 6.1., the reflectivity is related to the number of electrons in terms of the plasma frequency as:

$$R = \frac{\omega_p^2/\omega^2}{2 + \omega_p^2/\omega^2} \qquad \text{(eq. 6.4)}$$

The increase of number of free electrons increases the reflectivity of the material.

The particular case of the base material used in this thesis: ZrN

The stoichiometric zirconium nitride, ZrN, is the most thermodynamically stable phase of this binary system, revealing a metallic-like behaviour with a golden-yellow colour due to its metallic band structure [11]. On the contrary, the overstoichiometric phase, Zr_3N_4, is a metastable phase and presents an insulating character and is almost transparent [12].

The variation of the zirconium nitride composition results in the variation of free electron concentration, which mainly influences the optical properties of ZrN_y coatings [13]. Several authors already described optical properties evolution of zirconium nitride with increasing nitrogen content [4,14,15,16]. *Lamni et al.* [14] studied the optical properties of zirconium nitride films as a function of the nitrogen content, by optical reflectivity, transmission and spectroscopic ellipsometry and verified that the dielectric function, and the optical reflectivity, are characterized by a composition–dependent screened plasma energy $\hbar\omega_{SP}$ and reflectivity minimum energy $\hbar\omega_{\min}$ at photons energies proportional to the corresponding plasma energies $\hbar\omega_P$. *Benia et al.* [16] have used an extended Drude model to fit the reflectance spectrum.

The evolution of ZrN_x optical properties as a function of the chemical composition can be understood by tracking the changes of the band structure. As already referred (chapter 4), the zirconium nitride band structure comprises three bands, located between 3 and 8 eV below the Fermi level, which are derived essentially from two 2*p* nitrogen orbitals and from one *d* zirconium orbital. From the ionic model of transition metal nitrides, free electrons in *d* orbitals of transition metal atoms transfer to metalloid atoms to form transition metal nitrides [17]. This implies a charge transfer of roughly one more *p* electron to the nitrogen ion. One can then predict that when a nitrogen ion is removed from the stoichiometric ZrN, the charge transfer no longer takes place and the corresponding electron is returned to the Fermi level. If a nitrogen atom is inserted in an interstitial position, it is probable to bind an extra electron, removing it from the Fermi surface. In the same line of thinking, it is expected that a zirconium vacancy would deprive the conduction band of two electrons, and that a zirconium interstitial would contribute with two more electrons. This carrier concentration N_e variation at the Fermi level will implies an optical properties change with the variation of the optical constants.

In the case of a metallic coating like zirconium nitride, its golden colour is the consequence of a selective absorption/reflection in the visible spectral range. Visible light interacts with the

electrons in a metallic material via intraband transitions (interaction with free electrons, described by the Drude model) and interband transitions (interaction with bound electrons, Lorentz model). The contribution of intraband transitions is determined by the free electron density, which is related to the real plasma frequency, eq. 6.2.

Interband transitions modify the optical properties. In particular, they shift the plasma frequency (ω_p) to lower values [18]. If ω_p falls into the visible range, colours will occur because of a higher reflection of the red part as compared to the blue part.

6.2. Characterization techniques.

Spectrophotometry and colour space

In psychology, colour look is classified by means of visual sensation into three independent properties [19]: lightness, hue and saturation. Hue is what we usually mean when we ask "what colour is that?" It is s the classification in terms of red, blue, green, etc. Each hue corresponds to the relative spectral intensity that is very strong in particular ranges of wavelengths, saturation is related to chromaticity, saturation tells us how a colour looks under certain lighting conditions.

Colorimetry can describe the physiological colour perception by means of the *L*a*b** coordinates in the CIELAB colour space [20]. The horizontal axes, a* and b*, represent the chromaticity coordinates and their signs and magnitudes indicate hues and saturation, respectively.

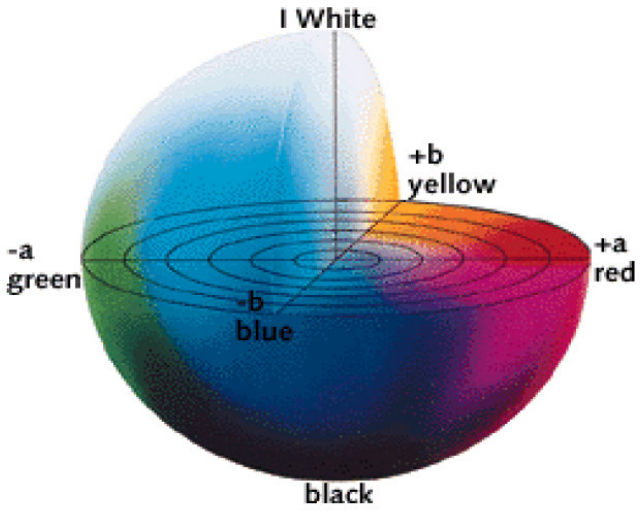


Fig. 6.3. *L*a*b** coordinates in the CIELAB colour space

Their magnitudes vary from zero at the centre of the sphere to 100 at the surface, in positive and negative directions. Regarding the a* coordinate, the "+" sign is attributed to colours in red and the "-" sign to those in green. Positive values of b* are assigned to colours in yellow and negative ones to colours in blue. The vertical axis, L*, represents brightness and its values vary from zero (pure black) to 100 (pure white) at the top of the sphere (Fig. 6.3).
The equations are expressed as follows:

$$L^* = 116\sqrt[3]{\frac{Y_{10}}{Y_{10}^0}} - 16 \qquad \text{(eq. 6.5)}$$

$$a^* = 500\left(\sqrt[3]{\frac{X_{10}}{X_{10}^0}} - \right) - \sqrt[3]{\frac{Y_{10}}{Y_{10}^0}} \qquad \text{(eq. 6.6)}$$

$$b^* = 200\left(\sqrt[3]{\frac{Y_{10}}{Y_{10}^0}} - \right) - \sqrt[3]{\frac{Z_{10}}{Z_{10}^0}} \qquad \text{(eq. 6.7)}$$

where X_{10}, Y_{10} and Z_{10} are the *XYZ* Tristimulus values for a CIE 10º Supplementary Standard Observer (1964) of the specimen. X_{10}^0, Y_{10}^0 and Z_{10}^0 are the *XYZ* Tristimulus values of a perfect reflecting diffuser as for calibration. The standard observer of the instrument simulates the colour sensitivity of the retina in the eye and recognizes colour as does the human brain. The value 10º indicates the field of view of 88 mm at 500 mm view distance. The Tristimulus values are the spectral sensitivity to red, green and blue light of three different cones in the retina and are obtained from the integral equations in the visible region as follows:

$$X_{10} = K\int_{380}^{780} S(\lambda)x_{10}(\lambda)R(\lambda)d\lambda \qquad \text{(eq. 6.8)}$$

$$Y_{10} = K\int_{380}^{780} S(\lambda)y_{10}(\lambda)R(\lambda)d\lambda \qquad \text{(eq. 6.9)}$$

$$Z_{10} = K\int_{380}^{780} S(\lambda)z_{10}(\lambda)R(\lambda)dy \qquad \text{(eq. 6.10)}$$

$$\text{where } K = \frac{100}{\int_{380}^{780} S(\lambda)y_{10}(\lambda)dy} \qquad \text{(eq. 6.11)}$$

$S(\lambda)$ is the relative spectral power distribution of the illuminant such as D_{65}, $R(\lambda)$ is the spectral reflectance of specimen, and $X_{10}(\lambda)$, $Y_{10}(\lambda)$and $Z_{10}(\lambda)$ are colour matching functions for the CIE 10º standard observer, which represents the sensitivity of the human eye to the visible spectrum.

The L*a*b* colour space indicates colour by accounting for both the reflectivity spectra of materials, which is the optical property of materials and the sensitivity to the visible spectra of human eye, which is different for each wavelength. Therefore, the L*a*b* colour space represents the colour evaluation of the human brain. The result is a well-defined colour [18], however do not present any information concerning the material's properties at the origin for this colour.

The characterization of films colour was represented in the CIELab 1976 colour space [20,21] by using a commercial Minolta CM-2600d portable spectrophotometer (wavelength range: 400-700 nm), with diffused illumination (D65 light source) at an 8º viewing angle (specular component included). This equipment is equipped with a 52 mm diameter integrating sphere and 3 pulsed xenon lamps. The observer was placed at a 10º angle.

Regarding the Reflectivity and Transmission were computed using a Shimadzu UV-2501 spectrophotometer.

Spectroscopic Ellipsometry

Ellipsometry is a non-destructive, optical technique that allows studying the optical properties of materials and the thickness of thin films (up to several microns). The basic procedure of this technique is based in the reflection of linearly polarized light in the surface of a material that is intended to be studied. The state of polarization of the light source changes from linear to ellipsoidal, and thus the particular name of this characterization technique. By measuring the polarization state of the reflected light, information related to the optical properties of the material is obtained. The degree of ellipticity of the light after reflection depends both on the optical properties of the coated materials as well as on the coating layers, but also on the thickness of the each layer. A very important characteristic of the ellipsometry technique is that the intensity of the reflected light has no influence on the analysis.

Physical principle

Ellipsometry is an optical technique, which is based on the theory of electromagnetic fields and the effect under investigation at the interfaces of different media. It can be described by the Maxwell equations and the boundary conditions at interfaces. These equations and their boundary conditions allow to determinate the effect of the interaction of the material in the reflection on the polarization state of a polarized light. Figure 6.4 shows two linearly polarized light beams (horizontal and vertical waves) with the same frequency and the same amplitude travelling along the same path.

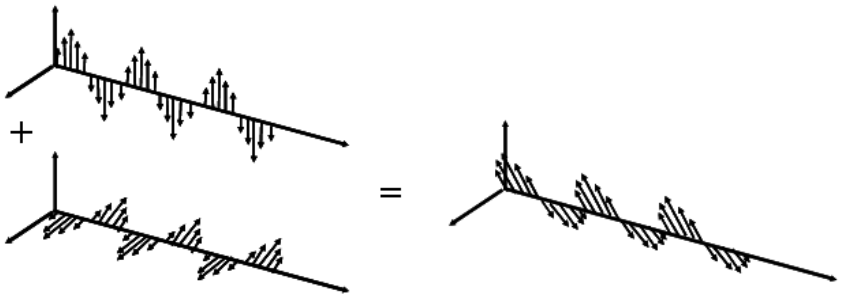


Fig. 6.4. Combination of two linearly polarized beams which are in phase and with the same frequency resulting in a linearly polarized light.

Note that the maximum, minimum and zero points of these waves coincide. When the vectors of the components of the two waves are added, the resultant wave is a linearly polarized wave, which is polarized at 45° to the vertical. *When two linearly polarized waves with the same frequency are combined in phase, the resultant wave is linearly polarized.*

Interaction between light and matter

When a light beam interacts at an interface between two semi-infinite media (air and material), several phenomena can occur. The wave generally changes direction (refraction), slows down, and it can be partially or completely absorbed (absorption), or transmitted (transmission), Fig. 6.5.

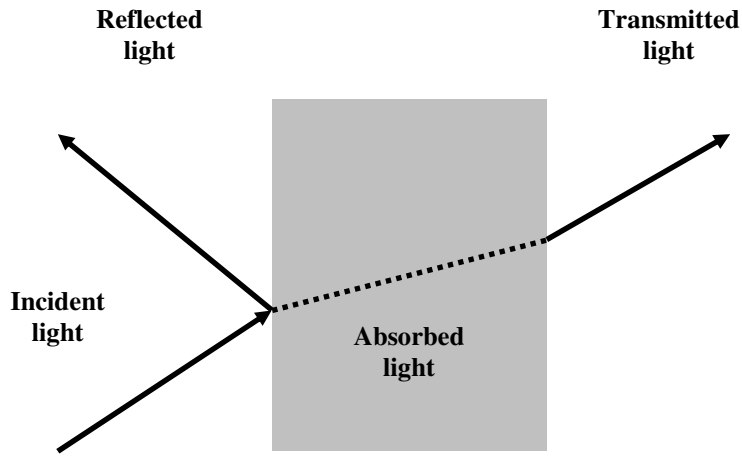


Fig. 6.5. Phenomena occurring due to the interaction between light and matter.

When a material interacts with a such light beam, two of its most important characteristics may be unfolded: its complex index of refraction, *N*, which is a combination of a real number or refraction index *n*, and an imaginary number or extinction coefficient *k*. From *k* one can obtain the absorption coefficient, α, of the material as:

$$\alpha = {4\pi k}/{\lambda} \qquad \text{(eq. 6.12)}$$

Reflection of linearly polarized light

Figure 6.6. shows a reflection of linearly polarized light at the interface between two media.

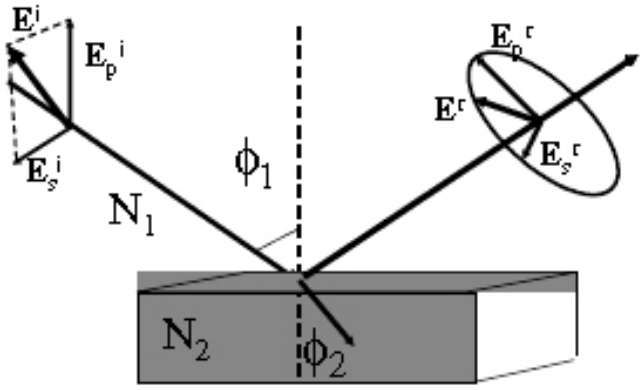


Fig. 6.6. Linearly polarized light after reflection at the interface between two media changes to elliptically polarized light.

The electric field vector can be decomposed by two orthogonal components, one parallel, (*p*) and other perpendicular (*s*) to the plane of incidence. The same may be done with the magnetic field vector. The effect of the reflection depends on the polarization state of the light and the angle of incidence. In the case of linearly polarized incoming light, two boundary conditions of the Maxwell equations have to be taken into account:

a) the component of the magnetic field normal to the plane of incidence (*s*) is steady at the interface;

b) the component of the electric field parallel to the plane of incidence e (*p*) is steady at the interface.

These conditions lead to a reflection of the light between two media (or Fresnel coefficient, *r*) for the components *s* and *p*:

$$\frac{E_p^r}{E_p^i} = r_p = \frac{N_2 \cos\phi_2 - N_1 \cos\phi_1}{N_2 \cos\phi_2 + N_1 \cos\phi_1} \qquad \text{(eq. 6.13)}$$

and,

$$\frac{E_s^r}{E_s^i} = r_s = \frac{N_1 \cos\phi_2 - N_2 \cos\phi_1}{N_1 \cos\phi_2 + N_2 \cos\phi_1} \qquad \text{(eq. 6.14)}$$

The polarization state of light before reflection must be known (the amplitudes of incident *s* and *p* waves, E_p^i and E_s^i). After the reflection, both E_p^i and E_s^i are changed and there is a phase shift between them.

To determine the degree of ellipticity of light, one must measure the amplitudes of electric field vector of *s* and *p* waves after reflection, E_p^r and E_s^r, and the phase shift (δ_s - δ_p), before and after reflection, for *s* and *p* waves. The fundamental principle of ellipsometry is to determine this degree of ellipticity.

For that, ellipsometry measures the complex ratio ρ, defined by:

$$\rho = \frac{r^p}{r^s} = \frac{\left|r^p\right|}{\left|r^s\right|} = \exp\{i(\delta_p - \delta_s)\} = \tan\Psi \exp\{i\Delta\} \qquad \text{(eq. 6.15)}$$

Equation 6.15 represents the fundamental equation of ellipsometry. In ellipsometry two ellipsometric angles (Ψ and Δ) are measured, from which the information about the optical properties of the medium can be derived (*N*). The relationship between Ψ, Δ and *N* is not linear, therefore, it is generally not possible to determine the optical properties of the material analytically from the ellipsometric data.

Let us consider now the particular case of this thesis, where more than one interface is present in the studied material, i.e., a layer on the top of a semi-infinite substrate (Fig. 6.7).

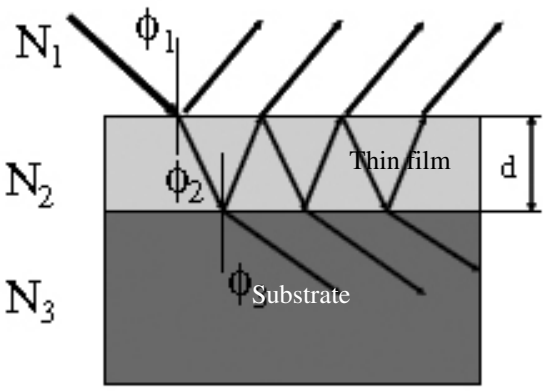


Fig. 6.7. Reflection of light from a thin film of thickness d, deposited on the top of a substrate.

In this case, the light will be reflected twice from two interfaces: the air-film one and that from film-substrate. There is an additional phase shift introduced by the presence of the thin film that can be expressed by:

$$\delta = 2\pi\left(\frac{d}{\lambda}\right)N_2 \cos\phi_2 \qquad \text{(eq. 6.16)}$$

It must be remembered that the relationship between Ψ, Δ and N is not linear, therefore, in order to determine the optical properties of the layer and its thickness analytically from the ellipsometric data, a correct model of the sample structure should be assumed.

Results and discussion

6.3. Optical behaviour of the zirconium oxynitride coatings

The colour coordinates of the coatings from series 1 as functions of the reactive gas flow, represented in the CIELAB 1976 colour space [20,21] are shown in figure 6.8. and 6.9. It is important to note that only the samples that were prepared with gas flows up to 15 will be presented in these two plots, since this is the limit to obtain intrinsic coloured samples.

From figure 6.8 one can immediately conclude that, again, there is a notorious consistency in the obtained results, where not only the same regions of sample mentioned in previous chapters are still present (in fact only the samples from zones I and II are plotted – the intrinsically coloured ones), but also their variation windows growth zones (see chapters 2 and 3). Regarding the brightness values there are two major regions.

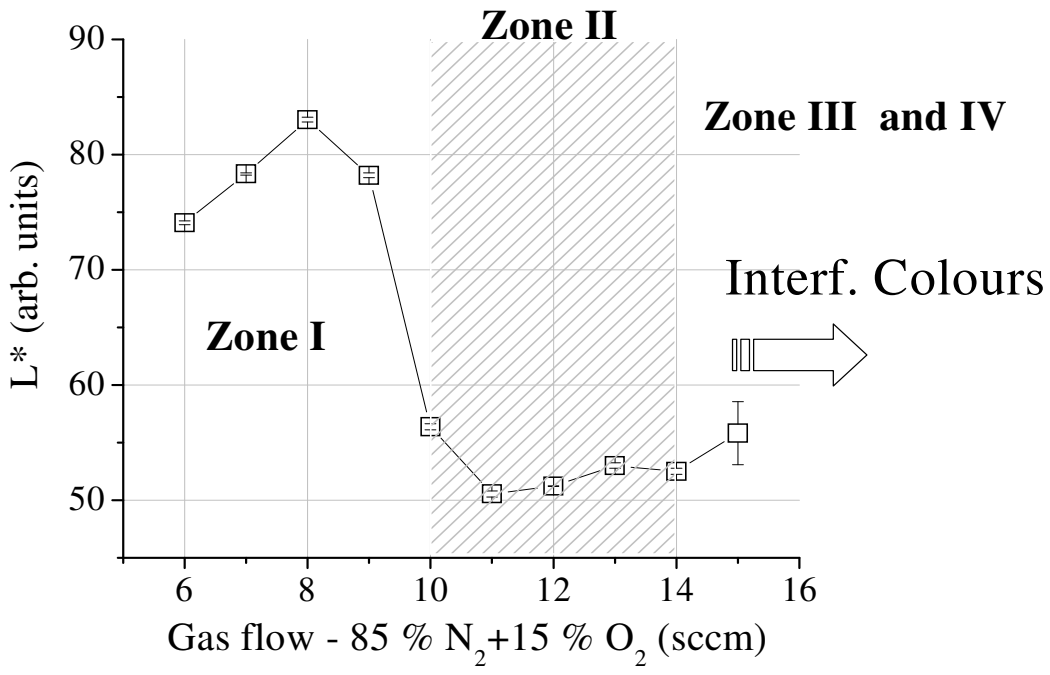


Fig. 6.8. L* coordinate of the CIELAB 1976 colour space [20,21], under the standard CIE illuminant D_{65}, for films prepared with different reactive gas flows from series 1. The error bar was determinate by maximum deviation to the average value.

The first of these regions (zone I in the plot) corresponds to high values of L*, and it is characteristic of the group of samples with non-metal to zirconium atomic ratios varying from ≈ 0.5 to 0.9, which revealed (by XRD structural characterization) to develop structural

arrangements very similar to those of ZrN-type films. The second region includes all the samples that were indexed in previous chapters as belonging to zones II. These samples present lower values of brightness, with colours varying from dark brown to dark blue.

In order to understand this differences between the samples of these two zones, one must keep in mind that the brightness of metallic materials is determined by interactions between incident photons and free electrons [22]. Thus, the decrease in brightness for the samples of zone II should be connected to a decrease in the density of states at the Fermi level [23], as already refereed in chapter 4. The samples within this second zone showed composition values, where the non-metal to zirconium ratios varied from 1.22 to 1.45. Moreover, XRD measurements were somewhat consistent with the development of a structural arrangement where some oxygen could be present in an orthorhombic Zr_3N_4-type structure.

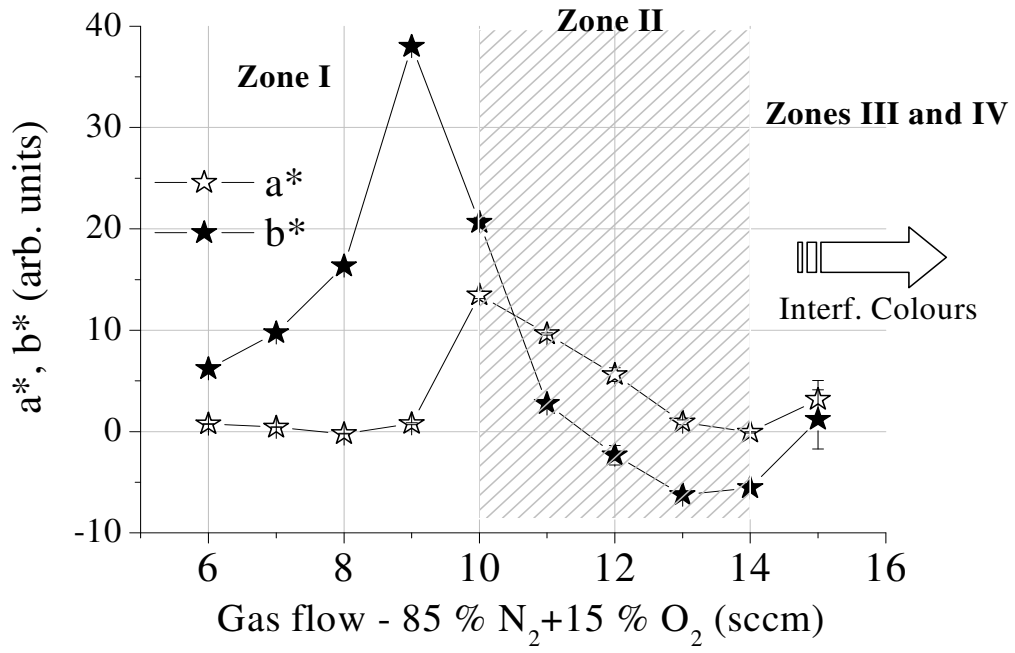


Fig. 6.9. Chromaticity coordinates (a* and b*) of the CIELAB 1976 colour space [20,21], under the standard CIE illuminant D_{65}, for films prepared with different reactive gas flows from series 1. The error bar was determinate by maximum deviation to the average value.

Regarding the chromaticity coordinates (Fig. 6.9.), the distinction between the two zones is again quite clear. When the flow rate increases from 6 to 9 sccm (samples from zone I) the values of a* show no significant changes, but the positive b* values (yellowness) increase significantly. The films colour changed from a very bright pale-yellow (sample deposited with a

gas flow of 6 sccm) to golden (9 sccm sample) with an increase of the yellowness (increase of the positive value of b*, see Fig. 6.3). With further increase of the reactive gas flow, and the consequent changes in composition and the formation of a new structure (Z_3N_4-type one), the samples showed a significant decrease of brightness (L* values) and the colour changed from red-brownish to purple to dark blue.

The reflectivity results of films deposited with reactive mixture flow values up to 9 sccm is shown in figure. 6.10.a). In this plot, each spectrum is associated with a certain reactive gas flow sample and its corresponding non-metal to zirconium ratio, $(C_N+C_O)/C_{Zr}$. To establish some possible correlations between the optical and electrical behaviour of the films, figure 6.10.b) shows also the variation of the electrical resistivity of the films.

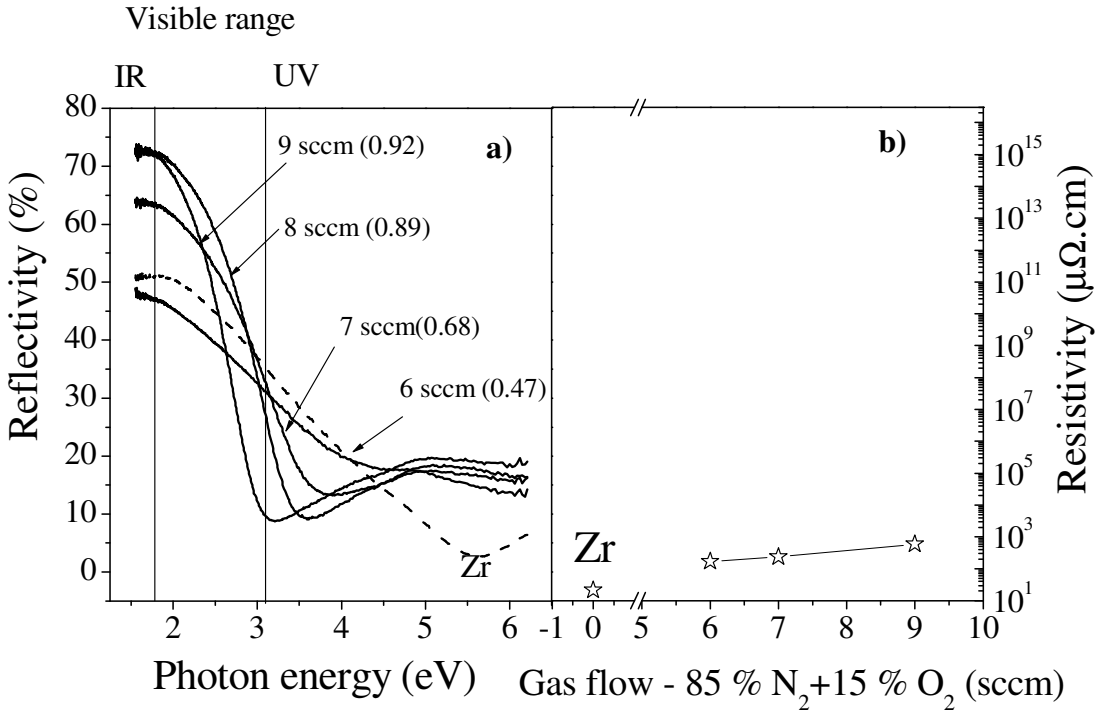


Fig. 6.10.a) Reflectivity spectra for samples from zone I of series 1, as a function of the photon energy; **b)** corresponding electrical resistivity values (at room temperature) as a function of the reactive gas flow.

Figure 6.10.a) shows that all films present high values of the reflectivity in the near-infrared region (NIR - $\hbar\omega < 1.7$ eV), an edge in the visible region ($1.7 < \hbar\omega < 3.1$ eV) and a reflectivity minimum in the UV region ($\hbar\omega > 3.1$ eV). The high values of the reflectivity in the NIR region are typical of good conductors and are the result of the free-carrier absorption mechanisms. The

presence of conduction electrons in high concentration in the materials under study is explained by an overlap between the *p* and *d*-type bands, so that the Fermi level lies inside the *d*-band [3], as already has been discussed in relation with the XPS studies (see, Chapter 4). This gives rise to electrical and optical "metallic-like" behaviour of the films.

The results of the electrical resistivity measurements are consistent with this conclusion, showing relatively low values, in the order of few hundreds of μΩcm, increasing slightly with the increase of gas mixture flow, in agreement with the gradual shift of the plasma edge seen in figure 6.10.a) (we shall return to this point below).

The increase of the non-metal content within this first set of films appears to favour higher values of the reflectivity in the NIR region and the formation of a sharper edge in the reflectivity spectrum. This behaviour of the reflectivity, revealing high values in the NIR, and transparency for shorter wavelengths, puts, in a first approximation, these film as good candidates to be used in heat mirrors [24]. Moreover, and still within this first zone of films (and, in fact, for all studied ones!), the highest reflectivity at low photon energies is reached for the nearly stoichiometric sample (8 sccm), which presented a golden yellow colour, typical of stoichiometric ZrN. Note that this sample exhibits a minimum reflectivity value of 10 % at 3.5 eV (within the UV region of the spectrum). The reflectivity starts dropping in the blue–green region (≈ 2.5 eV) and approaches the level of 25 % in the violet wavelength range (≈ 3.1 eV). The result of the increase of the additive mixture of red and green part of the reflected light gives yellow and, since there is a small destructive mixture of yellow with blue, that decreases the appearance of yellowness, and thus the colour appears as gold-like.

The samples deposited at lower reactive gas flows (< 8 sccm) show a lees pronounced decrease of reflectivity with photon energy in the visible region ($1.7 < \hbar\omega < 3.1$ eV). These samples present a lower effective reflectivity of additive mixture of red and green fractions of the reflected light, and a similar mixture of yellow with blue, and are consequently more silver-like in colour. Another important fact to be pointed out for the samples prepared within this zone I is the already mentioned shift of the reflectivity minimum to lower energies with the increase of the gas flow (increase of the non-metallic content, O + N). As first suggested by *B. Karlsson et al.* [25], the observed red shift of the reflectivity minimum can be attributed to the decreasing role of conduction electrons in determining the optical properties and, hence, to the less metallic character of the coatings [15]. Associated with this shift is the increase of the reflectivity

maximum at lowest energies and the formation of a well-defined edge in the visible region with the increase of the non-metal content (see Fig. 6.10.a).

The plasmon frequency, ω_p, which is characteristic of the plasma edge in the reflectivity spectra is given by equation 6.2. The concentration of the conduction electrons depends on the metal content in the coating, so that an increase in the non-metal content will decrease N and, accordingly, shift the plasmon energy, $\hbar\omega_p$, to a lower value as one can observe in the reflectivity plot (Fig. 6.10.a). *Bendavid et al.* [26] pointed out that the strong red shift of the plasmon energy may also suggest a change of the conduction band nature. However, in our case, the variation of $\hbar\omega_p$ with increasing reactive gas flow (particularly in those samples deposited with 7, 8 and 9 sccm, Fig. 6.10.a) is rather smooth and probably can be accounted for the transfer of the *d* electrons into the *p*-band (decrease of N). The sample deposited at 6 sccm shows no well-defined plasma edge. One possible explanation is the high amount of structural defects present in this sample, resulting from its considerably sub-stoichiometric condition. The high concentration of defects decreases the electron mobility and, consequently, increases the plasmon damping, leading to an overdamping of the plasma oscillations of the conduction electrons.

The observed variation of the reflectivity spectra agrees qualitatively with previously reported results for *fcc*-ZrN [14,16], measured with increasing the nitrogen content. However, the zirconium oxynitride system with similar metalloid contents presents always a shift of approximately 0.5 eV of the reflectivity minimum towards lower energies. In order to understand this, one has to keep in mind that the electronic structure of ZrN is characterized by the existence of a partially filled *d*-band (where the Fermi level is located) and a second band, some 6 eV below it, formed mainly by N 2*p* states. For the ZrN(O) system, the *p*-band is composed by N 2*p* and O 2*p* sub-bands. The transfer of the *d*-electrons occurs also to the O 2*p* sub-band and probably this process influences the reflectivity spectrum. The replacement of one atom of nitrogen by an oxygen atom in the unit cell leads to the formation of a hole in the valence band [27]. Consequently, the position of the Fermi level in the *d*-band could change, affecting the plasmon frequency. Moreover, and since the oxidation state of oxygen is -2 and that of nitrogen is -3, the difference in electronegativity between O-Zr (2.1) and N-Zr (1.7) results in a more ionic character for the former. According to the Pauling theory [28], ionicity of a single bond

increases with the difference in values of the electronegativity between the two elements forming the bond. The higher ionic character could explain the 0.5 eV shift of the reflectivity minimum for the ternary system ZrN(O), for instance, through the different correlation contribution to the Fermi energy.

Even though the metallic behaviour of the material can explain the high values of the reflectivity in the NIR region, the Drude model must be completed by taking into account the interband absorption in order to explain the reflection edge in the U.V. region [15,29]. This behaviour is quite similar to that of the noble metals where interband transitions are responsible for the characteristic colour [30]. For photon energies higher than the reflectivity minimum, the interband transitions start to dominate [31]. This can be taken into account phenomenologically, by introducing a Lorentz oscillator centred at ≈ 5 eV ($\lambda \approx 250$ nm) into the dielectric function, that can account for the optical properties of the material in the UV range [32]. Note, however, that this is a rather crude approximation, possible only for narrow bands.

In order to get further insight into the optical properties of the coatings, the reflectivity data were complemented by spectroscopic ellipsometry measurements in the energy range from 0.5 to 4.5 eV. The composition of the films inherently affects their dielectric constant [33], thereby causing an associated change in the optical constants: *n* and *k*. These two optical constants were analysed for films deposited on Si substrates, by a phase-modulated spectroscopic ellipsometer (UVISEL HR460, Jobin-Yvon Horiba Group) at an incidence angle of 70º in the energy range 0.75 – 4.50 eV.

The calculations of both *n* and *k* values were carried out using a sample structure model to fit the simulated ellipsometric angles, Ψ and Δ to the measured ones. In order to properly select the structure model to fit the simulated ellipsometric angles, the roughness was determined from the AFM analysis. This study showed that the samples lying in the first compositional zone present a homogeneous film surface. Associated to this homogeneity, the samples present a smooth surface, with R_a and R_q values close to 4 nm (fig. 6.11). This low values of roughness for this zone (zone I) suggest that the film growth mode could be the typical layer by layer [22].

Regarding the samples in zone II, it is possible to observe that the first samples within this zone (deposited with 10 to 13 sccm) present similar values to those of zone I (~4 nm).

Taking into account the opaque nature of these films (Zone I and II), the semi-infinite model was applied to treat the ellipsometry data. Using this model, *n* and *k* were directly calculated

from the measured ellipsometric angles. Moreover, and taking into account the relatively low values of surface roughness, it was assumed that they wouldn't affect significantly the optical parameters, and thus they were neglected.

With further increase of the reactive gas flow (15 sccm), there was an increase of R_a and R_q. This evolution of surface roughness could result from the change in the film growth mode from a typical layer by layer in the nitride regime (zone I), to that of Stranski–Krastanov type growth[22]. Associated to the increase of surface roughness is the increase of the difference between the R_a and R_q values, indicating a decrease of the surface homogeneity.

Regarding the samples lying in the third zone, there is a clear tendency to an increase of surface roughness, where the mean roughness (R_a) varies from ~15 nm to ~ 18 nm (see Fig. 6.11), and the mean square roughness varies from -19 to ~32 nm. The samples that present the highest surface roughness present a better-defined γ-Zr_2ON_2 structure (see Fig 4.10, chapter 3).

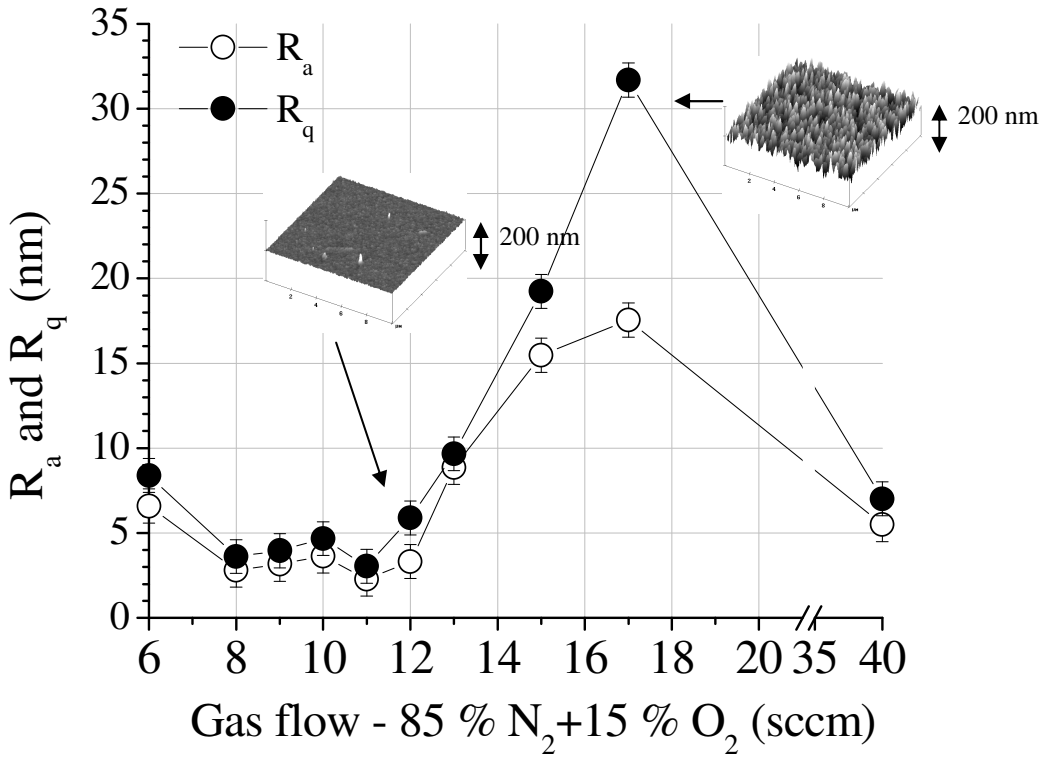


Fig. 6.11. Rms roughness determined from the AFM analysis on a 10x10 μm area of zirconium oxynitride films prepared with different gas mixture flows (series 1).

Regarding the sample deposited with a gas flow of 40 sccm (zone IV - ZrO_2), roughness results reveal low values (~ 5 nm) for both R_a and R_q, indicating a quite homogeneous surface. Taking the semi transparent nature of the films and the results of the surface roughness, for the samples within zone III and IV a two-layer model was used, consisting of a semi-infinite Si substrate, a 100 % dense Zr-O-N coating and a surface roughness layer. The roughness layer was modelled using a Bruggemann Effective Medium approximation [34], consisting of a mixture of 50 vol. % voids and 50 vol. % of a Zr-O-N coating.

Figure 6.10 presents the optical constants *n* and *k* as a function of the photon energy, for the samples prepared within zone I. In this plot, it is also indicated the reactive gas flow values used for the deposition, as well as the non-metal to zirconium atomic ratio for each sample. The *n* and k values were extracted from the Ψ and Δ spectra, using the semi-infinite model.

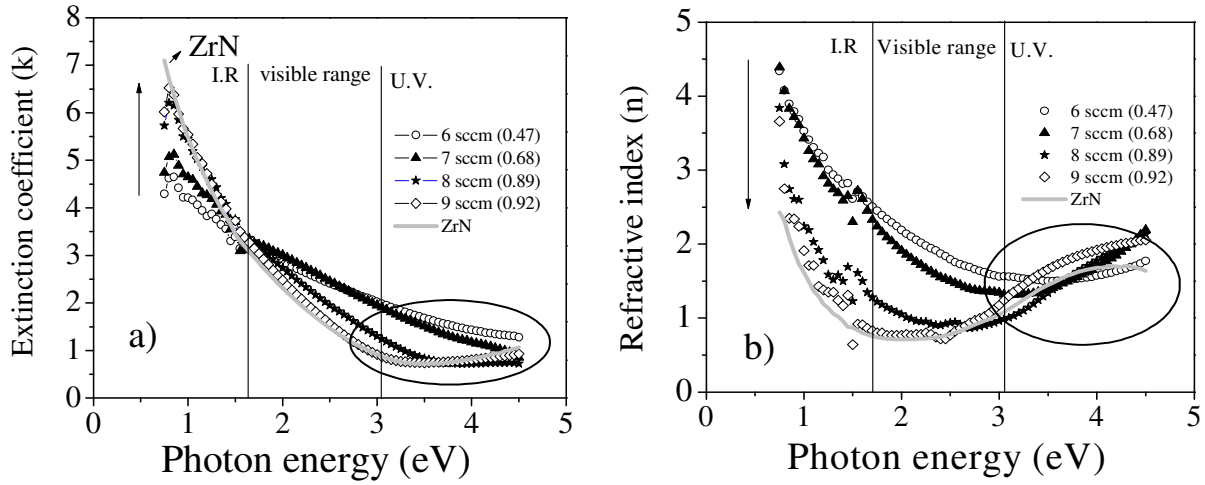


Fig. 6.12. Optical constants, *n* and *k,* as function of the photon energy, for samples from zone I of series 1.

For samples without any detectable oxygen and low metalloid content (samples prepared with reactive gas flows of 6 and 7 sccm), the refractive index, *n*, is below 2.5 in the visible region, (1.7-3.1 eV), while the extinction coefficient, *k*, decreases monotonically with the increase in energy from a high value in infrared region (~ 5 eV) to about 1.7 eV in the UV region. With further increase of the reactive gas flow (8 and 9 sccm), there are other non negligible changes. The coatings present higher absorption in the IR range (<1.7 eV) and lower absorption in the UV range. The increase of absorption in the IR region should result from the increase of free electrons mobility. A close look to figure 6.12.a) shows an increase of the slope

of *k* with energy associated to the increase of absorption in the IR region. One should keep in mind that these samples presented an increase of the non-metal content in comparison to the first two, with a stoichiometry close to one (chapter 2, Fig. 2.15). *D. Pilloud et al.* [35], studying the ZrN(Si) system, justified the decrease of the slope of *k* with energy with the decrease of the lifetime of the free electrons in the matrix. *R. Lamni et al.* [14] claimed that sub-stoichiometric ZrN presents higher charge carrier scattering time and could be described as a dirty metal, i.e., a metal in which the mean free path of the charge carriers is of the order of the interatomic spacing [36]. Since the optical properties of ZrN_x in the visible range are determined to a greater extent by interactions of photons with free electrons [37], the increase of free carriers mobility, could explain the increase of the of *k* at low energies (IR region), and the increase of the slope of *k* with energy.

Comparing the reflectivity spectra of the coatings from zone I with the extinction coefficient, *k*, it is possible to observe that the samples that presented a higher reflection in the visible range ,V.R., (8 and 9 sccm samples, Fig. 6.10.a) present a more pronounced slope of *k* with increasing photon energy (Fig. 6.12), but with lower values of the extinction coefficient, in the same range of energy (V.R.). As already mentioned, these high values of reflection in the visible range are associated with Drude plasmon reflection, and on this basis, the decrease of the *k* in the V.R., for the samples deposited with 8 and 9 sccm should result from the decrease of density of valence electrons with the increase of metalloid content.

The lower absorption in the UV range (Fig. 6.12), is also correlated with the minimum reflectivity values (Fig. 6.8.a)). This could result from the decreasing role of conduction electrons in determining the optical properties and the increase of the contribution of the bonded electrons [32].

Regarding the refractive index (see Fig. 6.12), there is an overall decrease with the increase of the non-metal content, associated with the formation of an edge in the UV region. The decrease of *n* in the samples close to the stoichiometric condition should result from the increase of the free electrons mobility within the material, and the formation of the edge in the UV region could be explained by the offset of inter-band transitions, due to the increase of charge transfer from zirconium 4*d* to the *p* band, already described. Figure 6.12 shows also the *n* and *k* parameters of a stoichiometric zirconium nitride film, where it is possible to observe that these parameters are quite similar those of the ZrN(O) sample deposited with a gas flow of 8 sccm,

with only a small difference in *n* in the UV range. Since this ZrN(O) sample presented a stoichiometry lower than one, with a non-metal to zirconium atomic ratio close to 0.9, it appears that the presence of oxygen as a dopant, could induce the same influence in the optical properties as higher amounts of nitrogen. As already referred, replacing a nitrogen atom for an oxygen one in the matrix, should leave one more electron in the *d* band, although the higher electronegativity difference between O-Zr, in comparison to that of N-Zr, should overcome this factor, resulting in an overall decrease of free electrons in the *d* band, and a decrease of the metallic bond character.

A more detailed interpretation of the influence of the electronic structure may be obtained by the energy loss function, ELF, (eq. 4.3) [38]. Figure 6.13 presents the ELF for the samples prepared within zone I, together with the ELF of stoichiometric ZrN, for comparison purposes.

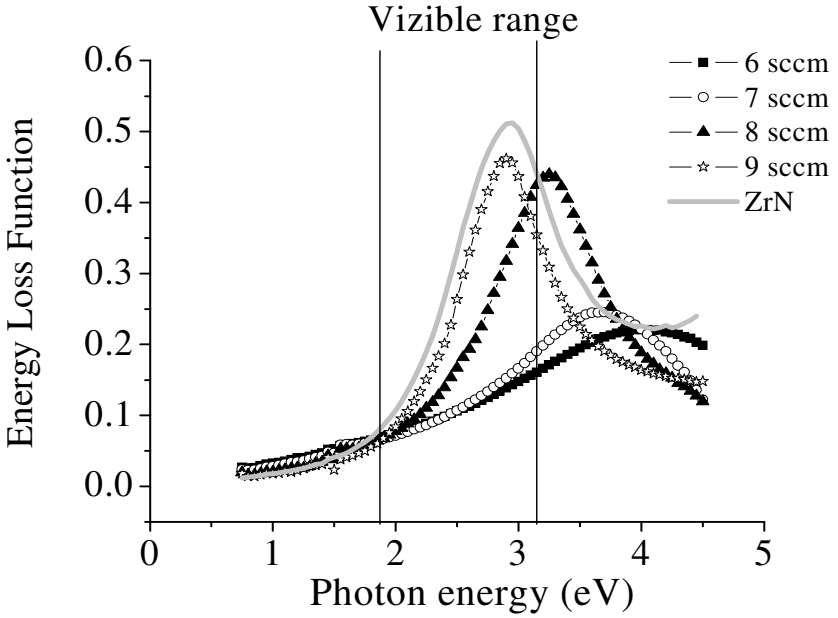


Fig. 6.13. Energy Loss Function as function of the photon energy of samples from zone I (series1).

Regarding the samples deposited with very low reactive gas flows (6 and 7 sccm), in which RBS revealed non-detectable oxygen in the films, the ELF shows a broad maximum, with a clear shift to higher energies, when compared to the samples prepared with higher gas flows (with compositions close to the stoichiometry), as well as that of "pure" ZrN. Moreover, these low gas flow samples (with a clear sub-stoichiometric condition), show also a significantly lower intensity of these energy loss maxima, indicating a considerable amount of conduction electron

damping [31], which can already be predicted from their weak and broad reflectivity minima (see Fig. 6.10.a).

Regarding the samples deposited with gas flows of 8 and 9 sccm (similar to "pure" ZrN), a well-defined maxima of the ELF are observed, indicating that the plasma resonant effect still overlaps the onset of the inter-band transitions [39]. If we look carefully to the energy loss function from these two samples (Fig. 6.13), it is possible to observe that the energy values of the now well-defined maxima is located between 2.5 and 3 eV, values of energy associated to the "plasma reflection" (see Fig. 6.10.a). As already discussed is chapter 4, in the electron energy loos spectroscopy study, the samples lying in this first zone presented a plasmon energy related to the *d*-electrons.

From the set of results already described, it may be assumed that the optical properties of these coatings indexed to zone I, are dominated by interactions of the incident light with free electrons and are thus expected to have the most pronounced metallic binding character. This is well correlated with already described valence band XPS and REELS analysis, where these samples presented a clear non-vanishing of the *d*-band, with an overlapping of the *d*-band with the *p*-band with a plasmon energy related to the *d*-electrons.

Moving from the samples of zone I to those of zone II, and beyond the significant changes that in composition (chapter 2, Fig. 2.14) inb structure (chapter 3, Fig. 3.9) and thus, in the electrical properties, significant changes are also observed in the optical behaviour, as in fact it is expected.

Figure 6.14.a) shows a summary of the reflectivity behaviour of the samples prepared in zone II, as a function of the photon energy, Again, and to establish a parallel between both optical and electrical behaviours, this figure shows also the electrical resistivity values of this group of samples as a function of the reactive gas flow.

The first observation to be noticed is the clear reduction of the reflectivity near the IR region and the continuous shift of the minimum reflectivity edge to lower energies (see Fig. 6.14.a).

Let us keep in mind that this shift has already been observed for the set of samples within zone I, which was attributed to the decrease of the role of free electrons in optical behaviour of the films. Regarding the values of the reflectivity maximum in the IR region, there is a clear reduction in the samples from this zone when compared to those from zone I (~75-50 % for zone I and 50-20 % for this second zone). This significant decrease of the reflectivity maximum near

de IR region indicates a clear reduction of the role of free electrons absorption mechanism in the optical properties of the coatings. Moreover, this initial reduction is continuous within all samples from this second zone, reaching values as low as 20 % for samples prepared with the highest gas flows. This evolution is well correlated with the evolution of REELS and XPS valence spectra, already discus in chapter 4, where a continuous decrease of the plasmon loss (1-3 eV) and a continuous depopulation of the *d*-band were observed, when going from films within zone I to those in zone II (see Fig. 4.16 and 4.8).

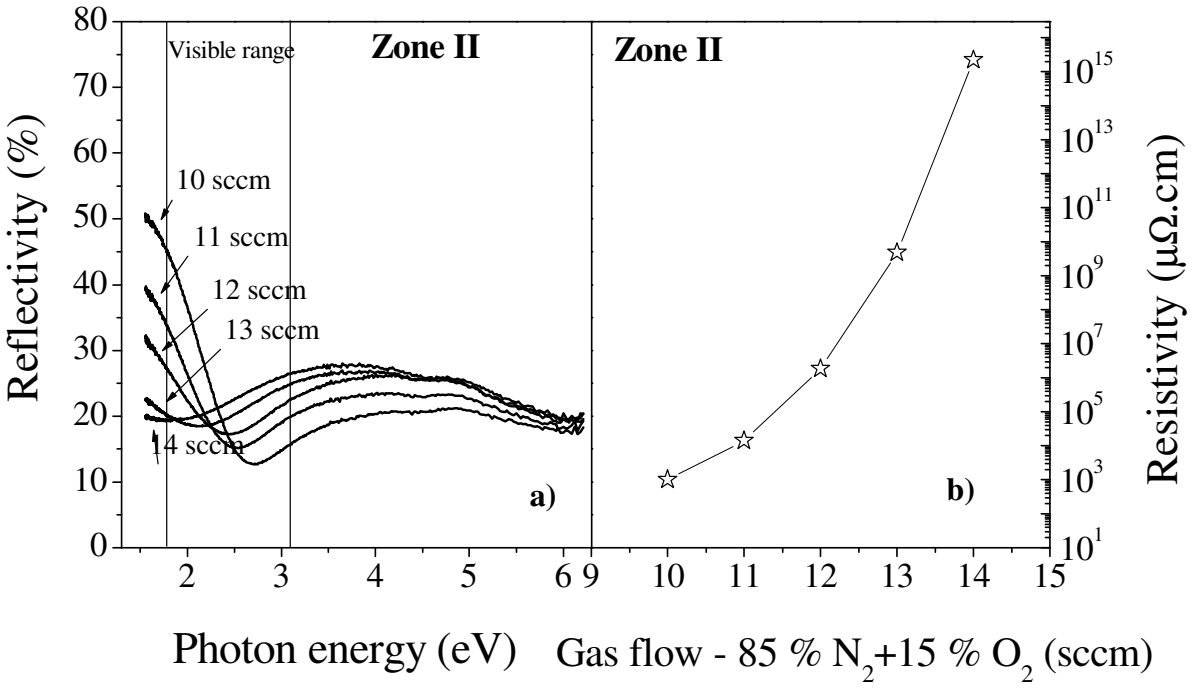


Fig. 6.14.a) Reflectivity spectra as a function of the photon energy correspondent to different reactive gas flow for the samples of zone II - series 1; **b)** electrical resistivity values (at room temperature) as a function of the reactive gas for the same samples.

The variation of *n* and *k* values as a function of photon energy of the ZrON films from zone II, are shown in figure 6.15. With the progressive formation of the insulating $Zr_3N_4(O)$ phase in this second zone (see chapter 3, Fig. 3.10), the coatings present a progressive decrease of the overall values of extinction coefficient and a progressive increase of the refractive index (Fig. 6.15). This optical behaviour evolution is well correlated with the significant increase of the electrical resistivity of the coatings in this zone as illustrated in figure 6.14.

The sample deposited with a reactive gas flow of 13 sccm shows an insulating behaviour with low *k* (< 1) and a *n* value close to 3 in the overall energy range. Optically, this sample behaves similarly to Zr_3N_4 films that present a *n* value higher than 2.5 in the visible range and *k*

lower than 0.3 over the total wavelength range [11]. The first two samples in this zone II (prepared with 10 and 11 sccm) present an extinction coefficient that monotonically increases with a higher value in the IR region, characteristic of metal-like materials, and present the lowest values of refractive index. This could be explained by the presence of a mixture of two compounds: ZrN (responsible for the increase of *k* with a higher value in the infrared region and a low refractive index) and *orth*-$Zr_3N_4(O)$ (responsible for the high refractive index and low extinction coefficient values) [40].

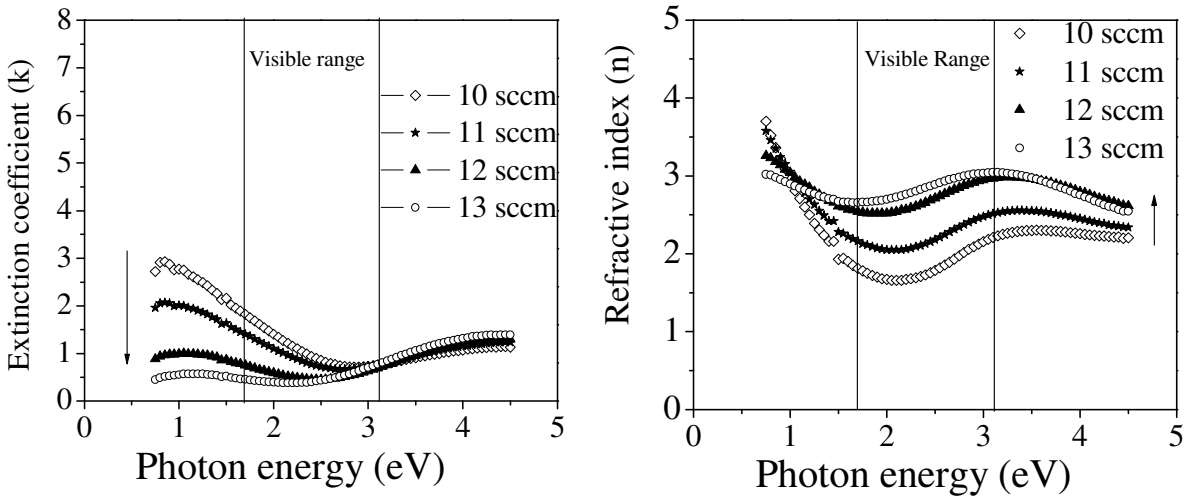


Fig. 6.15. Optical constants *n* and *k* as functions of the photon energy, for the samples belonging to the second zone of series 1.

Regarding the evolution of the energy loss function (ELF) for the samples within this zone (Fig. 6.16) the main result is the shift of the maximum to lower energies.

Associated to this shift, there is a decrease in intensity and broadening of the ELF peak. This is a strong indication that interband transitions are now playing a major role in determining the optical properties in the visible range [38], in the samples of this second zone. These results show that also the optical characterization clears out the notorious different character of samples in each of the two zones.

For samples lying in zone I, the free carriers absorption mechanisms were the main event taking place when the samples where subjected to light interaction, while in zone II, the interband transitions are becoming more and more the main event taking place, when determining the optical characteristics.

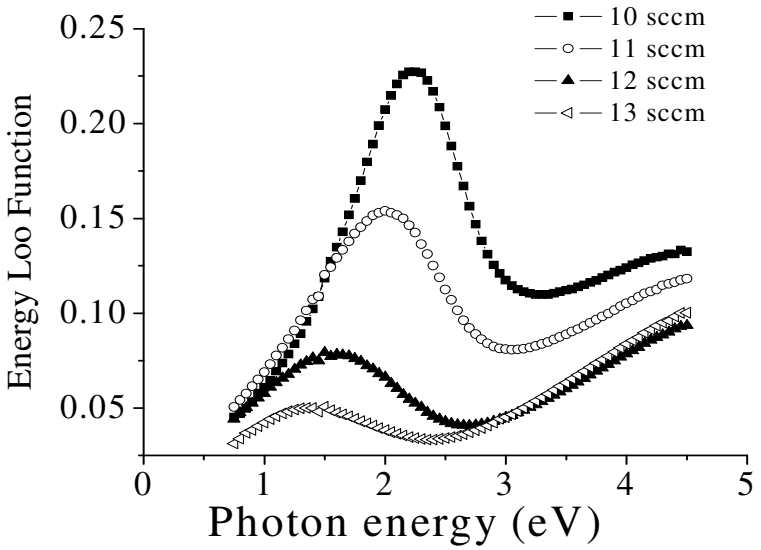


Fig. 6.16. ELF as function of photon energy for the samples of zone II from series 1.

Finally, and to complete the relationship between both optical and electrical behaviours, figure 6.17 shows the: a) reflectivity and b) electrical resistivity of the samples that were indexed to both zones III and IV.

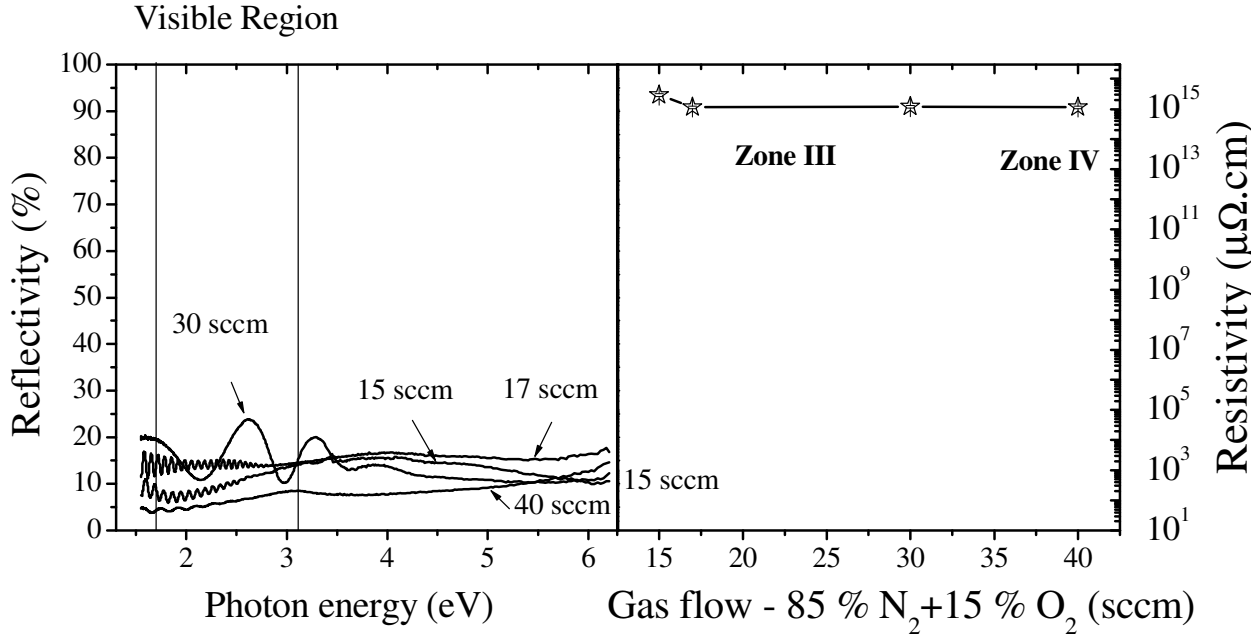


Fig. 6.17.a) Reflectivity spectra as a function of the photon energy for the films produced with reactive gas flow corresponding to the samples lying in the last two zones (zone III and IV) of series 1; **b)** electrical resistivity values (at room temperature) as a function of the reactive gas flow for the samples of the last two zones (zone III and IV) of series 1.

In these plots it is possible to observe that the samples of these last two zones present semi-transparent optical behaviour (interference fringes), and very high electrical resistivity values, in total agreement with the already reported compositional, crystalline and electronic structure results. Since these films present a clear semi-transparent optical behaviour, transmission spectra were acquired (Fig. 6.18).

As already mentioned during the Valence band XPS discussion (chapter 4, see Fig. 4.8), these coatings present a complete depopulation of the *d* band at the Fermi level, and a parallel growth of a broad band at energies between 3 and 8 eV, and thus the films became of semi-transparent/insulating-type. Nevertheless these coatings present similar reflectivity spectra, some non-negligible changes in the optical transmission might be drawn. The samples deposited with gas flows of 15 and 17 sccm present interference patterns indicating that the films are semi-transparent and a higher optical transmission could be achieved.

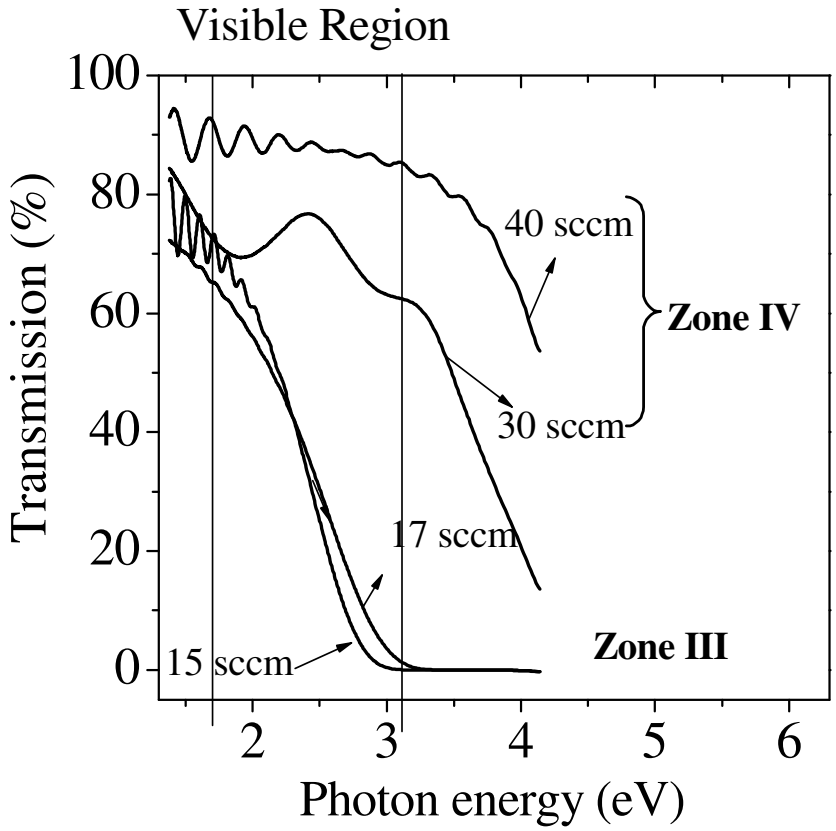


Fig. 6.18. Transmission spectra as a function of the reactive gas for the samples lying in the last two zones (zone III and IV) of series 1.

This evolution is well correlated with the composition, crystalline and electronic structure. These two samples present a C_O/C_{Zr} ratio close to 0.7, but the samples deposited with 30 and 40 sccm presented already values between 1 and 2 (1.2 and 1.8, respectively). This evolution of the optical transmission can also be correlated with the structural changes that are occurring. The samples within zone III presented a γ-Zr_2ON_2-type structure (see Fig. 4.10) that evolves to a ZrO_2 monoclinic-type one for the sample deposited with a gas flow of 40 sccm – zone IV. This last sample shows also a complete depopulation of the *d* band with an energy gap between the top of the valence band and the Fermi level of ~5 eV, and high values of optical transmission within the entire visible range. This is an expected result since the optical energy band gap of ZrO_2 films is commonly given as being close to 5 eV [41].

Figure 6.19 shows the variation of the refractive index *n* and extinction coefficient *k* as a function of energy, for the samples of zones III and IV. For comparison purposes, the characteristics of a "pure" ZrO_2 film is also presented.

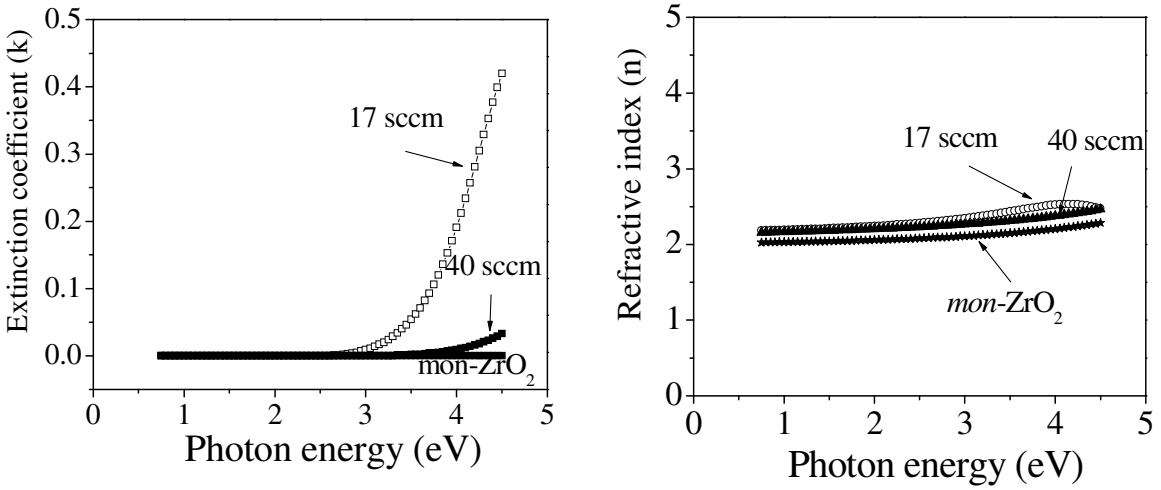


Fig. 6.19. Optical constants, *n* and *k,* as a function of the photon energy. Samples from series III and IV - series 1.

All the films from these two last zones present *n* and *k* values characteristic of insulators. From the plots of figure. 6.19, it can be seen that *k* is almost zero up to 3.1 eV, hence the films are fully transparent in the visible range, as in fact confirmed by visual inspection. Most insulators are transparent or slightly absorbing in VIS-UV region, and therefore their extinction

coefficient is close or equal to zero and increases when energy exceeds the energy of band gap (E_g). On the other hand, *n* values are higher than 2 over the whole explored range, showing a slow increase with energy. It is possible to observe in the plot of figure. 6.19, it is possible to observe that the refractive index *n*, slightly decreases when going from the samples from zone III to those of zone IV. The explanation for the observed behaviour is not easy to evaluate, but the reduction of *n* is often explained as resulting from the decrease of coatings density [42]. The reduction of *n* from the sample corresponding to the ZrO_2-type structure (40 sccm) when compared to the samples from zone III, may also result from the difference of polarizability between metal–nitrogen and metal–oxygen bonds. Since the polarizability of metal–nitrogen bonds tends to be lower than that of metal–oxygen bonds, leading to a higher polarizability of the metal–nitrides [22], the substitution of oxygen atoms by nitrogen should increase the refractive index. Regarding the extinction coefficient evolution, it is possible to observe that the knee in the extinction coefficient goes to higher values of energy, indicating an increase of the band gap.

Another point that is important to clear out is the evolution of the optical energy band-gap for the samples where this parameter can be calculated: zones II, III and IV. Direct or indirect optical transitions are possible in a polycrystalline material depending on the band structure [43]. The nature of the transition involved (direct or indirect) during the optical absorption process can be determined by studying the dependence of absorption coefficient α on photon energy $(\hbar\omega)$ [44] as:

$$\alpha = K(\hbar\omega - E_g)^{a/2} / (\hbar\omega) \qquad \text{(eq. 6..17)}$$

where *K* is constant, E_g is the gap between the valence band and conduction band, *a* is a constant equal to 1 for direct gap materials and 4 for indirect gap material [45,46]. The usual method of determining band gap is to plot $(\alpha\hbar\omega)^{1/a}$ against $(\hbar\omega)$ and look for that value of *a* which gives best linear tendency in the band edge region [46].

Plots of $(\alpha\hbar\omega)^2$ versus $(\hbar\omega)$ and $(\alpha\hbar\omega)^{1/2}$ versus $(\hbar\omega)$ were analyzed for all the samples of the last three zones. Figure 6.20 shows plots of $(\alpha\hbar\omega)^2$ against $(\hbar\omega)$ for representative samples lying in zones II, III and IV - series 1.

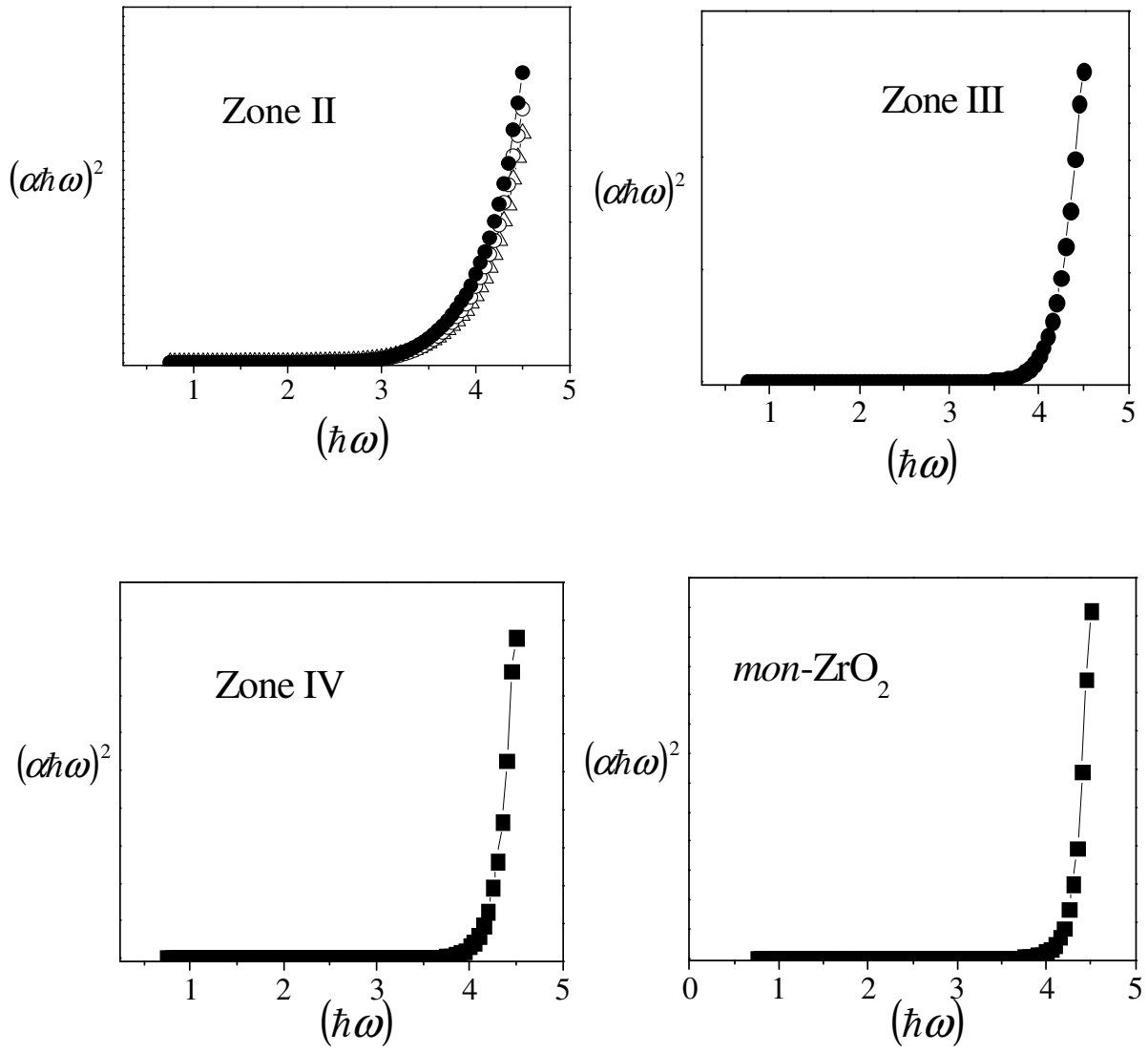


Fig. 6.20. $(\alpha\hbar\omega)^2$ against $(\hbar\omega)$ for representative samples from zones II, III and IV. For comparison purposes, the result from a "pure" ZrO_2 sample is also shown.

The steep increase of the absorption can be attributed to the $(\alpha\hbar\omega)^2$ *vs.* $(\hbar\omega)$ implies that direct transition nature for zirconium oxynitride films [47].

From the plot, the band gap energy was determined by extrapolating the linear part of the curve to zero absorption.

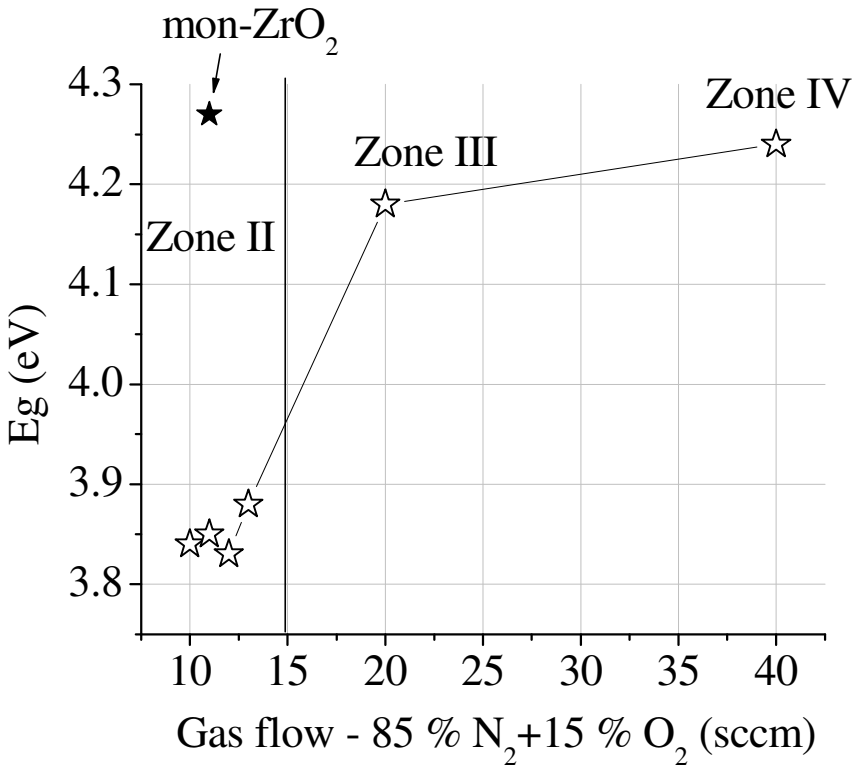


Fig. 6.21. Optical gap for representative samples lying in zones II, III and IV as well as for "pure" ZrO_2.

From this plot it is possible to observe an abrupt increase of the direct transition energies, when going from samples within zone II to those in zone III. Regarding the increase of the E_g for the samples of the last two zones, the main reason should result from the decrease of narrowing of the *p band*, associated to the decrease of N 2*p* bands contribution to the *p band*, already described in the valence band XPS section. Since for the nitrides and oxides, the energy difference between the Fermi level and the *p* group of bands has to be overcome for the interband transitions to start, the decrease of N 2*p* bands contribution to the *p band*, should explain the increase of E_g. *Asahi et al.* [48] found that the substitutional doping of N into TiO_2 leads to the band gap narrowing by mixing N 2*p* states with O 2*p* states. In our case, with the increase of oxygen content, there is a decrease of N 2*p* bands contribution to the *p band*. Thus, the overlap between N 2*p* states and O 2*p* states decreases leading to an increase in the band gap.

Variation of the optical response as a function of the preparation conditions for the other prepared samples (series 2, 3 and 4)

The main objective of this sub-chapter is to show the influence of the following preparation conditions:

i) composition of the reactive gas mixture (series 2);

ii) the application of a bias voltage to the growing film (series 3);

iii) the use of a pulsing process of one of the reactive gases (series 4),

on the optical characteristics of the prepared films.

The overall sets of samples and their particular optical characteristics will be shown together, with the purpose to clearly show the main differences that are present, and above all, to try to find a "basic model" that may explain the observed behaviours. More than an exhaustive display of results for each of the prepared sets of samples, the strategy will be to look for common behaviours and the reasons that may be in the basis of such optical characteristics. A clear understanding of basic relationships between the composition and structure and the optical properties of the coatings will allow the establishment of basic "guidelines" that may act as basis for the development of a large number of different coloured samples, a fundamental factor for a future industrial application.

Figure 6.22. shows the influence of such deposition parameters on the L* coordinate of the prepared films. The observation of this figure shows that there are greate similarities in the evolution of this colorimetric coordinate, showing in all series, Fig. 6.22 a) trough c), the development of two brightness zones, i) a first one with high values of this parameter (~ 70), and another ii) with relatively low values of L* (~ 55). Similar evolution was also observed for series 1, Fig. 6.22d). The samples lying in the first compositional/structural zone present the highest values of brightness, showing only small differences between them. The optical response similarities of the coatings is not based only in the L* absolute values but also in the evolution of this parameter. As can be seen from figure 6.22.a. and b, the initial increase of reactive gas flow induces an increase of brightness values, where, as explained previously for samples from series 1, the evolution of composition of the coatings and their metallic character (developing *fcc* ZrN-type crystalline structures) are the main parameters that may explain such behaviour

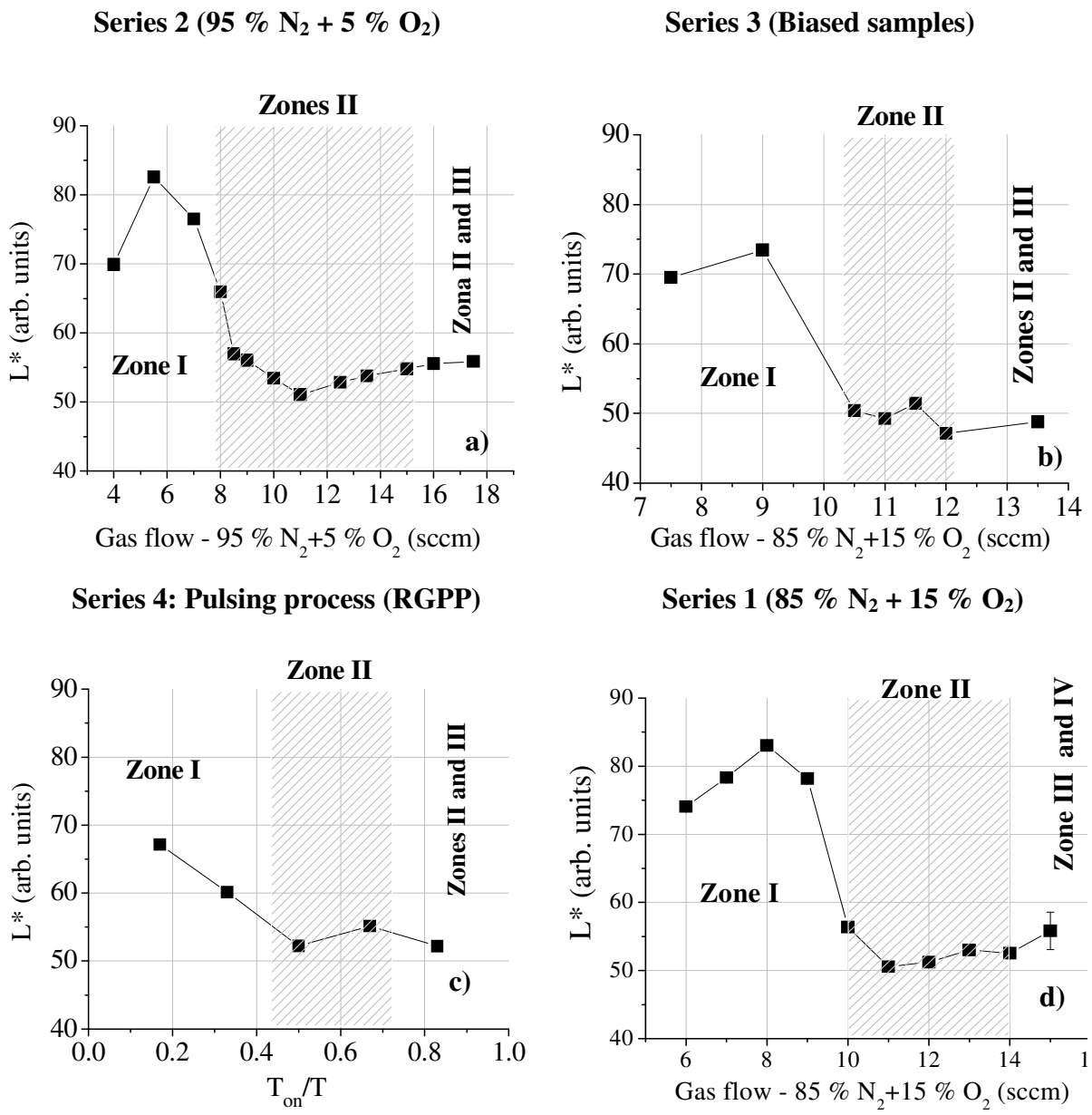


Fig. 6.22. L* coordinate of the CIELAB 1976 colour space [20,21], under the standard CIE illuminant D_{65}, for films from; **a)** series 2, **b)** series 3, **c)** series 4 and **d)** for comparison purposes, is also the L^* coordinate of series 1.

Regarding the evolution of L* from the samples from series 2 and 3, the initial increase is correlated with an initial increase of C_N/C_{Zr} ratio (see chapter 2, Fig. 2.19.a and 2.23.a) and oxygen content close to 5 at.% (see Fig. 2.18.a and 2.22.a). Regarding samples from series 4 there is no initial increase of L* values, which in fact is also coherent with the non-existence of that initial increase of C_N/C_{Zr} ratio and an increase of oxygen content from 5 to 10 at.%.

The samples corresponding to the second composition and structural zone present an abrupt decrease of brightness regarding the samples lying in the first zone. This decrease is associated with the structural change from *fcc*-ZrN trough *orth*-Zr_3N_4(O) crystalline phase as already referred in chapter 3. The chromaticity coordinates evolution is plotted in figure 6.23.

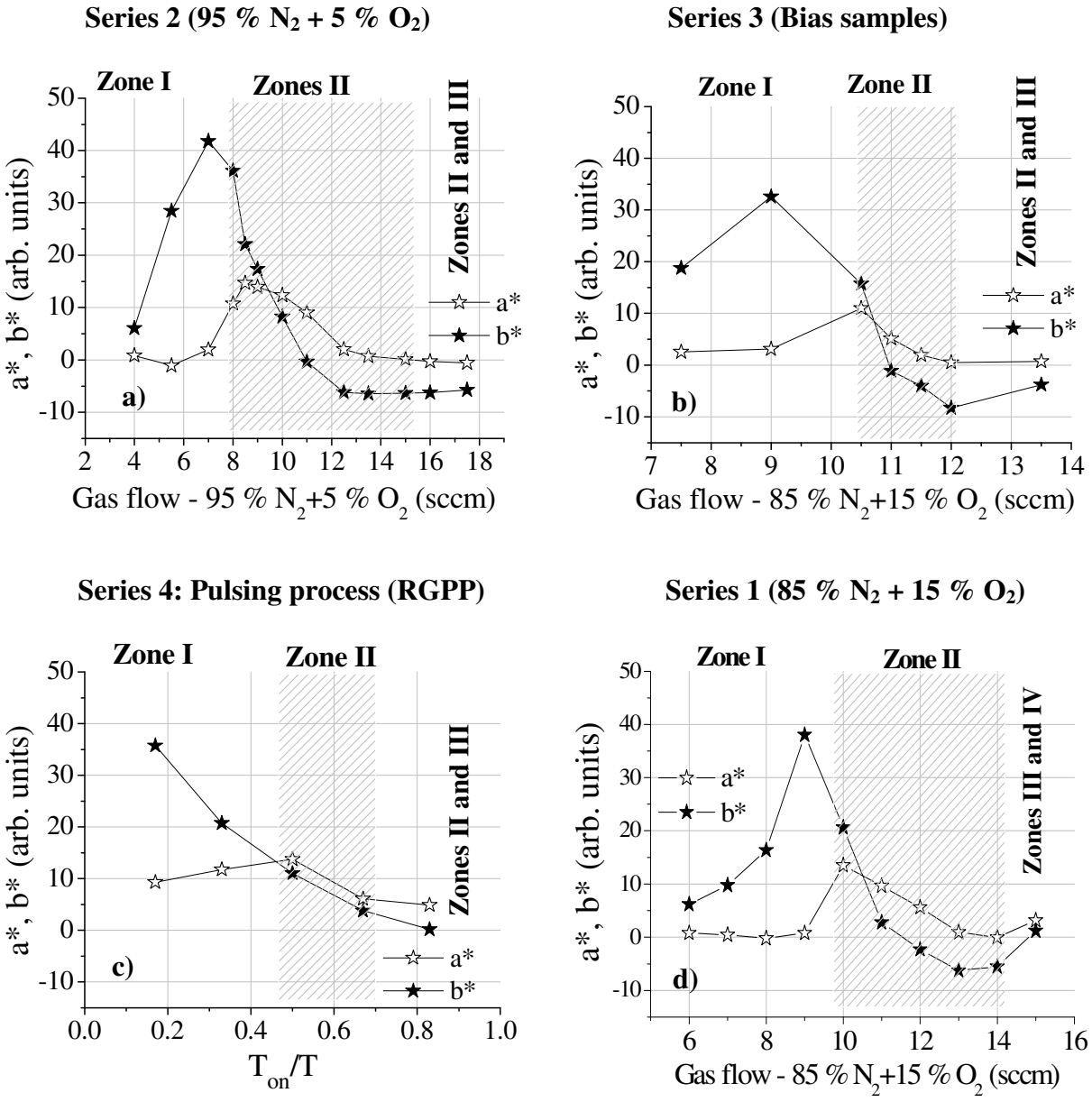


Fig. 6.23. Chromaticity coordinates (a* and b*) of the CIELAB 1976 colour space [20,21], under the standard CIE illuminant D_{65}, for films from; **a)** series 2, **b)** series 3, **c)** series 4 and **d)** for comparison purposes, is also showed the colorimetric coordinates of series 1.

Once again, not only the distinction between the two zones is again quite clear, but also the similar colour coordinates evolution is very similar for all the samples from the different series. As can be seen from figure 6.23, associated to the initial increase of reactive gas flow rate, the coatings deposited using the gas mixture system (Fig. 6.23.a), b) and d)), present values of a* approximately constant, while b* plus (yellowness) values increase. The colour changes from a bright metallic grey to pale yellow to a golden one. As already referred this colour evolution is correlated with increase of metalloid content specially due to the increase of C_N/C_{Zr} ratio.

Regarding the initial colour coordinates evolution of the series 4 (Fig. 6.23.c)), the initial increase of b* (yellowness) is not observed. Although this may seem a deviation from previous series, the fact is again related with the particular composition o these samples. Since the coatings do not present the initial increase of C_N/C_{Zr} ratio, the fact is that their particular composition is already associated to the decrease that was observed in the other series. This "higher stage" composition zone is also reflected in the evolution of the a* values that present a higher value (~10) regarding the samples deposited with the gas mixture system, that present a value for this parameter close to 0.

Regarding the colour coordinates of the samples lying in the second zone, all the coatings (series 1, 2, 3 and 4) present a decrease of a* and b* values. With the formation of the $Zr_3N_4(O)$ structure and the increase of C_O/C_{Zr} ratio, the colour of the coatings changed from red-brownish to dark blue-gray.

Figure 6.24 shows the reflectivity spectra of samples from series 2, 3 and 4. Similarly to what has been observed for series 1, two different optical behaviours are also present: i) one showing high reflectivity near the IR region and a minimum in the visible/I.R. range (Zone I) and another ii) with almost constant low values of this parameter in all the energy range. These two distinct optical behaviours are associated with the two different crystalline structures, already referred in chapter 3, the *fcc*-ZrN(O) and the *orth*-$Zr_3N_4(O)$ structures.

Comparing the reflectivity spectra of all the samples (see Fig. 6. 24) with the composition evolution of these samples (see figures 2.19.a, 2.23.a and 2.27.a), it is possible to conclude that if the non metal to zirconium ratio is lower than one, then the increase of metalloid content will induce an increase of reflectivity near the IR region. As a mater of fact, the sample from these series that present the highest values of reflectivity near the IR region is the sample of series 2 deposited with a gas flow of 5.5 sccm, which presented a C_N/C_{Zr} atomic ratio of one, and an

oxygen content lower than 5 at.%. This composition close to stoichiometric ZrN induces a similar reflectivity spectrum and consequently similar colour.

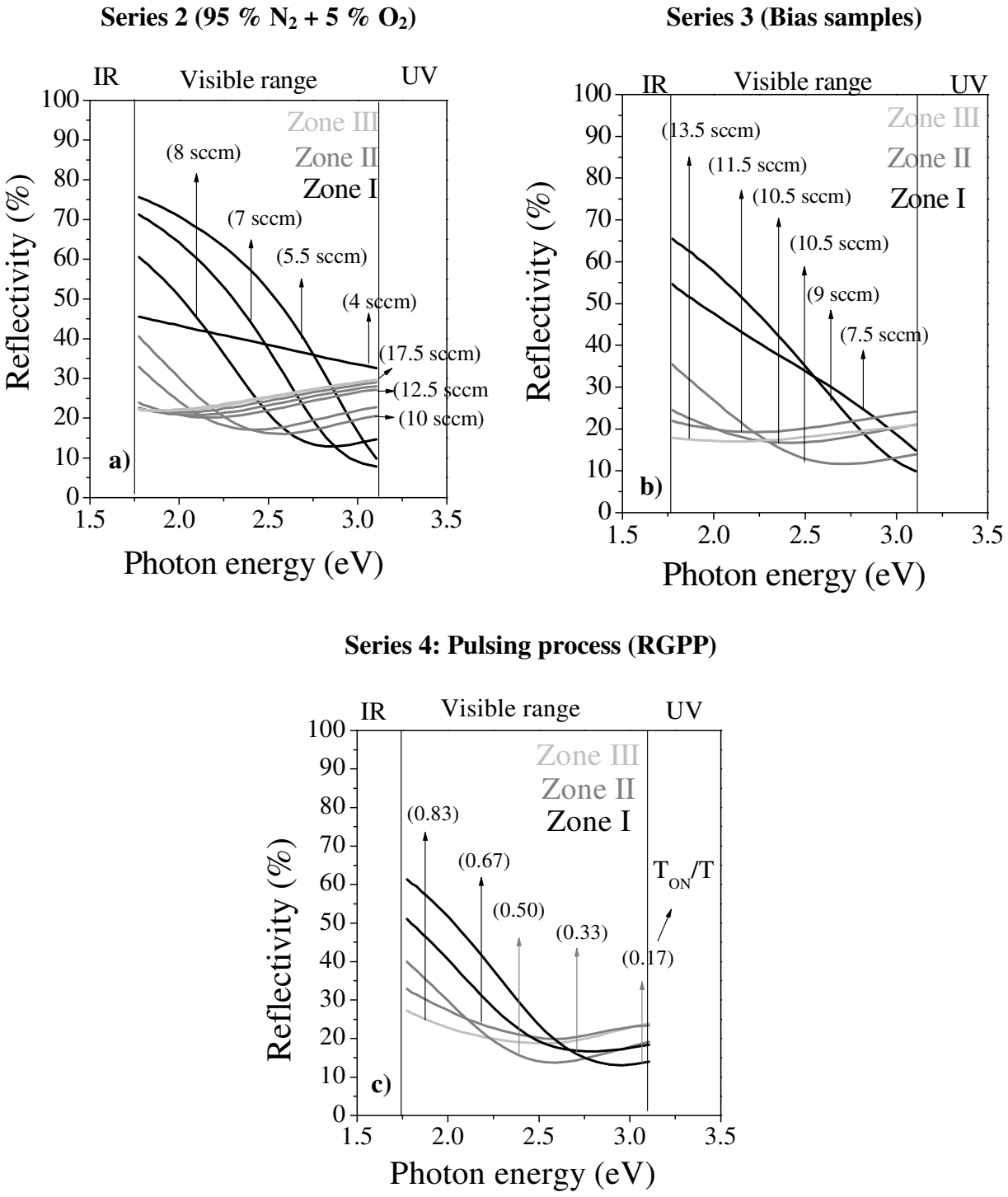


Fig. 6.24. Reflectivity spectra as a function of photon energy for samples from; **a)** series 2, **b)** series 3 and **c)** series 4.

If the non-metal to zirconium atomic ratio is higher than one, the increase of metalloid content will induce a decrease of reflectivity near the infra read region.

In site of the increase of the metalloid content could increase or decrease the maximum reflectivity near the infra read region, depending if the stoichiometry is lower or higher than one, the increase of nitrogen or oxygen will induce always a shift to lower energies of the reflectivity minimum. Although the overall metalloid content plays an important role in the optical response of the coatings, a deeper analysis show that oxygen and nitrogen increase have different degrees of influence in the optical evolution of the coatings.

If the increase of the metalloid content is due to the increase of oxygen content, the already referred changes (decrease of reflectivity near the IR region and a shift to lower energies of the reflectivity minimum) are more pronounced – acting as if oxygen has a catalytic effect, similarly to what has been discussed for the structural changes occurring in the oxynitride system when compared to the nitride one. This behaviour is observed by comparing the reflectivity spectra of the coating deposited with a reactive gas flow of 7 sccm (sample from series 2) and the sample deposited with a duty cycle of 0.33 (from series 4). Although both samples present an atomic ratio (C_O+ C_N) /C_{Zr} close to 1.2, the RGPP sample presents a higher C_O/C_{Zr} ratio (~0.2) and a lower C_N/C_{Zr} ratio (~1) in comparison with the gas mixture sample, which presents a C_O/C_{Zr} ratio close to 0.05 and a C_N/C_{Zr} ratio close to 1.1. This higher oxygen content for the RGPP sample induces a decrease of the reflectivity near the IR region form ~70 % to ~ 50 % (sample from series 4) and a higher shift to lower energies of the minimum reflectivity (see Fig. 6.24.a and c). This "catalytic" effect is confirmed by the evolution of the reflectivity spectra of zirconium nitride (deposited using only nitrogen as the reactive gas) for different reactive gas rates (see Fig. 6.25). Nevertheless, the binary ZrN_y system presents similar reflectivity spectra evolution (Fig. 6.25) when compared with the ternary ZrO_xN_y system corresponding to the first two compositional zones (Fig. 6.24). Due to the oxygen catalytic effect the consequence bonding-type change occurring when nitrogen is progressively replaced by oxygen. In the oxynitride system, the necessary reactive gas flow to trigger the change in the optical behaviour is close to 10 sccm, whereas for the binary system ZrN_y is close to 20 sccm, with similar depositions conditions in what concerns the erosion of the target and deposited in static mode.

Regarding reflectivity behaviour of the samples prepared within zone II, with increasing metalloid content the tendency of reduction of the reflectivity near the IR region and the

continuous shift of the minimum reflectivity edge to lower photon energy, still remains in all the coatings.

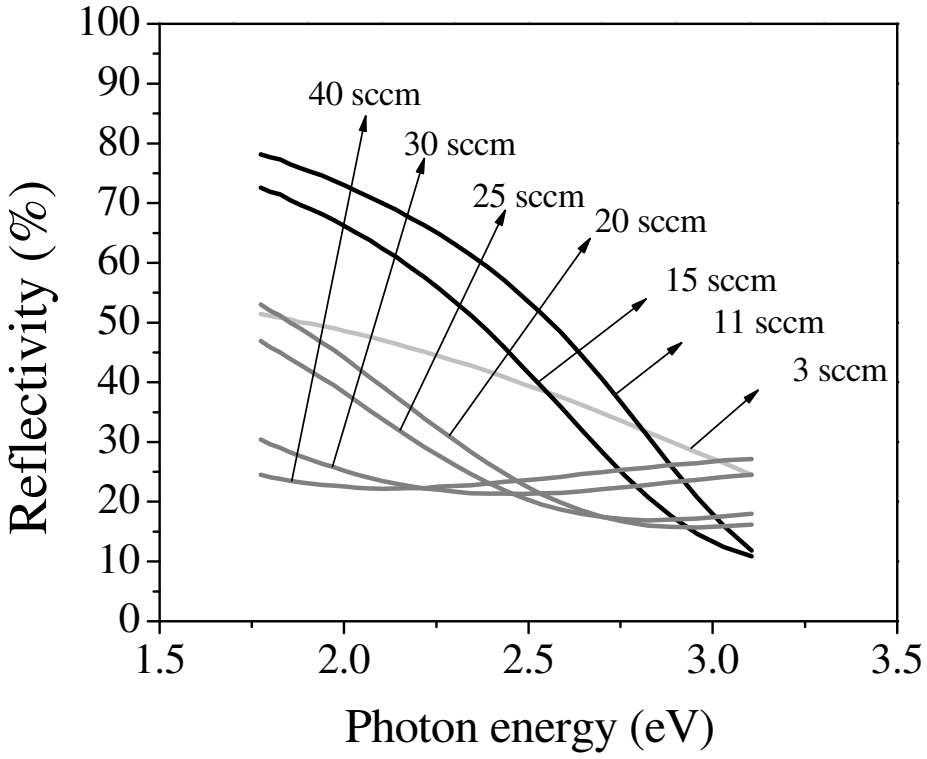


Fig. 6.25. Reflectivity spectra for ZrN_y films for different values of nitrogen flow.

Although the similarities between the reflectivity spectra of the samples lying in the second compositional zone, there are some non-negligible changes that must be referred. The minimum reflectivity spectra of the last two samples of the RGPP series appears to present a less pronounced shift to lower energies regarding the gas mixture samples (series 1, 2 and 3). The RGPP sample deposited with a duty cycle of 0.83 shows a reflectivity minimum close to 2.1 eV, whereas the gas mixture samples (14 sccm - *series 1*, 17.5 sccm- *series 2* and 13.5 sccm – *series 3*) present a reflectivity minimum close to 1.8 eV. Once again, the small differences in composition should explain the difference. A closer analysis of the non-metal to zirconium ratio of each sample shows that the RGPP sample present the lowest metalloid content, although with a similar C_O/C_{Zr} atomic ratio the others samples. This confirms that the increase of nitrogen and oxygen content in the coatings induce a shift to lowers energies the minimum of reflectivity, although the oxygen appears to present a more pronounced effect in this evolution.

The increase of nitrogen and oxygen induce a progressive transfer of zirconium 4*d* valence electrons to the O 2*p* and N 2*p* bands. However, the transference of an electron from the zirconium 4*d* band to the O 2*p* give rise to a higher shift of the *p* band to lower energies, since the O 2*p* is located at lower energies when compared with the N 2*p*. This small deference in electronic structure should play an important role in the "catalytic" effect of oxygen in the optical evolution of the coatings.

This small deference in electronic structure is also decisive to obtain a wider window of colours. The colour variation obtained with the zirconium nitride series showed that increasing the C_N/C_{Zr} atomic ratio, the colour change from bright yellow to golden yellow and then to brown and dark gray [49,51]. The presence of oxygen allows to further shift the reflectivity minimum to lower values (see Fig. 6.14.a, 6.24.a and b), reducing the contribution of red, and thus increasing the appearance of some tones of brown, purple or dark blue, dependent of the level of the shift.

6.4. Conclusions

The ternary system zirconium oxynitride is characterized by three major different optical behaviours, directly correlated with the compositional/structural features of the coatings. The small optical response variations in each zone result from small variations in composition. The coatings that present an *fcc*-ZrN structure present an optical behaviour similar to zirconium nitride, showing high reflectivity near the infrared region, an edge in the visible region and a reflectivity minimum in the UV region. The colour of these coatings varies from bright yellow to golden yellow.

The coatings lying in the second compositional zone, which present a $Zr_3N_4(O)$ structure, present an almost constant low values of reflectivity, showing colour variation from red-brownish to purple to dark blue. The coatings lying in the last two compositional zones, where the crystalline structure of the coatings change from Zr_2ON_2 to ZrO_2, present a semi transparent optical behaviour, with optical band gaps close to 4 eV.

6.5. References

[1]- C.A. Wert, R.M. Thomson, *Physics of Solids*, McGraw-Hill Series in Materials Science and Engineering, McGraw-Hill Book Co, New York, NY, 1964.

[2]- F. Abeles, *Optical Properties of Solids*, North–Holland Publishing Co, 1972.

[3]- Ana Delin, O. Eriksson, R. Ahuja, B. Johansson, M. S. S. Brooks, T. Gasche, S. Auluck, J. M. Wills, Phys. Rev. B 54 (1996)1673.

[4]- S. Niyomsoan, W. Grant, D.L. Olson, B. Mishra, Thin Solid Films 415 (2002) 187.

[5]- K. Nassua, Sci. Am. 243 (4) (1980) 140.

[6]- S. Nudelman, S.S. Mitra, *Optical Properties of Solids*, Plenum Press, New York, NY, 1969.

[7]- S. Logothetidis, I. Alexandrou, J. Stoernenos, Appl. Surf. Sci. 86 (1995) 185.

[8]- A Schlegel, P Wachter, J.J. Nickl, H. Lingg, Solid State Phys. (1977) 4889.

[9]- F. Seitz, D. Turnbull, Solid State Phys Adv. Res. Appl. 6 (1958) 313.

[10]- F. Seitz, D. Turnbull, Solid State Phys. Adv. Res. Appl. 15 (1963) 299.

[11]- A. Rizzo, M. A. Signore, L. Mirenghi, D. Dimaio, Thin Solid Films 515 (2006) 1486.

[12]- M. Yoshitake, T. Yotsuya, S. Ogawa, Jpn. J. Appl. Phys. 31 (1992) 4002.

[13]- S. Logothetidis, I. Alexandrou, A. Paperdopoulos, J. Appl.Phys. 77 (3) (1995) 1043.

[14]- R. Lamni, E. Martinez, S.G. Springer, R. Sanjinés, P.E. Schmid, F. Lévy, Thin Solid Films 447-448 (2004) 316.

[15]- M. Veszeilei, K. Andersson, C.G. Ribbing, K. Järrendahl, h. Arwin, Appl. Opt. 33 (10) (1994) 1993.

[16]- H.M. Benia, M. Guemmaz, G. Schmerber, A. Mosser, J-C. Parlebas, Appl. Surf. Sci. 200 (2002) 231.

[17]- M.V. Kuznetsov, M.V. Zhuravlev, E.V. Sharayeva, V.A. Gubanov, Thin Solid Films 215 (1992) 1.

[18]- O. Banakh, M. Balzer, M. Fenker, A. Blatter, Thin Solid Films 455-456 (2004) 650.

[19]- F.W. Billmeyer, M. Saltzman, *Principles of Color Technology*, Interscience Publishers, New York, NY, 1966.

[20]- Recommendations on uniform colour spaces, colour-difference equations, psychometric colour terms, CIE publ. 15, Suppl. 2– 70 CIE, Paris, 1978.

[21]- Colorimetry, CIE Publ. (Commission Internationale de L'Éclairage) 15 (1971).

[22]- M.Ohring, *The Materials Science of Thin Films*, Academic Press, San Diego CA, 1992.

[23]- J.F. Pierson, F. Bertran, J.P. Bauer, J. Jolly, Surf. Coat. Technol. 142-144 (2001) 906.

[24]- M. Veszelei, K. E. Andersson, A. Roos, Opt. Mater. 2 (1993) 257.

[25]- B. Karlsson, R.P. Shimshock, B.O. Seraphin, J.C. Haygarth, Solar Energy Mater. 7 (1983) 401.

[26]- A. Bendavid, P. J. Martin, R. P. Netterfield, T. J. Kinder, Surf. Inter. Anal., 24 (1996) 627.

[27]- D. I. Bazhanov, A. A. Knizhnik, A. A. Safonov, A. A. Bagatur'yants, M. W. Stoker, A. A. Korkin, J. Appl. Phys. 97 (2005) 044108.

[28]- L. Pauling, *The Nature of the Chemical Bond*, Chap. 3, Cornell University, Ithaca, New York, 1960.

[29]- B. Karlsson, R.P. Shimshock, B.O. Seraphin, J.C. Haygarth, Solar Energy Mater. 7 (1983) 401.

[30]- J. Taut, *The Optical Properties of Solids*, Proceedings of the International School of Physics (ENRICO FERMI), course XXXIV, Academic, New York, 1966, p. 106.

[31]- A. Schlegel, P. Wachter, J.J. Nickl, Lingg, Phys. C: Solid State Phys. (10) 1977.

[32]- D. Pilloud, A.S. Dehlinger, J.F. Pierson, A. Roman, L. Pichon, Surf. Coat. Technol. 174-175 (2003) 338.

[33]- B. Karunagaran, S.J. Chung, E.-K. Suh, D. Mangalaraj, Physica B 369 (2005) 129.

[34]- D.A.G. Bruggeman, Ann. Physik (Leipzig) 24 (1935) 636.

[35]- D. Pilloud, J.F. Pierson, L. Pichon, Materials Science and Engineering B 131 (2006) 36-39.

[36]- J.H. Mooij, Phys. Status Solidi A17 (1973) 521.

[37]- M. Veszelei, K. Andersson, C-G. Ribbing, K. Järrendahl, H. Arwin, *Legierungen*, Springer, Berlin, 1971.

[38]- R.E. Hummel, *Optische Eigenschaften*, Metallen und Legierungen, Springer, Berlin, 1971.

[39]- C. Mitterer, P.H. Mayrhofer, W. Waldhauser, E. Kelesoglu, P. Losbichler, Surf. Coat.Technol.108-109 (1998) 230.

[40]- S. Camelio, T. Girardeau, L. Pichon, A. Straboni, C. Fayoux, Ph. Guérin, Pure Appl. Opt. 2 (2000) 442.

[41]- Chee-Kin Kwok, Carolyn Rubin Aita. J Vac Sci Technol A (7) (3) (1989) 1235.

[42]- C. Kittel, *Introduction to Solid State Physics*, 4th ed, Wiley, New York, 1971, p. 146.

[43]- N.F. Mott, E.A. Davis, *Electronic processes in noncrystalline materials,* Oxford: Clarendon Press, 1979, pp. 273.

[44]- J. Tauc, *Optical Properties of Solids,* F. Abeles, Amsterdam: North-Holland, 1971, p 71.

[45]- I. Kosacki, V. Petrovsky, H. U. Anderson, Appl. Phys. Lett. 74 (1999) 341.

[46]- P. H. Soni, M. V. Hathi, C. F. Desai, Bull. Mater. Sci. 26, (7) (2003) 683.

[47]- X.D. Gao, X.M. Li, W.D. Yu, Thin Solid Films 468 (2004) 43.

[48]- R. Asahi, T. Morikawa, T. Ohwaki, K. Aoki, Y. Taga, Science 293 (2001) 269.

[49]- H.M. Benia, M. Guemmaz, G. Schmerber, A. Mosser, J.C. Parlebas, Appl. Surf. Scie. 211 (2003) 146.

[50]- Chuan-Pu Liu, Heng-Ghieh Yang, Thin Solid Films 444 (2003) 111.

[51]- H.M. Benia, M. Guemmaz, G. Schmerber, A. Mosser, J.C. Parlebas, Catalysis Today 89 (2004) 307.

Chapter 7

Functional properties

7.1. Introduction

Transition metal nitride films are used in several applications due to their remarkable mechanical and tribological properties, and chemical inertness [1,2]. There is a vast amount of literature concerning the technical applications of these compounds, primarily based on their high melting point, hardness, wear resistance, good thermal and chemical stability, as well as a relatively high corrosion resistance [3-7], which result from the unique combination of both metallic and covalent bonding characteristics [4,5] that are present in these materials.

Among the several examples of transition metal nitride films, zirconium nitride, ZrN, has been used in many industrial branches due to its ability to resist chemical attack in environments that could otherwise promote enhanced oxidation of single metal components. The tool industry is by far the biggest consumer of the protective transition metal compound coatings [3,8,9]. Similarly, the transition metal oxides have also found numerous industrial applications [10,11-16].

More than an exhaustive characterization of some of the mechanical properties of the prepared films, this chapter is focused on the most important basic properties that a thin film should reveal, and thus to test if the prepared ZrO_xN_y thin films may be used as decorative coatings. In this sense, their hardness, adhesion, corrosion resistance (namely in the most common environment in which they will operate, sweat normally) and biocompatibility will be characterized so that one may have a basic idea on the system's properties and its suitableness for its main purpose: to coat decorative objects/parts.

It is not a main purpose of this chapter to analyse in detail these properties and the main mechanisms that may rule them, but above all to show some figures that may "speak for themselves" in terms of the minimum requirements that this kind of coatings should reveal. In this way, only the main series will be characterized – series 1, which in fact represents the overall behaviour as already demonstrated in the previous chapters.

7.2. Functional properties

7.2.1. Hardness

Introduction

As an indicator of the material's ability against deformation, hardness has been studied for more than 100 years [17]. During the last 20 years, researchers have become more and more interested in the mechanical properties of ever smaller volumes, such as thin films [18-21], since this property (and in case of the thin film coated parts) has demonstrated to be of crucial importance for the in-service behaviour.

To test this important mechanical property, usually, a prescribed load is applied to an indenter in contact with a specimen and the area of the residual impression, A_r, is measured often by optical imaging after the load is removed. The hardness is then obtained through dividing the applied load by the variable A_r [17]. In specific terms, hardness is related to the elastic and plastic properties of a given material. The dimension of the produced permanent deformation depends on the resistance of the volume compression that results from the pressure induced by the indenter, the resistance to shear deformation and the resistance to the creation and motion dislocations.

There are three conditions that must be found for a material to be considered hard:

i) *the material must tolerate the volume decrease created by the applied pressure*, therefore must have a high bulk modulus (B);

ii) *the material must not deform in a direction different from the applied load*, meaning that it must have a high shear modulus (G);

iii) *the material must not deform plastically*, and thus the creation and motion of the dislocations must be as small as possible.

Bulk modulus, B, has very little dependence on ionicity, whereas the shear modulus, G, presents a relative decrease by a factor of more than three, owing entirely to the change from covalent to ionic bond character of the tested material [21]. Materials that exhibit limited bond bending are those with directional bonds in a high symmetry, three-dimensional lattice, with fixed atomic positions. Covalent materials are much better candidates for high hardness than ionic compounds because, in the last ones, the electrostatic interaction are omnidirectional and yield low bond-bending force constants, which result in low shear modulus [21]. Anyway, the main mechanisms responsible for hardness enhancement in nanocrystalline thin films are the

dislocation-dominated plastic deformation, the cohesive forces between atoms, and the nanostructure of materials [22].

Technique used to characterize hardness-Vickers indentation.

Vickers hardness test was developed in the early 1920s as an alternative method to measure the hardness of materials. Hardness, *H*, is conventionally determined by applying a load to a material via a geometrically defined indenter, and defined as the ratio of the applied load, $L_{máx}$, to the contact (or projected) area, *A*, of the resultant indentation impression,

$$H_V = \frac{L_{máx}}{A} = \beta \frac{L_{máx}}{d^2} \qquad \text{(eq. 7.1)}$$

where *d* is the size of resultant indentation impression, and β is a constant dependent only on the indenter geometry. Vickers method uses a pyramid with square base and an interfacial angle of 136º, which is pressed against the sample surface, with a pre-define load. Vickers hardness, H_V, is calculated using the contact area of the indentation impression and the parameter *d* in equation 7.1, is defined as the average of the two diagonals of the resultant square-shaped impression. This results in a β value of 1.8544. The determination of the impression area could be done by visualization by optical microscopy or by the load and unload curves as a function of depth [23], Fig. 7.1.

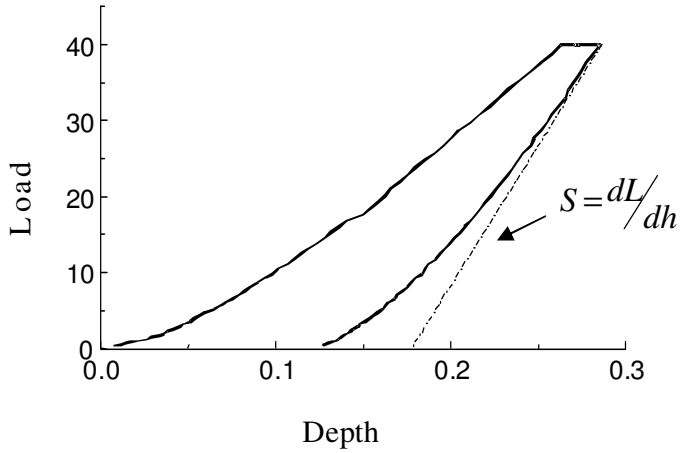


Fig. 7.1. Load and unload curves for a Vickers hardness test with creep.

From the load-displacement curve, the indentation modulus can also be derived. The indentation modulus can be slightly different from the Young's modulus because the first is a weighted average of the elastic properties in a certain sample volume and the Young's modulus is directional [22]. For the specific case of isotropic materials, both values should be equal.

In order to avoid the substrate influence on the in the measurements, the indentation depth should be lower than 10 % of the coating thickness [24]. Nevertheless, indentations with very low impression areas should be avoided, since the hardness values could be influenced by the surface roughness of the film.

The hardness experiments were carried out in a Fischerscope H100 ultramicrohardness tester [25], equipped with a Vickers diamond indenter. The applied load was increased in 60 steps (the same for unloading) until the nominal load reached the value of 30 mN (maximum load in all tests). The system has a load resolution exceeding 1 μN and the range of the nominal test load is between 4 mN and 1 N. The indentation depths were obtained with an accuracy of 2 nm. The testing process includes the correction of the experimental results for geometrical defects in the tip of the indenter, thermal drift of the equipment, and uncertainty in the initial contact [26].

7.2.2. Macro Stress

Introduction

In a qualitative approach, the macrostress σ, acting in a thin film is the result of two distinct contributions:

i) thermally induced stress, σ_{th}, due to the mismatch between the thermal expansion coefficients of both substrate and film material and;

ii) intrinsic stress, σ_i, resulting from the accumulation of crystallographic defects during the film deposition, and connected with the energy delivered to the growing film by bombarding ions and condensing particles [22].

Thus, the macrostress, σ, can be represented by:

$$\sigma = \sigma_{th} + \sigma_i \qquad \text{(eq. 7.2)}$$

where the thermal component can be estimated by:

$$\sigma_{th} = \mathrm{E}_f(\alpha_f - \alpha_s)(\mathrm{T}_s - \mathrm{T}) \quad \text{(eq. 7.3)}$$

where T_s represents the coating temperature during deposition and T the temperature at which the thermal stresses are determined, or at which the coating system operates in service. E_f is the film Young's modulus, while α_f and α_s represent the thermal expansion coefficients of film and substrate, respectively.

The macrostress σ in sputtered films can be controlled by the ratio T_s/T_m and the energy delivered to the going coating during the deposition, by condensing and bombarding particles. Here T_s represents the coating temperature during deposition and T_m the melting point of the deposit coating) [22].

The intrinsic stresses play a dominant role regarding the thermal stress at low values of T_s/T_m ratio, ($T_s/T_m \leq 0.3$) [27]. At T_s/T_m ratios higher than 0.3, intrinsic stresses do not generate or their values are very low [28].

Technique used to characterize stresses (deflection of the substrates)

Macrostresses of the as-deposited PVD coatings causes bending of the coating/substrate system. If macrostresses are present, and since the overall deflection is small compared to the substrate thickness, then by symmetry, the coated substrate will take up a spherical curvature in the region away from the edges [29]. The radius of curvature of the PVD coating/substrate system can be measured by means of profilometry by using a laser transducer (such the case of this work). The laser beam is applied on the non-coated substrate surface (to avoid the light dispersion) and height measurements are taken at intervals across the curved specimen surface. The laser transducer is fixed and the coating/substrate system is moved with the coating surface facing upwards. The base plate is then traversed under the laser beam and surface height measurements are made at regular intervals along the centre-line of the sample.

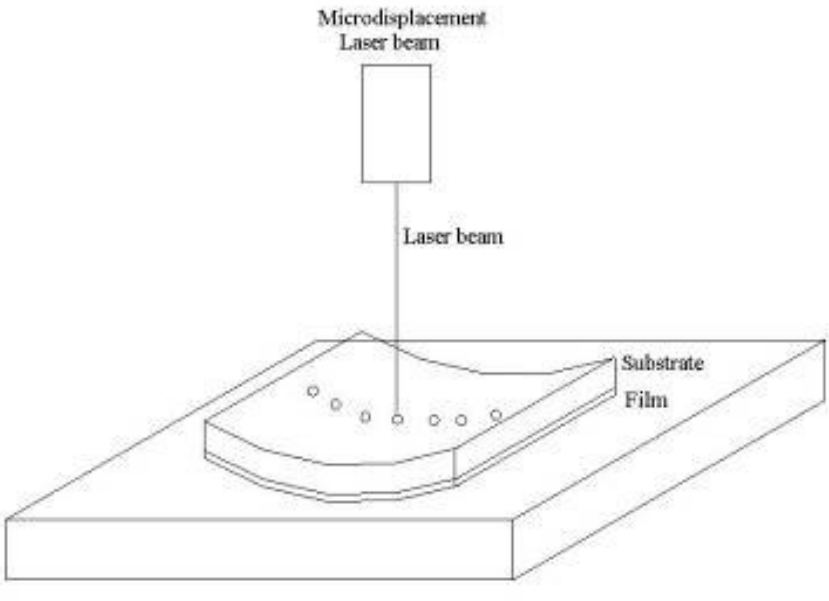


Fig. 7.2. Schematic representation of the curvature measurements in a coated sample.

The radius of curvature *r* allows to determine the macrostresses of the coating through the equation 7.4 [30]:

$$\sigma_f = \frac{(E_s t_s + E_f t_f)\left[E_s t_s \left(3t^2{}_f + t^2{}_s\right) + E_f t_f \left(3t^2{}_s + t^2{}_f\right)\right]R}{6 t_f t_s E_s \left(t_s + t_f\right)} - \frac{t_f t_s \left(E_f - E_s\right)^2 r}{2E_s \left(t_s + t_f\right)} \qquad \text{(eq. 7.4)}$$

where E_f and t_f represents the Young's modulus and thickness of the film respectively, and E_s and t_s the same quantities for the substrate.

Since the deflections (a few microns) are much smaller than the sample length (a few centimetres), the substrate's circular profile can be approximated to a parabola [31]. *P. M. Ramsey et al.* [32] developed a method in which the substrate's curvature radius can be obtained by a simulation of the substrate profile, before and after the deposition, using second order polynomial function:

$$\delta(x) = a + bx + cx^2 \qquad \text{(eq. 7.5)}$$

where $\delta(x)$ represent the deflection (z coordinate) as a function of x, and *a*, *b* and *c* are constants.

The curvature radius can then be determined by:

$$r = -1/(2c) \quad \text{(eq. 7.6)}$$

Assuming that the macrostresses are uniform in the coating and only present parallel components to the surface of the substrate, once the radius of curvature is determined, and since the coatings are thin compared to the substrate thickness, equation 7.4 can be simplified and the macrostresses in the coating (σ), can be determined using the Stoney's equation [33]:

$$\sigma = \frac{E_s}{1-\upsilon_s}\frac{t^2{}_s}{6t_c}\left(\frac{1}{r_c}-\frac{1}{r_{uc}}\right) \quad \text{(eq. 7.7)}$$

where E_s is the Young's modulus of the substrate, υ_s the Poisson's ratio of the substrate, r_{uc} the radius of the curvature of the uncoated substrate, r_c the radius of curvature of the coated substrate and t_c the coating thickness and t_s the substrate thickness.

To obtain these curvature radii, the substrates (stainless steel discs with 25 mm diameter and 0.5 mm thick) were measured with a high precision laser displacement meter (Keyence Corporation, Japan), by laser triangulation in two series of two orthogonal directions. The equipment enables to obtain the substrate profile, computing 330 vertical coordinates in each direction.

7.2.3 Adhesion

Introduction

The term adhesion is closely related to the strong interaction between existing atoms and molecules in the interface of two adjacent materials (namely coating/substrate), being commonly defined as the condition in which the surfaces of the two materials are kept together. This union is obtained by the force balance (essentially of the Van der Waals type), by mechanical processes related with the energy of interaction between atoms and molecules of the interface, or both.

A decisive requirement for the application of coatings in decorative applications is that the deposited films be well bonded to the substrate. However, and despite its great importance, adhesion continues to be one of the less understood properties, mainly because of the lack of an applicable method in the quantification of its value. In this way the adhesion tests must be seen not as strictly quantitative, but essentially qualitative methods, allowing important information concerning the quality, durability and functionality of a certain coating material deposited on a specific substrate. In practice, the necessary degree of adhesion between the coating and the structure (substrate) will be strongly dependent of the in-service conditions, Thus, one of the most important factors to take into account in the inquiry of the adhesion coating/substrate is the careful study of the correspondent interface.

In general, the adhesion in thin films prepared by sputtering is good, since it is usual to bombard the substrate with energetic ions – etching (with argon for example) before the deposition, which allows the removal of the oxide layer and some impurities that may exist. As a consequence of this process, some microdefects are created in its surface, promoting the formation of a transition region between substrate and film, promoting the degree of adhesion between them.

Coating technology is fundamentally dependent upon good adhesion between the coating and the substrate, and in many cases adhesion is the limiting factor for the wider application of the technology. To ensure this, several methods have been developed to measure the adhesion between a substrate and a coating [34-36], but each one with specific limitations. A particular problem is measuring adhesion of hard coatings to rather soft substrates, such as polymeric substrates. The simplest adhesion tests such as the scotch tape are purely qualitative which are not designed to quantify adhesion strength except to assert that the adhesion is greater than some arbitrary limiting value [34-36]. Nevertheless and in case of well-adherent coatings (such as the case of the films studied in this thesis), the scratch test is one of the most well-known, which has become widely established as a comparative method and is currently in widespread use [37,38].

Technique used to characterize adhesion- "Scratch test"

The scratch adhesion test is generally accepted as one of the simplest means of introducing a quantity of mechanical force or sufficient energy to detach a coating from the substrate. For this,

a hemispherical tipped diamond is driven over a coated surface to produce a scratch (see Fig. 7.3).

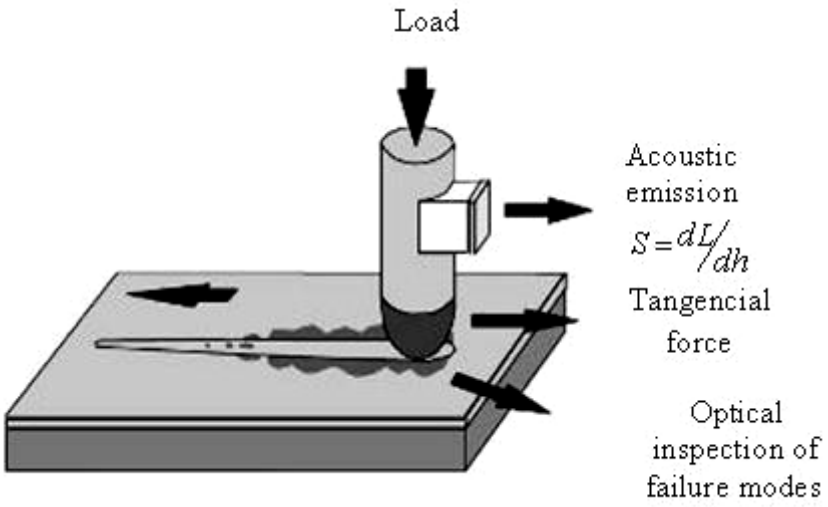


Fig. 7.3. Schematic representation of the "*scratch test*" principle.

The load on the diamond is linearly increased producing an increasing elastoplastic deformation of the film/substrate system causing the appearance of the so-called adhesion damages. These damages are caused by three main factors i) *debonding of the coating from the substrate - adhesive failure*, ii) *fracture of the coating itself - cohesive failure* or iii) *simply by fractures at the substrate (substrate failure).* The minimum load at which a cohesive failure occurs is called the first critical load (L_{C1}). The load at which the first adhesion failure is verified is called second critical load (L_{C2}). The load at which more than 50 % of the coating from the scratch area is removed from the substrate is called the third critical load (L_{C3}). Once obtained, these critical loads are representative of the coating adhesion. Depending on the coating/substrate system to be tested, these critical loads can be determined by three different methods:

a) *optical observation* - detection of the point where the coating has been removed from the substrate (L_{C2} and L_{C3}), and identification of failure modes present in the coating (L_{C1} included).

b) *analysis of the acoustic emission* - sudden decrease, or increase, in the acoustic emission.

c) *analysis of the frictional force curve* - in this third method the total failure (L_{C2}) is defined as the inflection point of the curve friction force as function of the load.

Accordingly, if one intends to study adhesion, more than determining the critical loads, it is

imperative to characterise these failures mechanisms in order to gain a better understanding of the mechanisms that rule the adhesion between a coating/substrate system. "Scratch Test Atlas of Failure Modes" cited in the Draft of European Standard prEN1071-3 presents a compilation of all the types of failures events.

Regarding the specific parameters of the scratch test analysis of the samples presented in this theses, a semi-spherical Rockwell C, with a 200 μm radius, was used, where the normal force of the indenter onto the sample surface increased continuously from 1 to 50 N, with a loading rate of 100 N/min. The value of the critical loads (the force at which the first damage event is occurred) was determined by optical microscopy. Four consecutive scratches were performed in order to evaluate the value of the critical loads. The coating-to-substrate adhesion and coating cohesion is evaluated according "Scratch Test Atlas of Failure Modes" cited in the Draft of European Standard prEN1071-3.

7.2.4. Corrosion behaviour

Introduction

Corrosion is defined as ''attack on a material by its reaction with the environment and the resulting deterioration of the materials properties'' [39,40]. Usually, it is related to an electrochemical reaction with a liquid or gaseous environment.

Concerning corrosion, a distinction has to be made between a homogeneous attack of the complete surface area and a local corrosion attack. This means, for coating-substrate systems, that either the total area of the coating is attacked or the substrate is locally corroded at damaged areas, depending on the nobility of coating and substrate material [41].

Different environments may cause different types of corrosion attack that may vary in appearance and corrosion mechanisms. Regarding the appearance, one can distinguish:

- Uniform Corrosion
- Pitting Corrosion
- Intergranular Corrosion
- Crevice Corrosion.

In terms of the corrosion mechanisms, there is:

- Galvanic Corrosion
- Stress Corrosion Cracking

- Corrosion Fatigue
- Electrolytic corrosion.

Vapour deposited coatings most often exhibit pores and pinholes through which a corrosive attack on the substrate material (less noble in most cases) takes place [41] leading to corrosive attack i.e. galvanic corrosion.

The corrosion behaviour was studied using two different approaches: by the application-oriented of the so called short-time tests, representing the exposure to a specific gaseous climate or a liquid (artificial sweat test), with subsequent qualitative evaluation of the corrosion damage [42]; electrochemical tests in liquid corrosive environment providing specific data on the behaviour of the system [43].

Techniques used to characterize the corrosion behaviour

Polarisation Tests

Polarization methods such as potentiostatic voltammetry are often used for laboratory corrosion testing. This technique can provide significant useful information regarding the corrosion mechanisms, corrosion rate and susceptibility of specific materials to corrosion in designated environments. Polarization methods involve changing the potential of the working electrode and monitoring the current, which is produced as a function of time or potential.

This technique polarizes an electrode in a series of potential steps, where the time spent at each potential is constant, while the current is allowed to stabilize prior to changing the potential to the next step. The step increase may be small, in which case, the technique resembles a potentiodynamic curve.

In order for an electrochemical process to take place, there must be an anode, a cathode, as well as both an ionic and electrical conduction path between the two. The ionic conduction path is provided through the solution separating the working and counter electrodes, while the electrical conduction path is provided through the potentiostat. This potentiostat is then used to control the driving force for electrochemical reactions taking place on the working electrode. Electrons flow from the *anode* to the *cathode* through the electrical path described above. As such, the anode is typically thought of as the negative electrode, and the cathode as the positive.

At the *anode*, oxidation takes place. In the case of metal oxidation, this may be represented by a reaction such as:

$$M \rightarrow M^{X+} + xe^{-} \quad \text{(eq. 7.8)}$$

where M represents the metal, M^{X+} represents the ion of the metal, and xe^{-} represents the number of electrons transferred in the process.

At the *cathode*, reduction takes place. Reactions such as the reduction of an oxide, or hydroxide, or nitride, present on the cathode surface, may take place;

$$M_X(OH)_Y + xe^{-} \rightarrow xM + yOH^{-} \quad \text{(eq. 7.9)}$$

The Potential (Thermodynamic Information)

The thermodynamic tendency for an electrochemical reaction to occur, such as metal oxidation, is determined by the free energy change associated with the reaction.

The free energy change associated with the reaction;

$$jJ + kK + xe^{-} \rightarrow lL + mM + \ldots \quad \text{(eq. 7.10)}$$

can be expressed in terms of the energy of formation of each specie within the reaction;

$$\Delta G = (lG_L + mG_M + \ldots) - (jG_J + kG_K + \ldots) = \sum v_i G_i \quad \text{(eq. 7.11)}$$

where G_x represents the Gibbs free energy of specie *X*, and ΔG is the Gibbs free energy change associated with the reaction. The change in free energy associated with any reaction may also be expressed as:

$$\Delta G = -EnF \quad \text{(eq. 7.12)}$$

where *E* is the thermodynamic potential, *n* is the number of electrons transferred in the reaction, and *F* is Faraday's constant.

At equilibrium $\Delta G = 0$. Combining the two expressions (eq. 7.11 and 7.12), we see that deviations from equilibrium may be accounted for by utilizing the chemical activity of each specie. Thus, if E° is used to represent the cell potential, the following expression is readily obtained:

$$E = E^0 - \frac{RT}{nF} \ln \frac{a_L^l \cdot a_M^m \cdot \ldots}{a_J^j \cdot a_K^k \cdot \ldots} \quad \text{(eq. 7.13)}$$

where *T* is the absolute temperature in Kelvin, *R* the universal gas constant, *a* is the chemical activity for the relevant species, *F* is the Faraday constant and *n* is the number of electrons transferred in the cell reaction.

It is important to note that the free energy change associated with a reaction, and hence the potential, is a thermodynamic property and is independent of the path which the reaction takes - it depends only on the initial and final states. While the magnitude of the energy change associated with a reaction provides information on whether or not a reaction can occur (i.e., there exists a driving force), it can not be used to predict the rate at which the reaction will take place (i.e., the kinetics of the reaction).

Electric Current density (Kinetic Information)

In a potentiodynamic experiment, the current represents the rate with which the anodic or cathodic reactions are taking place on the working electrode. Typically, the current is expressed in terms of the current per unit area of the working electrode, or the current density. Numerous variables will influence the rate of a given electrochemical reaction, including the temperature, the surface condition being interrogated, as well as the chemical environment in which the experiment is performed.

Regarding the specific conditions of the tested coatings, the polarization analysis were performed with deaerated solution with bubbling nitrogen, using potentiostat EG&G in an electrolyte composed by 0.8 M NaCl solution (pH 7) and a scan rate of 1 mV/s. The tests were performed at room temperature and the reference electrode used was a saturated calomel electrode (SCE).

Artificial sweat tests

Artificial sweat tests (immersion tests) according to DIN EN 1811 (especially for nickel release work) were performed on representative coatings of series 1, deposited onto stainless steel disks (SS316). The nickel released of the stainless steel through the coating was measured. Additional, the colour change due to this test and the release of the zirconium into the electrolyte was tested. Quantitative trace analysis of the artificial sweat solution after the tests was conducted by an inductive coupled plasma spectrometer (ICP-OES). The composition of artificial sweat solution used was; 0.5 wt. % NaCl, 0.1 wt. % lactic acid, 0.1 wt. % urea ($CO(NH_2)_2$) and 1.0 wt. % ammonia solution (NH_4) in deionised water. The samples were immersed in the described solution, which presented a pH value of 6.5 during one week at 30º C.

In order to verify the influence of the sweat tests in the colour variation of the coatings L*, a* and b* average values calculated from 5 measurements before and after the artificial sweat test were compared.

7.2.5. Biocompatibility

Introduction

Biocompatibility is "the ability of a material to perform with an appropriate host response in a specific application" [44] and is related with statements on low level of immune response of a specific material.

Biocompatibility of coatings increasingly occupies the consciousness of researchers dealing with materials that could be in contact with human skin. Besides the mechanical, optical and electrical properties, among others, situations involving biological interactions are a portion of the design problem, the additional materials limit of biocompatibility must be considered.

More than an exhaustive study of the biology performance of the prepared films, this study is focused in determine if the zirconium oxynitride coatings displays universally a "good" or harmonious behaviour in contact with body tissue.

Technique used to characterize the Biocompatibility- direct cytotoxicity test

The study of biocompatibility of the coatings studied in this thesis has the primordial objective to determine the possibility of being used as decorative coatings such as in watch bands, eye glass frames, door-handles etc.

On this basis, direct cytotoxicity tests based on the ISO norm 10993-5 were performed on selected zirconium oxynitride coatings from series 1.

To assess the cytotoxicity of coated glass specimens, 3T3 cells (embryonic mouse fibroblast cell line) were directly grown on the surface of the samples to be tested. Polystyrene (culture dish surface) was used as a negative control. The parameters investigated were viability, based on neutral red uptake, and metabolic activity, through an MTT (3-(4,5-dimethylthiazol-2-yl-)-2,5-diphenyltetrazoliumbromide) assay, which depends on the activity of intracellular enzymes. Both assays are widely accepted to assess viability and growth of cells in biocompatibility and cytotoxicity studies [45,46]. Three samples for each coating were analysed for the mentioned parameters.

Figure 7.4. presents the principles of of cell culture with 3T3 mouse fibroblast cell line.

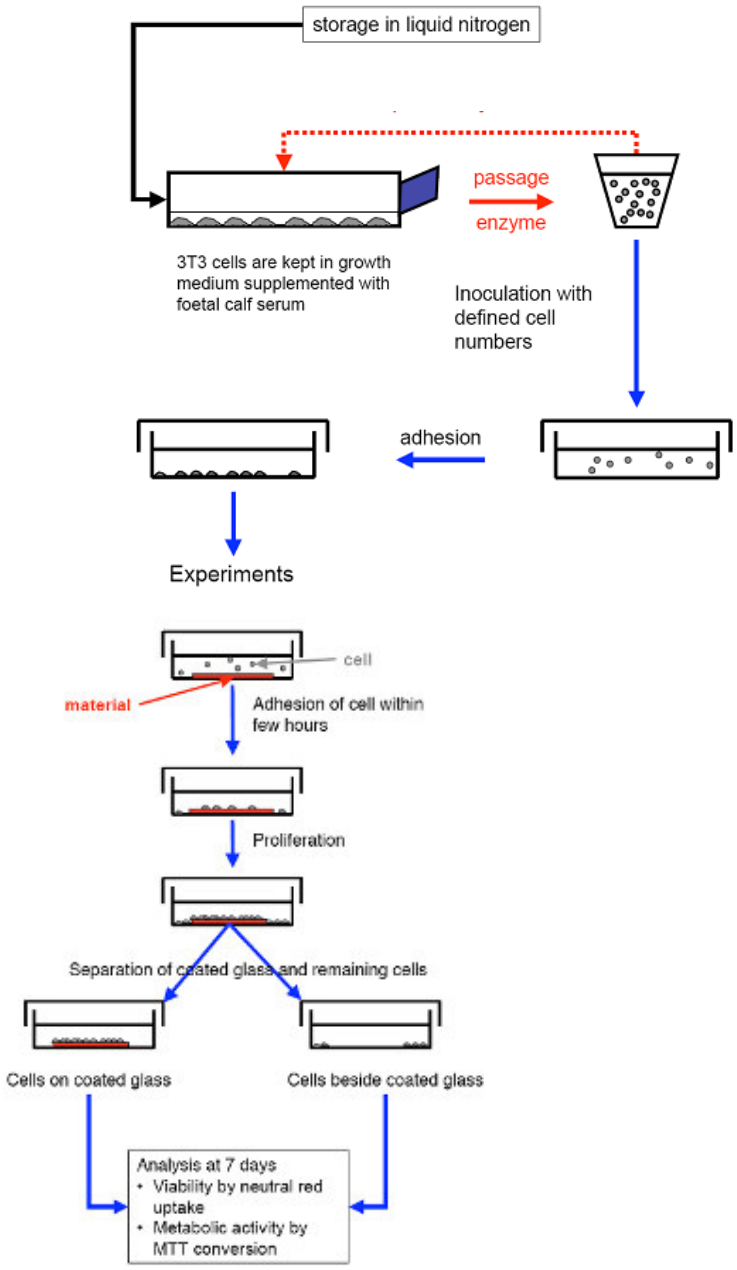


Fig. 7.4. Experimental set up to test cytotoxicity of coated glass slides.

Aliquots of 3T3 cells were taken out of liquid nitrogen, thawed and added to growth medium supplemented with 10 % foetal calf serum. When the bottom of the culture flaks was entirely

covered with cells, enzymes were used to release them. Viable cells were subsequently counted and diluted to reach the desired cell numbers.

The cells were allowed to expand in cell culture flasks for over 1 week (Fig. 7.4.). Then, the attached cells were enzymatically released. After centrifugation, viable cells were counted in a hemocytometer and inoculated at 2×10^4 cells/ml.

Before inoculation, the specimens (coating/substrate) were sterilized in 70 % ethanol during 5 minutes, and subsequently washed 3 times in phosphate buffered saline, pH 7.4. Subsequently, the coated samples were placed in 12-well plates and inoculated with the cells suspension previously prepared. All the cultures were kept at 37°C in a humidified atmosphere of 5 % CO_2 and 95 % air. One week later, the neutral red uptake and the MTT conversion testes were performed. The viability was mesuared by quantifing the uptake of neutral red into the cells. This is independent of the metabolic activity of the cells, which means all viable cells take the neutral red up into their lysosomes. After a washing and an extraction steps, the absorbance was quantified in a spectrophotometer, Fig. 7.5.

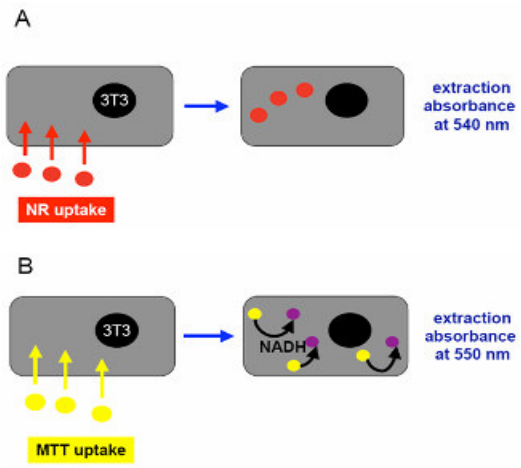


Fig. 7.5. Analysis of viability (A) and metabolic activity (B) of 3T3 cells at 7 days.

The metabolic activity was analyzed by the MTT assay. The cells up take MTT and this tetrazolium salt converted into a colored formazan product by NADH, which is produced by themetabolyc activity of the cell. After a solubilization step, the absorbance was quantified in a spectrophotometer. The absorbance of the supernatant was read at 550 nm versus DMSO (dimethylsulphoxide) in a SpectraMax 190 multiplate reader (Bucher Biotech, Switzerland). The

absorbance of the supernatant was read at 540 nm versus extraction buffer in the same equipment. The size of each coated glass slide was determined using a calliper rule. The values of the neutral red uptake and the MTT assay were normalized to the area on which the cells were growing. Three independent experiments were performed and the data were analyzed using SPSS 11 for Mac OS X software.

7.3. Results and discussion

7.3.1. Hardness and Young's modulus

The influence of the reactive gas mixture flow variation and its effect on composition and structural features of the films can also be correlated with the evolution of the mechanical properties, as illustrated in figure 7.6 by the change in film Vickers hardness (H_v).

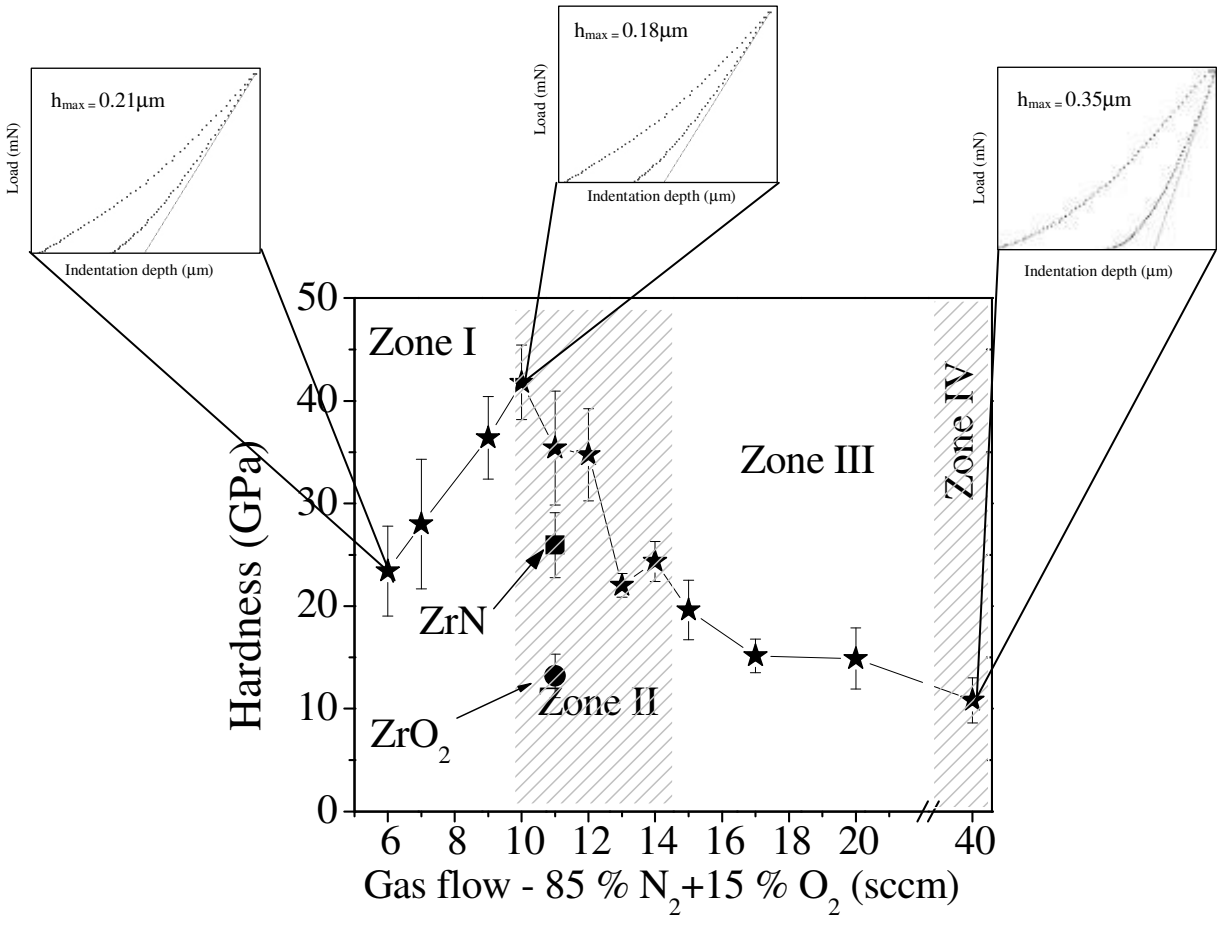


Fig. 7.6. Hardness values as a function of reactive gas flow for samples from series 1. The loading and unloading curves are also showed as a function of indentation depth. The error bar was determinate by maximum deviation to the average value.

The effect of coating Vickers hardness H_v on the loading/unloading curves is also shown in figure 7.6, with typical loading/unloading curves measured for representative coatings. The area between the loading and unloading curves represents the energy dissipated in the coating due to plastic deformation, and the area under the unloading curve represents the elastic energy for deformation.

All the coatings present loading and unloading curves that are approximately parabolic. This is a good indication that the deformation accommodated elastically is significant. Although the coatings lying in the last two compositional zones (zone III and IV) present a more abrupt decrease of the unloading curve (see Fig. 7.6). This could indicate a decrease of the elastic strains compared with the plastic strains, resulting in a decreasing of the elastic recovery of the indentation depth.

The first, and probably the most important result regarding the primordial application of these coatings (decorative applications), is that zirconium oxynitride films with intrinsic colorations (Zone I and II), present hardness values similar and, in some cases, even higher than those of zirconium nitride, which is a commonly used decorative coating.

Secondly, it is also notorious the increase in hardness in the first compositional/structural zone (samples presented a *fcc*-ZrN(O)-type structure), varying from ~23 up to ~42 GPa.

This initial increase is then followed by a systematic decrease of this film property, reaching a value of about 12 GPa for the sample prepared with the highest gas flow (40 sccm, which revealed an oxide-type composition and structure). Anyway, though this decrease in hardness can be observed throughout zones II to IV, there are few differences that are worth to point out. In fact, it is possible to observe that within zone II there is a much more pronounced decrease in hardness values, if compared to what happens in zones III and IV.

In terms of the main features that may explain this particular behaviour of hardness, it is important to state that, first of all, this evolution is well correlated with the structural (and thus its precursor – composition) evolution. In fact, a closer look to figure 7.6 shows that the previous indexed zones have particular trends that corroborate different behaviours according to the different zones. It seems clear that the change from zone I to zone II corresponds exactly to an inversion in the hardness evolution tendency. The continuous decrease of hardness values, within the last three zones, should result from the decrease of the covalent bonding character of the coatings [47].

As already referred, covalent nitrides like ZrN are a much better candidates for high hardness than ionic compounds (like ZrO_2) because electrostatic interaction are omnidirectional and yield low bond-bending force constants, which result in low shear moduli.

Figure 7.7 shows the Young's modulus (elastic modulus) values (E) as a function of the reactive gas flow.

Similarly to what has been shown for the hardness evolution, the Young's modulus presents also an initial increase in the first compositional and structural zone, followed by a tow-stage decrease. In zone II, where the structural analysis revealed a progressive formation of a $Zr_3N_4(O)$ type crystalline structure, the Young's modulus values present a significant decrease, while within the last two zones (those corresponding to oxynitride - γ-Zr_2ON_2 and oxide - *mon*-ZrO_2 type structures, this parameter decreases in a much smoother way.

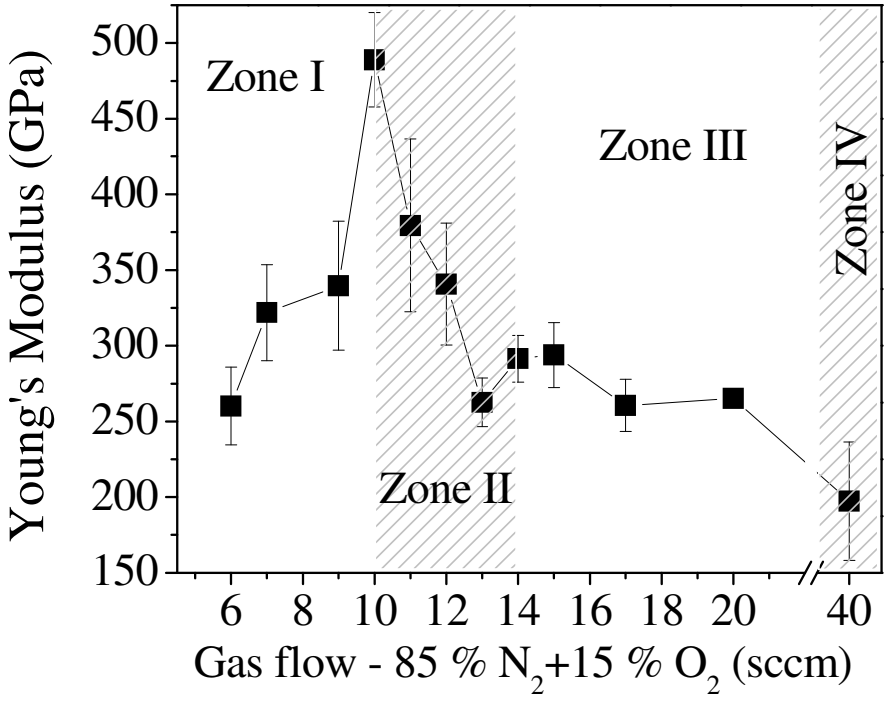


Fig. 7.7. Young's Modulus values as a function of reactive gas flow for the samples of series 1. The error bar was determinate by maximum deviation to the average value.

The notorious coherence in the variation tendencies of both properties shows that there is some kind of liner dependencies between both quantities. Figure 7.8 shows a plot of hardness versus the Young's modulus. The main conclusion that can be drawn is that the samples lying in

the first two compositional and structural zones appear to present a good linear evolution of hardness with Young's modulus, which is an indication of a brittle like behaviour [48].

Regarding zone III and IV the reduce numbers of points could not give any information about the hardness/Young's modulus ratio.

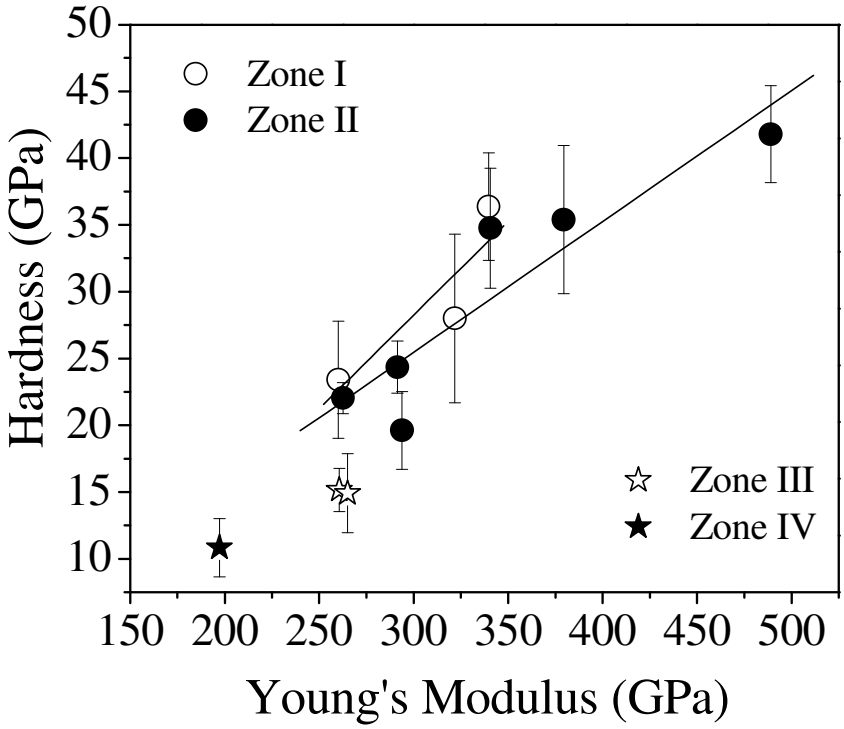


Fig. 7.8. Hardness values as a function of Young's Modulus for the series 1 samples. The error bar was determinate by maximum deviation to the average value.

The effect of oxygen addition

In transition metal compounds, the chemical bond and cohesion energy influences significantly their mechanical properties, where Young's modulus and hardness are the most well-known [49]. High cohesion energy and high hardness values normally correlate with a higher covalent character of the bonding [50]. In this case, and although the composition and structural changes already described (chapters 2 and 3) seem to dictate hardness and Young's modulus evolution, the particular behaviour in each zone suggests that other parameters may be playing important roles. In fact, there are several works in the literature that try to explain how hardness evolves, taking into account not only the particular crystalline structure of the films, but also others such as the lattice parameter variations, the peak intensity ratio and grain size, as well as other related parameters like the macrostress sates and bonding conditions, among others [22].

Regarding the initial increase of hardness values for the samples deposited within zone I, the *solid solution hardening* mechanisms should be an important factor regarding this initial increase. When using ternary nitrides, based on the introduction of a third element in a well-known binary nitride, such as the case here of adding oxygen to ZrN, the concentration of the added element is seen as a major parameter with a significant role for the observed behaviour [51]. In fact, and reporting to the case expressed here, the addition of low oxygen amounts to the films leads to an increase of hardness till a maximum of about 40 GPa, which can result from an increasing oxygen doping of the ZrN lattice, giving rise to a solid solution hardening mechanism. In fact, the sub- and close stoichiometry of the films within this region is certainly a factor that may facilitate this doping of the nitride lattice. With oxygen insertion, an increased strength of the material may arise as a consequence of the resultant lattice distortions [52]. The lattice distortions inhibit the mobility of the dislocations, thus an enhancement in hardness is expected. The fact that no bias voltage was used in the production of this set of films, no ion bombardment, nor high temperatures (substrate temperature was always below ~200 ºC) were present during the films growth, and thus low surface mobility of arriving species to the growing film, favouring in this way the oxygen insertions [51].

However the *solid solution hardening* should play an important role in the hardness evolution regarding the samples lying in the first compositional zone, several authors claim that the hardness and the elastic modulus of group IVb nitrides such TiN_x, ZrN_x and HfN_x decreases as the concentration of the non-metal vacancy increases [49,53-56]. *Seung-Hoon Jhi et al.* [57], in the study of vacancy hardening and softening in transition metal carbides and nitrides, claim that occupied metallic *dd* bonding states in TiN and ZrN, which give a negative contribution to the shear modulus, are enhanced as the vacancy concentration increases resulting in a decrease of the shear modulus (and correspondingly the hardness). Since the coatings lying in first compositional zone present an increase of metalloid content until a close stoichiometric condition is achieved, the reduction of the vacancy concentration could also play an important role in the increase of hardness values.

The effect of structural parameters

Previous studies have reported that preferred orientation is a very important factor to the film hardness enhancement. Major achievements in these studies have shown that the ⟨111⟩

orientation is the hardest orientation in the TiN films due to geometrical strengthening [58,59]. The hardness is expected to increase as the ⟨111⟩ texture coefficient increases. Since ZrN has the same NaCl crystal structure as TiN, ⟨111⟩ is thus supposed to be the hardest orientation of the ZrN film. As shown in figure 4.6 (chapter 4) the ⟨200⟩ texture coefficient increases up to the sample prepared with reactive gas flow of 9 sccm. Comparing the trend of ⟨200⟩ texture coefficient with that of hardness (Fig. 7.6), the variation of the film hardness is not consistent with that of ⟨111⟩ preferential growth. This suggests that preferred orientation, although an important factor, in this the case, is probably not a major factor that affects the hardness.

So far, it has been shown in the previous sub-sections that none of the parameters isolated can explain the overall behaviour of hardness, being quite clear that not one of those but the conjugation of different parameters can account for the entire hardness (and Young's modulus) variation. In order to check for other possible parameters that may have a role in hardness variation, plots of hardness versus lattice parameter and grain size were produced, (see, Fig. 7.9). Due to the particular structural features (developed phases and high degree of peaks broadening), only samples from zone I will be checked in this sub-section.

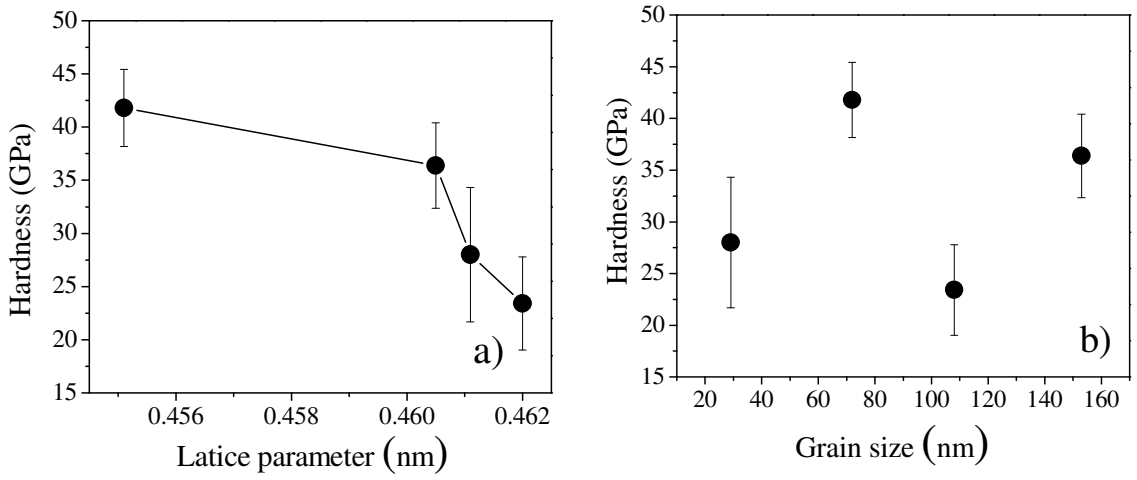


Fig 7.9. Hardness evolution as a function of; **a)** lattice parameter and **b)** grain size; for samples revealing a *fcc* ZrN-type structure. The error bar was determinate by maximum deviation to the average value.

Regarding the evolution of hardness as a function of lattice parameter (Fig. 7.9.a)), it is possible to observe that these samples present a decrease of hardness values with increasing lattice parameter. As already referred in chapter 3, the samples of zone I show a slight decrease

in the lattice parameter as a function of the increase of the of the non-metal to zirconium atomic ratio due to a better arrangement of the adatoms decreasing the lattice disorder, and decreasing the lattice parameter. Associated to this increase of metalloid content is the increase of covalent bonding character with the consequential increase of hardness.

Figure 7.9.b) shows that there is no correlation between the hardness evolution and grain size values indicating that no *Hall-Petch* effect (direct or inverse) is observed. This non dependence of the *Hall-Petch* effect should result from the composition variation which change from $(C_N+C_O)/C_{Zr}$ close to 0.5 through ~0.9.

The effect of macrostresses

Figure 7.10.a) shows the macrostress evolution as a function of reactive gas flow. For an easier analysis, the plot of hardness evolution is also shown in Fig. 7.10.b).

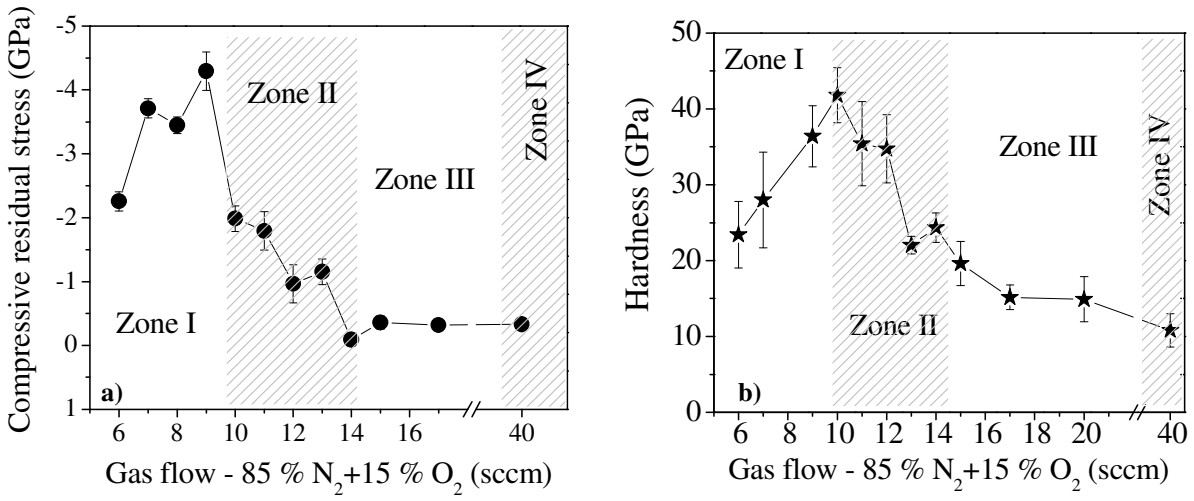


Fig. 7.10.a) Residual stress and **b)** hardness evolution; as a function of reactive gas flow. The error bar was determinate by maximum deviation to the average value.

In sputter deposited hard polycrystalline films, stresses are regularly observed. Compressive stress is generated by *atomic peening* mechanism: the creation of interstitials or implanted argon in the growing film [60].

The first important feature form both plots (Fig. 7.10.a) and b)) is that both properties reveal similar variation tendencies, meaning that beyond the already mentioned structural parameters, the compressive macrostress states of the samples is also a factor to take into account.

Nevertheless, there are also some particularities that may be worth mention. In fact, if these two properties are plotted one as a function of the other, these particularities maybe easier to observe, Fig. 7.11. This figure shows some increasing tendency of the hardest films to be those with higher macrostresses, namely in what concerns to the films within zones I and II. The relatively high macrostresses of samples from the first compositional zone is most likely to result from the already mentioned incorporation of oxygen within the ZrN lattice, which would induce lattice defects and thus increasing the stress levels.

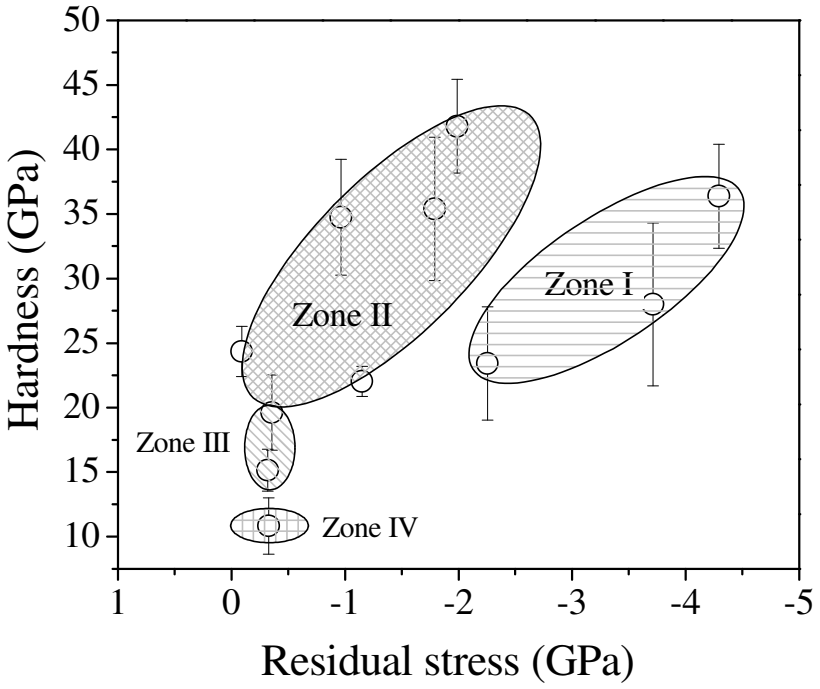


Fig. 7.11. Hardness evolution as a function of macrostress values for the samples belonging to series 1. The error bar was determinate by maximum deviation to the average value.

However, the hardest samples (those prepared with gas flows varying from 9 to 12 sccm, and having the hardness values ranging from ~35 to ~40 GPa), show macrostress states that actually decrease from ~ -4.5 to about -1 GPa. This clearly shows that stresses are still not the only important parameter for the interpretation of the hardness data. Moreover, a closer look to figure 7.11 shows that there are films with hardness values ranging from 20 to ~10 GPa (zones III and IV), but with similar macrostress values - around -0.5 GPa.

As a conclusion, it is possible to claim that the hardness evolution must be correlated with the different composition and structural features, including macrostress.

7.3.2. Adhesion

The knowledge about how coatings fail on coated parts/objects is essential to assess not only the system (coating + substrate) mechanical behaviour, but above all the coating suitableness for its particular purpose. In addition, the magnitude of the failure event is often more decisive to discriminate between different quality coatings than the difference in critical load values. Since the fundamental objective of this thesis was to produce decorative coatings, adhesion studies were only carried out in the samples that presented intrinsic coloration, namely those from the first two compositional zones. For comparison purposes, a sample belonging to the third zone (deposited with 17 sccm) and a ZrN coated sample were also included.

Figure 7.12. shows the "typical" failure events evolution of the zirconium oxynitride system with increasing load.

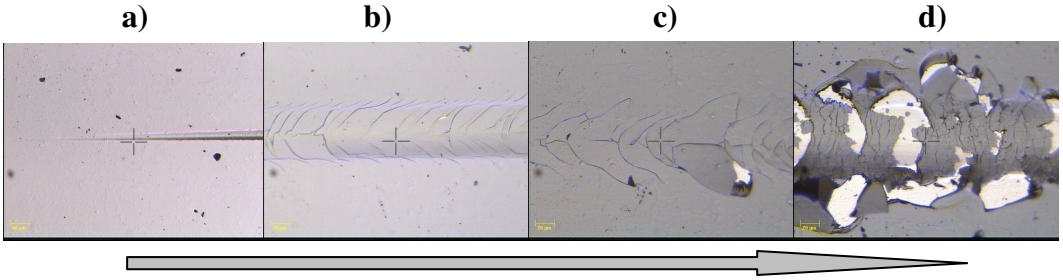


Fig. 7.12. "Typical" failure events evolution of the zirconium oxynitride system with increasing load.

The evolution of the failure events with increasing load is similar in all the analysed coatings (zone I, II and III) and is characterised by a plastic deformation of the coating without showing any failure event (Fig. 7.12.a)), followed by a *chevron* type crack with tensile type Hertzian cracks (Fig. 7.12.b)), with increasing load *conformal type buckling cracks* start to appear (Fig. 7.12.c)). Finally *gross interfacial shell-shaped spallation* (Fig. 7.12.d)) occur, marking what one could call the "end of the coating".

Figure 7.13. shows the critical loads of representative samples as a function of reactive gas flow. Lc_1 and Lc_2 represent the critical adhesion loads for the first cohesive and first adhesive failures, respectively, Lc_3 represents the load at which more than 50 % of the coating is removed from the substrate.

Regarding the evolution of critical load values (Fig. 7.13), the first general observation is that the adhesion of the samples to the substrate tend to decrease with the increase of the reactive gas flow and the consequential changes in composition and structure. *O. Banakh et al.* [61] studying the adhesion of magnetron sputtered tantalum oxynitride to high speed steel substrates, also claimed the decrease of coatings adhesion with increase of metalloid content.

Although the critical load values (L_{C1}, L_{C2} and L_{C3}) show a clear decrease tendency in the compositional zones analysed (zone I, II and III), some remarks regarding which specific zone should be made.

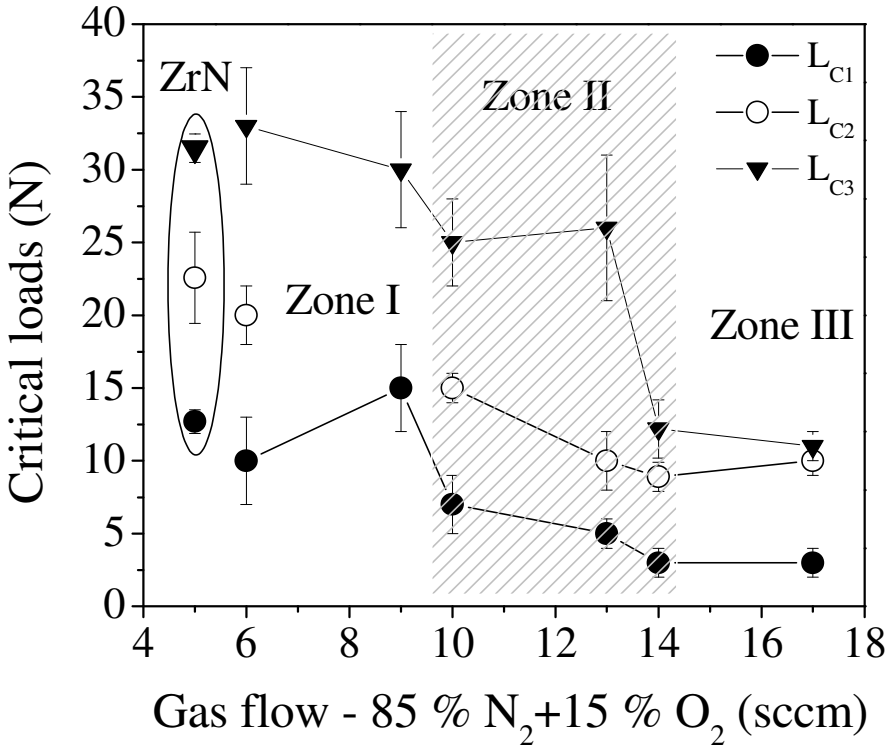


Fig. 7.13. Critical loads values as a function of reactive gas flow regarding zone I, II and III, series 1. For comparison purposes, a ZrN sample was also included. The error bar was determinate by maximum deviation to the average value.

The samples lying in the first zone (reactive gas flows below 10 sccm), present the highest critical load values L_{C1}, L_{C2} and L_{C3} in the zirconium oxynitride system, with similar values from the ones of the zirconium nitride sample. This was an expected result since these coatings present an *fcc*-ZrN(O) type structure (see chapter 3, Fig. 3.5) and a stoichiometry close to ZrN (see Fig. 2.15).

Regarding the samples lying in the second compositional zone, figure 7.13. shows a decreasing tendency of all critical loads values. Although this tendency the sample deposited with 14 sccm of the reactive gas flow present a small increase of the L_{C3} values. This increase may not represent a "real" increase of the L_{C3} values but resulting from the measurement resolution itself, since the error bar of this value is much higher than the other samples. The third zone reference sample presents similar values regarding the last sample of zone II.

Although compositional and structural features appear to present a dominant role in the critical loads evolution, other factors were also taken into account. Regarding the adhesion evolution as a function of the thickness of the coatings, both adhesion critical load values (L_{C2} and L_{C3}) increase with thickness as expected [63].

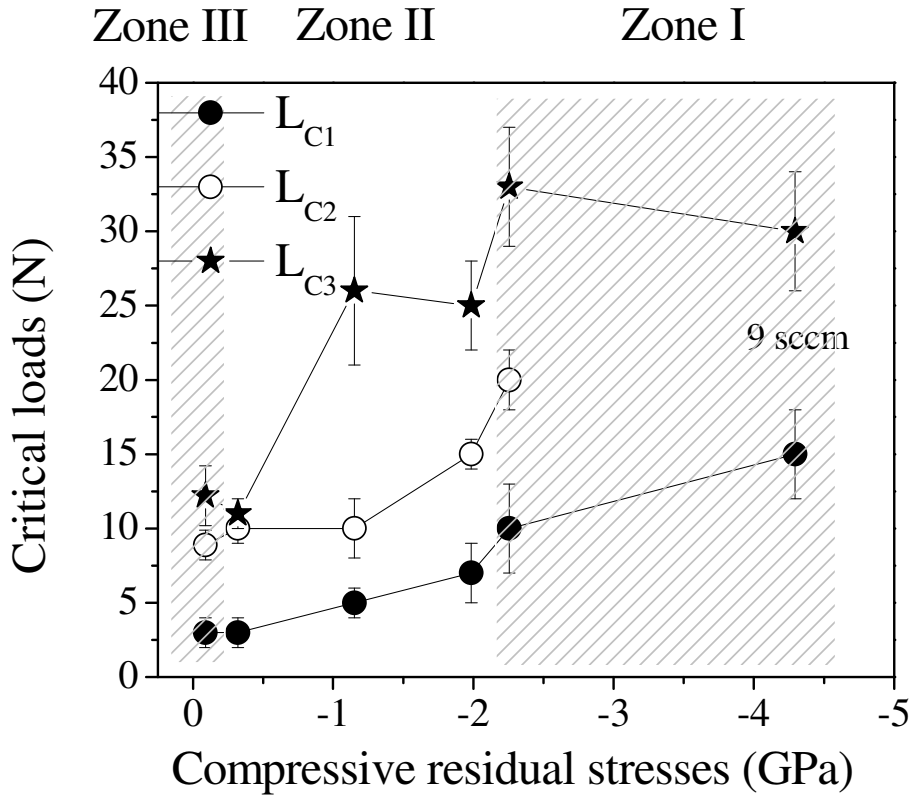


Fig. 7.14. Critical loads values a function of the macrostresses of the coatings. The error bar was determinate by maximum deviation to the average value.

Regarding the correlation between adhesion and macrostress, figure 7.14 presents L_{C1}, L_{C2} and L_{C3} values as a function of the macrostresses. This figure (Fig. 7.14) shows that critical load values trend to increase with macrostress. This tendency could indicate that the increase of

residual stress could be associated to the increase of adhesion, however this should not be the case.

It is expected that coatings with higher residual stress present higher tendency to flake or debond from the substrate with applied exterior loads. A close example of this behaviour is sample deposited with a reactive gas flow of 9 sccm, which doesn't present the second critical load value (L_{C2}) , and the first adhesion failure was characterized to be a *gross interfacial spallation*-type. This sample (9 sccm) present the highest macrostress and the highest hardness values (~4.3 GPa and ~42 GPa respectively).

In brittle films, if cohesive strength is higher than adhesion, the coating tends to debond or flake away at the edges of the groove [62].

The apparent correlation between the increase of adhesion with the increase of residual stress, should be a related with the specific type of material involved and the consequential changes in the interface strength. It must be remembered that the decrease of the macrostresses is correlated with the change in from ZrN(O) through Zr_3N_4(O) and Zr_2ON_2 compounds.

As a conclusion the adhesion of the coatings present a clear relationship with the compositional/structural zones. In spite of the basic deposition conditions of these coatings (no bias, no adhesion layer, no external heating) it appears they are enough to originate coatings with sufficient adhesion for using them in decorative applications. However, to improve adhesion several methods are possible to be applied, namely: using negative substrate bias, heating the substrate, using ion gun bombardment or deposit an interlayer [63].

7.3.3. Corrosion behaviour

Figure 7.15. shows the potentiodynamic polarization curves of representative samples from series 1, prepared with the variation of reactive gas flow. All potentials were measured and expressed with reference to a standard calomel electrode (SCE), and a platinum wire with an area of 1 cm^2, which was used as a counter electrode. For comparison proposes, the polarization behaviour of the substrate (M2 steel) is also plotted.

The plot clearly shows that the corrosion resistance and pitting of the of the coated M2 steel is clearly enhanced regarding the uncoated M2 steel. Similar results were reported by *E. Ariza et al.* [64] in the study of corrosion resistance of ZrN_xO_y thin films deposited by rf reactive magnetron sputtering.

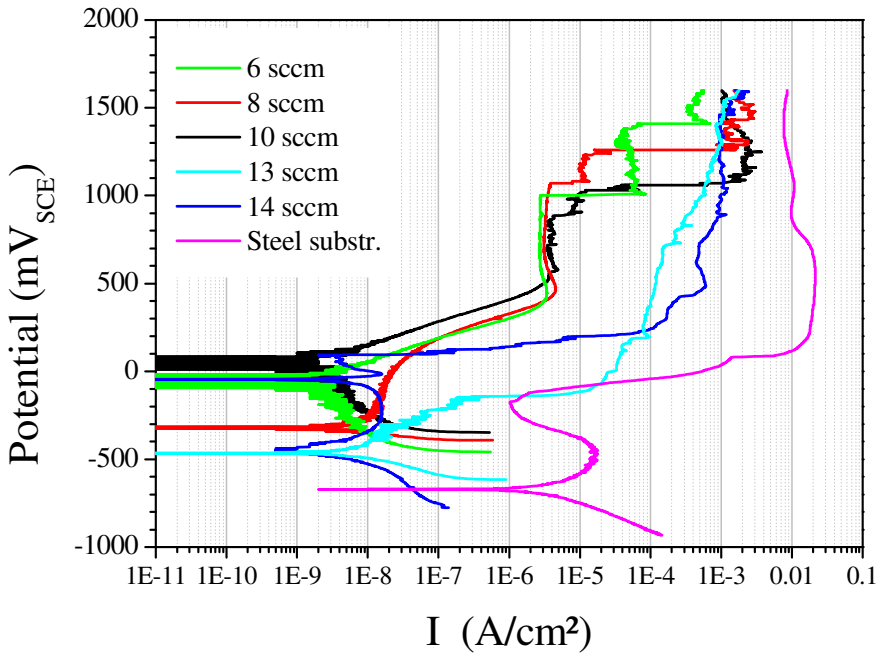


Fig. 7.15. Potentiodynamic polarization curves of representative of samples of series 1.

The first observation that can be drawn is the existence of two different potentiodynamic polarization behaviours for the samples deposited with reactive gas flow higher and lower than 10 sccm. The samples that still present the *fcc*-ZrN structure (prepared with a gas flow ranging from 6 to 10 sccm) revealed pitting potentials of about 1000 mV (SCE), showing at this values of pitting potential a well-defined large potential independent region, indicative of a passive plateau. These samples present a corrosion current density varying from ~0.1 to about 0.3 μA/cm^2, three orders of magnitude lower than the uncoated M2 steel. Similar values were obtained by *E. Ariza et al.* [64].

Regarding the samples deposited with reactive gas flows of 13 and 14 sccm, they present poorer corrosion behaviour, showing pitting potential values of ~200 and ~400 mV, respectively, and corrosion current densities close to 0.7 μA/cm^2. Although these samples present worse corrosion resistance, they still present a clear higher corrosion resistance if compared with the M2 steel.

Although composition and structural features appear, once again, to have an important influence in this property, in order to further understand the origin of the different corrosion behaviours, morphology (by Scanning Electron Microscopy) and surface analysis (by optical microscopy) were performed.

One important factor concerning the corrosion resistance is the quality of the film's surface. In fact, if one intends to use a particular part with a coating material, the number/density of surface defects will have a major role on the part oxidation/corrosion resistance, and thus a unique importance for the in-service behaviour and durability of the coated part. *E. Ariza et al.* [64] claimed that several features, such as the thickness of the film, the density of superficial defects and/or the chemical composition and morphology of the coatings are expected to influence the corrosion behaviour of zirconium oxynitride thin films. Figure 7.16 shows the film's surface defects density of representative samples from series 1. From this figure (Fig. 7.16) it is possible to observe an increase of density of defects for the samples deposited with reactive gas flow between 10 and 14 sccm. From the analysis of the density of defects and the potentiodynamic polarization curves (Fig. 7.16 and 7.15 respectively), it is possible to observe a close relationship between the corrosion behaviour and the surface quality.

The increase of density of defects is followed by a decrease of the corrosion resistance, indicating that the surface quality is a very important parameter for the corrosion resistance of the coatings. This could be explain by the fact that superficial defects can act as preferential routes for the penetration of the solution through the coating [65,66].

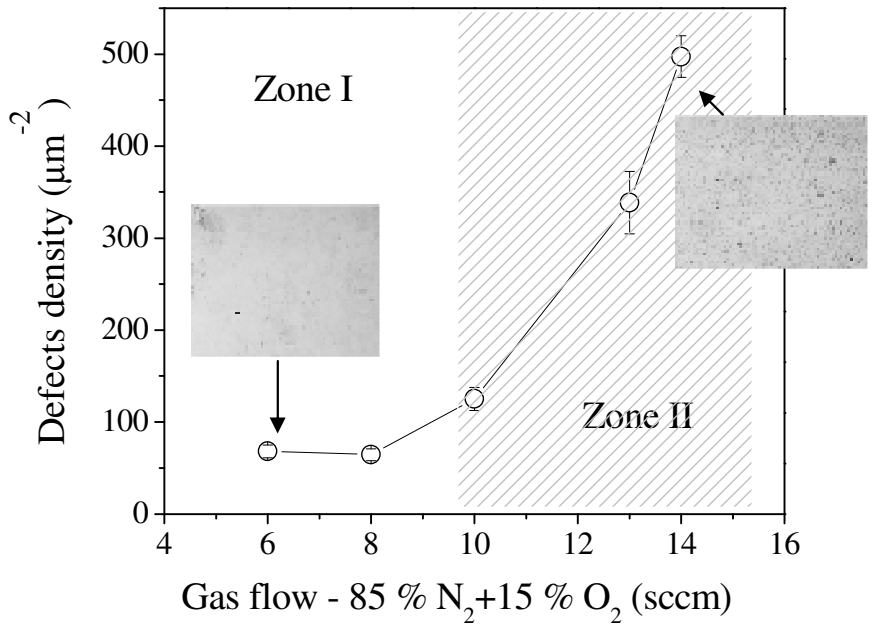


Fig. 7.16. Density of superficial defects of representative samples of series 1. The error bar was determinate by maximum deviation to the average value.

In order to further study the influence of other parameters in the corrosion resistance of the

coatings, a morphology study of the coatings were performed. Figure 7.17. presents Scanning Electron Microscopy (SEM) micrographs of the cross-section morphologies of those films that were previously indexed to zone I. For comparison purposes, Fig. 7.17.d) shows also the cross sections morphology of a "pure" ZrN film prepared in similar conditions as those of the ZrO_xN_y ones (no ion-bombardment, temperature, pressure, etc.), which, in fact, presents a very similar microstructure when compared to the other films belonging to this zone. From this figure it is possible to observe that the films grow with a compactly fibrous microstructure, with no clear development of the very common PVD columnar-type morphology. The increase of gas flow (moving towards the stoichiometric condition, see chapter 2) seems to result in less compact microstructures and more fibrous-type films or even to what may be called a "quasi" columnar-type morphology.

If indexed with the Thornton's zone model, the samples in this zone could be indexed to the zone I of Thornton's zone model, which is consistent with the ratio of the film melting and deposition temperature since these coatings present a T_s/T_m ratio lower than 0.14.

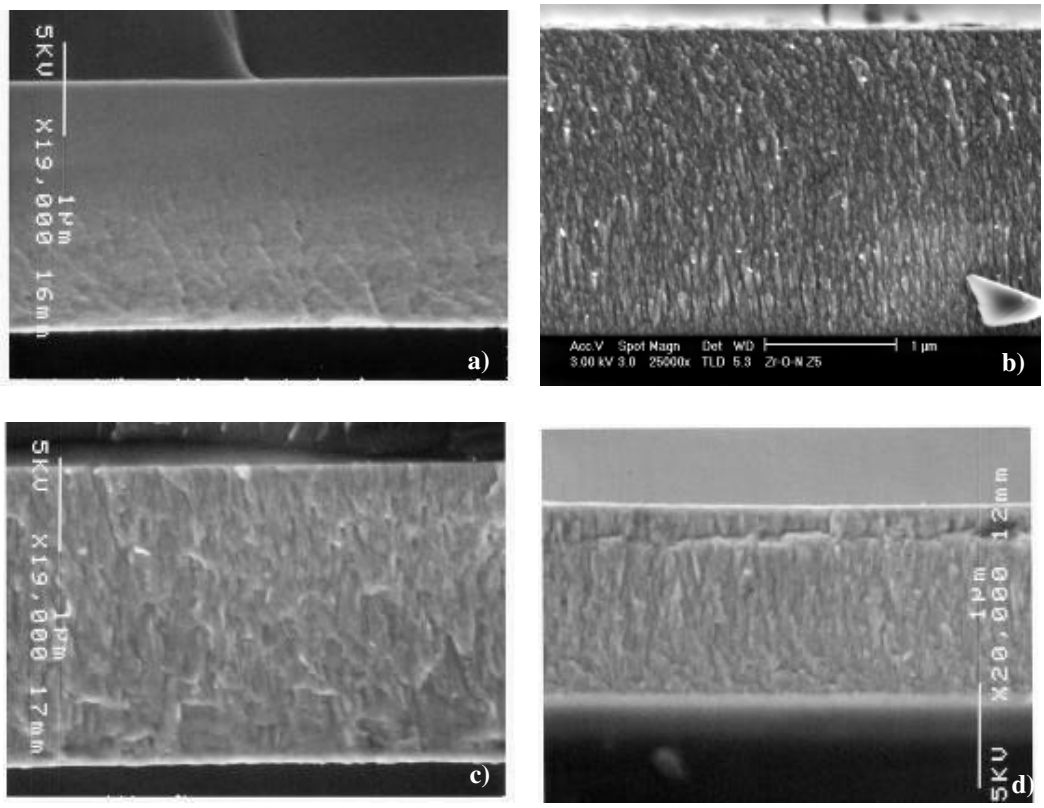


Fig. 7.17. SEM cross-sections of the films lying in the first zone. Films prepared with a gas mixture flows of; **a)** 6 sccm; **b)** 8 sccm and **c)** 9 sccm. The micrograph presented in **d)** corresponds to a "pure" ZrN film.

Figure 7.18. presents SEM cross-section micrographs of the samples that were indexed, from composition analysis, to zone II (series 1). From the observed micrographs, a first point seems quite clear, which is that one related with the notorious differences when comparing the edge samples (samples prepared with a gas flow of 10 sccm, Fig. 7.18.a) and 14 sccm, Fig. 7.18.d)) and those within this second zone. In fact, the sample deposited with gas flows of 10 sccm still presents clear traces of that fibrous microstructure of the films prepared within zone 1, while the sample prepared with 14 sccm is already revealing some differences from the previous samples, which in fact is similar to what will be shown for samples of zone III.

Regarding the films prepared within this second zone (excluding the edge ones), there is a clear change in their morphology, that changed from that fibrous microstructure (zone I) to quasi-featureless morphologies, micrographs from Fig. 7.18.b) trough c). Nevertheless, and although with the mentioned differences, the characteristic morphologies of these films should also be indexed to zone I of Thornton's zone model.

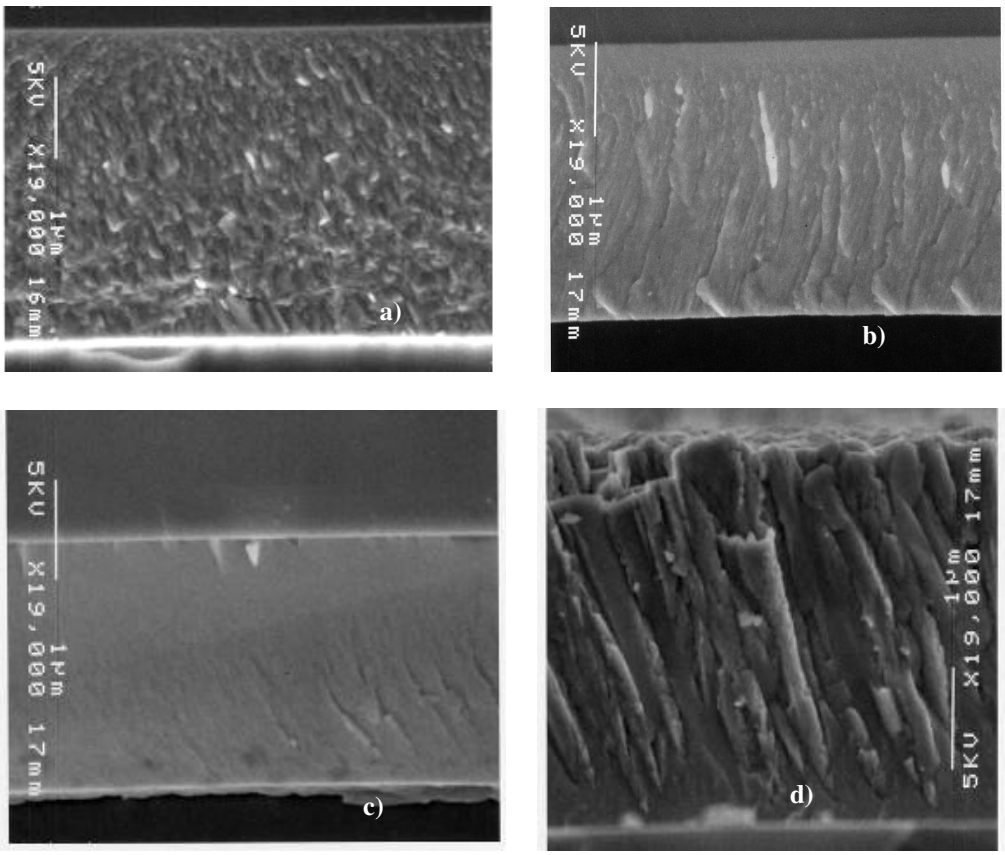


Fig. 7.18. Cross-sections observed by SEM of the films lying in the second zone of series 1; film prepared with a gas mixture flow of **a)** 10 sccm; **b)** 11 sccm; **c)** 13 sccm; and **d)** 14 sccm.

Regarding the upper limit of this second zone (sample prepared with a gas flow of 14 sccm represented in the micrographs Fig. 7.18.d)), the sample starts to develop a typical columnar microstructure with the development of a V-shaped morphology, where the columns present a superficial dome-rounded shape. This sample shows already some similarities to the morphological features of Thornton's transition zone, zone T.

With further increase of the reactive gas flow, zones III and IV (series 1), the micrographs of samples cross-sections (Fig. 7.19) showed that there are no significant changes in films morphology.

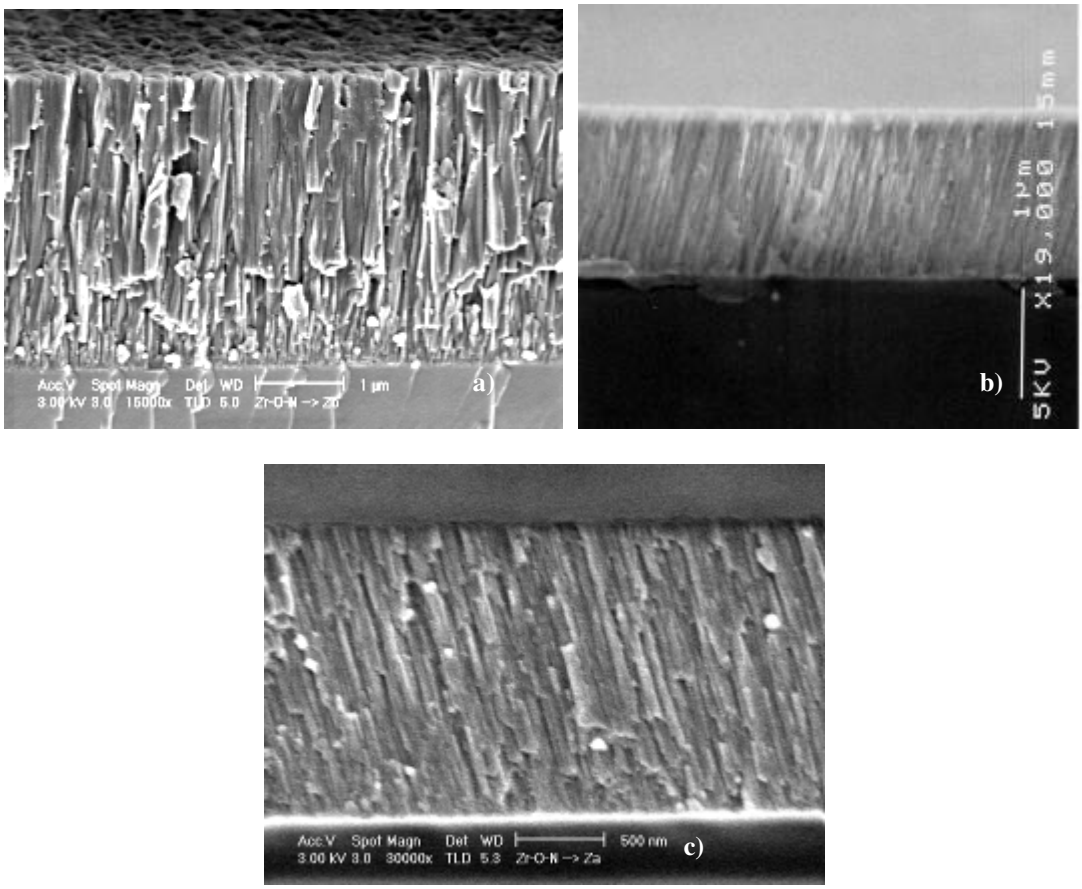


Fig. 7.19. Cross-sections observed by SEM of the films lying in zones III and IV of series 1; film prepared with a gas mixture flow of **a)** 17 sccm (zone III) and **b** and **c)** 40 sccm (zone IV).

The samples from zone III (Fig. 7.19.a)) present a less pronounced columnar morphology when compared to the sample deposited with a reactive gas flow of 14 sccm (upper limit of zone II), but the columns present also a superficial dome-rounded shape. The sample from the last

zone (zone IV) presents also a columnar morphology, with lees pronounced superficial dome-rounded shape. In terms of an indexation to the Thornton's zone model, both zones seem to develop thin films with a morphology that could be located between zone I and zone T.

Comparing the morphological features with the corrosion behaviour is possible to observe some coincident results. The samples presenting better corrosion behaviour (zone I) also present a compactly fibrous microstructure, with no clear development of columnar-type morphology. The samples deposited with 13 and 14 sccm which present a clear decrease in corrosion resistance regarding the samples lying in the first compositional zone, show a change from quasi-featureless morphology through well define columnar microstructure with the development of a V-shaped morphology. These results indicate that the morphology of the coatings could also play an important role in the corrosion resistance of the coatings.

Decorative coatings that are in contact with the human skin are exposed to corrosive sweat environments, and therefore need to be tested in these conditions and verify if the contact of the coating with the skin could release nickel from the stainless steel substrate. High doses of inorganic nickel may cause acute toxicity and is a frequent cause of contact dermatitis [67]. The results of the inductive coupled plasma spectrometer (ICP-OES) measurements of the artificial sweat solution after the tests (one week) regarding representative samples of series 1 are listed in table 7.1. Good results have been found for the selected zirconium oxynitride coatings. No release of elements from the SS316 (Fe, Ni, Cr) or from the coatings could be measured within the detection limit.

Reactive gas flow	Cr (mg/l)	Fe (mg/l)	Ni (mg/l)	Zr (mg/l)
8 sccm	<0.1	<0.1	<0.1	<0.1
10 sccm	<0.1	<0.1	<0.1	<0.1
13 sccm	<0.1	<0.1	<0.1	<0.1
14 sccm	<0.1	<0.1	<0.1	<0.1
M23 (SS316)	<0.1	<0.1	<0.1	<0.1

Table 7.1. Concentration of elements from the SS316 substrate (Fe, Ni, Cr) or from the zirconium oxynitride coatings of the artificial sweat solution after the tests.

Additionally, the colour change due to this test and the release of the zirconium into the electrolyte was tested. The influence of the artificial sweat test on the colour of the coatings can be seen in figure 7.20.

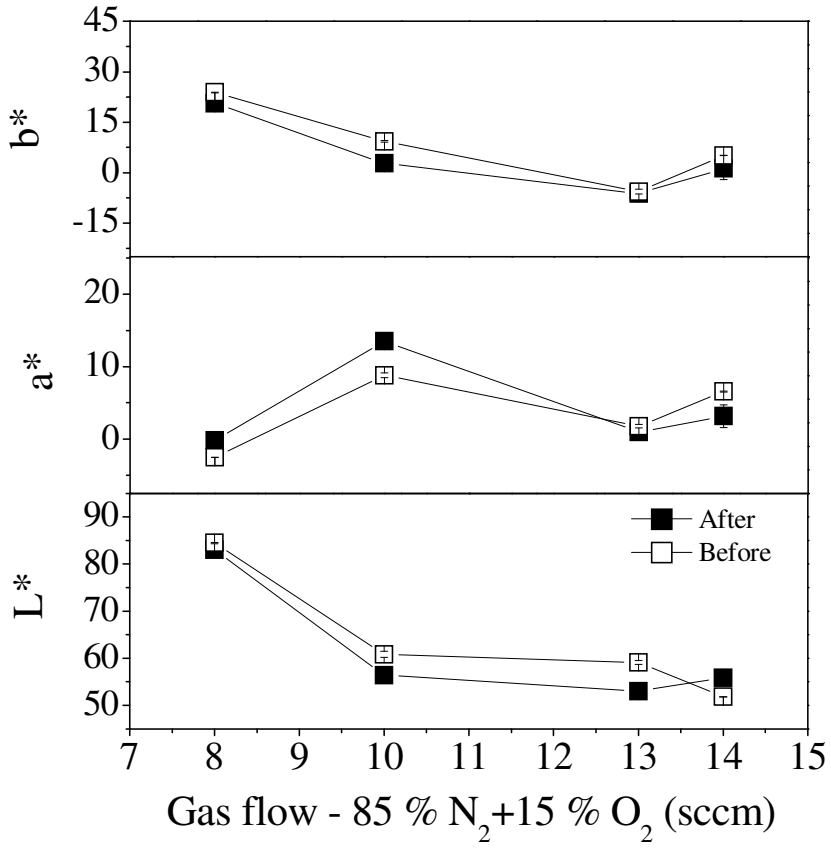


Fig. 7.20. Colorimetric coordinates CIELAB 1976 colour space [68,69] of representative of samples of series 1 before and after the artificial sweat test . The error bar was determinate by maximum deviation to the average value.

For the four analysed samples, the variation of the colour within the five measurements before and also after the artificial sweat test is negligible. The results of the artificial sweat tests revealed that decorative zirconium oxynitride coatings are very stable in artificial sweat solution and can be used in applications where the coated parts may be in contact with human skin. The coatings analysed present high colour stability against artificial sweat. Therefore, the chemical and colour stability is excellent for analysed decorative zirconium oxynitride films coated on stainless steel substrates.

7.3.4. Biocompatibility

Results from the cytotoxicity tests revealed an unusual finding. The cells grown on the control surface had visually a lower intensity of neutral red staining in their lysosomes as compared with the others groups. Similar findings were detected with the MTT conversion. Due to less intense staining with neutral red, the quantification of the neutral red uptake and the MTT conversion was lower in the control as compared to all other goups (Fig. 7.21.a) and b)) however no significant statistical differences were found between the control and the experimental groups regarding neutral red uptake or MTT conversion.

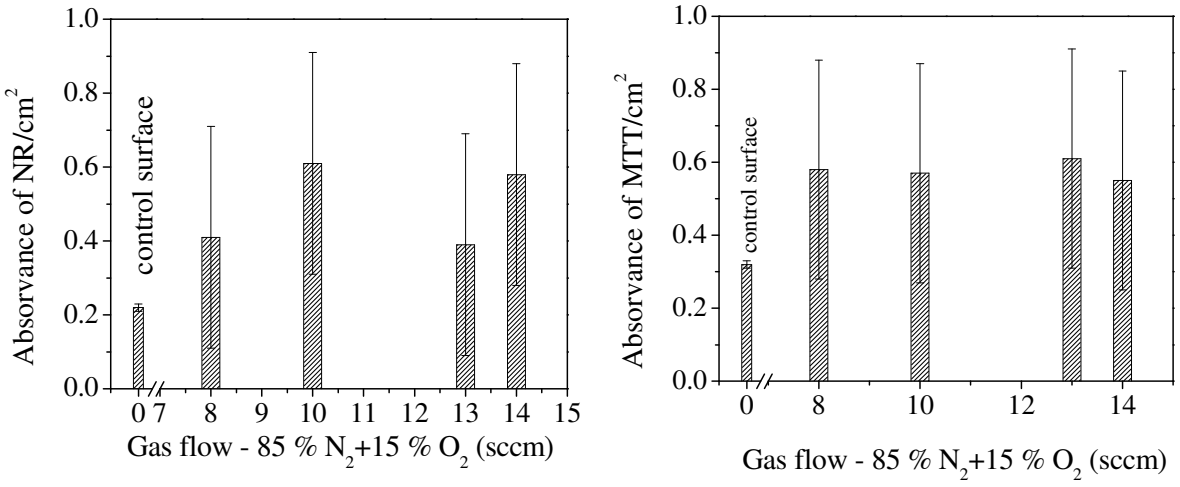


Fig. 7.21.a) Viability measured by neutral red uptake (NR); **b)** Metabolic activity measured by MTT conversion.

This results indicates good biocompatibility of the decorative zirconium oxynitride coatings.

7.4. Application of the deposited coatings in several parts.

Since one of the primordial application for the zirconium oxynitride system is in the decorative market in this section will be presented images of the film's appearance after coating the different substrates. Figure 7.22 present colour appearance from films used for property analysis, deposited using the gas mixture and RGGP system.

High speed steel

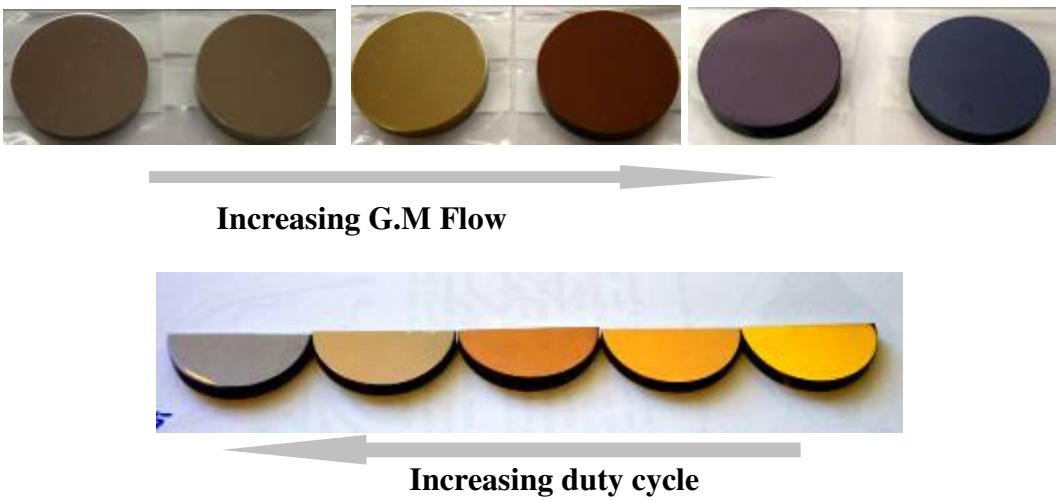


Fig 7.22. Photos of coatings deposited on high speed steel

Stainless steel

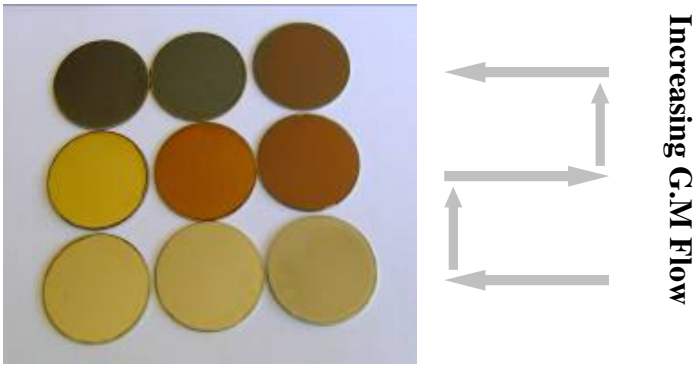


Fig 7.23. Photos of coatings deposited in stainless steel.

Beyond the substrates used for characterization techniques and to be subjected to the different property analyzes, there was another set of sample substrates, which were delivered by the industrial partners of the European project in which the work presented in this thesis is integrated. These substrates were also to be coated with zirconium oxynitride films. Figure 7.24. shows an image of these different substrates before coating deposition.

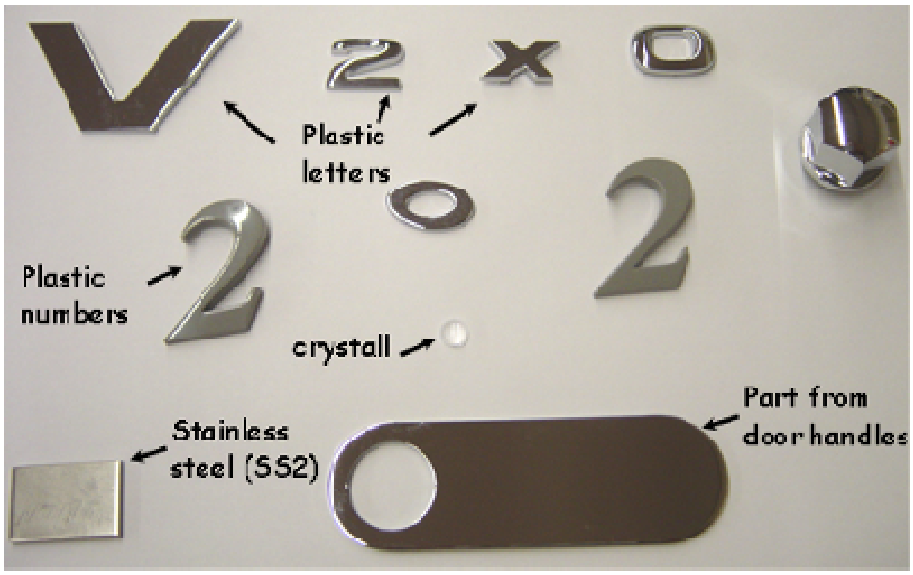


Fig. 7.24. Different substrates delivered by partners before film depositions

In figure 7.25 are presented photos of bathroom door-handles coated with different duty cycles. It is to mention that these substrates were coated using only the gas pulsing (RGPP) approach.



Fig. 7.25. Different coated bathroom door-handle.

Figure 7.26 show photos of different watch parts coated with different duty cycles.



Fig. 7.26. Different watch parts coated.

Figure 7.27 show photos of cutlery parts coated with different duty cycles.

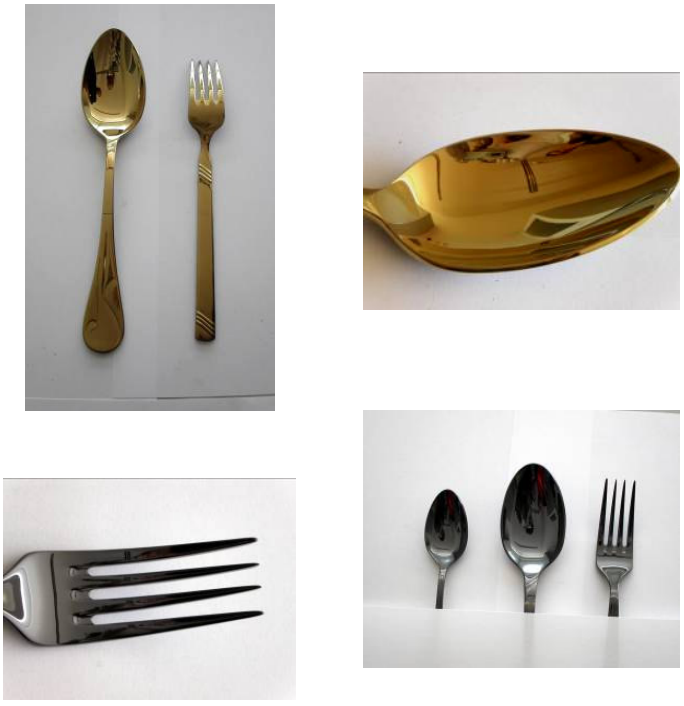


Fig. 7.27. Different cutlery parts coated

All the coatings deposited in metallic substrates presented high colour homogeneity and appear to have good adhesion since any of the coated pieces show flaking or debonding of the thin film. Figure 7.28 show photos of car accessories (polymeric substrates) coated with different duty cycles.



Fig. 7.28. Different car accessories coated.

Figure 7.29 show photos of plastic and crystal parts coated with different duty cycles.

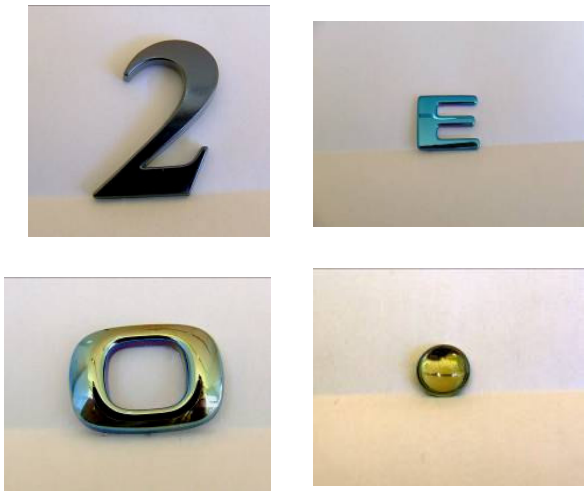


Fig. 7.29. Different plastic and crystals parts coated.

Regarding the polymeric and glass substrates the colours homogeneity is similar to that one achieved with the metallic substrates but these coatings present lower adhesion to these kind of substrates.

7.5. Conclusions

The zirconium oxynitride coatings which show intrinsic coloration (zone I and II) show that, in spite of the basic conditions selected for these samples (no ion bombardment, now external heating and no adhesion layer), the coatings present good mechanical properties.

These coatings present hardness values higher then 20 GPa and Young's Modulus higher then 250 GPa. Regarding adhesion, the coatings lying in the first compositional zone present critical load values similar to zirconium nitride. The samples lying in the second compositional zone show a decrease of the critical load values indicating a decrease of the adhesion of the coatings to the substrate. However, due to the basic deposition conditions a better adhesion is expected when using negative substrate bias, substrate heating and/or deposition of an interlayer.

Regarding the corrosion behaviour, a similar evolution was verified with the samples belonging to zone I showing similar corrosion resistance as zirconium nitride. The samples belonging to the second zone present lower corrosion resistance. However, the introduction of an interlayer, should increase the corrosion resistance performance of the coatings, serving as an extra barrier to corrosion.

The biocompatibility and the artificial sweat test showed that these coatings can be successfully used in decorative applications that that may be in contact with human skin.

The application of the zirconium oxynitride coatings in real parts shows promising results. All the coatings present very good colour homogeneity and present good adhesion to metallic substrates, however the coatings deposited in polymeric substrates showed tendency to debond.

7.6. References

[1]- L. Hultman, Vacuum 57 (2000) 1.

[2]- S. Ventkartaraj, O. Kappertz, R. Jayavel, M. Wuttig, J. Appl. Phys. 92 (5) (2002) 2461.

[3]- L.E. Toth, *Transition Metal Carbides and nitrides*, Academic, New York, 1971.

[4]- P. Honer, R. Sanjines, F. Lévy, Surf. Coat. Technol. 94/95 (1997) 398.

[5]- J.H. Kang, K.J. Kim, J. Appl. Phys. 86 (1) (1999) 346.

[6]- T. Takahashi, Y. Oikawa, T. Komori, I. Ito, M. Hashimoto, SW & Coating 51 (1992) 522.

[7]- A.A. Bauer, Reactor Technol. 15 (1972) 87.

[8]- J. E. Sundgren, Thin Solid Films 128 (1985) 21.

[9]- W.D. Sproul, J. Vac. Sci. Technol. A 4 (6) (1986) 2874.

[10]- H.K. Pulker, Coatings on glass, *Thin Film Science and Technology*, vol. 6, Elsevier, Amsterdam, 1984.

[11]- H. Bach, N. Neuroth, *The Properties of Optical Glass*, Springer, Heidelberg, 1995.

[12]- T. Koch, P. Ziemann, Thin Solid Films 303 (1997) 122.

[13]- F. Jones, J. Vac. Sci. Technol. A 6 (1988) 3088.

[14]- Zirconia'88, *Advances in Zirconia Science and Technology*, edited by S. Meriani, Elsevier, New York, 1989.

[15]- V. M. M. Mercier, P. Van der Sluis, Solid State Ionics 145 (2001) 17.

[16]- W. H. Lowdermik, D. Milam, F. Rainer, Thin Solid Films 73 (1980) 155.

[17]- D. Tabor, *The Hardness of Metals*, Clarendon Press, Oxford, 1951.

[18]- L.M. Qian, X.D. Xian, Q.P. Sun, T.X. Yu, Appl. Phys. Lett. 84 (2004) 1076.

[19]- L.M. Qian, F. Tian, X.D. Xiao, Tribol. Lett. 15 (2003) 169.

[20]- L.M. Qian, G. Luango, E. Perez, Europhys. Lett. 61 (2003) 268.

[21]- J.Haines, J.M. Léger, G. Bocquillon, Annu. Rev. Mater. Res. 31 (2001)

[22]- Albano Cavaleiro, Jeff Th. M. De Hosson, *Nanostructured Coatings*, Series Editor: David J. Lockwwood, FRSC, Ontario, Canada, 2006.

[23]- A. Trindade, A. Cavaleiro E J. Fernandes, Journal of Testing and Evaluation, 22 (4) (1994) 365.

[24]- J. Musil, F. Kunc, H. Zeman, H. Poláková, Surf. Coat. Technol. 154 (2002) 304.

[25]- L. McClaine, C. Coppel, A. D. Little Inc. tech. Rept. AFML-TR-65-299, part I (1965).

[26]- J.M. Antunes, A. Cavaleiro, L.F. Menezes, M.I. Simões, J.V. Fernandes, Surf. Coat. Technol. 149 (2002) 27.

[27]- H.S. Kim, Scr. Mater. 39 (8) (1998) 1057.

[28]- J.A. Thornton, D.W. Hoffman, Thin Solid Films 172 (1989) 5.

[29]- P.A. Flinn, D.S. Gardner, W.D. Nix, IEEE Trans. Electron Devices ED-34 (13) (1987) 689.

[30]- C. Hudson, R.E. Somekh, J. Vac. Sci. Technol. A 14 (4) (1996) 2169.

[31]- V. Teixeira, M. Andritschky, W. Fischer, H.P. Buchkremer, D. Stöver, J. Mat. Proc. Technol. 92-93 (1999) 209.

[32]- Maple V release 5.00a - MVR4 Campus Wide Version, Waterloo Maple Inc.

[33]- G. G. Stoney, Proc. R. Soc. Lond. A 82 (1909) 172.

[34]- S.J. Bull, D.S. Rickerby, *Advanced Surface Coatings*, Chapman and Hall, 1991, p. 315.

[35]- R. Jacobson, Thin Solid Films 34 (1976) 191.

[36]- J. Valli, J. Vac. Sci. Technol. A 4 (6) (1986) 3007.

[37]- Fresenius, J. Anal. Chem. 358 (1997) 281.

[38]- A.J. Perry, Surface Eng. 2 (3) (1989) 183.

[39]- Corrosion education Manual, Swedish Corrosion Institut, Stockholm, 1974.

[40]- DIN 50 900 Blatt 1, Beuth Verlag Berlin, April 1982.

[41]- H.A. Jehn, Surf. Coat. Technol. 125 (2000) 212.

[42]- F. Altmayer, Choosing an accelerated corrosion test, in: M. Murphy (Ed.), *Metal Finishing*: 65th Guidebook and Directory Issue 97, Elsevier, New York, 1997, p. 559.

[43]- H.A. Jehn, A. Zielonka, Corrosion Testing, ASM Handbook, Vol. 5: Surface Engineering, ASM, 1994, p. 635.

[44]- Williams DF, ed. Definitions in biomaterials: progress in biomedical engineering. Amsterdam: Elsevier, 1987

[45]- I. Gerber, I. Gwynn, M. Alini, T. Wallimann. Eur Cell Mater 10 (2005) 8.

[46]- S. Buzzi, K. Jin, P.J. Uggowitzer, S. Tosatti, I. Gerber, J.F. Loffler, Intermetallics, 14 (7) (2006) 729.

[47]- J. Haines, J.M. Léger, G. Bocquillon, Annu. Rev. Mater. Res. 31 (2001) 1.

[48]- S. Veprek, A.S. Argon, J. Vac. Sci. Technol. B 20 (2) (2002) 650.

[49]- H. Holleck, J. Vac. Sci. Technol. A 4 (1986) 2661.

[50]- F. Lévy, P. Hones, P.E. Schmid, R. Sanjinés, M. Diserens, C. Wiemer, Surf. Coat. Technol. 120–121 (1999) 284.

[51]- P. Carvalho, F. Vaz, L. Rebouta, L. Cunha, C. J. Tavares, C. Moura, E. Alves, A. Cavaleiro, Ph. Goudeau, E. Le Bourhis, J. P. Rivière, J. F. Pierson, O. Banakh, , J. A ppl. Phys. 98 (2005) 023715-1-8.

[52]- D. Sherman, D. Brandon, *Handbook of Ceramic Hard Materials*, edited by Wiley-VCH, New Jersey, 2000.

[53]- W. S. Williams, Mater. Sci. Eng. A 105/106 (1988) 1.

[54]- S.-H. Jhi, J. Ihm, S. G. Louie, M. L. Cohen, Nature (London) 132 (1999) 152 .

[55]- S.-H. Jhi, J. Ihm, Phys. Rev. B 56 (1997) 13826.

[56]- X. Jiang, M. Wang, K. Schmidt, E. Dunlop, J. Haupt, W. Gissler, J. Appl. Phys. 69 (1991) 3053.

[57]- Seung-Hoon Jhi, Phys. Rev. Lett. 86 (15) (2001) 3348.

[58]- Z. Wokulski, Phys. Status Solidi (a) 120 (1990) 175.

[59]- W.-J. Chou, G.-P. Yu, J.-H. Huang, Surf. Coat. Technol. 140 (2001) 206.

[60]- F. M. D'Heurle, Metall. Trans. 1 (1970) 725.

[61]- O. Banakh, C. Csefalvay, P.-A. Steinmann, M. Fenker, H. Kappl, Surf. Coat. Technol. 200 (2006) 6500.

[62]- F. Ashrafizadeh, Surf. Coat. Technol. 130 (2000) 186.

[63]- R.F. Bunshah, *Handbook of Hard Coatings*, Noyes Publications, New Jersey, 2001.

[64]- E. Ariza, L.A. Rochaa,b, F. Vaz, L. Cunha, S.C. Ferreira, P. Carvalho, L. Rebouta, E. Alves, Ph. Goudeau, J.P. Rivière, Thin Solid Films 469-470 (2004) 274.

[65]- L.A. Rocha, E. Ariza, J. Ferreira, F. Vaz, E. Ribeiro, L. Rebouta, E. Alves, A.R. Ramos, Ph. Goudeau, J.P. Rivière, Surf. Coat. Technol. 180-181 (2004) 158.

[66]- C. Liu, Q. Bi, A. Matthews, Corros. Sci. 43 (2001) 1953.

[67]- Ilko Kuljanac, Eva Knežević, Hrvoje Cvitanović, Med Jad 36 (3-4) (2006) 87.

[68]- Colorimetry, CIE Publ. (Commission Internationale de L'Éclairage) 15 (1971).

[69]- Recommendations on Uniform Color Spaces, Difference-difference equations, psychometric color terms, CIE Publication, Suppl. Nº 2-70 (Commission Internationale de L'Éclairage) 15 (1978).

Outputs and Future Research

This Ph.D. project aim was the development of new functional coatings, mostly for decorative applications, but also to explore new application areas, including micro-optoelectronics, electric, mechanical and other optical applications that may arise from the most relevant results. On this basis, coatings from the ternary system of zirconium oxynitride, ZrO_xN_y, were deposited on several different substrates and a detailed characterization of their most relevant properties was carried out.

The ZrO_xN_y coatings were prepared by reactive DC sputtering using different processing conditions (reactive gas mixtures and bias voltages). In order to further explore the potentialities of this system, a new gas feed method was also used - the *R*eactive *G*as *P*ulsing *P*rocess: RGPP, by pulsing the admission of one of the most important elements for these coatings, because of its reactivity: the oxygen.

The general idea within this work was basically to combine the excellent mechanical properties of the well known nitrides, such as zirconium nitride, ZrN, with the specific optical characteristics of the correspondent oxides, ZrO_2 in the present case. By tuning the deposition conditions, it was possible to obtain coatings with compositions varying from nitrides to oxides, thus allowing exploring a wide range of electrical, optical and functional properties.

Regarding the most relevant conclusion, it might be worth mention that a systematic decrease in the deposition rate with the increase of the oxygen content (increase of reactive gas flow or duty cycle) was observed, revealing the existence of three main sputtering modes – a metallic mode, a transition mode and an oxide mode. These different modes can be explained by the target poisoning by the reactive gases, nitrogen and oxygen.

The composition variations were obtained by the variation of the reactive gas mixture flows, and beyond the upper mentioned different sputtering modes, it was also possible to conclude about the existence of four different regions of films, which were shown throughout the all text that were consistent with the different behaviours that were observed in the films. The electrical, optical and mechanical properties were a particular case of such influence.

These different regions were explained taking into account the variations in the film's concentrations, which was then used to explain the film's bonding structure and structural

features. The combination of composition, electronic and crystalline structure was essential to understand the particular features of the electrical, optical and mechanical properties of the films.

Structural characterization revealed a strong dependence on the oxygen content, exhibiting a change from a face centred cubic B1 NaCl-type films for low gas flows or low duty cycle (low oxygen contents) to a structure that might be similar to that of Zr_3N_4, with oxygen inclusions, at intermediate gas flows or duty cycles (intermediate oxygen contents). For relatively high gas flows or duty cycles (high oxygen amounts), the films exhibited only crystalline structures that were indexed as oxynitride and oxide phases. These structural changes were straightly connected with the particular bonding characteristics of the films, and also correlated with their electrical, optical and mechanical properties.

In terms of electronic structure, the films are ruled by the Zr 4*p* levels, but the O 2*s,* N 2*s* and molecular orbitals associated with O 2*p*/N 2*p* and Zr 4*d* valence levels. Going from zone I to zone IV, the films present a progressive transfer of zirconium 4*d* valence electrons to the O 2*p* and N 2*p* bands, with a shift to lower energies of the "*p band"*, until the complete depopulation of the *d-band*, where the films become of insulator-type. These electronic structure evolutions were also correlated with the electrical and optical properties of the films.

Regarding the electrical features, the initial low values of resistivity was found to be related with the roughly metallic nature of the films, with compositions between that of Zr and sub-stoichiometric ZrN(O). The resistivity of the films increased with the increase of the oxygen content, which can be explained by the decrease the metallic bond contribution and the formation of an oxygen-doped ZrN crystalline phase towards a nitrogen + oxygen rich phase, quite similar to that of Zr_3N_4. Particularly noticeable was the result of electrical resistivity of films for intermediate oxygen contents (between about 8 to 15 at. % - films from zone II), where in spite of the films were revealing almost no changes in Zr and N contents, the resistivity values increased about twelve orders of magnitude (~10^3 to ~10^{15} μΩ cm), which may be a relevant result for the future application of these films in other devices beyond those of purely decorative purposes. For very high oxygen contents, films revealed to be very close to a ZrO_2-type stoichiometry, and thus the electrical behaviour was correspondent to the expected for such compounds: very high values of resistivity, around that value of 10^{15} μΩ cm.

Regarding the optical evolution of the zirconium oxynitride coatings, similarly to what was observed in the electrical evolution, three major behaviours were again observed. For films

within compositional zone I, results revealed the presence of films that present an optical behaviour similar to zirconium nitride, with high reflectivity near the infra read region, and a minimum in the visible range. In zone II, with the formation of the Zr_3N_4(O)-type structure, the films presented almost constant low values of reflectivity, showing optical constants characteristic of the Zr_3N_4 phase. In the last two zones, the coatings presented a semi-transparent optical behaviour, showing an optical band gap close to ~4 eV, in close agreement with the results obtained by XPS- valence band, where a energy gap between the top of the valence band and the Fermi level close 5eV was observed.

The colour of the coatings in the first two compositional zones changes from a very bright yellow-pale in the metallic regime to golden one in zone I, to red-brownish and dark blue in zone II. Films from Zones III and IV had only interference-like colorations, consistent with their semi-transparent characteristics.

Regarding the functional properties, the coatings which presented intrinsic colorations (films from zones I and II) revealed promising results for decorative applications, with a relatively wide pallet of colours, as previously mentioned. The hardness and adhesion behaviour showed the existence of a strong correlation with the different compositions and crystalline structures, revealing relatively high values for the films from the ZrN-like films - Zone I, followed by a systematic decrease of these film properties within the last three zones. The films with intrinsic coloration, presented critical adhesion loads and hardness values similar or even higher than those of zirconium nitride, which are known to be widely used for decorative applications, thus reinforcing the positive properties of these films. Anyway, if the adhesion of the films to high speed steel, stainless steel, silicon, brass and other metallic substrates appears suitable for decorative applications, on the other way around, the application of these coatings in polymeric substrates indicated that further studies are recommended in order to optimize the adhesion. On this basis, depositions using negative substrate bias voltage and the use of interlayers are recommended.

Regarding corrosion, the potentiodynamic polarization tests revealed that the deposited films clearly improve the corrosion properties of the coated substrates (M2 steel was selected) and the artificial sweat tests showed that no release of elements from the coated substrate (AISI 316) or from the coatings to the artificial sweat. From the cytotoxicitytests were possible to conclude that zirconium oxynitride coatings present good biocompatibility.

The set of all these results reinforce our positive opinion about he use of these coatings in decorative applications, but also to explore other possibilities in electrical, mechanical and optical devices.